# Mechanical confinement induces the emergence of a unique bacterial phenotype characterized by major changes in cell growth and size

Laure Le Blanc

Université Paris Cité
École Doctorale Frontière de l'Innovation en Recherche et Éducation (ED 474)
Spécialité Sciences du Vivant appliquées et Biotechnologies
Unité Pathogénèse des Infections Vasculaires, Institut Pasteur

# Mechanical confinement induces the emergence of a unique bacterial phenotype characterized by major changes in cell growth and size

Thèse de doctorat
soutenue publiquement par

**Laure LE BLANC**

Le 25 Septembre 2023

Dirigée par Guillaume DUMÉNIL & Daria BONAZZI
En collaboration avec Morgan DELARUE

Devant le jury composé de:

| | | |
|---|---|---|
| Pr. Charles BAROUD | École Polytechnique | Président |
| Pr. Petra LEVIN | Washington University in St Louis | Rapportrice |
| Dr. Alexandre PERSAT | EPFL | Rapporteur |
| Dr. Christophe BELOIN | Institut Pasteur | Examinateur |
| Dr. Guillaume DUMÉNIL | Institut Pasteur | Directeur de thèse |
| Dr. Daria BONAZZI | Institut Pasteur | Co-directrice de thèse |
| Dr. Morgan DELARUE | LAAS-CNRS | Membre invité |

# Mechanical confinement induces the emergence of a unique bacterial phenotype characterized by major changes in cell growth and size

Laure LE BLANC

# Thank you !

Merci à toutes les personnes qui ont participé de près ou de loin à l'accomplissement de ma thèse et à mon épanouissement personnel.

**Guillaume,** merci de m'avoir donné l'opportunité d'effectuer cette thèse au sein d'un environnement très interdisciplinaire, de m'avoir fait confiance et d'avoir cru en moi au cours de ces années.
**Daria,** merci pour ton soutien, ta présence et ton humanité. Merci aussi pour ta précieuse aide, notamment au cours de la préparation de la présentation de thèse.
Guillaume, Daria, je vous remercie tout particulièrement pour la liberté que vous m'avez laissée. Je ressors grandie, fière du travail effectué, accomplie scientifiquement, confiante pour l'avenir, et prête à continuer la recherche avec autant d'implication et de passion.

**Sylvie,** merci pour toutes les souches que tu as construite dans le cadre de mon projet. Merci aussi pour tout ce que tu m'as appris en microbiologie.
**Morgan,** merci pour ton énorme soutien quand j'essayais de faire marcher les puces en silicium, lors du développement des puces en PDMS, et lors du développement de la valve de quake. Merci de m'avoir toujours chaleureusement accueillie au LAAS, où j'ai toujours été ravie de me rendre. Aussi, ça n'a pas été évident de monter ce genre de manips dans un labo dont ce n'était pas le domaine d'expertise, mais ça a toujours été rassurant pour moi de savoir que tu serais disponible pour en discuter, si jamais j'étais vraiment à court d'idées.
**Baptiste,** merci pour ton investissement grandissant dans le projet. Merci pour ton aide essentielle dans le développement des puces en PDMS pour bactéries, pour ta présence lors de mes missions souvent riche en péripéties.
**Laurent,** merci pour ton expertise, ta sympathie et surtout ton investissement. Tu as toujours fait de ton mieux pour débugger le stepper (souvent capricieux !), et je t'en suis très reconnaissante. Merci aussi de toujours t'être beaucoup intéressé au projet et à ce que je faisais à Pasteur, ça m'a toujours fait chaud au cœur.
**Ivan, Maureen, Marie-Flo,** merci pour votre entrain et l'aide cruciale en microbiologie que vous m'avez apportée. Merci Ivan pour toutes les souches originales, dont j'ai rapidement compris que ton labo était une véritable mine d'or.
**Samy, Jérôme, Emmanuel,** merci infiniment pour les équipements à la plateforme microfluidique, pour vos conseils, pour votre disponibilité et votre sympathie. Sans vous, je n'aurais jamais pu fabriquer une puce, et donc jamais pu faire mon projet.
**Jean-Yves,** merci pour ta bienveillance et ton entrain quotidien. Merci infiniment pour l'opportunité que tu m'as donnée, en m'incluant dans le projet TrackMate. Ça a été un plaisir de travailler avec toi, et merci d'avoir été autant fasciné par les images de microscopie que je générais.

**Laura,** tu es arrivée récemment, il y a un peu plus d'un an dans le cadre de ton stage de M2, dont l'objectif principal était d'adapter la pipeline d'analyse d'image que j'avais développée en agar pad, dans le confineur de bactéries. Depuis un an, tu travailles à mes côtés et je t'en remercie infiniment. Déjà, merci pour ton travail et ton aide sans limite. Au début, j'ai eu du mal à déléguer, à laisser quelqu'un faire ce que je faisais. Mais finalement, tu étais aussi perfectionniste que moi, et j'ai rapidement vu, que ce qui était fait, l'était parfaitement. Merci aussi pour ce que tu m'as appris, en termes d'encadrement. J'ai beaucoup appris grâce à toi, et je suis ravie que l'on ait si bien travailler ensemble.
**Molly, Laura et Léa,** merci pour votre motivation grandissante !
**A tous mes incroyables collaborateurs,** vous avez été essentiels ! Merci de croire en ce projet, de vous investir comme vous le faites, et de permettre à ce projet, que j'ai la chance de mener, de briller.

**Aux membres du jury,** merci d'avoir accepté d'évaluer ma thèse.
**Charles,** merci de m'avoir recommandé le labo de Guillaume il y a quatre ans, et d'avoir accepté d'être le président du jury.
**Christophe,** merci pour ton entrain, de nous avoir mis sur la piste Rcs, et de ton aide si bienveillante. Je garde un excellent souvenir des JDD de microbio.
**Petra,** thank you for learning me everything in terms of bacterial division. This was very important for the project. Your papers are always clear and concise, even for people who were not familiar with the field at the beginning. Thank you for your very constructive feedbacks. I am very happy that you come here, and I hope you will have good memories about your stay in Paris.
**Alex,** since my first year of PhD, I know that I would be happy if you reviewed my PhD work. Your work in general is very inspiring to me. I am very glad that we met at the EMBL conference in Heidelberg. As I told you, this week, you and your lab really question the next episode of my scientific carrier.

**Margot,** tu es la transition parfaite vers le monde non-professionnel. Merci pour ta présence ces quatre années : on a commencé notre thèse ensemble, et on la finira (presque) ensemble. Au-delà d'être une collègue, on a rapidement formé un binôme inséparable, qui nous a bien aidé à avancer le long de ce chemin sinueux et escarpé. Je garderai toujours un excellent souvenir de ces soirées, derrière le rideau du microscope, pendant lesquelles j'étais en train de lancer mes manips, et où tu me rejoignais pour discuter. Ces moments-là vont me manquer.
**Léa,** je te remercie d'être arrivée au labo. Après ton arrivée, j'avais enfin une oreille à qui parler des soucis du quotidien rencontrés par tout microfluidicien !
Je remercie aussi tous **mes amis,** de prépa, de l'ESPCI, et de thèse, d'avoir toujours été là pour moi. Vous avez toujours été importants pour moi.
Je remercie aussi **ma famille** pour m'avoir toujours encouragée. Si je suis arrivée ici aujourd'hui, c'est grâce à vous et je vous en remercie.

Enfin, je remercie la personne la plus importante à mes yeux, qui a tant fait pour moi depuis le début de ma thèse, en restant toutefois toujours dans l'ombre. Merci **Thibault** pour tout ce que tu fais pour moi, pour ton soutien, tes conseils et ton amour quotidien. Merci de m'avoir toujours soutenu, même si au fond, tu aurais aimé que je m'investisse moins. En effet, j'ai toujours traité mes bactéries comme mes petites princesses, mais je te le redis encore une fois, dans mon cœur, c'est toi le roi !

*« S'il est terrifiant de penser que la vie puisse être à la merci de la multiplication de ces infiniment petits, il est consolant d'espérer que la Science ne restera pas toujours impuissante devant de tels ennemis »*

Louis Pasteur (1878)

*« If it is a terrifying thought that life is at the mercy of the multiplication of these minute bodies [microbes], it is a consoling hope that Science will not always remain powerless before such enemies »*

Louis Pasteur, translated by Charles Ernst (1910)

# Preface

This PhD project started four years ago in the host lab on the following observation. *Neisseria meningitidis*, a pathogenic bacterium responsible for life-threatening vascular infections, rapidly colonizes and proliferates within space-limited blood vessels in the form of dense biofilm-like aggregates, ultimately occluding the entire lumen a few hours post-infection. Also, this bacterial occlusion is known to happen concurrently with the emergence of key pathophysiological features, which are the emergence of antibiotic resistance and vascular damage, leading to vascular breach, bacterial dissemination, and disease progression *(Deuren et al., 1993)*. Interestingly, this situation is not specific to *Neisseria meningitidis*-caused infections. Similarly, the uropathogenic bacterium *Escherichia coli* also forms dense aggregates within host cells during urinary tract infections *(Mulvey et al., 2001)*. Again, the intracellular bacterial lifestyle is often associated with complicated disease outcomes, characterized by highly persistent bacterial strains and recurring infections *(Hunstad and Justice, 2010)*.

Intrigued by these similar pathophysiological consequences on disease progression, we have come to the idea that these two situations, which at first glance appear to be different, share some key features. Indeed, in both cases, bacteria form dense colonies by proliferating in a space limited either by the blood vessel in the case of *Neisseria meningitidis*, or by host cell structures in the case of *Escherichia coli*. More generally, we believe that **bacterial growth in a limited space (also named growth upon confinement) is a widespread situation that could determine disease progression**, by favoring the emergence of antibiotic resistance and damaging the host.

To assess these hypotheses, we had to overcome several technical challenges, such as the fabrication of microhabitats as a model of space-limited environments. Driven by the desire to better understand how *"life is at the mercy of the multiplication of these minute bodies"*, I had the feeling that, with my engineering background at the interface between physics and biology, I had the right profile to investigate this question, in an interdisciplinary context bridging microbiology, physics, and microfluidics. Thus, I started my PhD in the lab of Guillaume DUMÉNIL at Institut Pasteur (Paris, France) under the supervision of Daria BONAZZI, in tight collaboration with Morgan DELARUE, an expert in confinement in the eukaryotic kingdom (LAAS-CNRS, Toulouse, France).

In the following pages, I hope I managed to transcribe the amazing journey I had throughout my Ph.D., during which I discovered the fascinating bacterial world and tried to decipher how these minute bodies face (mechanical) confinement to our detriment.

# Abstract

Microbes frequently proliferate within complex space-limited environments, where they experience and adapt to mechanical forces to survive and proliferate. However, the mechanisms involved in mechanical sensing and their physiological impact on bacterial communities remain poorly understood. To address this question, we designed microfluidic chambers connected to 400nm-wide channels to monitor bacterial growth upon confinement in a well-defined mechano-chemical environment, mimicking features of the complex environment encountered by bacteria during infection or biofilm formation. This device has been validated on various bacterial species with different shapes and envelopes, including pathogens. To decipher the impact of mechanical confinement on bacterial physiology, we use the biofilm-forming model organism *Escherichia coli*. We find that, as soon as bacteria become confluent in the chambers, their proliferation generates large mechanical forces on the surrounding microenvironment (~300kPa). Using high-resolution microscopy together with a machine-learning-based image analysis pipeline, we show that mechanical stress induces a strong uncoupling between growth and division rates at the onset of confinement. This leads to a reversible morphological transition from rod-shaped to small quasi-isotropic bacteria, through multiple, fast divisions followed by division arrest. These non-dividing mini cells are characterized by a strong transcriptional reprogramming that favors bacterial survival, and an increase in cytoplasmic crowding, both being concomitant with mechanical stress build-up. In our current model, we propose that bacterial division is triggered early on upon confinement via a crowding-mediated fast increase in the concentration of a key component of the divisome machinery FtsZ, that bypasses the regulation of division by the envelope stress response. An additional increment in intracellular crowding up to a certain threshold finally inhibits bacterial division, potentially through nucleoid occlusion and the activity of the FtsZ polymerization antagonist SlmA. Altogether, we show that mechanical sensing via the bacterial envelope together with crowding sensing at the cytoplasmic level induce a unique physiological state in bacteria to adapt to large mechanical constraints, with important implications in bacterial survival and infection outcome.

**Keywords:** Confinement, Mechanical constraints, Bacterial physiology, Microfluidics, Mechano-microbiology, *Escherichia coli*

# Résumé

Les microbes prolifèrent fréquemment dans des environnements restreints, où ils sont sujets à des contraintes mécaniques auxquelles ils s'adaptent pour survivre et proliférer. Cependant, les mécanismes impliqués dans la perception de ces contraintes et leur impact sur les communautés bactériennes restent méconnus. Afin d'explorer cette question, nous avons mis au point des chambres microfluidiques connectées à des canaux nanométriques, de largeur 400nm. Ces chambres nous ont permis d'étudier la prolifération des bactéries sous confinement dans un environnement mécano-chimique contrôlé, représentatif des environnements rencontrés par les bactéries au cours de l'infection, tel qu'au sein des biofilms. Ce système expérimental a été utilisé pour confiner plusieurs espèces bactériennes, y compris pathogènes, avec des formes et des enveloppes variées. Pour comprendre l'impact du confinement mécanique sur la physiologie bactérienne, nous avons utilisé la bactérie modèle *Escherichia coli*. Nous avons montré que la prolifération des bactéries, une fois à confluence, génère des contraintes mécaniques considérables sur le microenvironnement (~300kPa). Grâce à la microscopie de haute résolution combinée à une méthode d'analyse d'image basée sur le machine-learning, nous avons montré que ces contraintes mécaniques induisent un découplage immédiat de la croissance et de la division. Ce découplage conduit à l'émergence de changements morphologiques majeurs, au cours desquels les bactéries initialement en batônnets deviennent plus petites et adoptent une forme quasi isotropique. Cette transition morphologique est initiée par une série de divisions successives sans que les bactéries ne croissent, et conduit in fine a un arrêt de la division. Ces mini bactéries sont caractérisées par une reprogrammation transcriptionnelle, qui permet leur survie sous confinement, ainsi qu'une augmentation de l'encombrement cytoplasmique, tous deux induits par le confinement. Dans notre modèle actuel, nous proposons que la division bactérienne est rapidement déclenchée sous confinement, par l'augmentation de la concentration de FtsZ, un composant essentiel du complexe protéique responsable de la division, médiée par l'encombrement, contournant ainsi la régulation médiée par la voie de réponse au stress à l'enveloppe. Une augmentation supplémentaire de l'encombrement finit par inhiber la division, potentiellement via un mécanisme protecteur de l'ADN qui pourrait être régulé par la protéine SlmA, antagoniste de la polymérisation de FtsZ. Au cours de ce travail de thèse, nous avons donc montré que la perception des contraintes mécaniques à la fois au niveau de l'enveloppe et au niveau du cytoplasme induit un état physiologique unique chez les bactéries, qui leur permet de s'adapter aux contraintes mécaniques, avec des conséquences importantes dans la survie bactérienne et l'issue de l'infection.

**Mots clés** : Confinement, Contraintes mécaniques, Physiologie bactérienne, Microfluidique, Mécano-microbiologie, *Escherichia coli*

# Résumé substantiel

La résistance aux antibiotiques est un problème majeur de santé publique qui a récemment été définit par l'OMS comme étant l'une des dix plus grandes menaces pour notre société. Il s'agit de la capacité de certaines bactéries à modifier leur comportement sous conditions de stress, par l'acquisition de facteurs génétiques et/ou par l'adaptation à un environnement particulier, pour survivre et proliférer. Toutefois, malgré les nombreuses études sur cette thématique, les conditions environnementales, notamment mécanique, qui y conduisent restent encore trop mal comprises pour espérer vaincre ce fléau. L'objectif de ce projet de thèse est d'explorer l'une des origines possibles de ce problème : **la croissance des bactéries dans un espace limité.** Par exemple, c'est le cas de la bactérie *Escherichia coli* lorsqu'elle prolifère dans le cytoplasme de cellules de vessie infectées, ou dans l'espace limité par la matrice extracellulaire au sein des biofilms.
Dans le cadre de ce projet, nous faisons l'hypothèse, qu'au sein d'un espace limité : 1. la prolifération des bactéries conduit rapidement à un manque d'espace, générant une pression de croissance sur les bactéries voisines. 2. Cette pression pourrait induire des changements physiologiques chez les bactéries, et potentiellement 3. favoriser l'émergence d'un nouveau phénotype bactérien résistant aux antibiotiques. Ce projet pose donc une question générale dont les réponses promettent un impact scientifique, économique et sociétal.

Afin d'investiguer cette question, nous avons développé les deux outils décrits ci-dessous.

1. **Le confineur de bactéries,** un système nano/microfluidique pour confiner les bactéries dans un environnement perfusé, dont le développement est détaillé dans la partie Résultats, chapitre 1 (Collaboration étroite avec M.Delarue, LAAS-CNRS, Toulouse)

Le système est composé de chambres connectées à des canaux nanométriques de largeur 400nm, qui permettent un renouvellement efficace du milieu de culture, tout en empêchant le passage des bactéries. Au sein de ces chambres, les bactéries prolifèrent et occupent rapidement tout l'espace disponible, elles sont alors confinées. Grâce à ce système expérimental, nous avons pu d'étudier la prolifération des bactéries sous confinement, dans un environnement mécano-chimique contrôlé, représentatif des environnements rencontrés par les bactéries au cours de l'infection. Ce système a été utilisé pour confiner plusieurs espèces bactériennes, y compris pathogènes, avec des formes et des enveloppes variées.

2. **Une analyse d'image utilisant le machine-learning** pour segmenter et tracker les bactéries confinées à l'échelle de la cellule unique, dont les principales

étapes sont décrites dans la partie Résultats, chapitre 2 (Collaboration avec J.-Y.Tinevez, Institut Pasteur)

Ces outils nous ont ensuite permis d'étudier l'impact du confinement mécanique sur la physiologie bactérienne en utilisant comme organisme d'étude la bactérie modèle, *Escherichia coli*, dont les résultats sont décrits dans la partie Résultats, chapitre 3.

Dans un premier temps, nous avons montré que la prolifération des bactéries au sein des chambres sous confinement génère des contraintes mécaniques considérables sur le microenvironnement, de l'ordre de 300kPa. A titre illustratif, cette pression est similaire à la pression contenue dans les pneus de voitures !

Dans un deuxième temps, nous nous sommes demandés quel était l'impact de telles contraintes mécaniques sur la physiologie des bactéries. Pour comprendre comment cette pression influence la physiologie bactérienne, nous nous sommes d'abord intéressés à l'impact de la pression sur la morphologie. L'analyse quantitative de la longueur et de la largeur des bactéries nous a permis d'observer une sévère dérégulation du contrôle de la taille sous confinement. En effet, sous confinement, les bactéries sont en moyenne 2 à 3 fois moins longues qu'en absence de confinement. Ces mini bactéries confinées ressemblent davantage à une sphère, mais retrouvent rapidement leur forme initiale en bâtonnet dès que la pression est relâchée.

Dans un troisième temps, nous avons essayé d'identifier le(s) mécanisme(s) responsable(s) de ces changements morphologiques. Dans cet optique, nous avons suivi chaque bactérie présente dans la chambre, de sa naissance à sa division afin de reconstituer les lignées cellulaires, et par suite quantifier la croissance et la division sous confinement.

Nous avons d'abord montré que les contraintes mécaniques induites par la prolifération des bactéries sous confinement provoquent un découplage immédiat de la croissance bactérienne et de la division. Ce découplage entre la croissance et la division est responsable de la transition morphologie décrite précédemment. En effet, sous confinement, tandis que les bactéries cessent de croîtrent, elles subissent malgré tout une série de divisions successives conduisant à la formation de mini bactéries, plus petites et de forme quasi isotropique. De plus, nous avons montré que ces mini bactéries arrêtent *in fine* de se diviser après avoir atteint une taille minimale critique.

Ensuite, nous avons cherché à identifier le(s) mécanisme(s) régulant(s) la division bactérienne sous confinement. Pour commencer, nous nous sommes intéressés à l'induction de voies de réponse au stress localisées à différents niveaux de l'architecture bactérienne. En utilisant des rapporteurs transcriptionnels fluorescents, nous avons montré que le confinement induit l'expression des réponses au stress membranaires (Rcs, Cpx) et cytoplasmique (IbpA), mais pas la voie de réparation des dommages à l'ADN (RecA).

En s'appuyant sur ces résultats, le premier mécanisme auquel nous avons pensé concerne l'activation de la voie de réponse au stress Rcs, connue dans la littérature pour réguler l'expression de la protéine FtsZ, l'un des composants essentiel du complexe protéique responsable de la division (aussi appelé divisome). Pour comprendre le rôle de cette voie dans l'adaptation des bactéries au confinement, nous avons utilisé une souche bactérienne possédant une délétion du gène *rcsB*. En étudiant le comportement de cette souche sous confinement, nous avons montré que cette voie joue un rôle dans le maintien de la forme des bactéries localisées au bord des chambres, là où elles sont davantage prolifératives, sans toutefois perturber la division des bactéries situées au centre. Ces résultats suggèrent que la voie de stress Rcs est en partie responsable de la division des bactéries sous confinement, mais qu'un autre mécanisme joue probablement un rôle plus important.

Le deuxième mécanisme que nous avons étudié est l'encombrement cytoplasmique. En effet, le découplage entre la croissance et la division induite par le confinement pourrait induire une augmentation de la concentration en protéines dans le cytoplasme et par suite de son encombrement. Ceci pourrait perturber le déplacement des protéines, et par conséquent l'ensemble des processus biologiques, dont la division. Pour ce faire, nous avons exprimé des nanoparticules fluorescentes de diamètre 40nm, appelées GEMs, dans le cytoplasme des bactéries. Nous avons observé que le confinement induisait en effet une réduction significative du coefficient de diffusion des GEMs, c'est-à-dire une augmentation de l'encombrement du cytoplasme. De plus, cette augmentation de l'encombrement est associée à une augmentation de la concentration en protéines comme indiqué par l'augmentation de la fluorescence moyenne d'une protéine GFP, exprimée de manière constitutive.

Le troisième mécanisme auquel nous nous sommes intéressés concerne l'occlusion du nucléoïde, c'est-à-dire le mécanisme protecteur qui bloque l'assemblage du divisome au-dessus du nucléoïde. En effet, nos observations montrent que les mini bactéries sous confinement sont caractérisées par un ratio nucléo-cytoplasmique plus élevé qu'en absence de confinement. En d'autres termes, alors que l'ADN est compacté au sein du cytoplasme en absence de confinement, celui-ci occupe tout l'espace cytoplasmique disponible sous confinement. De plus, nos résultats montrent que le ratio nucléo-cytoplasmique suit la tendance inverse au cours du temps que la taille des bactéries, et la même tendance au cours du temps que la fraction de bactéries qui ne se divisent pas. Ces résultats suggèrent que la taille minimale critique atteinte sous confinement est déterminée par le nucléoïde, et pointent la présence d'un potentiel mécanisme protecteur de l'ADN qui pourrait inhiber la division.

Dans l'ensemble, nos résultats montrent que le confinement induit l'émergence d'un phénotype bactérien unique caractérisé par des changements majeurs en terme de taille et de croissance. Dans notre modèle actuel, nous proposons que ces changements sont induits par une dérégulation de la croissance et la division sous

confinement. Plus précisément, nous proposons que la division bactérienne est rapidement déclenchée sous confinement, par l'augmentation de la concentration de FtsZ, un composant essentiel du complexe protéique responsable de la division, médiée par l'encombrement, contournant ainsi la régulation médiée par la voie de réponse au stress à l'enveloppe. Une augmentation supplémentaire de l'encombrement finit par inhiber la division, potentiellement via un mécanisme protecteur de l'ADN qui pourrait être régulé par la protéine SlmA, antagoniste de la polymérisation de FtsZ.
De manière intéressante, des changements morphologiques similaires à ceux étudiés dans ce projet ont été rapportés dans la littérature au sein des colonies bactériennes intracellulaires formées par la bactérie *Escherichia coli* au cours des infections urinaires. Grâce à cet exemple, nous essayons donc maintenant de démontrer la présence du confinement dans le contexte infectieux.

Au cours de ce travail de thèse, nous avons donc montré que la perception des contraintes mécaniques auto-générées par la prolifération des bactéries dans un espace limité, à la fois au niveau de l'enveloppe et au niveau du cytoplasme, induit un état physiologique unique chez les bactéries, qui leur permet de s'adapter aux contraintes mécaniques, avec des conséquences importantes dans la survie bactérienne et l'issue de l'infection.

# Table of content

**INTRODUCTION ..... 31**

**1 THE MICROBIAL WORLD ..... 33**

**1.1 GENERALITIES ..... 33**
1.1.1 A TINY AND MIGHTY WORLD ..... 33
1.1.2 COMPARISON WITH THE EUKARYOTIC WORLD ..... 33
1.1.3 AN UNDERAPPRECIATED, DIVERSE AND HIGHLY ADAPTATIVE WORLD THAT DESERVES TO BE STUDIED ..... 37
**1.2 BACTERIAL PHYSIOLOGY SEEN FROM AN INTERDISCIPLINARY POINT OF VIEW ..... 39**
1.2.1 BACTERIAL ARCHITECTURE ..... 39
1.2.2 BACTERIAL GROWTH AND DIVISION ..... 55
1.2.3 BACTERIAL ADAPTATION TO CHANGING ENVIRONMENTS ..... 60
**1.3 HOW IS THE MICROBIAL WORLD CLASSICALLY STUDIED IN THE LAB? ..... 68**

**2 IMPACT OF THE MECHANICAL ENVIRONMENT ON BACTERIAL PHYSIOLOGY ..... 69**

**2.1 OVERVIEW OF THE MECHANICAL STRESSES ENCOUNTERED IN THE MICROBIAL WORLD ..... 69**
2.1.1 MECHANICAL STRESSES EXPERIENCED AT THE SINGLE CELL LEVEL ..... 69
2.1.2 MECHANICAL STRESSES EXPERIENCED AT THE MULTICELLULAR LEVEL ..... 69
**2.2 INSPIRATION FROM EUKARYOTIC CELLS ..... 72**
2.2.1 HOW EUKARYOTIC CELLS SENSE MECHANICAL STRESSES? ..... 72
2.2.2 IMPACT OF MECHANICAL STRESSES ON EUKARYOTIC CELL PHYSIOLOGY ..... 72
**2.3 BACTERIAL RESPONSE TO MECHANICAL STRESSES ..... 75**
2.3.1 BACTERIAL RESPONSE TO MECHANICAL STRESSES AT THE SINGLE-CELL LEVEL ..... 75
2.3.2 BACTERIAL RESPONSE TO MECHANICAL STRESSES AT THE MULTICELLULAR LEVEL ..... 81

**3 HOW TO EXPERIMENTALLY CONFINE BACTERIA? ..... 85**

**3.1 EXTERNAL CONFINEMENT ..... 85**
**3.2 SELF-INDUCED CONFINEMENT ..... 86**
**3.3 WHY ARE CURRENT TECHNIQUES NOT SUFFICIENT FOR US? ..... 88**

**4 HOW TO MEASURE GROWTH-INDUCED PRESSURE? ..... 89**

**4.1 BULK DEFORMATION-BASED PRESSURE MEASUREMENTS ..... 89**
**4.2 MEMBRANE DEFORMATION-BASED PRESSURE MEASUREMENTS ..... 89**
**4.3 DEFORMATION-BASED LOCAL PRESSURE MEASUREMENTS ..... 90**

**5 HOW TO FOLLOW BACTERIAL GROWTH? ..... 91**

**5.1 FLUORESCENT DYES ..... 91**

**5.2 Fluorescent fusion proteins ..... 92**

**6 How to extract quantitative data at the single-cell level under confinement? ... 93**

**6.1 Available image analysis softwares at the beginning of my Ph.D. ..... 93**
**6.2 Why are these image analysis softwares not sufficient for us? ..... 93**

**THESIS OBJECTIVES ..... 95**

**RESULTS ..... 97**

**1 The bacterial confiner: development of a microfluidic set-up with nanometric features to study bacterial confinement ..... 99**

**1.1 Development of a silicon-based microfluidic set-up to confine bacteria ..... 100**
1.1.1 Chip design ..... 100
1.1.2 Chip fabrication ..... 100
1.1.3 Chip loading ..... 100
1.1.4 Application to bacterial confinement ..... 101
**1.2 The bacterial confiner: development of a versatile PDMS-based microfluidic set-up with nanometric features to confine bacteria in a controlled mechanical environment ..... 104**
1.2.1 Chip design ..... 104
1.2.2 Master fabrication ..... 104
1.2.3 Chip fabrication ..... 105
1.2.4 Chip loading ..... 105
1.2.5 Application to bacterial confinement ..... 105
**1.3 Optimization of the bacterial confiner to characterize the mechanical environment encountered by bacteria upon confinement ..... 109**
**1.4 Silicon and PDMS-based microfluidic chips are two complementary systems to study bacterial growth upon confinement (technical discussion) ..... 112**
1.4.1 Chip deformability ..... 112
1.4.2 Chip permeability ..... 112
1.4.3 Chip porosity ..... 112
**1.5 Conclusion ..... 113**

**2 Development of an image analysis workflow to quantify bacterial growth under confinement at the single cell level ..... 115**

**2.1 Establishment of a semi-automatic image analysis workflow to quantify bacterial growth under 2D confinement (agar pad) ..... 116**
**2.2 Extension to bacterial growth under 3D confinement (bacterial confiner) ..... 120**
**2.3 Comparison of the present pipeline with state-of-the-art segmentation approaches ..... 122**
**2.4 Application of the image analysis pipeline to the description of the diplococcus cell cycle: present work and outlooks ..... 122**
**2.5 Conclusion ..... 128**

3 QUANTITATIVE CHARACTERIZATION OF BACTERIAL PHYSIOLOGY UPON CONFINEMENT ..... 129

3.1 IN THE BACTERIAL CONFINER, BACTERIA PROLIFERATE IN THE FORM OF TIGHTLY PACKED AGGREGATES AND SURVIVE IN THE PRESENCE OF A CONTROLLED CHEMICAL ENVIRONMENT ..... 129
3.2 BACTERIAL GROWTH UNDER CONFINEMENT LEADS TO THE GENERATION OF LARGE COMPRESSIVE FORCES ..... 130
3.2.1 CHARACTERIZATION OF THE MECHANICAL ENVIRONMENT ..... 130
3.2.2 THE NUMBER OF BACTERIA AS A READOUT OF THE GROWTH-INDUCED PRESSURE ..... 132
3.3 BACTERIAL ADAPTATION TO THIS NEW MECHANICAL ENVIRONMENT IS CHARACTERIZED BY A MAJOR MORPHOLOGICAL TRANSITION, LEADING TO "MINI" CELLS ..... 134
3.3.1 BACTERIA UNDERGO STRONG CELL SHAPE CHANGES UPON CONFINEMENT ..... 134
3.4 MECHANICAL CONFINEMENT INDUCES AN UNCOUPLING BETWEEN GROWTH AND DIVISION, LEADING TO GROWTH AND DIVISION ARREST ..... 140
3.4.1 RELATION BETWEEN GROWTH AND DIVISION UPON CONFINEMENT ..... 140
3.4.2 DYNAMICS OF THE DIVISOME MACHINERY UPON CONFINEMENT ..... 142
3.5 WHICH MECHANISMS REGULATE BACTERIAL DIVISION UPON CONFINEMENT? ..... 144
3.5.1 BACTERIAL STRESS MAPPING ..... 144
3.5.2 A ROLE FOR THE RCS ENVELOPE STRESS RESPONSE? ..... 148
3.5.3 A ROLE FOR CYTOPLASMIC CROWDING? ..... 150
3.5.4 A ROLE FOR NUCLEOID OCCLUSION? ..... 154
3.6 CONCLUSION ..... 156

DISCUSSION ..... 157

1 WHAT IS THE COMPLEX MECHANISM AT PLAY FOR E. COLI ADAPTATION TO CONFINEMENT? 159

1.1 MEASUREMENT OF BACTERIAL GROWTH-INDUCED PRESSURE ..... 160
1.2 CONFINEMENT INDUCES A MORPHOLOGICAL TRANSITION BY UNCOUPLING GROWTH AND DIVISION ..... 162
1.2.1 BACTERIA UNDERGO MAJOR MORPHOLOGICAL CHANGES UPON CONFINEMENT ..... 162
1.2.2 ON THE PATH TO IDENTIFY THE MECHANISMS INVOLVED IN CONFINEMENT-INDUCED MORPHOLOGICAL ADAPTATION ..... 162
1.3 WORKING MODEL ..... 167

2 CAN BACTERIA TEACH US SOMETHING ABOUT A UNIVERSAL RESPONSE TO CONFINEMENT? 168

2.1 WHAT IS THE ORIGIN OF GROWTH-INDUCED PRESSURE? ..... 168
2.2 WHICH STRATEGIES ARE USED BY BACTERIA TO SUSTAIN GROWTH-INDUCED PRESSURE? ..... 170
2.2.1 ROLE OF THE BACTERIAL CELL ENVELOPE ..... 170
2.2.2 ROLE OF THE BACTERIAL CELL SHAPE ..... 170
2.2.3 ROLE OF BACTERIAL CELL DEATH ..... 174
2.3 TOWARDS A UNIVERSAL RESPONSE TO MECHANICAL CONFINEMENT? ..... 176
2.3.1 SIMILARITIES BETWEEN PROKARYOTIC AND MAMMAL CELLS ..... 176
2.3.2 SIMILARITIES BETWEEN PROKARYOTIC AND YEASTS CELLS ..... 176
2.3.3 DIFFERENCES BETWEEN PROKARYOTIC AND EUKARYOTIC CELLS: IMPACT OF CROWDING ..... 177

**3 HOW COULD CONFINEMENT DETERMINE INFECTION OUTCOME? ..... 179**

**3.1 IS CONFINEMENT RELEVANT IN THE INFECTIOUS CONTEXT? ..... 179**
**3.2 WHAT ARE THE FUNCTIONAL BENEFITS PROVIDED BY CONFINEMENT DURING INFECTION? ..... 180**
3.2.1 A WAY TO INCREASE BACTERIAL DISSEMINATION DURING INFECTION? ..... 180
3.2.2 A WAY TO ESCAPE THE IMMUNE RESPONSE? ..... 181
3.2.3 A WAY TO TOLERATE ANTIBIOTIC TREATMENT? ..... 181

**GENERAL CONCLUSION & OUTLOOK ..... 187**

**MATERIALS & METHODS ..... 191**

**APPENDIX ..... 217**

**REFERENCES ..... 227**

# Index of figures

**Figure 1**: Comparison of the structure of a bacterial prokaryotic cell compared to eukaryotic one ..... 25
**Figure 2**: The diversity of bacterial shape across the phylogenic tree ..... 28
**Figure 3:** Structure of the bacterial envelope for Gram-negative and Gram-positive bacteria ..... 29
**Figure 4:** The Gram-negative bacterial envelope is a complex multilayered structure, with peculiar chemical, physical and mechanical properties ..... 31
**Figure 5:** The Gram-negative peptidoglycan cell wall is composed of cross-linked peptidoglycan chains whose biogenesis is a dynamic process, which involves various players ..... 34
**Figure 6:** Illustration of the crowded cytoplasm of the bacterium *Escherichia coli*, drawn using images from electronic microscopy by the artist David Goodsell ..... 38
**Figure 7:** The bacterial cytoplasm is a highly crowded space characterized by physical properties, which depend on the size of the particle and the metabolic state of the bacteria ..... 40
**Figure 8:** The nucleoid is characterized by a protruding morphology, whose size linearly scales with the size of the bacteria in homeostatic conditions ..... 43
**Figure 9**: Cell cycle progression for the bacterium *Escherichia coli* ..... 46
**Figure 10:** Spatiotemporal regulation of bacterial division through the Min system and nucleoid occlusion ..... 49
**Figure 11:** Mechanisms used by bacteria to adapt gene expression in response to changing environmental conditions ..... 52
**Figure 12**: Overview of the Rcs and Cpx envelope stress responses, and the DNA damage stress response ..... 54
**Figure 13:** Overview of the mechanical stresses encountered by bacteria at the single-cell and multicellular level ..... 60
**Figure 14:** Mechanotransduction in eukaryotic cells ..... 63
**Figure 15:** Components of the bacterial architecture experiencing mechanical stresses, including appendages such as pili and flagella, and outer membrane proteins ..... 67
**Figure 16**: Impact of mechanical forces on bacterial morphology ..... 69
**Figure 17:** Hypotheses of this PhD work ..... 85
**Figure 18**: A silicon-based microfluidic chip with nanometric features to study bacterial proliferation in spatially constrained environments ..... 93
**Figure 19:** The bacterial confiner, a PDMS-based microfluidic chip with nanometric features to study bacterial proliferation in spatially constrained environments ..... 97
**Figure 20:** Optimization of the bacterial confiner to facilitate the characterization of the mechanical environment encountered by bacteria ..... 101

**Figure 21**: Summary of the microfabrication developments that have been performed in this Ph.D. work to study bacterial confinement …… 104
**Figure 22:** Development of an image analysis workflow to quantify bacterial growth under 2D confinement at the single cell level …… 109
**Figure 23**: Application of the presented image analysis pipeline to quantify bacterial growth in the bacterial confiner …… 111
**Figure 24**: Characterization of *N.meningitidis* diplococci growth on agar pads ....115
**Figure 25:** Proposed model for diplococci growth …….. 117
**Figure 26**: In the bacterial confiner, *Escherichia coli* bacteria proliferate in the form of tightly packed aggregates and survive in the presence of a strong medium supply 121
**Figure 27**: *Escherichia coli* proliferation upon confinement generates large forces 123
**Figure 28**: Bacterial physiology upon confinement is characterized by strong morphological changes …… 125
**Figure 29:** *Escherichia coli* bacterial generally adapt to confinement through morphological changes …….... 127
**Figure 30**: Confinement-induced morphological changes are reversible upon pressure release …… 129
**Figure 31**: Mechanical confinement uncouples growth and division, leading to reversible growth and division arrests …… 131
**Figure 32:** Mechanical confinement often impairs bacterial division by hindering Z-ring constriction …… 133
**Figure 33**: Bacterial physiology upon confinement is characterized by a strong transcriptional reprogramming …… 137
**Figure 34:** The Rcs envelope stress response favors bacterial survival and shape maintenance upon confinement at the edges of the chamber, where bacteria are much more proliferative, but not in the center …… 139
**Figure 35**: Characterization of GEM40 diffusion within the cytoplasm as a way to assess change in cytoplasmic crowding …… 141
**Figure 36:** Bacterial physiology upon confinement is characterized by an increase in cytoplasmic crowding …….. 143
**Figure 37:** Bacterial physiology upon confinement is characterized by a change in nucleoid-to-cytoplasmic ratio …….. 145
**Figure 38:** Impact of culture medium perfusion on growth-induced pressure build-up ……151
**Figure 39:** Confinement-induced morphological changes correlate with changes in DNA occupancy …… 155
**Figure 40**: Proposed model for *Escherichia coli* morphological adaptation to mechanical confinement …….. 157
**Figure 41:** The Gram-positive *Staphylococcus aureus* generates higher growth-induced pressure upon confinement than the Gram-negative *Escherichia coli* ….. 159

**Figure 42**: Bacterial viability upon confinement for *Escherichia coli* WT, Δ*rcsB*, and delta Δ*cpxR* mutants strains ..... 161
**Figure 43:** Morphological changes occurring during *Neisseria meningitidis* confinement ..... 163
**Figure 44:** *Neisseria meningitids* adaptation to confinement is characterized by a higher rate of autolysis ..... 165
**Figure 45:** In the absence of confinement, *Escherichia coli* bacteria rapidly die in the presence of ciprofloxacin ..... 174
**Figure 46:** Upon confinement, *Escherichia coli* bacteria survive much longer to ciprofloxacin ..... 175
**Figure 47:** After 10 hours of antibiotic treatment, confined bacteria eventually regrow, yet without dividing ..... 176
**Figure 48:** Deformable hydrogel beads can be used as local force sensors within the bacterial confiner ..... 179
**Figure 49**: Validation of the fluorescence stress reporters' induction upon chemical stress ..... 188
**Figure 50:** Description of the microfabrication process developed in this work, which uses stepper-based photolithography by comparison with standard photolithography ..... 191
**Figure 51**: Quake valve calibration process ..... 194
**Figure 52:** Validation of growth-induced pressure measurement ..... 198

# Index of tables

**Table 1:** Overview of the sigma factors expressed in *Escherichia coli* ..... 51
**Table 2:** Overview of the experimental strategies used to study bacterial growth in a limited space ..... 77
**Table 3:** Overview of the fluorescent membrane stainings tested with *Escherichia coli* in the bacterial confiner ..... 106
**Table 4:** Overview of the transcriptional reporters tested upon chemical and mechanical stresses ..... 134
**Table 5:** List of the *Escherichia coli* strains used in this study ..... 184
**Table 6:** List of the *Neisseria meningitidis* strains used in this study ..... 184
**Table 7:** Experimental conditions used to verify *Escherichia coli* stress reporters' induction upon chemical stress ..... 187
**Table 8:** Quantification processes used to measure the parameters of interest .... 204

# Introduction

In this chapter, I first remind key fundamental concepts in microbiology, that are important to understand how bacterial physiology is impacted by confinement (Section 1). Then, I highlight the importance of new approaches to revisit these concepts in more physiological conditions, by providing a better understanding of how the microbial world adapts to mechanical constraints in a dynamic context (Section 2). Finally, I describe the state-of-the-art methods that served as a starting point to study the impact of mechanical confinement on bacterial physiology, and the corresponding technical challenges I had to overcome (Sections 3 – 4 – 5 – 6).

# 1 The microbial world

## 1.1 Generalities

### 1.1.1 A tiny and mighty world

The microbial world is composed of micro-organisms that are by definition invisible to the naked eye, including viruses, protists, fungi, and the prokaryotes that are the bacteria and the archaea. Among them, bacteria represent the first lifeform on Earth and the second most abundant one after plants. Bacteria are present in almost every environment, including extreme areas where no other form of life can survive such as in the depth of the Earth's crust *(Chivian et al., 2008)*, which highlights their incredible adaptability. Bacteria shape our life, for the good but also the bad. Indeed, while Humanity's first experience with bacteria was through their ability to cause deadly diseases, it is increasingly clear that we also owe much of our existence and biology to these tiny microbes that live in and on our body *(Kong and Segre, 2012; Relman, 2012)*. Therefore, understanding the various roles bacteria play in our lives, how they behave, and how the environment shapes their behavior is of primary interest and promises to change people's view of this microscopic world, that has long been underappreciated.

### 1.1.2 Comparison with the eukaryotic world

Bacteria have long been invisible to the scientific community, because of their small size. They were observed for the first time by the pioneer A. Leeuwenhoek about 10 years after eukaryotic cells, while remaining invisible to the scientific community over the next century *(Lane, 2015)*. Because of this, bacteria have been described and characterized in comparison to their eukaryotic counterparts, in particular mammal cells and fungi including yeast.

#### 1.1.2.1 Similarities

As all living organisms, bacteria and eukaryotic cells share a common purpose: to survive and proliferate. In addition, most of them grow in the form of multicellular communities, called biofilms in the bacterial world and tissue in eukaryotic one. To do

so, both prokaryotic and eukaryotic comrades contain all the material they need in the cytoplasm enclosed within a membrane, that delimits the cell and physically separates it from the external environment. In essential terms, all cells contain DNA, the genetic set of instructions that organize their survival and proliferation, and all the machines belonging to the so-called central dogma and allowing to convert sequence information between biopolymers (*e.g.* DNA, RNA, and proteins) through machineries such as the replisome, polymerases, and ribosomes. Finally, proteins execute the instructions and perform a vast array of cellular functions, in some cases by using the energy they metabolize. Beyond this, more and more similarities with eukaryotic cells have also been discovered at the molecular level, notably cytoskeletal proteins forming a dynamic network of interconnected filaments that regulate essential functions such as cell shape, DNA segregation, and cell division *(Ent et al., 2001)*.

#### 1.1.2.2 Differences

Even though bacteria and eukaryotic cells face common goals, they undertake them quite differently. While the eukaryotic approach is sophisticated and intricate, the bacterial one is optimized to form small, robust, and architecturally simple cells. Among the differences between the eukaryotic and prokaryotic worlds, here are the most important structural differences *(Harper and Hernandez, 2020)* (Figure 1):

- **Dimensions:** While eukaryotic cells have a characteristic size of around 10µm for mammal cells and 5µm for yeasts, bacteria have a smaller size in the order of 1µm.
- **Cell envelope:** Mammal cells are separated from the external environment by a single phospholipid bilayer, called the plasma membrane. In yeasts, this phospholipid bilayer is additionally connected to a thick cell wall. Like yeast, the bacterial envelope is a complex multilayered structure composed of the membrane(s) and a cell wall, that determine both the shape and the mechanical properties of the prokaryotic cell (while these properties are conveyed by the cytoskeleton in eukaryotic cells).
- **Magnitude of cytoplasmic pressure:** Cells regulate intracellular osmolarity to maintain a specific volume. This gives rise to a cytoplasmic pressure, that can vary from the order of 1 kPa in the case of mammal cells *(Fischer-Friedrich et al., 2014; Rojas and Huang, 2018)*, 100 kPa in bacteria, where it is called turgor pressure, up to 1MPa in yeasts *(Rojas and Huang, 2018)*. This large difference is due to the presence of the cell wall in the bacterial and yeast envelope, a structure that can sustain much higher mechanical stresses and results in higher membrane tension in prokaryotic and yeast cells, compared to mammal cells.

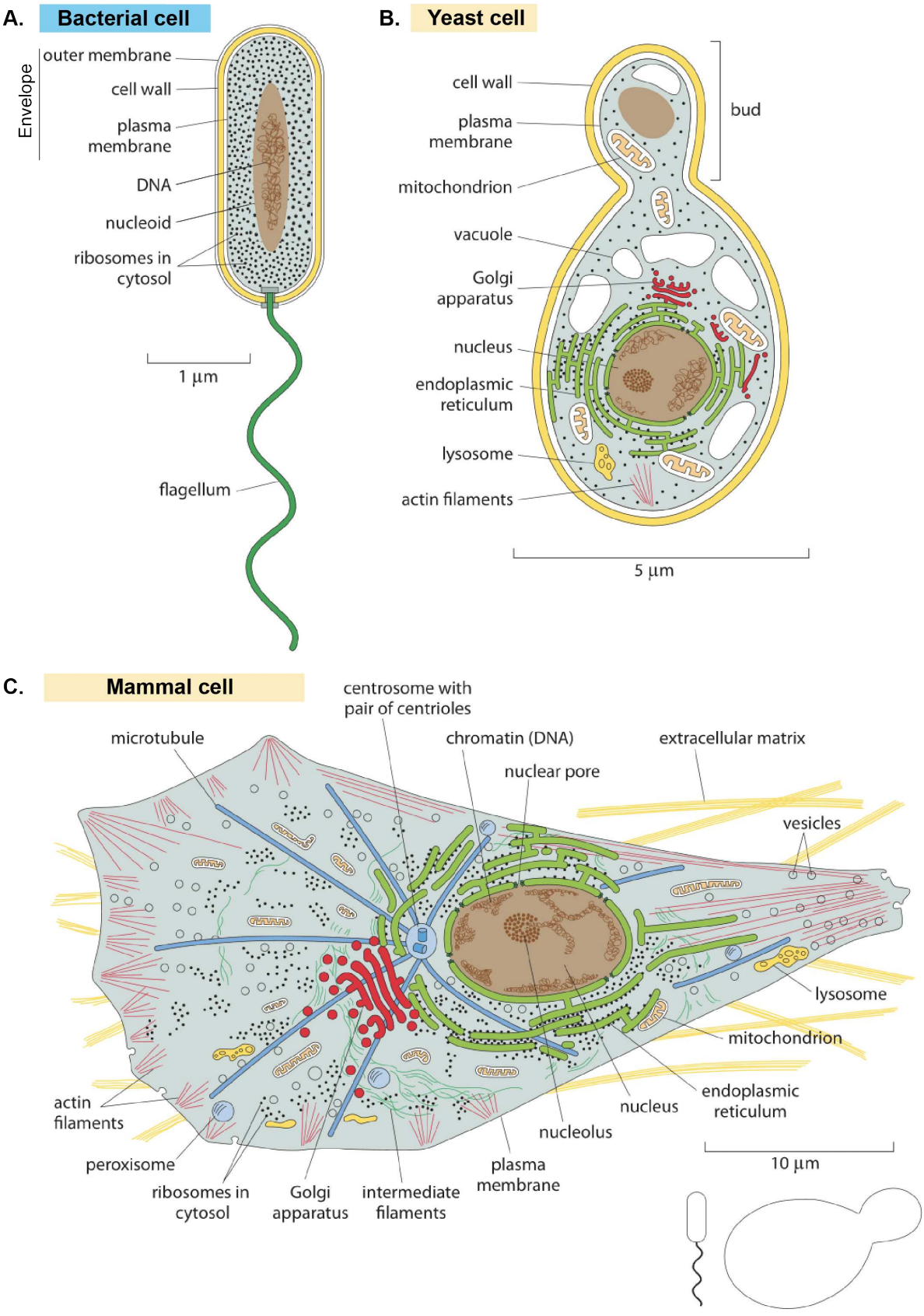


**Figure 1: Comparison of the structure of a bacterial prokaryotic cell (blue) compared to an eukaryotic one (yellow).** The bacterial structure is represented in A., the one of eukaryotic yeasts in B., and the one of eukaryotic mammal cells in C. Adapted from (Milo and Phillips, 2015).

- **Subcellular compartmentalization:** Importantly, eukaryotic cells have many membrane-bounded organelles, while bacteria have not. This allows eukaryotic cells to be structurally organized and to allocate different tasks to different regions of the cell, especially in the case of large cells such as oocytes.

- **Genome:** Similarly, eukaryotic cells have a membrane-bounded nucleus contrary to bacteria. In bacteria, the DNA is not compartmentalized but rather floating in the cytoplasm. Consequently, the transcription and the translation are coupled in bacteria, while they are not in eukaryotic cells. Yet, the universality of coupled transcription-translation in the prokaryotic kingdom has been recently questioned by a few studies *(Irastortza-Olaziregi and Amster-Choder, 2021; Kannaiah et al., 2019)*.

Even though a large literature exists on the subcellular structures and molecular mechanisms regulating bacterial physiology, there are still a lot of open questions on their fundamental functions that remain to be addressed in comparison to their eukaryotic counterparts.

### 1.1.3 An underappreciated, diverse and highly adaptative world that deserves to be studied

Due to their small size, bacteria have long been thought to be simple "bags of enzymes", characterized by simple shapes devoid of internal organization, thus remaining in the shadows of their eukaryotic counterparts. Thanks to the development of high-resolution optical microscopy and genetic and chemical tools to stain specific cellular structures, scientists have discovered an astonishingly diverse world, so far invisible. By contrast to their widespread reductionist belief, bacteria exhibit a wide range of shapes, ranging from rod and cocci, to helical and star-shaped *(Young, 2006)*, as illustrated in Figure 2.

The diversity of bacterial morphology is shaped by the environment in which bacteria proliferate, as a result of the combination of various selective pressures (nutrient uptake, attachment, dispersal, evasion, physical constraints) that define the complex environment bacteria live in *(Kysela et al., 2016)*. As an example, the curved shape of the bacterium *Caulobacter crescentus* has been shown to promote bacterial colonization in moderate-flow environments compared to a straight one *(Persat et al., 2014)*. Thus, far from the simple bag belief, bacteria exhibit a myriad of shapes and can dynamically adapt them in response to the environment!

Beyond their shape, bacteria actively sense and adapt to the extracellular environment by modulating gene expression to survive and proliferate. The first observation of bacterial response to a (chemical) stimulus dates from 1936 when P. Pappenheimer and S. Jonhson noticed that the bacterial *C. diphteriae*'s toxin increases in conditions of low iron concentration, that are typical of the host pharynx. This notion of adaptation is nowadays rising in interest notably with the introduction of the concept of microbiota, which refers to a population of micro-organisms within a specific environment. For instance, the composition of the gut microbiota that is related to the emergence of various pathologies such as obesity, has been recently shown to be largely influenced by the environment, much more than host genetics *(Ahn and Hayes, 2021; Rothschild et al., 2018; Schmidt et al., 2022)*.

To conclude, I hope I convey that the bacterial world is fascinating because of its diversity and adaptability, that there is still a lot that remains to be understood, and that these studies promise to unveil many unexpected discoveries in the future.

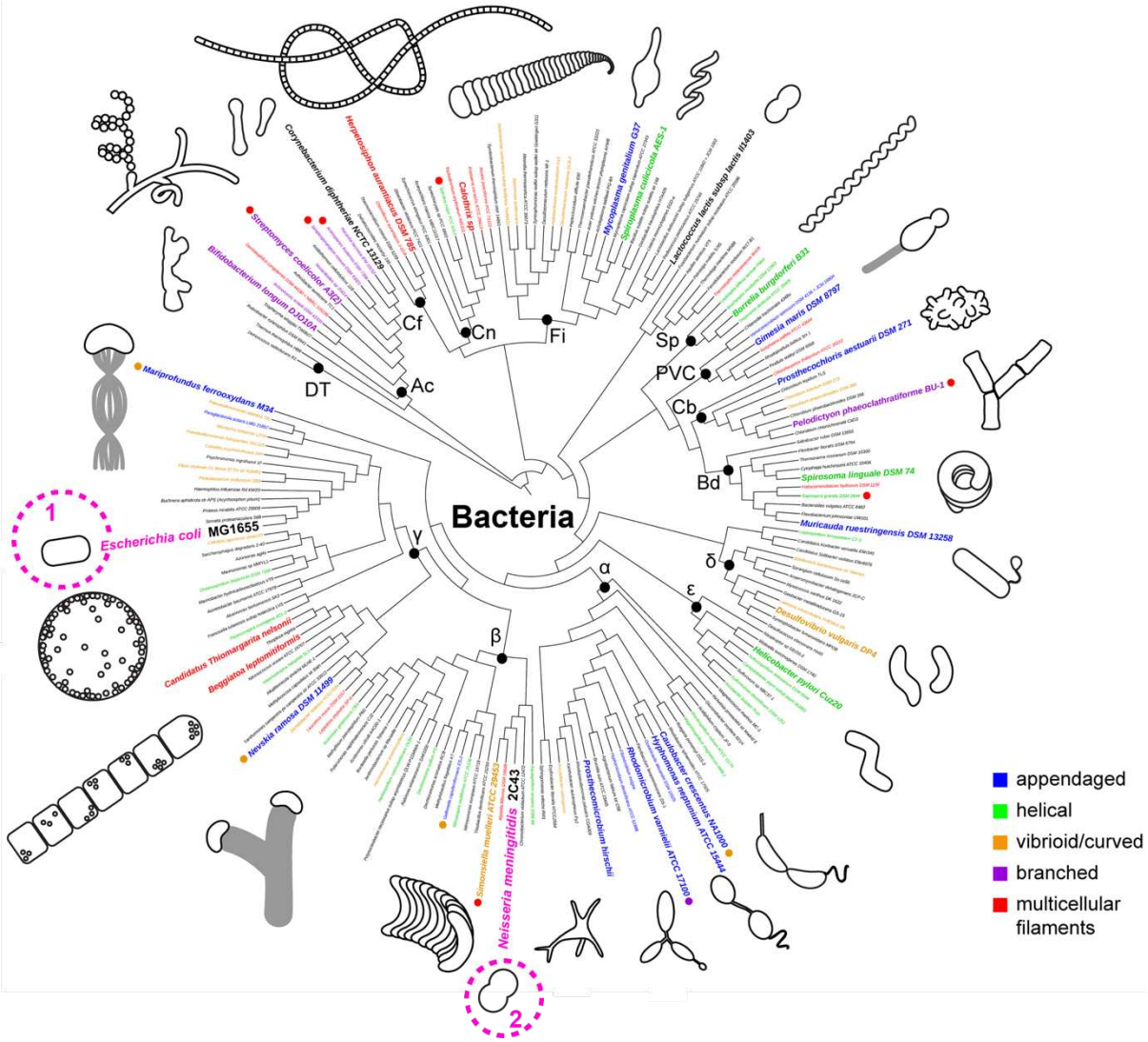


**Figure 2: The diversity of bacterial shape across the phylogenic tree.** The two bacteria of particular interest in the scope of this work are depicted in magenta. *Adapted from* (Kysela et al., 2016).

## 1.2 Bacterial physiology seen from an interdisciplinary point of view

### 1.2.1 Bacterial architecture

By definition, a bacterium is a single-cell organism composed of a cell envelope, that encloses the cytoplasm in which the DNA sits. In the following, I detail the architecture of a bacterium, both in structural, chemical, and mechanical terms.

#### 1.2.1.1 The envelope, the frontier between the cell and its environment

The bacterial envelope is a complex multilayered structure that protects the cell from the external environment, as a selective barrier. It is also a port of communication between the outside and the inside of the cell as many biochemical reactions occur within it. Based on its structure, bacteria are classified either as Gram-negative or Gram-positive. Gram-negative bacteria are surrounded by a thin peptidoglycan cell wall, itself surrounded by the outer membrane (and for this reason they are termed diderms – Figure 3A), while Gram-positive bacteria are only surrounded by a thick peptidoglycan cell wall (and are hence named monoderms – Figure 3B). These three layers constituting the envelope of Gram-negative bacteria, *e.g.* the outer membrane, the peptidoglycan cell wall, and the inner membrane, are characterized by their own protein composition and properties that are described below.

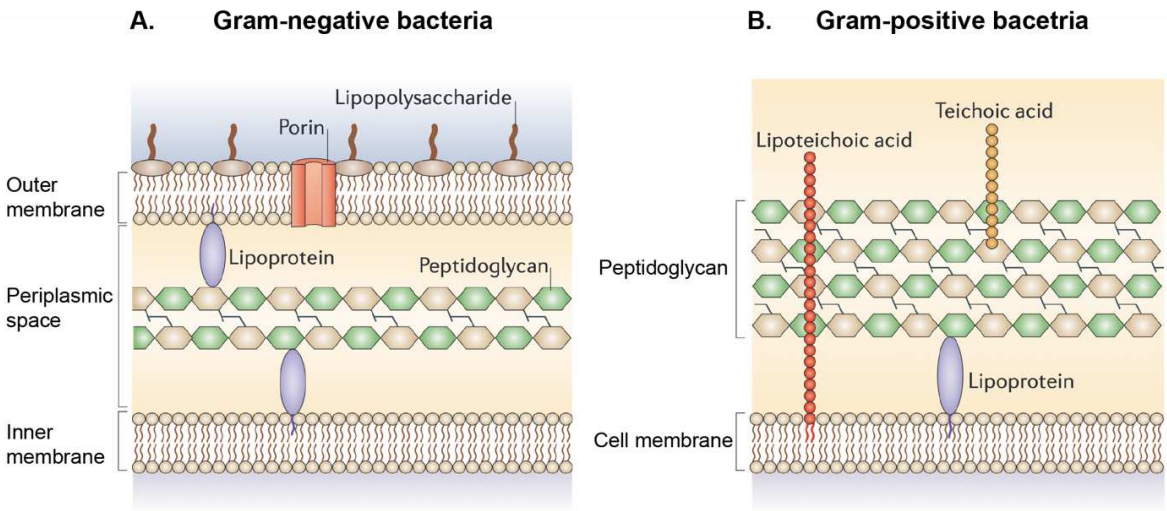


**Figure 3: Structure of the bacterial envelope for Gram-negative (A) and Gram-positive bacteria (B).** Adapted from *(Brown et al., 2015)*.

#### 1.2.1.1.1 The outer membrane

*Chemical composition*

The outer membrane is specific to Gram-negative bacteria. It is an asymmetric lipid bilayer, made of lipopolysaccharide (LPS) at the outer leaflet and phospholipids at the inner leaflet. It is mainly composed of lipoproteins embedded at the inner leaflet and transmembrane proteins characterized by a beta-barrel structure, called outer membrane proteins (OMP) (Figure 4A). These outer membrane proteins cover about 70% of the bacterial surface *(Jarosławski et al., 2009)* while being mostly immobile, thereby conferring a gel-like behavior to the outer membrane with limited diffusivity *(Sun et al., 2021a)* (Figure 4B). Importantly, these outer membrane proteins have several functions. One of them is to ensure passive diffusion of small hydrophilic molecules (< 700 Daltons), including most of the nutrients such as mono/disaccharides or amino acids, across the outer membrane. The outer membrane is also the location of several environmental sensors *(Belas, 2014; Konovalova et al., 2016)*. Among these sensors, one can find the RcsF lipoprotein that is anchored at the inner leaflet and spans the outer membrane via the beta barrel lumen of an outer membrane protein *(Konovalova et al., 2016)* (Figure 4A).

*Permeability properties*

The outer membrane is a protective and selective chemical barrier, that prevents the loss of periplasmic material outside of the cell together with the entry of toxic molecules such as antibiotics, but still favors the entry of nutrients. This barrier function relies mostly on LPS glycolipid structure. Indeed, LPS is made of three moieties: a lipid A whose hydrophobic part forms the outer leaflet of the outer membrane, linked to a hydrophilic core oligosaccharide domain, further connected to a hydrophilic O antigen (Figure 4A). As well as being largely impassable to large hydrophilic molecules due to its lipidic nature, the outer membrane is also impermeable to hydrophobic compounds due to core oligosaccharide and O-antigen hydrophilicity. The effectiveness of the barrier is enhanced by the dense packing of the LPS, mediated by hydrophobic lateral interactions between the acyl chains of the lipid A *(Bertani and Ruiz, 2018; Nikaido, 2003)*. Thus, due to its amphiphilic nature and its tight binding with its neighbors, LPS hinders the passage of both hydrophobic and large hydrophilic molecules rendering the outer membrane an efficient selective barrier.

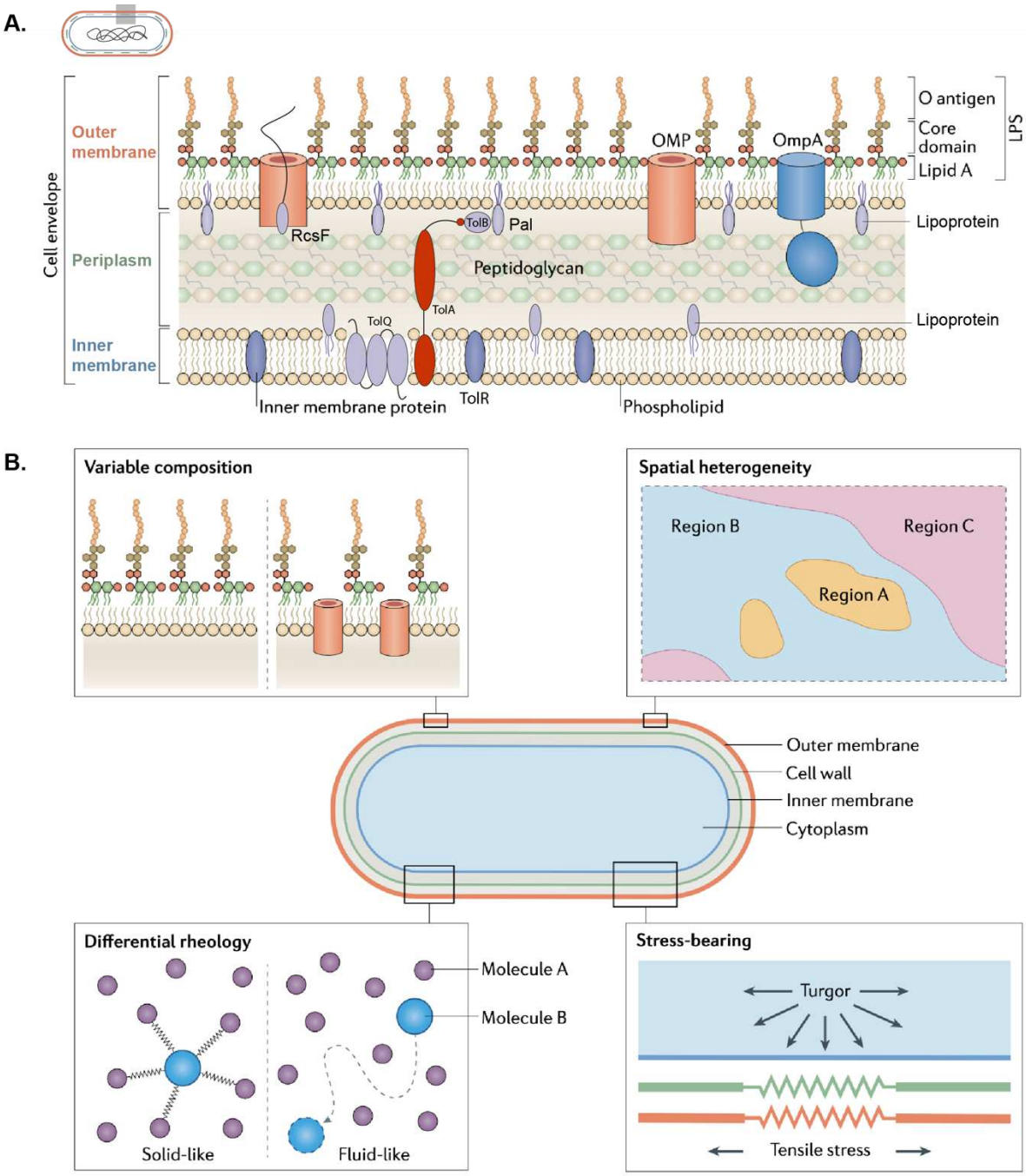


**Figure 4: The Gram-negative bacterial envelope is a complex multilayered structure, with peculiar chemical, physical and mechanical properties.** A. Structure and chemical composition of the bacterial envelope. B. The variable composition of the outer membrane, with immobile outer membrane proteins, defines heterogeneous domains, which confer peculiar rheological and stress-bearing mechanical properties. *Adapted from* (Sun et al., 2021a).

*Mechanical properties*

Already suggested in the past but only recently shown, the outer membrane is one of the stress-bearing mechanical components of the bacterial cell *(Rojas et al., 2018; Sun et al., 2021a; Yao et al., 1999)* (Figure 4B). Indeed, Rojas and colleagues have shown that mechanical stresses are balanced between the cell wall and the outer membrane in Gram-negative bacteria. By applying large hyperosmotic shocks sufficient to induce plasmolysis (*i.e.* to deplete turgor pressure) in *Escherichia coli* (written *E. coli, or Ec*), the authors observed a sudden bacterial reduction in size, showing that the envelope is, as expected, expanded in part by turgor pressure. Under the hypothesis that the cell wall is the sole stress-bearing component in the envelope, the cell envelope should be stress-free after plasmolysis.

To answer this question, the authors further treated the cell with a detergent to remove the membranes. Interestingly, they observed an additional reduction in length by 40%, showing that, in these osmotic conditions, the outer membrane stabilizes the cell wall in a stretched state, by bearing the compressive stress within it.
Outer membrane mechanics is intrinsically linked to its molecular components *(Auer and Weibel, 2017)*. Indeed, various factors play a role in outer membrane mechanics, including LPS *(Herrmann et al., 2015)* and lipoproteins linked to peptidoglycan such as Pal and Lpp *(Mathelié-Guinlet et al., 2020)*. Importantly, the chemical composition of the outer membrane and its associated stiffness are tightly regulated to monitor the extent to which the envelope deforms upon environmental perturbations, functioning as a direct sensor of external stress for bacteria *(Trivedi et al., 2018).*

Thus, due to its chemical composition, the outer membrane protects against chemicals and provides a resistance to turgor pressure and other mechanical stresses.

#### 1.2.1.1.2 The peptidoglycan cell wall

The peptidoglycan cell wall bathes in the periplasmic space, delimited on one side by the outer membrane and on the other side by the inner membrane (Figure 3A). This cellular structure encases the cytoplasmic membrane by a cross-linked polymeric structure, that dictates cell shape and confers mechanical strength to the envelope.

*Chemical composition*

The peptidoglycan cell wall, also called peptidoglycan sacculus, is made of a covalently cross-linked solid-like peptidoglycan network, that forms a giant sac surrounding the cytoplasmic membrane *(Sun et al., 2021a)* (Figure 3A). Its thickness varies between Gram-negative and Gram-positive bacteria. While the peptidoglycan of Gram-negative bacteria is only 1-3 layers (~2-10nm) thick, it is 10-20 layers (~30 nm) thick in Gram-positive bacteria *(Auer and Weibel, 2017)*. In both cases, peptidoglycan strands are composed of monomers of N-acetylglucosamine (GlcNAc)

and N-acetylmuramic acid (MurNAc), covalently bounded by peptide stems emerging from MurNAc monomers.

As the peptidoglycan cell wall surrounds the inner membrane, bacteria must add new material to the peptidoglycan meshwork during cell elongation and division. Enlargement of the sacculus is a dynamic process that involves two multiprotein complexes, that include the divisome which specializes in the synthesis of peptidoglycan during division, and the elongasome which specializes in the synthesis of the peptidoglycan during elongation (Figure 5A). In both cases, biosynthesis of the sacculus involves two groups of enzymes, the synthases and hydrolases *(Egan et al., 2020; Typas et al., 2012)*. The synthases are composed of glycosyltransferases (also written GTases) that polymerize glycan chains and DD-transpeptidases (written TPases, also called Penicillin-Binding-Proteins – written PBPs) that crosslink the peptides to attach the new peptidoglycan material to the existing sacculus. The hydrolases are composed of amidases, glycosidases, and peptidases. Their role is to cleave covalent bonds of the existing peptidoglycan to insert the newly synthesized material, thereby maintaining a constant thickness of the peptidoglycan sacculus *(Höltje, 1998)* (Figure 5B). The released fragments of the peptidoglycan sacculus are then reused to form about 45% of the new peptidoglycan strands, thanks to an efficient peptidoglycan-recycling pathway *(Goodell, 1985; Park and Uehara, 2008)*.

*Mechanical properties*

The peptidoglycan cell wall is characterized by unique mechanical properties, which allow it to fulfill various functions. First, the cell wall is a stress-bearing material. Indeed, by degrading the peptidoglycan sacculus by lysozyme or penicillin during cell growth, it has been shown that bacteria burst and die in a non-isotonic medium *(Lederberg, 1956)*. Thus, the cell wall is a stress-bearing material able to withstand the large outward-facing intracellular pressure, called turgor pressure (Figure 4B). Second, the peptidoglycan cell wall is a non-linear elastic material by contrast with a longstanding belief. Indeed, as peptidoglycan sacculi isolated from *Ec* cells retain their rod shape, scientists have for a long time seen the cell wall as a rigid shell. Yet, by looking at the area of the sacculi, it appears that their surface area is 40% smaller than the one of living bacteria *(Koch et al., 1987; Vollmer et al., 2008a)*, showing that the cell wall is rather an elastic network *(Doyle and Marquis, 1994; Koch et al., 1987; Koch and Woeste, 1992; Yao et al., 1999)*, expanded by cytoplasmic turgor pressure and stabilized by the outer membrane in living cells *(Rojas et al., 2018)* (Figure 4B). More precisely, the cell wall is a non-linear elastic material, that is stress-stiffening, meaning that the more it is deformed, the more stress is needed to further increase the deformation *(Rojas, 2020)*. The peptidoglycan cell wall is also a porous material, whose porosity favors the diffusion of proteins up to 50kDa towards the outer membrane. For bigger proteins such as fimbriae, the activity of specific hydrolases is required to locally open the peptidoglycan network *(Vollmer et al., 2008a, 2008b)*.

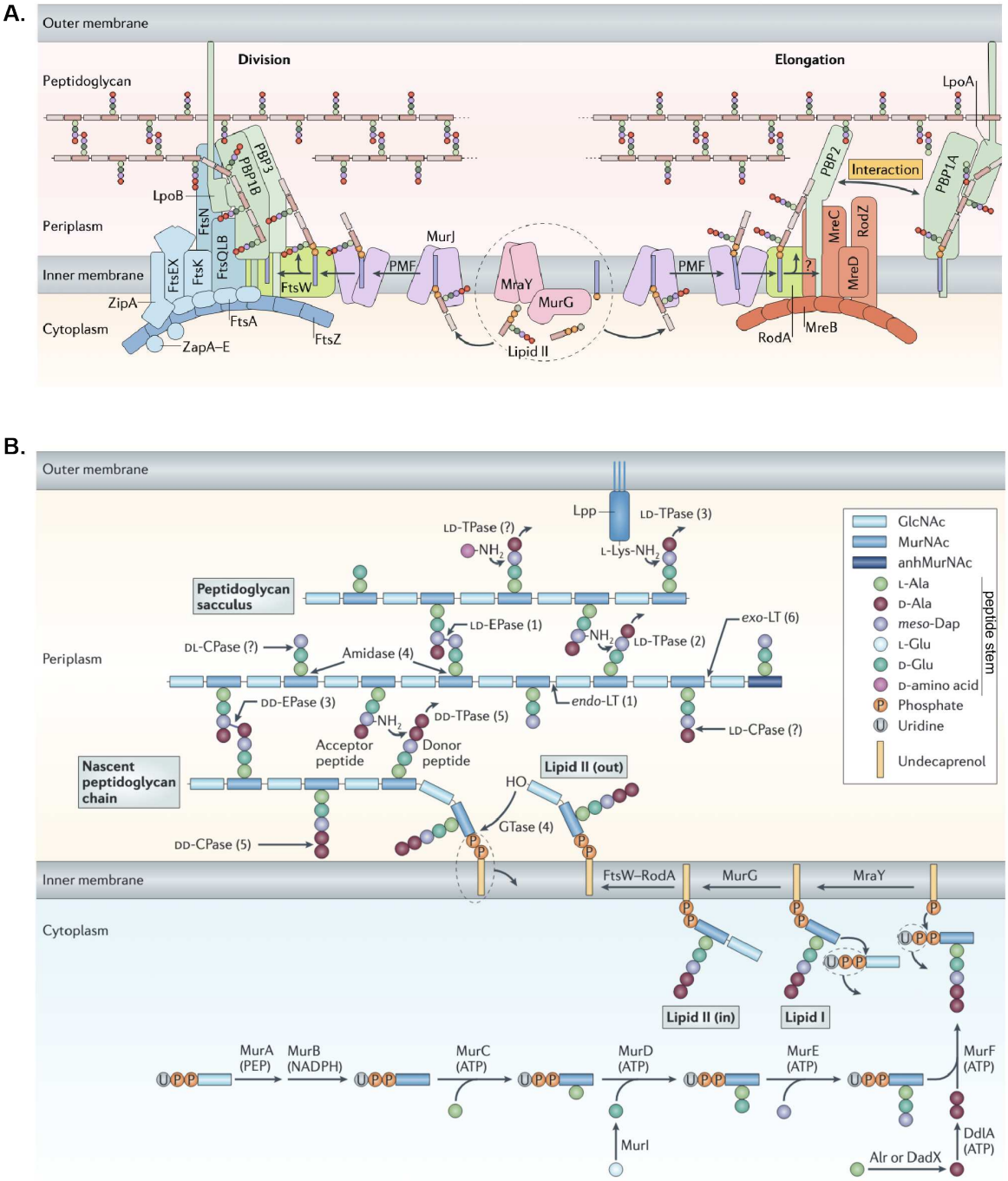


**Figure 5: The Gram-negative peptidoglycan cell wall is composed of cross-linked peptidoglycan chains whose biogenesis is a dynamic process, which involves various players.** A. Cross-linked peptidoglycan chains are synthesized by two multiproteins complexes: the divisome is specialized in the synthesis of peptidoglycan at the division site, while the elongasome is specialized in peptidoglycan synthesis during elongation. Reproduced from (Egan et al., 2020). B. Peptidoglycan synthesis and cleavage involved the coordinated action of various synthetic (GTases, TPases) and degrading enzymes (amidases, endopeptidases written EPases, carboxypeptidases written CPases) (B.). Adapted from (Typas et al., 2012).

In sum, the peptidoglycan cell wall is not a hard shell contrary to a longstanding belief, but rather a flexible and porous structure, that sustains large intracellular pressure.

#### 1.2.1.1.3 The inner membrane

The inner membrane is the final barrier between the external environment and the cytoplasm (Figure 3A). More importantly, it is also the location of many biochemical reactions (such as lipid biogenesis, and envelope precursors formation), that occur in membrane-bounded organelles in eukaryotic cells.

*Chemical composition*

The inner membrane is a highly dynamic double phospholipid bilayer, characterized by a fluid-like behavior *(Sun et al., 2021a)* (Figure 4B). It contains about 1/3 of the proteins expressed by the bacteria, of which 1/3 is associated with transport functions. Inner membrane-associated proteins can be classified into two groups: transmembrane proteins that pass through the membrane, and lipoproteins that are attached to the outer leaflet *(Silhavy et al., 2010)* (Figure 4A). As indicated by the large fraction of proteins located within it, the inner membrane is the location of many biochemical reactions and a crucial port of communication between the different components of the bacterial architecture. In particular, it allows the bacteria to sense various environmental stresses and convert them into a cytoplasmic signal, further triggering specific bacterial responses by modulating gene expression. Consequently, all the stress response pathways rely on a few inner membrane proteins *(Mitchell and Silhavy, 2019)* (Figure 12).

*Permeability properties*

The inner membrane is characterized by a more selective permeability than the outer membrane. Indeed, its double phospholipid bilayer allows the diffusion of only small, uncharged molecules either hydrophilic or hydrophobic (such as water, gas, or glycerol), but prevents the entry of charged or large molecules, that need to pass into the cytoplasm through transport systems. This holds to be true for outer membrane and cell wall proteins, for which the synthesis and the assembly do not occur in the same compartment of the bacterial architecture.

*Mechanical properties*

There has been little investigation into the mechanical properties of the inner membrane compared to the outer one. Yet, one study characterized the inner membrane mechanical properties by performing micropipette aspiration on *Ec* wall-less and outer-membrane-less cells, called spheroplasts *(Sun et al., 2021a)*. In this work, Sun and colleagues observed that, after increasing the tension in the inner membrane by aspiration, the area of the spheroplasts follows a relaxation process characterized by a fast increase followed by a plateau. This mechanical behavior is reminiscent of a viscoelastic material, by contrast with pure phospholipid bilayers

known to be elastic *(Rawicz et al., 2000)*. This viscoelastic behavior has been proposed to rely on the protein composition of the membrane, notably the presence of stretch-activated ion channels whose opening could mediate turgor relief, thereby softening the membrane *(Rojas, 2020).*
Thus, thanks to its viscoelastic mechanical behavior, the inner membrane can sustain large deformations without breaking.

Altogether, the envelope is a complex multilayered shield characterized by unique chemical and mechanical properties, which efficiently protect the bacteria from external perturbations.

#### 1.2.1.2 The cytoplasm: the decision center of the cell

Since the cytoplasm of bacteria does not contain any membrane-bounded organelles, it contains all the materials required for bacterial metabolism (*i.e.* the chemical reactions essential to bacterial survival and proliferation), including the DNA as the set of instructions to follow, ribosomes and amino acids to translate them into proteins, and proteins to execute these functions. As an order of magnitude, the cytoplasm contains 65% of the proteins, of which 20% are ribosomes. Overall, it is now well appreciated that the bacterial cytoplasm is a highly crowded space (Spitzer and Poolman, 2013), as depicted by the artist David Goodsell in numerous illustrations (Goodsell, 2009) (Figure 6).

This high cytoplasmic crowding has several consequences on the biophysical properties of the cytoplasm.

*A compartment under pressure*

The high concentration of solute impermeable to the inner membrane, such as amino acids, generates an osmotic concentration differential across the inner membrane, resulting in the generation of a hydrostatic intracellular pressure, called turgor pressure. The turgor pressure is facing outward, leading to cytoplasmic swelling and cell wall expansion, further balanced by mechanical stress within the envelope (Figure 4B). As an order of magnitude, the turgor pressure is about 100kPa in Gram-negative bacteria and 1MPa in Gram-positive bacteria *(Rojas and Huang, 2018)*. Interestingly, turgor pressure has been shown to regulate growth in Gram-positive bacteria through transient membrane depolarization *(Rojas et al., 2017)*. For now, no direct link between turgor pressure and growth has been found in Gram-negative bacteria. At least, turgor favors cell wall expansion after cell wall precursor insertion *(Rojas and Huang, 2018)*.

*A crowded compartment*

Another consequence of the high concentration of macromolecules within the cytoplasm is the emergence of macromolecular crowding (also written as cytoplasmic crowding). Macromolecular crowding refers to the high occupancy of the cytoplasmic volume by macromolecules, thus physically unavailable to other molecules by steric exclusion *(Ellis, 2001)*. These physical interactions have energetic consequences that largely impact protein behavior within the cytoplasm, thereby affecting signaling dynamics *(Minton, 1983; Wolde and Mugler, 2014; Zhou et al., 2008; Zimmerman and Minton, 1993)*. More precisely, due to the presence of other crowders, a particle of a given size will not be able to access any part of a crowded space. This unavailable volume is called excluded volume and depends on the size of the particle (Figure 7A). Indeed, the smaller a particle is compared to the crowders, the more space will be available to it. In the opposite case, big particles will be sterically excluded in this crowded space, resulting in higher effective concentrations (Figure 7A).

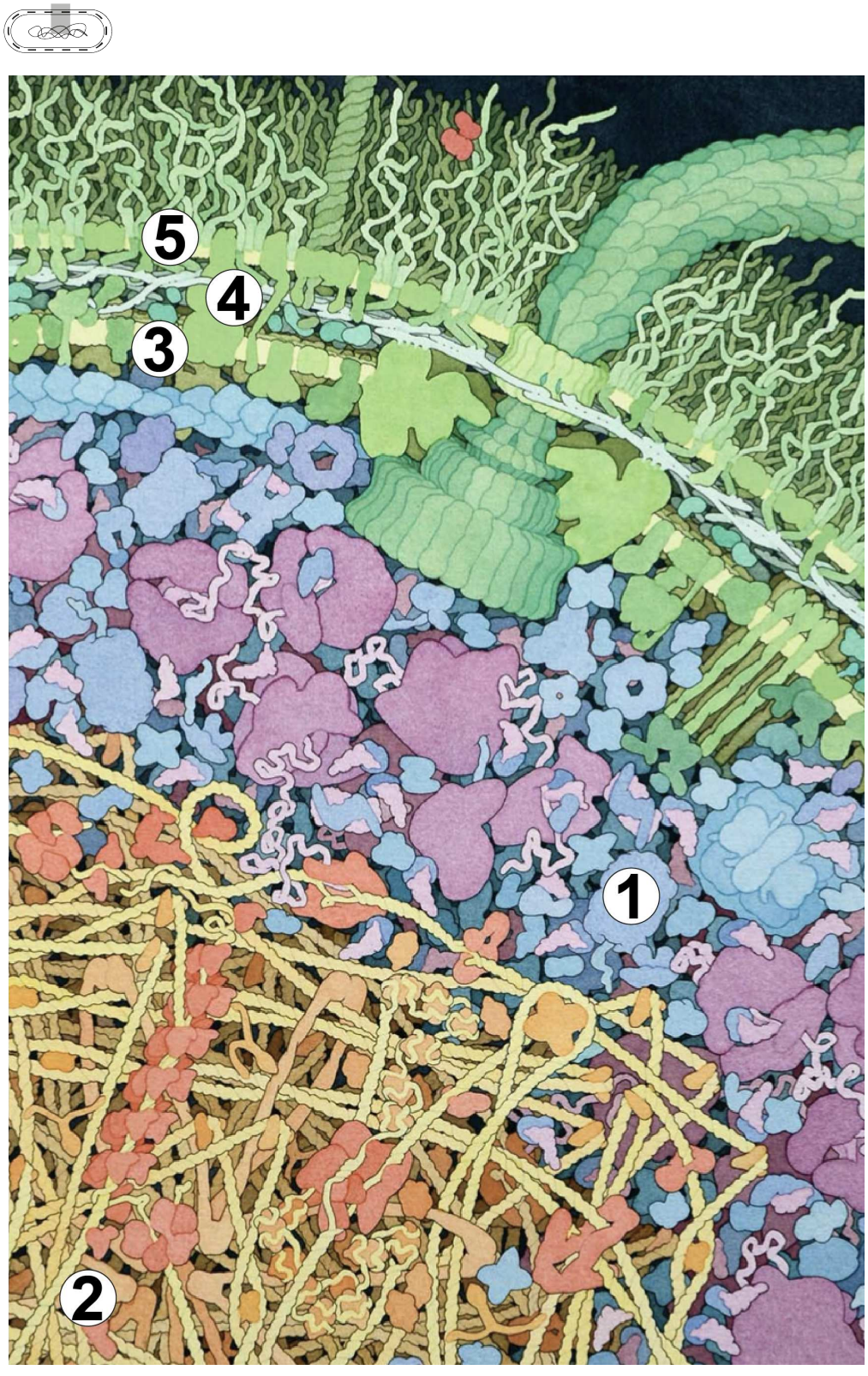


**Figure 6: Illustration of the crowded cytoplasm of the bacterium *Escherichia coli*, drawn using images from electronic microscopy by the artist David Goodsell.** The bacterial cytoplasm (1) contains the DNA (2), and is separated from the external environment by the cell envelope composed of the inner membrane (3), the cell wall (4) and the outer membrane (5). *Adapted from The Machinery of Life, 2009.*

A strong consequence of this size-dependent "concentrated effect" is the non-linear dependence of the reaction rate concerning the size and concentration of the particle, characterized by a bell shape (Figure 7B). It means that, while crowding first leads to an increase in reaction rate by increasing local concentrations, it ultimately hinders chemical reactions by preventing protein dynamics. While this concept is occurring in the cytoplasm of both eukaryotic and prokaryotic cells, it is particularly important in the bacterial kingdom where protein motion is only mediated by diffusion *(Pedrero, 2013)*. The importance of macromolecular crowding in bacteria has been notably exemplified by several publications *(Parry et al., 2014; Xiang et al., 2021)*. By tracking the diffusive motion of various particles of various sizes (plasmids, crescentin, granules, 100µm-wide µNS particles), it has been experimentally shown that the bacterial cytoplasm is characterized by glass-like properties, which depend on particle size *(Parry et al., 2014; Xiang et al., 2021)* (Figure 7C, D) and also on metabolic activity *(Parry et al., 2014)* (Figure 7E).

To summarize, cytoplasmic crowding can have both positive and deleterious effects on protein dynamics and strongly impact bacterial physiology *(Mourão et al., 2014)*. Given that bacteria are highly crowded organisms, one can wonder if and how bacteria control their cytoplasmic composition to remain in the crowding positive range. In search of an answer, Van den Berg and colleagues have recently proposed that bacteria maintain crowding homeostasis by regulating the local concentrations of macromolecules within their cytoplasm, by playing for instance on their spatial organization *(Berg et al., 2017)*.

*A spatially organized compartment*

Contrary to a longstanding belief, the bacterial cytoplasm is highly organized in time and space *(Mathews, 1993; Rudner and Losick, 2010; Shapiro et al., 2009)*, where proteins precisely position in subcellular domains either at the cell poles (in a process referred to as cell polarity *(Bowman et al., 2011)* or at mid cell. The dynamics and organization of the cytoplasm are essential for various aspects of bacterial physiology, including cell cycle progression, differentiation, virulence, chemotaxis, adhesion, and motility *(Kühn et al., 2023, 2021; Laloux and Jacobs-Wagner, 2013; Thanbichler and Shapiro, 2008; Treuner-Lange and Søgaard-Andersen, 2014)*. As an illustrative example, Viable But Not Culturable cells, which are non-growing and non-dividing cells that survive under extreme conditions, are characterized by a loss in cytoplasmic organization *(Trevors et al., 2012)*. Of note, this loss of intracellular organization correlates with an increase in cytoplasmic crowding compared to a growing and dividing cell with a similar macromolecule concentration *(Trevors et al., 2012)*. A similar observation has been reported by Pittas and colleagues, who have shown that cell wall damage induces an increase in cytoplasmic crowding, yet without impacting cell volume nor macromolecule concentration, but rather by impacting cytoplasmic spatial

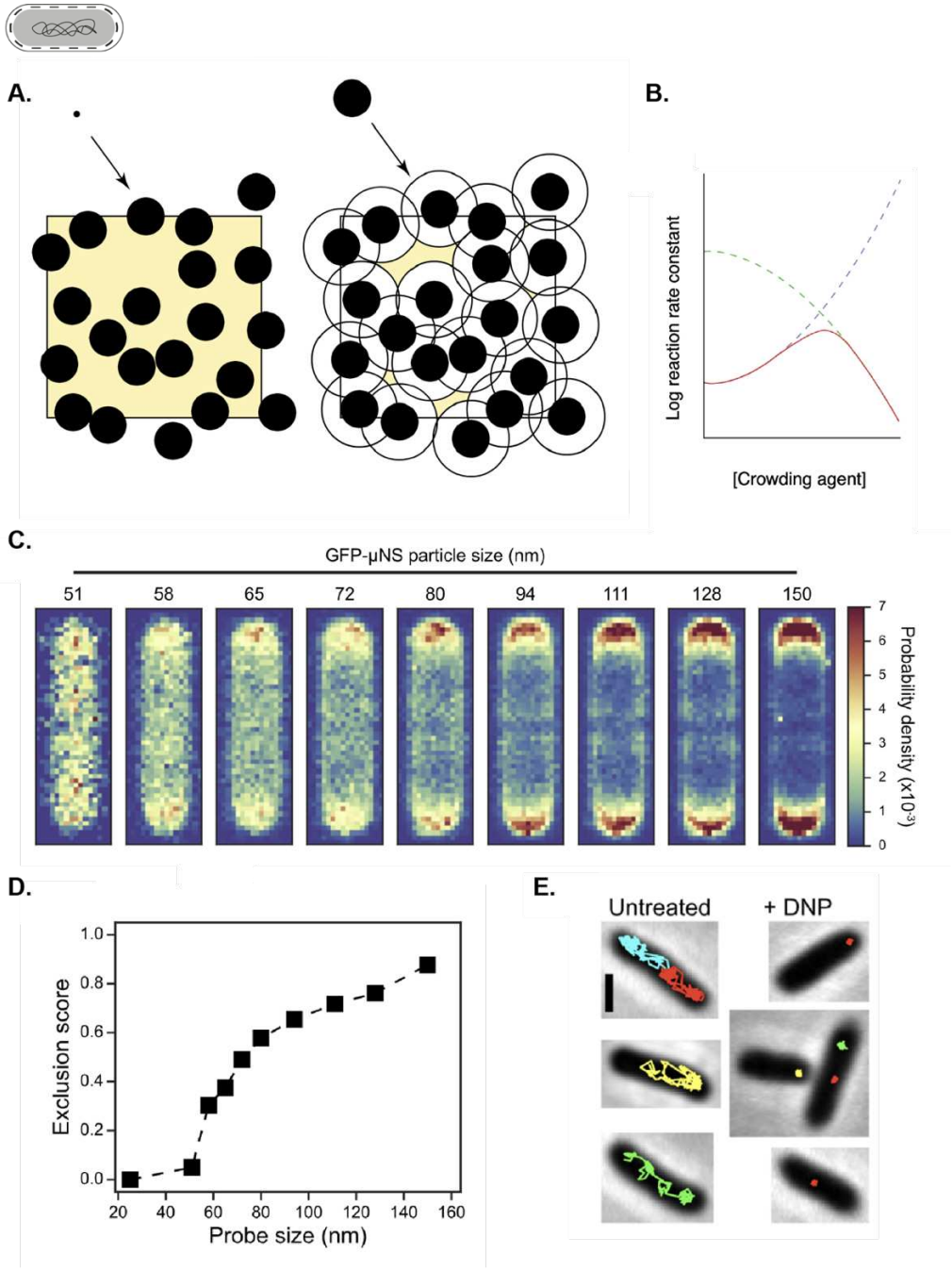


**Figure 7: The bacterial cytoplasm is a highly crowded space characterized by physical properties, which depend on the size of the particle and on the metabolic state of the bacteria.** A. In a crowded environment, the center of a particle smaller than the crowders has theoretically access to the whole space (in yellow, left). By contrast, the center of a particle with a size similar to the one of the crowders cannot approach them from a distance less than the one depicted by the white circles due to steric exclusion (right). Reproduced from (Ellis, 2001). B. Dependence of the reaction rate on the amount of crowding (red). Blue curve: transition state-limited reaction. Green curve: diffusion-limited reaction. Reproduced from (Ellis, 2001). C. Probability density maps of the localization of GFP-μNS particles of various size in the Escherichia coli cytoplasm. Reproduced from (Xiang et al., 2021). D. Corresponding exclusion scores. Reproduced from (Xiang et al., 2021). E. Diffusion trajectories of GFP mini-RK2 plasmids in E. coli cytoplasm under control condition and metabolic depletion (DNP treatment). Reproduced from (Parry et al., 2014).

organization potentially through cytoplasmic mixing and nucleoid expansion *(Pittas et al., 2023)*. Thus, these studies show that cytoplasmic crowding is modulated by cytoplasmic organization.
Interestingly, it has been proposed that crowding itself could participate in cytoplasmic spatial organization, through the formation of cytoplasmic membrane-less microdomains by phase separation *(Gao et al., 2021)*, a physical phenomenon already observed in eukaryotic cells over the past decade *(Hyman et al., 2014)*. Liquid-liquid phase separation (written LLPS) is promoted by macromolecular crowding through depletion forces *(André and Spruijt, 2020)*. It usually occurs at a threshold concentration and leads to the formation of dynamic compartments within the cell similar to oil-in-water droplets *(Hyman et al., 2014)*. While LLPS is responsible for the formation of several bacterial microcompartments, such as RNA polymerase condensates *(Ladouceur et al., 2020)* and potentially the nucleoid *(Rojas, 2020; Wu et al., 2019; Yang et al., 2020; Zhang et al., 2009; Zimmerman and Murphy, 1996)*, its widespread organizing role has only started to be investigated in these last years. In addition, the emergence of new tools to artificially control cytoplasmic condensates is going to provide a better understanding of the regulation of cytoplasmic intracellular organization in bacteria *(Guo et al., 2022)*.

Thus, the bacterial cytoplasm is a dynamic, pressurized, highly crowded, and organized compartment, whose chemical and physical properties largely depend on the bacterial physiological state, together with the physicochemical environment encountered by the bacteria.

### 1.2.1.3 The nucleoid: the code of life

By contrast with eukaryotic cells, DNA is not enclosed within a membrane-bounded organelle. Rather, in bacteria, the genome (that is made of one single chromosome) is contained in a membrane-less compartment, called nucleoid. As an order of magnitude, the nucleoid occupies 60% of the cytoplasmic area at mid-cell in normal growth conditions *(Gray et al., 2019)*.

*Structural organization*

The nucleoid is characterized by a highly compact shape with protruding lobes, located in the middle of the bacterial cytoplasm (Figure 8A). To quantify the compact shape of the nucleoid over various conditions, Gray and colleagues have defined the nucleocytoplasmic ratio (*i.e.* the nucleoid area divided by the bacterial area at mid-cell - written N:C), based on similar studies on eukaryotic cells. The authors have noticed that the size of the nucleoid scales linearly with the size of the bacteria independently of the growth rate, which corresponds to a constant N:C ratio (Figure 8B). Interestingly, they have also shown that bacteria characterized by different N:C ratios exhibit also different cytoplasmic biophysical properties *(Gray et al., 2019)*. Thus, as mentioned previously, the nucleoid occupies a limited fraction of the bacterial volume. Yet, it is not enclosed within an envelope. Thus, why is the DNA so compact within the cytoplasm?

The compaction of DNA is mediated by three factors: DNA supercoiling (mediated by histone-like HU proteins *(Tanaka et al., 1995)*, nucleoid-associated proteins, and cytoplasmic crowding *(Dame, 2005)*. While the role of cytoplasmic crowding in DNA sizing has been well studied by Wu and colleagues *(Wu et al., 2019)*, another related explanation has been provided by Xiang et. al, who proposed that DNA compaction is favored by the poor solvent quality of the cytoplasm *(Xiang et al., 2021)*. Interestingly, by performing rifampicin treatment to inhibit transcription, the authors have shown that the nucleoid occupies all the volume of the bacteria (Figure 8C). Based on this result, Xiang and colleagues have proposed that transcription may contribute to cytoplasmic poor solvent quality *(Xiang et al., 2021)*.

*Mechanical properties*

Although the mechanics of DNA has been extensively studied *ex situ (Benham and Mielke, 2005)*, it is important to assess it *in situ* to understand the link between DNA mechanics and physiology. To this end, Pelletier and colleagues have trapped bacteria within a microfluidic system, induced lysis, and followed DNA behavior upon cytoplasmic release. Interestingly, the authors have shown that, after cytoplasmic release, the chromosome quickly extends to its rest length and reaches a size 10 times larger than its compacted one. The rate of expansion depends on the physiological state of the bacteria: it is quicker for stationary cells than cells in the exponential phase.

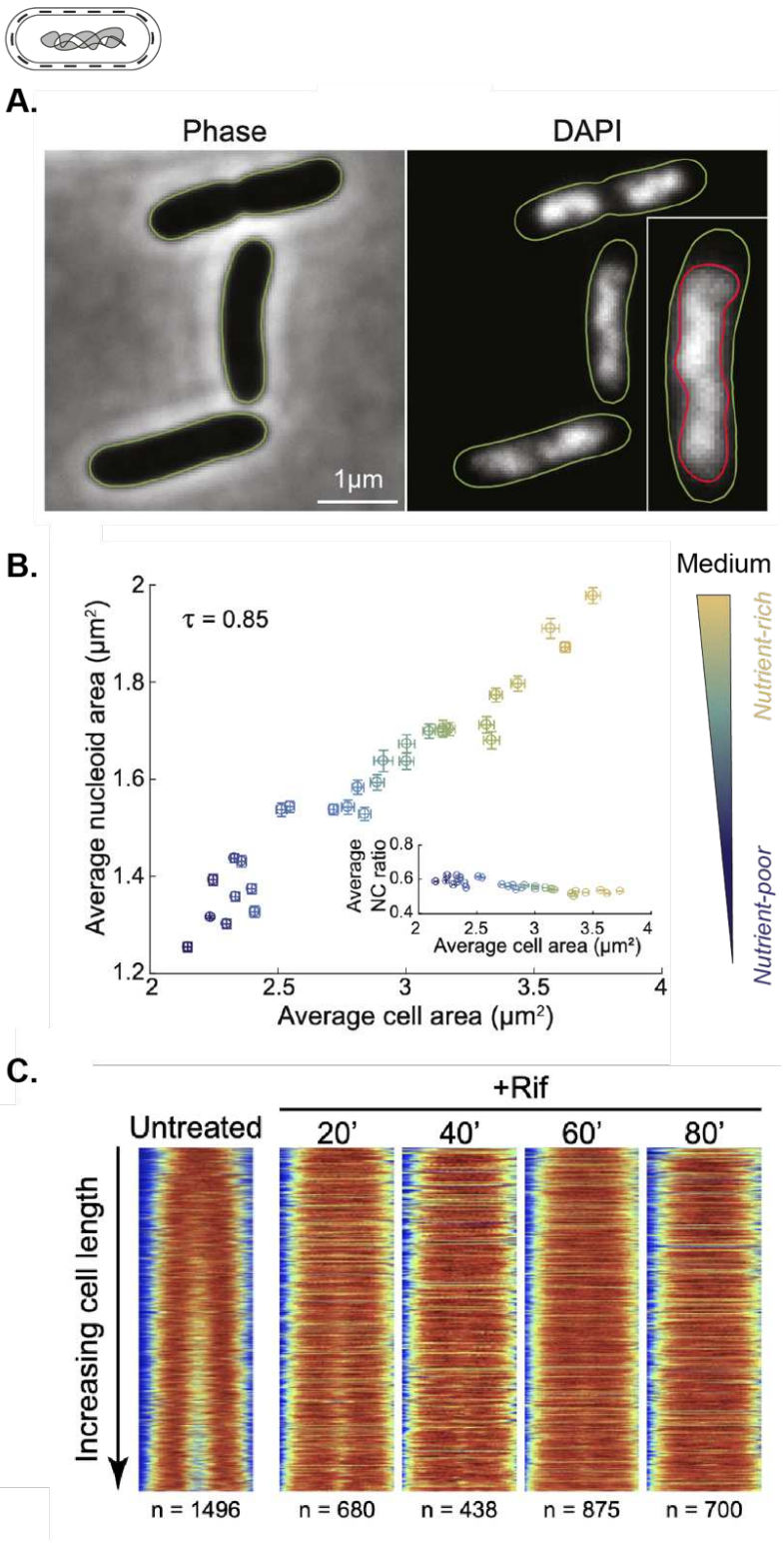


**Figure 8: The nucleoid is characterized by a protruding morphology, whose size linearly scales with the size of the bacteria in homeostatic conditions.** A. Morphology of the nucleoid stained with DAPI in Escherichia coli bacteria. The area of the nucleoid is depicted in red and the area of the bacteria in green. Reproduced from (Gray et al., 2019). B. Relationship between the nucleoid area and the bacterial area for various growth rate. Inset: N:C ratio as a function of the bacterial area. Reproduced from (Gray et al., 2019). C. Kymographs of the nucleoid fluorescence over the bacterial length in control conditions and upon rifampicin treatment. Reproduced from (Xiang et al., 2021).

By coupling the set-up with optical tweezers, Pelletier and colleagues have also noticed that DNA *in vivo* compaction is reached by applying a compression force on DNA that is about one-thousandth of the typical turgor pressure, pointing out that DNA is extremely soft compared to the bacterial envelope that sustains large turgor pressure. Importantly, the authors have also reported that molecular crowding-driven forces alone are sufficient to induce DNA compaction *(Pelletier et al., 2012).*

Thus, the bacterial nucleoid is a highly compact and soft material, whose shape is mainly influenced by its reorganization over the cell cycle and cytoplasmic properties.

In conclusion, bacterial architecture is far from being simple. Instead, it is a multilayered structure, each of these layers being characterized by unique intertwined chemical and mechanical properties. As a whole, the complementarity of these tightly regulated properties allows bacteria to grow and divide while coping with a myriad of environmental stresses.

### 1.2.2 Bacterial growth and division

By looking at bacterial proliferation under the microscope, it is striking that bacteria robustly maintain their favorite size over multiple generations, in a process called size homeostasis. Like eukaryotic cells *(Murray and Hunt, 1994)*, bacteria tightly coordinate in concert their growth and their division to maintain their size over multiple generations through various mechanisms, that are detailed in this section.

#### 1.2.2.1 Cell size homeostasis

How are bacterial growth and division coordinated to ensure cell size control over multiple generations? Before addressing this question, we first describe bacterial growth over the cell cycle. At first glance, bacterial growth seems to be a relatively simple process. Indeed, one could depict bacterial growth as in the following. First, bacteria increase their mass by replicating DNA and synthesizing new proteins. This process is coupled with an increase in their size and volume by water influxes to maintain a roughly constant density *(Neurohr and Amon, 2020)*. Then, bacteria divide at mid-cell to give birth to two daughter cells of equivalent mass, size, volume, and density. Yet, by zooming in at the level of bacterial architecture, it appears that cell size control during bacterial growth results from the coordination of multiple tightly regulated events. Indeed, during growth, bacteria double their mass and size, initiate and terminate chromosome replication, segregate the two sister chromosomes, assemble the division machinery precisely at the mid-cell, and coordinate the 3 layers-envelope invagination with its synthesis to form a septum that will physically separate and give birth to two independent daughter cells *(Haeusser and Levin, 2008)* (Figure 9). The proper order of all these events throughout the cell cycle is ensured through various checkpoints, which act as gatekeepers, although these mechanisms are less understood in bacteria than in their eukaryotic counterparts *(Boye and Nordström, 2003)*. But how is cell size control achieved throughout the cell cycle?

While various models of growth have been proposed in the past to explain the control of cell size (adder, sizer, timer) mostly for rod-shaped bacteria *(Taheri-Araghi et al., 2014)*, it seems that they are too simple to explain precisely bacterial growth in general (Willis and Huang, 2017). Thanks to intensive research on the topic, we are understanding more and more how bacteria coordinate their growth and division to reach cell-size homeostasis. In particular, we now have evidence that bacteria finely tune both the timing of DNA replication and division in regards to bacterial size, together with the spatial positioning of the division site to ensure cell size control over time *(Chien et al., 2012)*.

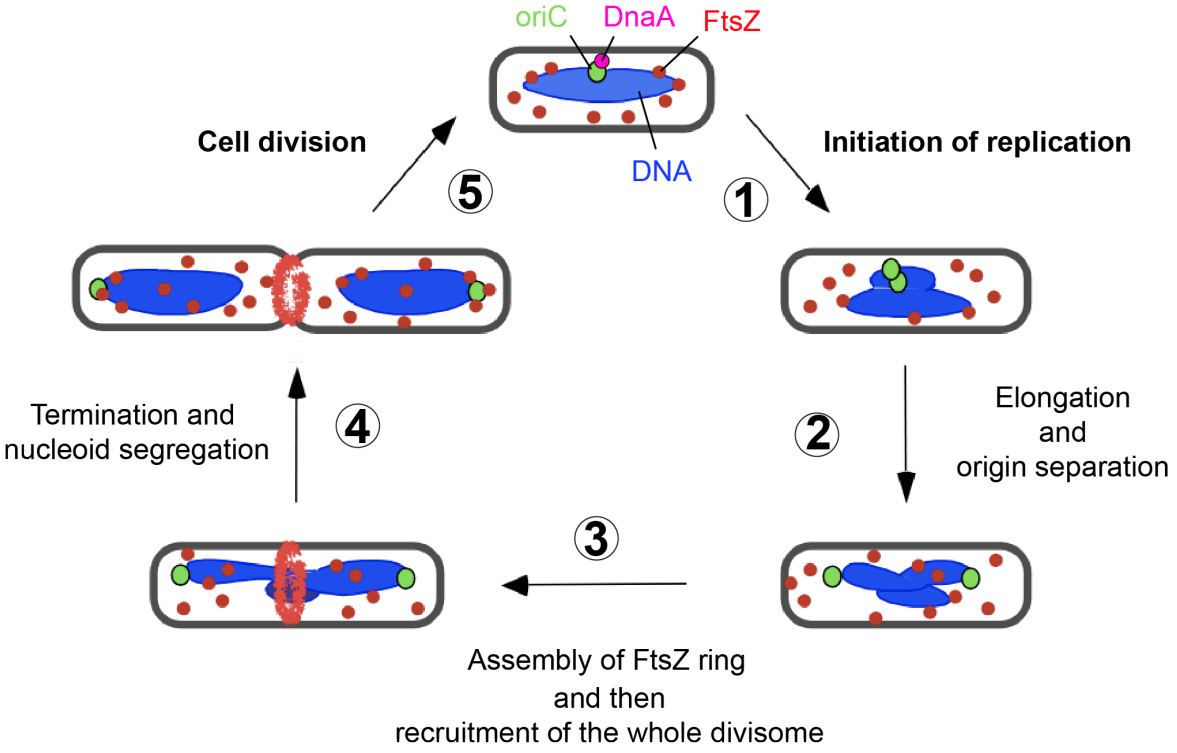


**Figure 9: Cell cycle progression for the bacterium *Escherichia coli*.** First, the binding of DnaA to the origin of replication (oriC) induces the initiation of DNA replication (step 1). After chromosome replication initiation, the origins of replication separate and the bacterium elongates (step 2). Once the replication is complete, the FtsZ ring assembles over the nucleoid that is segregating (step 3). Once the chromosomes are well separated, the FtsZ ring constricts (step 4) and gives birth to two daughter cells of similar size than the mother cell. Adapted from (Chien et al., 2012).

### 1.2.2.2 Initiation of DNA replication under the control of cell size

The first observation supporting this hypothesis is that the initiation of DNA replication occurs at a specific cell size in *E. coli (Donachie, 1968)*. At the molecular level, the initiation of DNA replication is triggered by the binding of DnaA, a highly-conserved ATPase, on a specific region on the origin of replication of the chromosome (Figure 9). Its binding opens the DNA double helix near AT-rich regions and favors the formation of the replication complex (called replisome) and further DNA replication. While several studies support the hypothesis of a growth-dependent accumulation of DnaA triggering event of DNA *replication (Hill et al., 2012; Ho and Amir, 2015; Løbner-Olesen et al., 1989)*, some suggest that it is unlikely to be the only mechanism at play to ensure cell size homeostasis. Notably, when initiation of replication is triggered earlier in bacteria, it has been shown that they spend a longer time waiting for divisome assembly, showing that DnaA accumulation alone is not sufficient to trigger division at a specific cell size *(Boye et al., 1996)*. Indeed, if DNA replication initiation would be the sole cell size regulator, bacteria would be unprotected against further unexpected cell size perturbation, and thus unable to control their size as robustly as they do.

### 1.2.2.3 Initiation of division under the control of cell size

To maintain size homeostasis across generations, division is coupled with cell growth to occur only once bacteria have doubled in size. To do so, bacteria need to sense their size and communicate it to the division apparatus. In most bacteria, division is initiated by the formation of a highly dynamic FtsZ ring-like structure at mid-cell, which defines the future division site *(Harry et al., 2006; Romberg and Levin, 2003)* (Figure 9). This FtsZ ring-like structure, often called the Z ring, serves as a scaffold for the recruitment of the whole division machinery. The division machinery is composed of dozens of proteins, such as ZipA which participates in the anchoring of the Z ring to the inner membrane, and directs peptidoglycan synthesis for septum formation *(Adams and Errington, 2009; Du and Lutkenhaus, 2017)* (Figure 9). Although the nature of the signals triggering Z-ring assembly and constriction is still unknown, several studies have investigated a potential relationship between Z ring formation and cell size control. In particular, it has been shown that FtsZ cytoplasmic concentration remains constant throughout the cell cycle, but that Z ring assembly occurs at a growth rate-dependent frequency *(Weart and Levin, 2003)*, suggesting a cell size control of division initiation. Following this observation, Si and colleagues have shown that bacteria divide after accumulating a threshold number of FtsZ monomers *(Si et al., 2019)*. As FtsZ is constitutively expressed, the number of FtsZ available in the cytoplasm is directly dependent on the growth rate. In other words, one necessary condition for division initiation is that the total amount of FtsZ monomers (that is proportional to cell size) is sufficiently high, meaning that division initiation occurs in a size-dependent process *(Chien et al., 2012)*. Importantly, while Z

ring formation is not a sufficient condition for division *(Levin and Angert, 2015)*, bacterial division alone is responsible for cell-size homeostasis *(Si et al., 2019)*.

#### 1.2.2.4 Spatial control of the division site by the Min system and nucleoid occlusion

As mentioned previously, the signals favoring Z ring assembly at mid-cell to ensure progeny equality are unknown. However, there is evidence of the presence of two mechanisms, that prevent Z ring assembly at aberrant locations within the bacterial body (Figure 10).

Among these mechanisms, one can cite the Min system that prevents Z ring assembly near the cell poles (Figure 10, in brown) and the consequent birth of anucleate daughter cells *(Lutkenhaus, 2007)*. Interestingly, Männik and colleagues have remarkably shown that this mechanism is limited in bacteria with irregular morphologies *(Männik et al., 2012)*.

Another mechanism used by bacteria to prevent Z ring constriction over non-segregated DNA is nucleoid occlusion *(Adams et al., 2014; Lewis, 2008; Wu and Errington, 2012)* (Figure 10, in blue). In *E. coli*, nucleoid occlusion is partly mediated by the protein SlmA *(Bernhardt and Boer, 2005)*. SlmA is a FtsZ antagonist, that has been shown to directly interact with FtsZ by disrupting preformed FtsZ polymers *(Cho et al., 2011)*. Of note, nucleoid occlusion has been reported to happen, sometimes, independently of SlmA *(Männik et al., 2012; Tiruvadi-Krishnan et al., 2022)*.

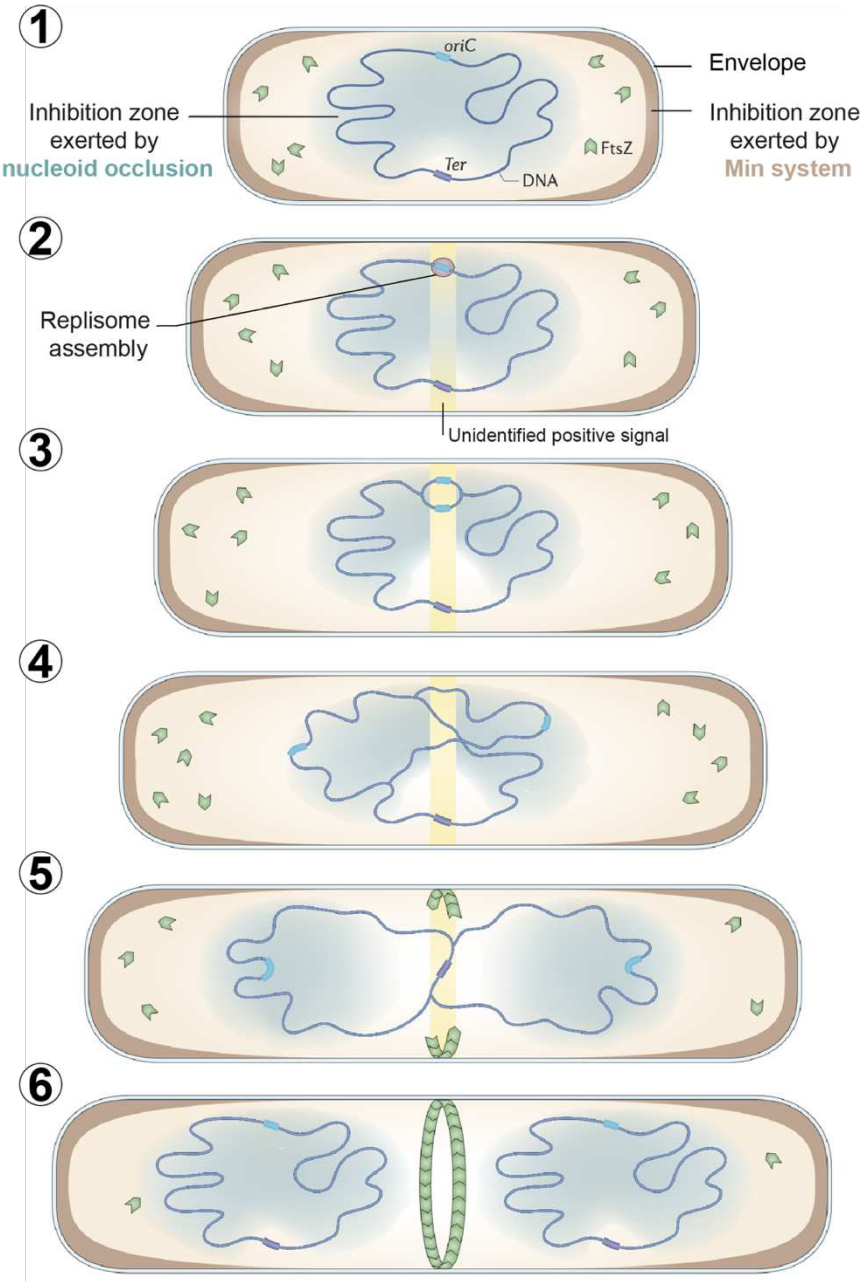


**Figure 10: Spatiotemporal regulation of bacterial division through the Min system (in brown) and nucleoid occlusion (in blue).** During the first steps of the cell cycle (steps 1 to 4), the Min system prevent Z-ring assembly near the poles, while nucleoid occlusion prevents Z-ring assembly closely to the DNA. Once the replication is almost over, a nucleoid occlusion and Min-free zone appears at mid-cell, allowing FtsZ assembly. Then, once DNA replication is complete and the chromosomes segregated, the whole divisome machinery assembles and further constricts. Reproduced from (Wu and Errington, 2012).

### 1.2.3 Bacterial adaptation to changing environments

In the wild, bacteria experience a wide range of changing environmental conditions, often called stresses, to which they need to adapt to survive. For instance, bacteria living in marine environments cope with a wide range of salt concentrations. Yet, how do single-celled bacteria sense and adapt to changing environmental conditions through their multilayered architecture? In this section, I describe how bacteria generally cope with these environmental stresses, before focusing on specific pathways that could be of interest upon mechanical perturbations.
In the following, a stress response is defined as the transcriptional regulation of a specific set of genes in response to a given environmental condition.

#### 1.2.3.1 Two-component systems, a general and efficient way used by bacteria to reprogram gene expression in response to changes at the extracytoplasmic level

To rapidly and reversibly respond to changing environments, bacteria have evolved various sophisticated molecular systems to sense extracytoplasmic environmental changes and adapt by modulating gene expression. These systems, called two-component (regulatory) systems (TCS), allow bacteria to sense many types of extracytoplasmic stress and convert this signal into a biochemical one. This signal will consequently be used to transcriptionally regulate gene expression through the activation of a stress response, and ultimately favor bacterial survival (Figure 11A). As an order of magnitude, *E. coli* encodes about 30 two-component systems *(Choudhary et al., 2020)*, underscoring that TCS are a widespread mechanism used by bacteria to cope with stress. Typically, a TCS is composed of two components (as its name suggests), that are a transmembrane sensor and its cytoplasmic cognate response regulator. While the sensor detects a specific signal either external or internal to the cell, it also transduces it to its cognate regulator, which will further interact with the transcription machinery to modulate gene expression. In practice, the sensor is often a phosphorelay such as a histidine kinase. The signal reception induced the activation of the kinase domain, which in turn leads to the phosphorylation of the histidine part. Then, the phosphate group is transferred to the cognate regulator. As a result, the regulator's properties are modified, such as its capacity to interact with promoters of various genes of interest to modulate their transcription. Once the response is triggered, the regulator loses its phosphate group and comes back to its initial state *(Storz and Hengge, 2020)*.

Thus, TCS is a widespread mechanism used by bacteria to convert extracytoplasmic changes into a cytoplasmic signal, thereby serving as a first step towards bacterial adaptation.

### 1.2.3.2 Alternative σ factors, an efficient way used by bacteria to reprogram gene expression in response to changes at the cytoplasmic level

Once these changes occur at the cytoplasmic level, bacteria often take advantage of the flexibility of their transcription machinery to reprogram gene expression at the transcriptional level. In bacteria, transcription is initiated by the attachment to of the RNA Polymerase holoenzyme, which is composed of a core enzyme bound to a σ subunit, to DNA strands. The σ subunit (often called σ factor) is a general transcriptional factor that reversibly binds to the RNA Polymerase core enzyme to determine which specific set of genes will be transcribed.

To cope with various environmental conditions, bacteria have evolved several σ factors, which are summarized in Table 1 (*adapted from the book Microbiologie, DUNOD, 2021*). In normal conditions, the RNA Polymerase core enzyme is bound to the housekeeping $\sigma^D$ subunit, which ensures metabolism and housekeeping functions. However, upon stressful conditions (*e.g.* conditions that deviate from a homeostatic, physiological condition), bacteria rely on alternative σ factors that in turn control the expression of specific sets of genes (called stress response or σ regulon), allowing bacterial adaptation (Figure 11B). As an example, the $\sigma^H$ subunit is activated upon heat shock and promotes the transcription of genes involved in protein folding.

The activation of all these σ factors relies on a similar mechanism. In normal conditions, the alternative σ factor is not available in the cytoplasm, thereby preventing the formation of the corresponding RNA Polymerase holoenzyme. The unavailability of the alternative σ factor is ensured by either its low synthesis, its active degradation, or its sequestration by other proteins. However, upon stressful conditions, the alternative σ factor is either synthesized, enriched, or released from sequestration, allowing it to bind to the RNA Polymerase core enzyme and enter into action *(Helmann, 2019)*.

| *Gene* | *Name* | *Stress?* | *Number of targeted genes* | *Function of targeted genes* |
|---|---|---|---|---|
| rpoD | $\sigma^D$ | No | >1000 | Metabolism and housekeeping functions |
| rpoS | $\sigma^S$ | Yes | ~ 100 | General stress response |
| rpoH | $\sigma^H$ | Yes | ~ 40 | Cytoplasmic protein folding |
| rpoE | $\sigma^E$ | Yes | ~ 5 | Extracytoplasmic protein folding |
| rpoF | $\sigma^F$ | Yes | ~ 40 | Flagella and chimiotactism |
| fecI | $\sigma^{fecI}$ | Yes | ~ 5 | Iron citrate import |
| rpoN | $\sigma^N$ | Yes | ~ 15 | Nitrogen metabolism |

**Table 1: Overview of the sigma factors expressed in *Escherichia coli*.** *Adapted from Microbiologie, DUNOD (2021)*

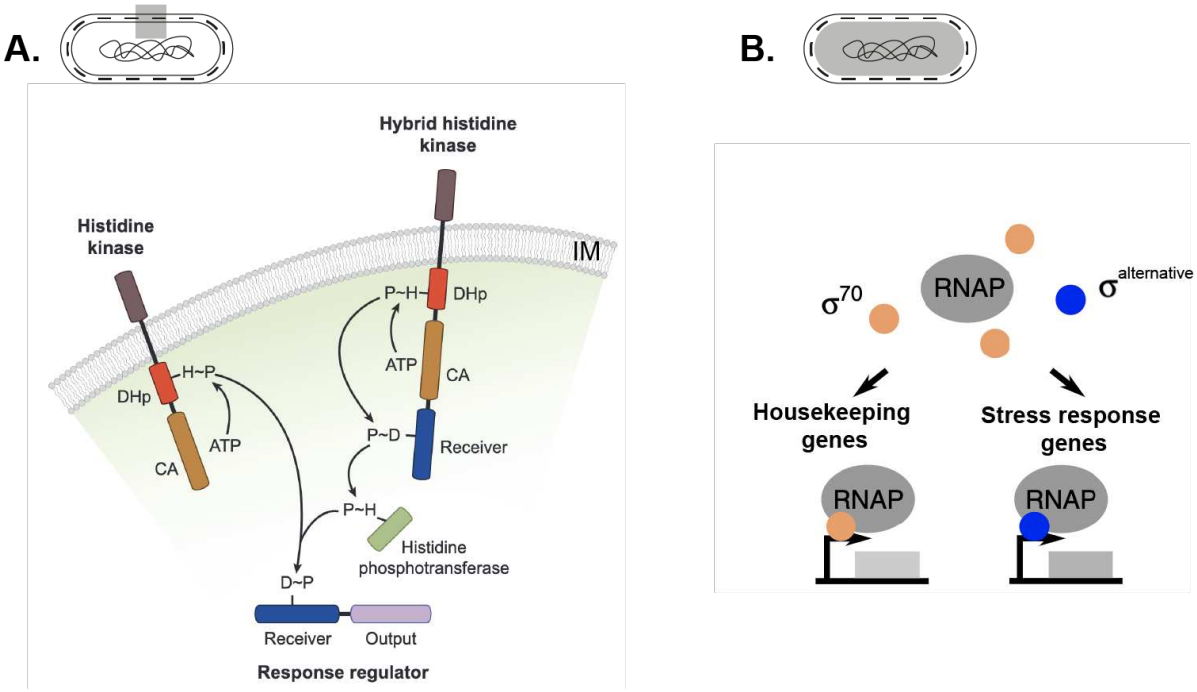


**Figure 11: Mechanisms used by bacteria to adapt gene expression in response to changing environmental conditions.** A. When changes occur in the extracytoplasmic space (outer membrane or periplasm), bacteria use two component systems (left, such as Cpx response) or hybrid two component systems (right, such as Rcs response) to reprogram gene expression. Reproduced from (Laub and Goulian, 2007). B. When changes occur in the cytoplasmic space, bacteria take advantage of the alternative sigma factors to reprogram gene expression. Upon binding to the RNA polymerase holoenzyme, sigma factors determine the set of genes that will be transcribed to further mount an appropriate response. Adapted from (Patange et al., 2018).

Thus, alternative σ factors are a powerful mechanism to modulate gene expression rapidly and efficiently in response to changes at the cytoplasmic level, thereby allowing quick and efficient bacterial adaptation.

### 1.2.3.3 A few examples of stress response pathways

To efficiently adapt to changing environments, bacteria have evolved several stress response pathways, each of them being dedicated to one specific stimulus. In the following, I briefly detail a few stress response pathways investigated in this PhD work that could be activated in response to mechanical stresses.
In practice, the activations of these stress responses are usually assessed using transcriptional reporters, many of their plasmidic versions being available in Uri Alon's collection *(Zaslaver et al., 2006)*.

#### 1.2.3.3.1 The Rcs and Cpx envelope stress responses

As the envelope is the first line of defense against a changing environment, bacteria use at least five different envelope stress response pathways (Rcs, Cpx, Psp, Bae, and $\sigma^E$) to ensure envelope homeostasis. These adaptation pathways allow bacteria to sense various perturbations that impact the integrity of the envelope, and to trigger an appropriate response that will repair or contain the damage. In response to a given change, bacteria often activate several of these pathways as they are associated with different transcriptional responses, each of their individual contributions ultimately allowing the mounting of a full adaptive response *(Bury-Moné et al., 2009)*. Among them, the Rcs (Figure 12A) and Cpx (Figure 12B) pathways are the two ones known to be involved in contact sensing, which is of particular interest in the scope of this work.

*Triggering signals*

Rcs activation has been reported upon bacterial adhesion on surfaces and in the presence of defects in OM and/or cell wall. Similarly, Cpx activation has been related to adhesion on hydrophobic surfaces and in the presence of periplasmic misfolded proteins, and defects in the cell wall *(Delhaye et al., 2016)*. However, the molecular nature of the activation signal is still a mystery for these two pathways.

*Mechanisms involved in the Rcs and Cpx stress responses*

The Cpx pathway relies on a classical TCS (Figure 11A) while the Rcs pathway relies on a hybrid TCS system (Figure 11B). Both are activated by a lipoprotein anchored at the inner leaflet of the outer membrane. While the Rcs pathway requires the activation of its TCS by the RcsF lipoprotein, the Cpx pathway can be activated even without NlpE lipoprotein activation of its TCS. The Rcs pathway relies on the RcsC sensor and the RcsB regulator (whose auxiliary activator protein is RcsA) (Figure 12A). Similarly, the Cpx pathway relies on the CpxA sensor (whose kinase activity is modulated by the CpxP protein) and the CpxR regulator (Figure 12B).

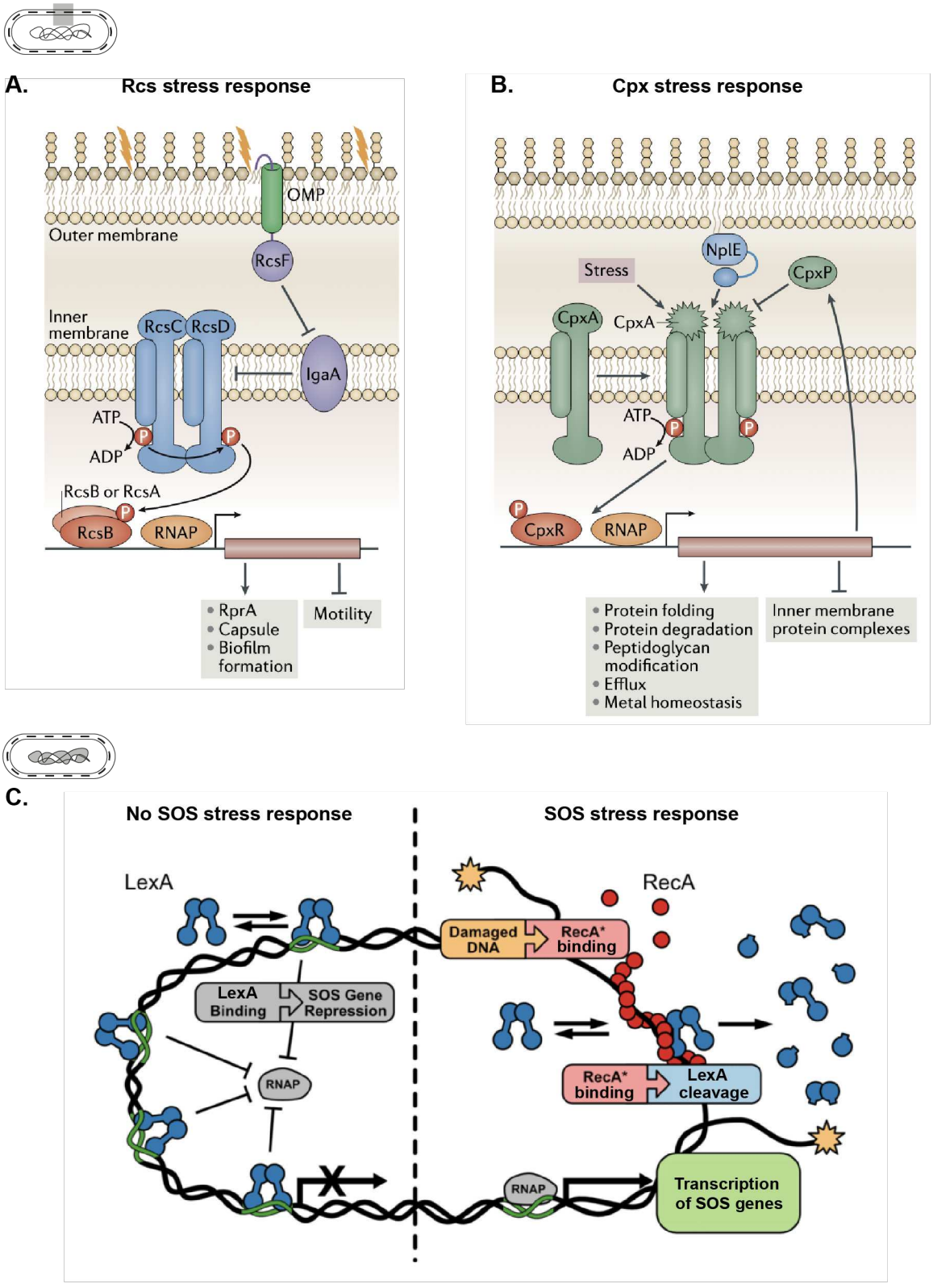


**Figure 12: Overview of the Rcs (A) and Cpx (B) envelope stress responses, and the DNA damage (C) stress response.** Reproduced from (Mitchell and Silhavy, 2019) (A, B) and (Hostetler, 2018) (C).

Together, these two pathways provide a molecular connection between all the strata that compose the bacterial surface architecture and are part of the adaptation strategy to cope with extracytoplasmic changing conditions.

*Adaptation mediated by Rcs and Cpx pathways*

Activation of the Rcs pathway plays a crucial role in the late stage of biofilm formation. In particular, Rcs pathway triggers the expression of genes involved in capsule synthesis, together with the production of extracellular matrix, while it downregulates motility-related genes, such as flagellar synthesis (Figure 12A). Interestingly, many of the genes regulated by Rcs are also regulated by $\sigma^S$, meaning that Rcs regulates a subset of $\sigma^S$-controlled genes. Similarly, certain genes expressed in biofilms are $\sigma^S$-dependent *(Majdalani and Gottesman, 2005)*.

Regarding Cpx, activation of this pathway has been shown to ensure the selective maintenance of the envelope. Notably, it has been reported to regulate periplasmic protein folding factors, peptidoglycan remodeling enzymes, and inner membrane proteolysis, while it downregulates envelope-localized proteins such as pili or flagella (Figure 12B).

Importantly, both Rcs and Cpx envelope stress responses have been shown to play a crucial role in the emergence of antibiotic resistance *(Guest and Raivio, 2016)*. Cpx seems also implicated in the emergence of virulence *(Hews et al., 2019; Raivio, 2005)*.

#### 1.2.3.3.2 The protein misfolding stress response (or heat shock response)

The protein misfolding stress response, or more generally the cytoplasmic protein quality control system used by bacteria to deal with misfolded/unfolded proteins, is a highly conserved cellular response, whose main role is to ensure protein and ribosome homeostasis *(Storz and Hengge, 2020)*.

*Triggering signals*

This stress response pathway is triggered by the level of unfolded proteins within the cytoplasm, induced by temperature shifts or other changing conditions. Notably, mechanical stresses have also been shown to induce this response *(Chu et al., 2018)*.

*Mechanisms involved in the protein misfolding stress response*

This stress response pathway is mediated by the activation of the alternative σ factor $\sigma^H$. In normal conditions, $\sigma^H$ is bound to DnaK chaperones, hindering the binding of the $\sigma^H$ subunit to RNA Polymerase. Under stressful conditions, DnaK chaperones are recruited to fold misfolded proteins, which in turn release $\sigma^H$ from DnaK. This allows its binding to the RNA Polymerase core enzyme, thereby triggering the transcription of a specific set of genes. Once the stress is released, DnaK binds again to $\sigma^H$ leading to its inactivation *(Storz and Hengge, 2020)*.

*Adaptation mediated by protein misfolding stress response*

Upon activation, this stress response tunes the transcription, translation, and repair machineries to deal with unfolded proteins, through the production of chaperones, that favor protein folding, and proteases, that degrade unfolded proteins. IbpA (Inclusion Body binding Protein A) is one of the small heat shock proteins (chaperone) whose function is to sequestrate misfolded proteins within a microcompartment, called inclusion body *(Mogk et al., 2011; Tyedmers et al., 2010)*. To a smaller extent, this stress response also maintains the integrity of the inner membrane under stress.

#### 1.2.3.3.3 The DNA damage stress response

The DNA damage stress response, also called SOS response, aids bacterial survival from lethal lesions within its chromosome. This adaptation pathway is characterized by a spontaneous induction in less than 1% of *E. coli* bacteria, showing that DNA damage occasionally occurs in normal conditions *(Storz and Hengge, 2020)*. Notably, this stress response has been previously reported to be induced by large hydrostatic pressures (~ 100 MPa) *(Aertsen et al., 2004; Aertsen and Michiels, 2005)*.

*Triggering signals*

The DNA damage stress response is induced by the presence of single-strand DNA within the cytoplasm. Single-strands DNA are either caused by incomplete replication or double-strand breakage. In particular, upon large hydrostatic pressure, double-strand breakage has been reported to be induced by the activation of the Mrr restriction endonuclease, which is an enzyme that cleaves double-strand DNA *(Aertsen and Michiels, 2005)*.

*Mechanisms of the DNA damage stress response*

This stress response pathway is mediated by both LexA and RecA proteins. More precisely, RecA first forms a filament over the single-strand DNA. Then, this filament interacts and cleaves the LexA repressor, thereby allowing the expression of the LexA regulon genes involved in DNA repair (Figure 12C) *(Storz and Hengge, 2020)*.

*Adaptation mediated by the DNA damage stress response*

Most of the LexA-repressed genes have been shown to play a role in DNA repair, including excision repair (through the expression of SOS DNA polymerase that are able to replicate broken DNA) and recombinational repair (homologous recombination to repair single strand gaps) *(Storz and Hengge, 2020)*.

#### 1.2.3.3.4 Stationary phase stress response

The stationary phase stress response, also called the general stress response, allows bacteria to adapt during slow growth conditions. The induction of this stress response serves as a harbinger of other stresses and provides to the bacteria with the broad

resistance mechanisms essential for bacterial survival in stressful conditions. Upon its induction, bacteria become resistant to various environmental changing conditions, that seem yet related to different adaptation pathways.

*Triggering signals*

To date, we know that this pathway is not activated when growth and nutrient conditions are optimal, while it is activated in many other conditions including slow growth, high cell density, nutrient starvation, heat shock, high osmolarity, and DNA damage *(Storz and Hengge, 2020).*

Similar to the protein misfolding stress response, the activation of the stationary phase stress response relies on the binding of the alternative σ factor $\sigma^S$ to the core RNA Polymerase. To date, $\sigma^S$ activation is known to rely on many different pathways, one of them depends on the ppGpp-mediated stringent response *(Battesti et al., 2011),* and another one on the Rcs envelope stress response *(Gottesman, 2019).*

*Mechanisms involved in the stationary phase stress response*

The $\sigma^S$ general transcriptional factor is the key regulator of the stationary phase response in a highly complex manner *(Battesti et al., 2011; Storz and Hengge, 2020).* So far, what we know is that $\sigma^S$ synthesis increases in the presence of the activation signal (*e.g.* ppGpp concentration or Rcs pathway induction) while its degradation is inhibited.

*Adaptation mediated by the stationary phase stress response*

Once activated, this general transcriptional factor triggers the expression of the downstream regulon. The gene *yiaG* belongs to this regulon *(Lacour and Landini, 2004; Weber et al., 2005),* and is an excellent reporter for both $\sigma^S$ activation and entry in dormancy *(Saint-Ruf et al., 2014).* More generally, the stationary phase stress response pathway favors bacteria survival under various stressful conditions, including growth arrest, nutrient starvation, high temperature, and osmotic stress. Importantly, bacteria that induce this stress pathway are characterized by an ovoid morphology, change in metabolism, and change in membrane composition together with a biofilm lifestyle.

Altogether, bacteria use various sophisticated mechanisms to adapt to a wide range of changing conditions, that could occur in all the strata of their architecture. These adaptation pathways make them stronger and more resistant to environmental changes, ultimately favoring their survival upon both chemical and mechanical perturbations.

## 1.3 How is the microbial world classically studied in the lab?

In the previous sections, we have seen that the bacterial world is fascinating because of its diversity, its structural complexity, and, last but not least, its adaptability. However, most of the knowledge we have, to date, about this tiny world arises from experiments in steady-state conditions eventually in the presence of antibiotics. Indeed, classical microbiology experiments are performed either on solid agar plates, in liquid suspension, or under agar pad. Although these steady conditions are far from the physiological ones encountered by bacteria in the wild, these experimental setups have enabled scientists to gain a first understanding of bacterial physiology in optimal and steady conditions. Yet, as bacteria dynamically adapt their growth and behavior to environmental cues, it is necessary to integrate this spatiotemporal dimension into the study of bacteria and move towards a robust and precise reconstitution of their physiological environment.

These approaches have evolved over the past 15 years, notably thanks to the development of microfabrication and microfluidics for life sciences. By using for example photolithography or micropatterning techniques, scientists have been able to design and fabricate *in vitro* microhabitats with more or less complexity and apply them to study bacterial behavior in highly controlled growth conditions *(Rusconi et al., 2014)*. Together with fluorescence microscopy, microfluidics has greatly extended the frontiers of microbiology, by allowing the visualization in real time of bacterial physiology both at the single-cell and multiscale level, in response to a controlled chemical or mechanical cue.

# 2 Impact of the mechanical environment on bacterial physiology

Bacteria proliferate in environments characterized by complex mechanical cues they need to cope with to survive. Yet, the mechanisms at play and the potential impact of mechanics on bacterial behavior is a burning question, that is at the heart of the mechano-microbiology field over the past 10 years.
In this section, I describe the current knowledge about how bacterial physiology, both at the single-cell and multicellular level, is impacted by the mechanical environment.

## 2.1 Overview of the mechanical stresses encountered in the microbial world

In the wild, bacteria encounter a wide range of mechanical stimuli, whose nature and consequences slightly differ depending on whether bacteria are isolated or embedded within a multicellular aggregate, as in the case of biofilms.

### 2.1.1 Mechanical stresses experienced at the single-cell level

During their life, single bacteria often proliferate in liquid environments in which they bind to a surface, thereby experiencing extrinsic mechanical stresses such as flow-induced shear stress, surface-induced adhesive stress, and friction stress *(Persat et al., 2015b)* (Figure 13A). These forces are called extrinsic forces, as they arise from the external environment. This is the case of uropathogenic *E. coli* infecting the bladder through adhesion to uroepithelial bladder cells before invading them intracellularly. Within the bladder, bacteria are submitted to the hydrodynamic shear forces induced by the urine flow. Once bacteria adhere to the uroepithelial surface, they experience adhesive forces, that are perpendicular to the surface. In addition, when bacteria move on the surface to reach the neighboring cell, they experience friction forces, that are tangential to the surface.

### 2.1.2 Mechanical stresses experienced at the multicellular level

Most of the time, single bacteria ultimately proliferate in the form of multicellular aggregates, such as biofilms *(Hall-Stoodley et al., 2004)*. In this case, bacteria experience additional forces, that vary depending on their location within the aggregate *(Persat et al., 2015b)*. More precisely, bacteria located at the edge of the aggregate mainly experience extrinsic mechanical stresses, such as flow-induced shear stress, while bacteria located in the core of the aggregate are mainly subjected to intrinsic (or internal) mechanical stresses. Among the intrinsic stresses, one can cite those arising from both cell-cell interaction *(Pönisch et al., 2018)* and growth in a limited space (Figure 13B).

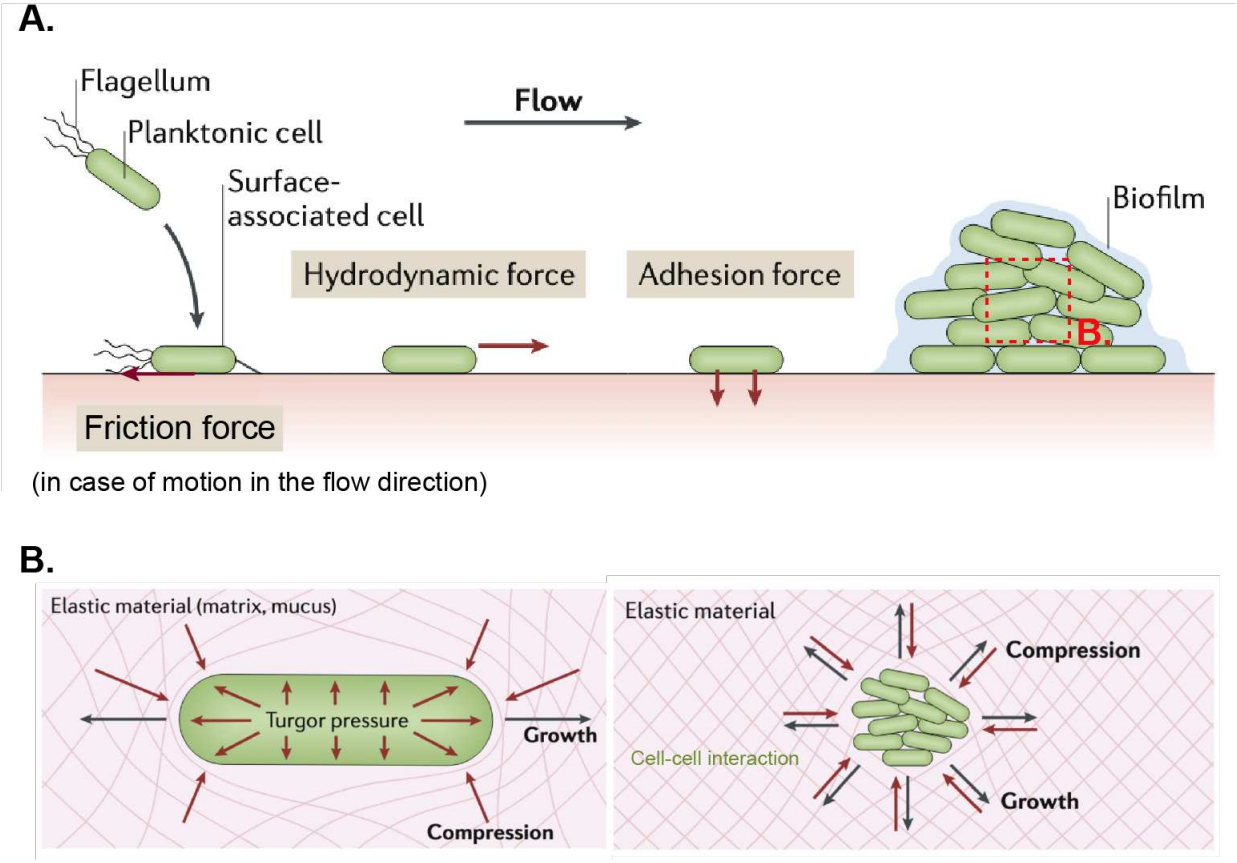


**Figure 13: Overview of the mechanical stresses encountered by bacteria at the single cell and multicellular level.** A. Extrinsic stresses experienced by single bacteria in flow environments: friction stress, flow-induced stress, adhesion stress. B. Intrinsic stresses experienced by biofilm-dwelling bacteria. In this context, bacterial growth in this space-limited environment ultimately deforms the surrounding matrix, which in turn exerts compressive stresses on the bacterial envelope. At the multicellular level, bacteria also experience cell-cell physical interaction. Adapted from (Dufrêne and Persat, 2020).

Indeed, in such a crowded environment, bacteria proliferate until they fill up the whole free space available, leading to bacterial confinement. Upon confinement, aggregate-embedded growing bacteria locally push on their neighbors to accommodate some space to increase in size and divide, thereby generating (and in turn experiencing) compressive mechanical stresses *(Dufrêne and Persat, 2020; Rivera-Yoshida et al., 2018)*.

In a more general view, many (if not all) bacteria face such mechanical forces during their journey within our body, underscoring the strong need to understand how mechanical cues impact bacterial physiology.

## 2.2 Inspiration from eukaryotic cells

The concept that bacteria could leverage mechanical cues to tune their behavior has arisen thanks to numerous studies conducted over the past 30 years on their eukaryotic counterparts, whose lessons serve as a source of inspiration for the emerging field of mechano-microbiology *(Iskratsch et al., 2014; Mishra et al., 2022)*.
In the following, I detail how eukaryotic cells perceive mechanical signals and how this in turn impacts cell physiology.

### 2.2.1 How do eukaryotic cells sense mechanical stresses?

The first lesson from mechanobiology studies is that eukaryotic cells, including yeasts and mammal cells, possess structural components that provide strength, allowing them to withstand mechanical stresses. For this, the cytoskeleton is the key mechanical structure of eukaryotic cells *(Fletcher and Mullins, 2010)*.
The second lesson is that eukaryotic cells experience and respond to a wide range of mechanical cues coming from the environment, such as fluid flows and contact with the extracellular matrix (substrate) or neighboring cells *(Zuela-Sopilniak and Lammerding, 2022)*. For instance, depending on the rigidity of a substrate, cells are characterized by different shapes and behaviors *(Discher et al., 2005)*.
The third lesson is that eukaryotic cells can sense and respond to a mechanical signal, by complex molecular pathways involving gene expression, generally called mechanotransduction (Figure 14). This mechanotransduction process requires the recruitment of several proteins to sense the mechanical signal (*e.g.* integrins in mammal cells, cell surface sensors such as Wsc1 containing a serine/threonine rich domain in yeasts), the conversion into a biochemical signal (*e.g.* linker proteins, Wsc1) and transmission to other subcellular compartments including the nucleus (e.g. LINC complex, MAPK cascade) ultimately tuning gene expression *(Humphrey et al., 2014)*.

### 2.2.2 Impact of mechanical stresses on eukaryotic cell physiology

Several studies have investigated how cell physiology is impacted by mechanical stresses, and more importantly by compressive stresses which are of particular interest in the scope of this work. Compressive forces have been reported to impact cell cycle progression, cytoplasmic crowding, and drug response, as illustrated in the following.

#### 2.2.2.1 Compressive stresses impact cell cycle progression

Compressive stresses have been reported to slow down cell cycle progression, by accumulating cells in the G1 phase, thus delaying DNA replication by the G1/S checkpoint. This result has been obtained in three different ways: by compressing spheroids through osmotic shocks *(Delarue et al., 2014)* or within an alginate capsule *(Meglio et al., 2022)*, or by confining the eukaryotic yeast *S.cerevisiae* using microfluidic chambers *(Delarue et al., 2016)*.

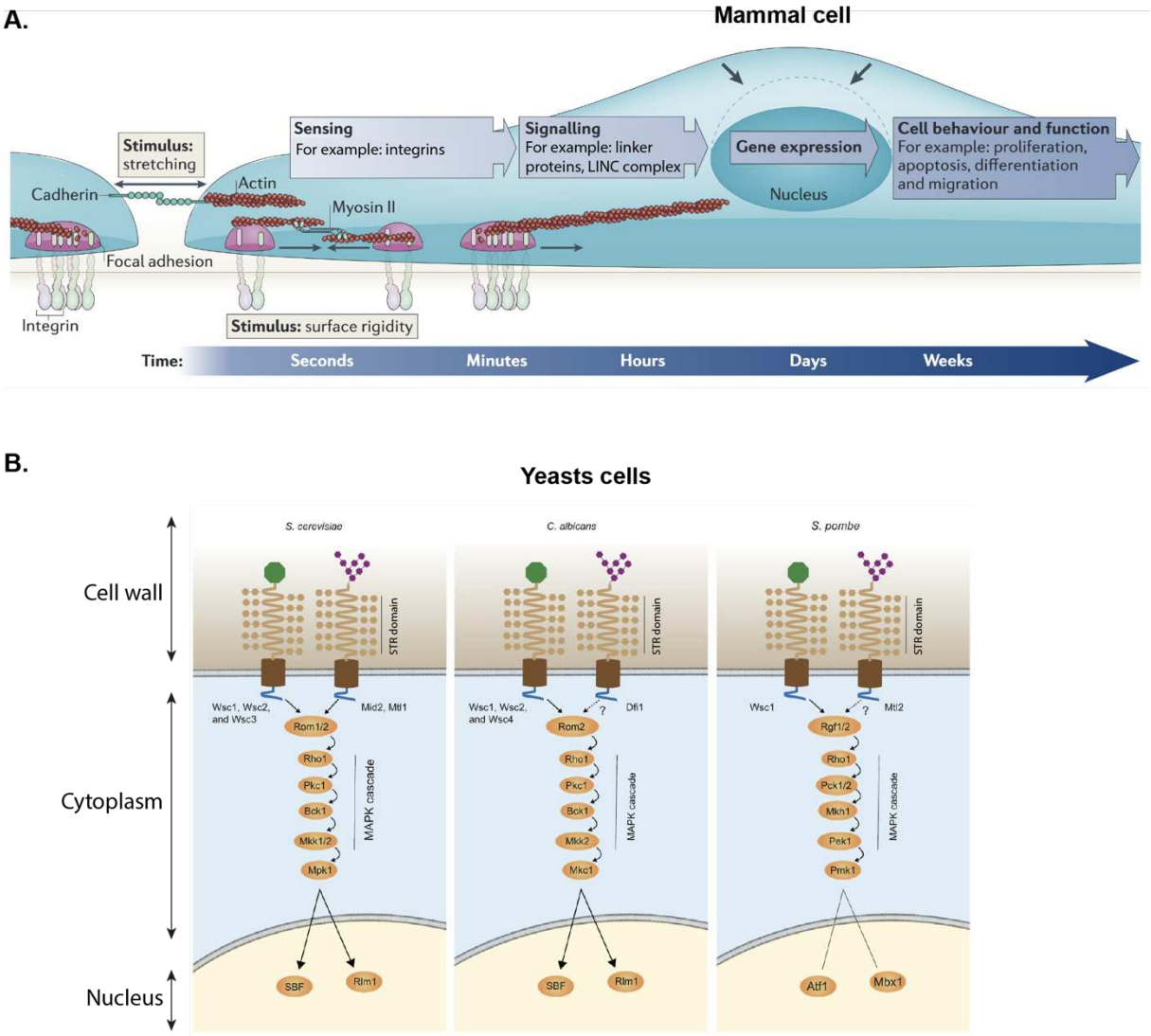


**Figure 14: Mechanotransduction in eukaryotic cells.** A. Mammal cells sense mechanical stimuli (mechanosensing – integrins) such as surface rigidity or stretching, convert this information into a biochemical signal (mechanotransmission – linker proteins, LINC complex) and adapt gene expression (mechanoresponse) in order to mount an adaptive cellular response. Adapted from (Iskratsch et al., 2014). B. Yeasts cells sense mechanical stimuli through the deformation of the cell wall surface sensor Wsc1 containing a serine/threonine-rich (STR) domain (mechanosensing). This in turn activates the MAP kinase cascade (mechanotransmission), leading to a mechanoresponse. Adapted from (Mishra et al., 2022).

#### 2.2.2.2 Compressive stresses increase cytoplasmic crowding

By monitoring the diffusive motion of nanoparticles expressed within *S.cerevisiae* cytoplasm, Alric and coworkers have shown that confinement-induced compressive stresses increase cytoplasmic crowding, ultimately limiting yeast growth upon confinement *(Alric et al., 2022)*.

#### 2.2.2.3 Compressive stresses increase drug resistance

Importantly, compressive stresses have also been reported to decrease drug efficacy. To this end, Rizutti and colleagues have characterized the impact of confinement-induced compressive stresses on spheroid size upon treatment with the chemotherapy drug gemcitabine *(Rizzuti et al., 2020)*. Interestingly, the authors have shown that in the presence of the drug, while uncompressed spheroids stop growing, confined spheroids continue to grow 2 days more, highlighting how cells become less susceptible to drugs upon compressive stresses.

In sum, mechanobiology studies provide a first insight into the central role of mechanical stresses on eukaryotic cell physiology. Likewise, the study of bacterial response to mechanical stresses promises to be rich in discoveries, by uncovering new roles of bacterial mechanics and their impact during the infection of eukaryotic hosts.

## 2.3 Bacterial response to mechanical stresses

More and more evidence over the past 10 years has shown that, as their eukaryotic counterparts, bacteria also sense and respond to mechanical signals *(Dufrêne and Persat, 2020; Gordon and Wang, 2019; Persat et al., 2015b; Persat, 2017)*. In this section, I describe the current knowledge regarding how bacteria probe and adapt to mechanical stresses, first at the single-cell level, and then at the multicellular one.

### 2.3.1 Bacterial response to mechanical stresses at the single-cell level

#### 2.3.1.1 How do single bacteria sense extrinsic mechanical stresses?

Single bacteria use a variety of strategies to probe the surrounding environment to sense mechanical signals (mechanosensing) and to convert them into a biochemical response (mechanotransmission), which further drives bacterial adaptation (mechanoresponse).

##### 2.3.1.1.1 Mechanosensing strategies: pili, flagella, and outer membrane proteins

To sense mechanical signals, bacteria rely on components anchored at the cell envelope, such as active organelles or envelope proteins *(Gordon and Wang, 2019; Persat, 2017)*.

*Active organelles: type-IV-pili and flagella*

Among the active organelles used by bacteria to sense mechanical signals, one can cite type-IV-pili (written T4P) which are long appendages that extend and retract from the bacterial body upon polymerization/depolymerization *(Craig et al., 2019)* (Figure 15A). As an example, this is the strategy used by the bacterium *Pseudomonas aeruginosa*, which has been shown to sense surface contact upon binding and further retraction of T4P *(Persat et al., 2015a)*. Instead of using their T4P as a mechanosensor, bacteria can also rely on their flagella (Figure 15B). In the case of *Shewanella oneidensis*, bacteria use both flagella and T4P to sense surface attachment, leading to changes in cell size and growth rate. Because of this surface-mediated mechanoresponse, mutants that either lack T4P or flagella are characterized by a growth rate similar to the one of bacteria in suspension, highlighting that both T4P and flagella are upstream mechanosensors responsible for major changes in cell function *(Lee et al., 2016)*.

*Outer membrane proteins*

Another way used by bacteria to probe mechanical signals is to sense the deformation of the envelope through mechanosensing proteins anchored at the outer membrane (Figure 15C). Indeed, surface contact has been reported to be enough to induce local measurable deformation of the outer membrane itself *(Chen et al., 2014)*. In the bacterium *E. coli*, the CpxAR TCS has been reported to be involved in mechanotransduction, in a NlpE-dependent manner. Indeed, upon attachment of the *E. coli* enteropathogenic strain (written EHEC) to endothelial cells, the activation of the CpxAR TCS has been shown to mediate the activation of a set of genes controlling virulence factors. Interestingly, such activation is loosed in the CpxA mutant, suggesting that CpxA plays a role in mechanotransmission. In addition, the activation of the Cpx TCS is dependent on the lipoprotein NlpE, suggesting its mechanosensory function *(Otto and Silhavy, 2002; Persat, 2017)*. Yet, experiments conducted at the single-cell level seem to contradict this finding, thereby questioning the role of the NlpE-Cpx system in mechanosensing *(Kimkes and Heinemann, 2018)*. Another attractive candidate involved in mechanosensing is the Rcs system. Indeed, two unpublished studies have recently reported the activation of the Rcs pathway in a RcsF-dependent manner upon 2D mechanical compression, which pinpoints a potential mechanosensory role for the RcsF lipoprotein *(Mason and Rojas, 2022; Zietek et al., 2022)*. However, the molecular mechanisms leading to RcsF activation upon mechanical stimulation are unknown.

#### 2.3.1.1.2 Mechanotransduction strategies: TCS and second messenger molecules

After sensing a mechanical signal, bacteria transmit it to the ground control center, *i.e.* the cytoplasm. To this end, bacteria rely on the TCS and/or second messenger molecules, which are cytoplasmic molecules that relay signals from the envelope to the cytoplasm. As an example, in the bacterium *Bacillus subtilis*, the inhibition of the flagellum rotation activates the DegS-DegU TCS, which in turn induces the transcription of various genes *(Dufrêne and Persat, 2020; Persat, 2017)*. Similarly, upon inhibition of flagellum rotation, the bacterium *Caulobacter crescentus* produces the second messenger molecule c-di-GMP, that further modulates gene expression *(Dufrêne and Persat, 2020; Hug et al., 2017)*.

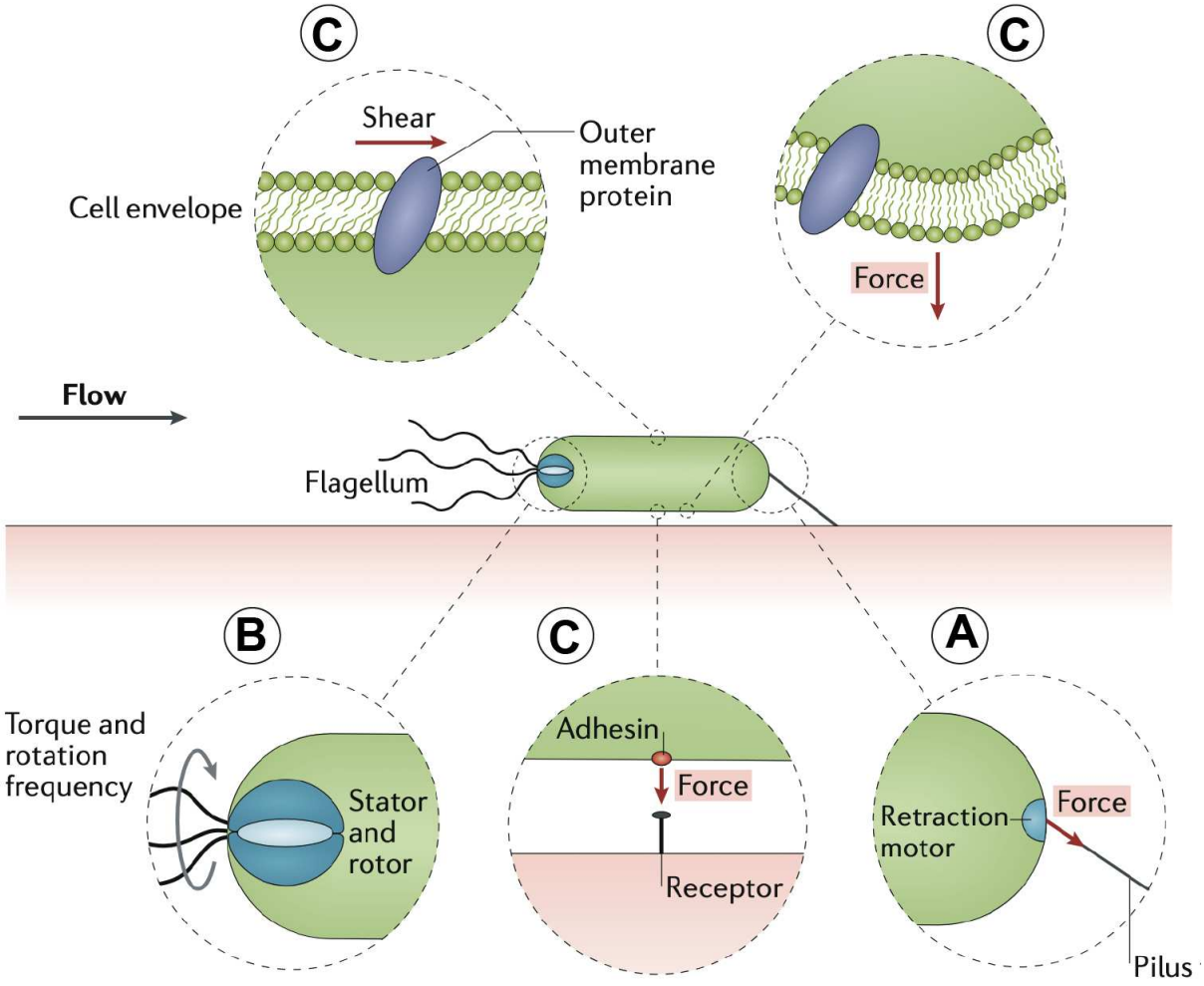


**Figure 15: Components of the bacterial architecture experiencing mechanical stresses, including appendages such as pili (A) and flagella (B), and outer membrane proteins (C).** Reproduced from (Dufrêne and Persat, 2020).

#### 2.3.1.2 How do single bacteria respond to extrinsic mechanical stresses?

Contrary to the longstanding belief, bacteria sense and respond to mechanical stresses. It is increasingly clear that mechanical stresses have a strong impact on various bacterial features, including adhesion, motility, morphology, virulence, and biofilm development.

*Impact on adhesion*

Several bacteria have been proposed to enhance their adhesion to a surface upon mechanical stress *(Dufrêne and Persat, 2020; Paiva et al., 2023; Talà et al., 2019; Thomas et al., 2002)*. As an example, the bacterium *E. coli* uses type-1-fimbriae to adhere to a surface. Interestingly, this adhesion is strengthened in the presence of shear stress, by the conformational change of the protein FimH at the tip of the fimbriae and the formation of catch bonds in the presence of tensile forces *(Yakovenko et al., 2008)*.

*Impact on motility*

Several bacteria have also been reported to adjust their motility in response to mechanical stresses *(Dufrêne and Persat, 2020)*. For instance, the bacterium *E. coli* is known to adapt the rotation of its flagellum within highly viscous liquid environments. This is favored by the recruitment of motor proteins in response to a decrease in rotation frequency *(Lele et al., 2013; Wadhwa et al., 2019)*. In another example, *Pseudomonas aeruginosa* has been shown to control the direction of twitching motility in response to the mechanical signals that arise from its motility machinery, in a process called mechanotaxis *(Kühn et al., 2021)*.

*Impact on morphology*

Few studies have shown that 2D compressive stress impacts bacterial morphology. By squeezing *E. coli* bacteria for a few hours within silicon-based 250nm-high channels, Männik and colleagues have shown that bacteria exhibit irregular aberrant shapes, far from their initial rod shape *(Männik et al., 2009)* (Figure 16A). Similarly, by squeezing bacteria under a membrane, Si and coworkers have reported that *E. coli* bacteria exhibit a pancake-like shape *(Si et al., 2015)* (Figure 16B), while the growth rate, division rate, protein synthesis, and DNA synthesis were not impacted by 2D compression *(Si et al., 2015)*. Interestingly, in both cases, it has been observed that these bacteria ultimately come back to their rod shape a few generations after the mechanical stress is released (Figure 16C). In addition, in a very recent unpublished study, Huang and Typas labs have also reported that, upon mechanical squeezing, *E. coli* exhibits a pancake-like shape characterized by the induction of the Rcs stress response *(Zietek et al., 2022)*.

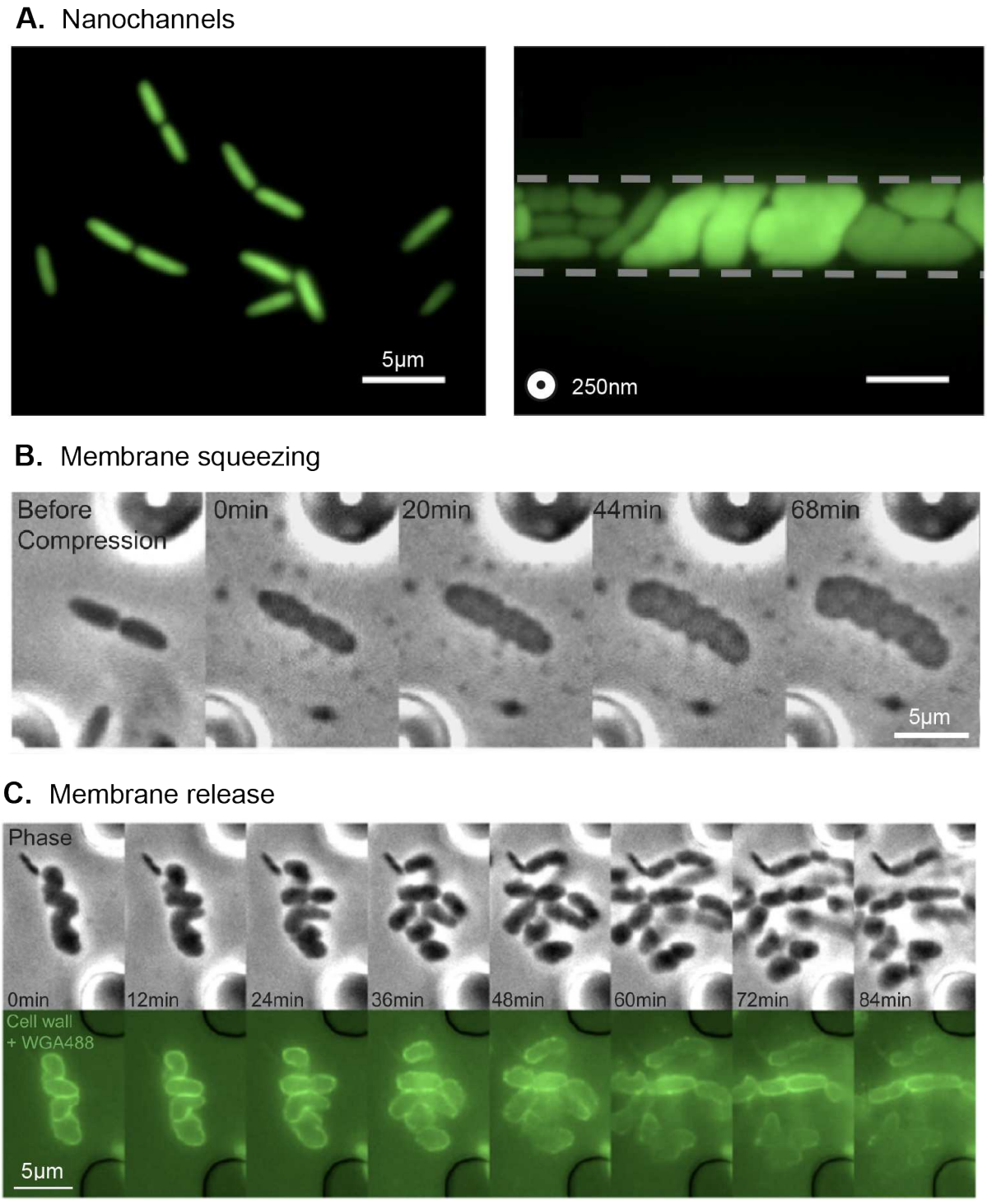


**Figure 16: Impact of mechanical forces on bacterial morphology.** A. *Escherichia coli* rod-shaped bacteria (left) exhibit aberrant pancake-like shapes when confined in 250nm-deep nanochannels (right). Reproduced from (Männik et al., 2012). B. Escherichia coli rod-shaped bacteria (left) exhibit a pancake-like shape upon 2D confinement induced by membrane squeezing at time 0. Reproduced from (Si et al., 2015). C. Upon pressure release, Escherichia coli tend to recover their rod shape in the membrane squeezing assay. Reproduced from (Si et al., 2015).

Interestingly, in a second preprint, the same authors have also shown that Rcs activation, yet in the absence of mechanical stress, is accompanied by a decrease in cell length by a factor of 1.5 only when growth rate decreases *(Miguel et al., 2022)*. Whether this holds to be true upon mechanical compression remains to be investigated.

*Impact on virulence*

The activation of envelope proteins involved in stress responses in the absence of mechanical stresses is often associated with the activation of virulence factors, including secretion systems and capsule synthesis *(Hews et al., 2019; Meng et al., 2021)*. Yet, only a few studies have investigated a similar link between activation of envelope proteins and virulence expression upon mechanical stimulation. In *E. coli*, it has been shown that the activation of the CpxAR envelope stress response upon surface contact by the lipoprotein NlpE participates in the regulation of the type III secretion system *(Shimizu et al., 2016)*. In addition, very recently, the activation of the Rcs pathway upon mechanical stimulation has been reported to induce capsule biosynthesis as a defense mechanism against bacteriophage infection *(Mason and Rojas, 2022)*. Similarly, in *Pseudomonas aeruginosa*, T4P-sensed surface contact has also been shown to induce virulence genes *(Persat et al., 2015a; Siryaporn et al., 2014)*.

*Impact on biofilm development*

Mechanical stresses have also been reported to initiate biofilm development. For instance, in the case of *Pseudomonas aeruginosa*, shear stress promotes extracellular matrix production, which is an indicator of the biofilm lifestyle *(Rodesney et al., 2017)*.

To conclude, mechanical forces shape bacterial behavior at the single-cell level on various aspects, including bacterial morphology and virulence. Yet, how do bacteria respond to mechanical stresses in the wild when they are part of a multicellular aggregate?

### 2.3.2 Bacterial response to mechanical stresses at the multicellular level

In the wild, single bacteria attached to a surface proliferate, ultimately leading to the formation of dense multicellular aggregates, such as biofilms. Within a biofilm, bacteria are embedded inside a self-secreted polymeric matrix that both ensures the cohesiveness of the aggregate and protects it from the external environment *(Flemming and Wingender, 2010; Hall-Stoodley et al., 2004)*. At the multicellular scale, additional intrinsic mechanical stresses self-generated by the biofilm-dwelling bacteria become dominant, including those mediated by cell-cell interaction (detailed in part 2.3.2.2) and bacterial growth upon confinement (detailed in part 2.3.2.3).

#### 2.3.2.1 Evidence of the existence of intrinsic forces

Biofilm morphology *per se* strongly suggests the existence of intrinsic mechanical stresses. Indeed, instead of being flat and smooth, biofilms usually adopt complex morphologies characterized by the presence of wrinkles visible to the naked eye, when growing on agar plates or at the air-liquid interface *(Rivera-Yoshida et al., 2018; Trejo et al., 2013)*. These wrinkles have been recently shown to result from mechanical instability. While the combination of bacterial growth and cell-cell cohesion leads to the build-up of gradual tension on the substrate, this in turn increases the friction between the growing adhesive microcolony and the surface, thereby resulting at some point in a buckling instability *(Cont et al., 2020; Yan et al., 2018)*.

#### 2.3.2.2 Physical cell-cell interactions

One of the main intrinsic mechanical stresses sensed by bacteria within a multicellular aggregate is mediated by cell-cell interactions, that arise from the tight proximity between a bacterium and its neighbors. These physical interactions are mediated by envelope structures such as adhesins, extracellular matrix, and/or molecular motors such as T4P, which have been broadly studied by quantitative approaches over the past decade *(Maier, 2021)*. First, T4P-mediated bacterial interactions have been shown to generate substantial forces. For instance, piliated bacteria use T4P to exert forces on their neighbors by pilus-pilus interaction followed by pilus retraction. Upon retraction, T4P generates forces reaching up to 100pN for individual fibers *(Maier et al., 2002)* and the nN range in the case of bundles *(Biais et al., 2008)*. Importantly, these physical interactions participate in the cohesiveness of the aggregate. For instance, by tuning cell-cell interactions, *Neisseria meningitidis* bacteria (written *N.meningitidis*) switch between gas-like, liquid-like to solid-like behavior *(Bonazzi et al., 2018)*. Finally, heterogeneous physical interactions can also shape bacterial aggregates. As an example, piliated bacteria with large rupture forces (*i.e.* the highest T4P density) are located in the center of the colony while non-piliated (*i.e.* the lowest T4P density) bacteria are sorted at the boundaries *(Oldewurtel et al., 2015)*.

Interestingly, this force heterogeneity is correlated with differential gene expression *(Pönisch et al., 2018)*.

#### 2.3.2.3 Growth upon confinement

Within multicellular aggregates, bacterial growth takes place in a crowded and limited space, where bacteria are eventually encased within a polymeric matrix. Upon a few cell cycles, bacteria occupy the whole space available and end up in tight contact with the surrounding microenvironment (bacteria, matrix). They are confined. During their growth under confinement, bacteria locally stretch and compress their surrounding environment, thus exerting growth-induced mechanical stress *(Dufrêne and Persat, 2020)*.

##### 2.3.2.3.1 Estimation of growth-induced mechanical stress

Several studies have estimated the global internal pressure within a biofilm by using different methods. The first measurement was done by Douarche and colleagues on *Bacillus subtilis* biofilms. To this end, bacteria were grown on a plate connected to a mobile plate further connected to a force sensor on one edge. After a few days of growth, the displacement of this mobile edge was recorded upon the cut of the biofilm, to release the internal pressure. By doing so, the authors estimated an internal growth-induced pressure of about 100Pa independently of the biofilm dimensions *(Douarche et al., 2015)*. A second measurement was done by Chu and colleagues on *E. coli*, *Pseudomonas aeruginosa* and *Staphylococcus cohnii*. To this end, bacteria were grown within enclosed microfluidic chambers and the deformation of the chamber roof was monitored. The authors found a maximal growth-induced pressure of about 10kPa for all the bacterial species after about 7 hours of growth *(Chu et al., 2018)*. A third measurement was done by Cont and colleagues on *Vibrio cholerae* and *Pseudomonas aeruginosa*. To this end, the authors monitored hydrogel substrate deformation upon biofilm growth after 12 hours and measured the corresponding stress by using traction force microscopy. By doing so, they have found that biofilm exerts large traction stresses on the substrate, up to 100kPa *(Cont et al., 2020)*, suggesting that biofilm internal mechanical stress should be in a similar order of magnitude.

In sum, bacterial growth within multicellular aggregate generates large mechanical stresses as reported for various bacterial species, despite current estimations do not agree on its order of magnitude.

##### 2.3.2.3.2 Bacterial response to growth-induced mechanical stress

Biofilm-dwelling bacteria are subjected to large mechanical stresses induced by their growth within a limited space, however, the impact of these stresses on bacterial

function and behavior remains poorly understood. Among the very few studies that have investigated this question, growth-induced mechanical stress has been reported to locally induce bacterial death, initiate biofilm development, and participate in the emergence of antibiotic tolerance.

*Bacterial death*

In one study, Asally and coworkers have characterized bacterial viability upon wrinkle formation in *Bacillus subtilis* biofilms. In particular, they have shown that wrinkle formation colocalizes with bacterial death and proposed that bacterial death allows to release of local compressive stress *(Asally et al., 2012)*, therefore mediating biofilm morphogenesis.

*Initiation of biofilm development*

One key step in the initiation of biofilm development is the production of extracellular matrix by the bacterial population *(Flemming and Wingender, 2010).* Interestingly, growth-induced mechanical stress has been reported to initiate the production of extracellular matrix in *Bacillus subtilis* biofilms *(Asally et al., 2012)*, and during *E. coli* growth within space-limited microfluidic chambers *(Chu et al., 2018)*.

*Impact on antibiotic tolerance*

Growth-induced mechanical stress has also been reported to participate in the emergence of antibiotic tolerance during *E. coli* growth within space-limited microfluidic chambers. Interestingly, Chu and coworkers have reported that stress-induced secretion of a negatively charged extracellular matrix provides a selective permeability barrier against antibiotics, by hindering the diffusion of positively charged antibiotics such as gentamycin. Indeed, while bacterial death in response to gentamycin was localized at the edges of the aggregate before mechanical stress build-up, no substantial death was detected after mechanical stresses increased. By contrast, in this work, biofilm formation does not impact the diffusion of positively charged molecules (such as fluoroquinolones). Whether bacteria become more tolerant to antibiotics in such a situation was not investigated. Consequently, the authors have proposed that stress-induced biofilm formation leads to biochemical changes at the boundary of the aggregate, which provide selective antibiotic tolerance to compressed bacteria *(Chu et al., 2018)*.

Another study has briefly investigated the response of *Vibrio cholerae* bacteria embedded within agarose gels with various rigidities in the presence of antibiotics. In this case, bacterial death in response to tetracyclin is localized at the edges of the aggregate upon high compression, while it occurs within the aggregate upon lower compression *(Zhang et al., 2021)*.

In addition, a recent study has also shown that, once embedded in rigid hydrogels, *E. coli* bacteria downregulate their tricarboxylic acid cycle, which results in a decrease in antibiotic susceptibility *(Han et al., 2023)*.

In sum, while all these studies propose that mechanical stresses increase antibiotic tolerance, the first study is the only one to investigate this question in a relevant environment, in which bacteria are progressively confined because of their proliferation in a limited space. Yet, in this study, whether the emergence of antibiotic tolerance is fully related to mechanical stress build-up and not to a potential density-induced decrease in aggregate permeability remains not fully characterized.

Altogether, these studies highlight the rising role of intrinsic mechanical stresses generated by growth in a limited space in biofilm morphogenesis and bacterial response at a global scale.

In the following, I detail state-of-the-art methods that served as a starting point for my Ph.D., and the technical challenges I had to overcome to study how these intrinsic mechanical constraints induced by bacterial growth in a limited space impact bacterial physiology at the single cell level.

# 3 How to experimentally confine bacteria?

So far, various microfabrication techniques have been developed to study bacterial growth in a limited space either induced by an external mechanical component (called external confinement) or self-induced by bacterial growth within microcompartments (called growth-induced confinement). These experimental techniques are detailed in the following and summarized in Table 2.

## 3.1 External confinement

One way to investigate bacterial response to confinement has been to study their behavior within artificially limited space. In practice, this can be obtained by using:

- **A Sykes-Moore chamber,** which consists of a deformable membrane on top of a single bacterium, thereby compressing the underneath bacteria *(Si et al., 2015; Zietek et al., 2022)*.
  Despite being easy to use, this experimental strategy does not allow to precisely control the pressure applied on the bacteria, thereby strongly limiting the reproducibility of the experiments. One advantage is that the chemical environment is easily controllable in such devices.

- **Tapered channels** to trap bacteria, in a process called "extrusion loading", similar to micropipette aspiration *(Genova et al., 2019; Mason and Rojas, 2022; Sun et al., 2014)*. Despite being easy to use, the pressure applied onto the bacteria in this experimental setup is not uniform, so that bacteria are confined on one side only. The medium supply is also easy to control.

- **Constrictions** with a smaller size than the bacterial one *(Männik et al., 2012, 2009)*. This method requires to fabricate nanochannels, which is not easy to settle in practice. By tuning the dimensions of the constrictions, one can easily control the level of confinement. Medium supply should be easily controlled here also.

Despite these experimental strategies provide a first understanding of the impact of confinement on bacterial behavior, none of them allow to study the impact of growth-induced mechanical stresses in physiological conditions. Indeed, in these systems, confinement is externally applied on single cells, which is far from the context of a biofilm, where biofilm-embedded bacteria self-generate mechanical stresses on the surrounding bacterial population.

## 3.2 Self-induced confinement

A more realistic way to confine bacteria is to design and fabricate microcompartments in which bacteria proliferate until they fill up the whole space available for their progeny, ultimately leading to self-induced confinement. Several microfabrication techniques allow to attain this goal *(Wessel et al., 2013)*, including:

- **Microfluidic confining chambers**: This experimental strategy allows to both control the chemical and the mechanical environment encountered by the bacteria. Two versions have been developed so far: one adapted to bacteria in which the medium supply is ensured by diffusion *(Chu et al., 2018)* adapted from *(Groisman et al., 2005)* and another one adapted to yeasts cells in which the medium is ensured by advection *(Delarue et al., 2016)*.

- **Water-in-oil droplets**: This experimental strategy allows to trap few bacteria within a droplet, and to study their proliferation within its enclosed space *(Boedicker et al., 2009; Geersens et al., 2022; Jakiela et al., 2013; Kaminski et al., 2016; Quellec et al., 2023)*. One advantage of this technique is its high throughput, as several experimental devices allow to monitor hundreds of droplets in one field of view. However, its main drawback relies on the medium supply that is not renewed through the oil interface. For this reason, this strategy is often used to study small populations of bacteria for short periods as nutrients rapidly become limiting to bacterial proliferation. Also, growth-induced pressure cannot be inferred easily for small droplets (radius ~ 10-30µm) due to the large Laplace pressure within it that opposes droplet deformation. Thus, while this experimental strategy is optimized to study bacterial proliferation in various chemical environments in a high throughput manner, it is not well adapted to study bacterial growth within both a controlled chemical and mechanical environment.

- **Microcavities**: This experimental technique allows to trap bacteria within microcompartments, similar to droplets, except that they are surrounded by a polymeric shell of various well-defined mechanical properties *(Ahn et al., 2021; Connell et al., 2013, 2010; Jeong et al., 2023)*. However, this technique has two major drawbacks, one of them being the size of the microcavities which is usually 100µm-wide (so very big compared to bacterial dimensions), and the second being the diffusive medium supply through the shell.

- **Hydrogels:** This experimental strategy is probably the easiest one. It consists of embedding bacteria within hydrogels of known stiffness *(Eun et al., 2011; Zhang et al., 2021)*. Yet, in these experimental setups, compressive stresses are applied on single bacteria, that need to push on their environment to grow even at the beginning of the experiment. Thus, this situation is quite different from the one bacteria most frequently face during infection. In addition, the

medium supply is ensured only by diffusion within the polymeric networks, so not easy to be stably replenished.

In sum, all these experimental strategies allow to study bacterial proliferation within a limited space, despite each of them being better suitable for a different specific application.

| *Method* | *Scale* | *Mechanical environment* | *Chemical environment* | *Adapted to bacteria?* |
|---|---|---|---|---|
| *External confinement* | | | | |
| *Sykes-moore chambers* | Single cell | Not controlled | Controlled | Yes |
| *Extrusion loading* | Single cell | Not controlled | Controlled | Yes |
| *Nanochannels* | Single cell | Fixed | Controlled | Yes |
| *Growth-induced confinement* | | | | |
| *Microfluidic confining chambers* | Population | Measurable in time | Controlled (advection) | No |
| | Population | Measurable in time | Controlled (diffusion) | Yes |
| *Droplets microfluidics* | Small population | Not measurable | No renewal | Yes |
| *Microcavities* | Population | Measurable | Diffusion | Yes |
| *Hydrogels* | Population | Measurable | Diffusion | Yes |

**Table 2 : Overview of the experimental strategies used to study bacterial growth in a limited space.** References are provided in the main text.

## 3.3 Why are current techniques not sufficient for us?

In my PhD, we wanted to investigate how self-induced (1) mechanical confinement (2) impacts bacterial (3) physiology (see Thesis Objectives).To this end, we needed an experimental setup that allows us to:

- (1) Trap bacteria within a limited space, so that they will become confined after a few cell division cycles
- (2) Control the mechanical environment in order to quantify confinement-induced physiological changes regarding the growth-induced pressure build-up
- (2) Control the chemical environment by advection in order to favor bacterial growth, while reducing as much as possible nutrient starvation effects
- (3) Ideally, confine various bacterial species to determine the specificity or the generality of our observations

Based on these requirements, it appears that the microfluidic chambers developed to confine yeast cells in the presence of a strong advective medium supply is the experimental strategy that fulfills the majority of our requirements *(Delarue et al., 2016)*. However, these chambers were not adapted to bacterial size. To this end, we have established a tight collaboration with M. Delarue (LAAS-CNRS, Toulouse, France), which was determinant for the success of this project.

# 4 How to measure growth-induced pressure?

To control the mechanical environment encountered by bacteria upon confinement, we aimed to measure in real-time the growth-induced pressure generated by bacterial proliferation in a limited space. To date, several methods have been used to measure pressure within (PDMS-based) microfluidic devices, by taking advantage of the chip material deformability in different ways, which are detailed in the following.

## 4.1 Bulk deformation-based pressure measurements

The easiest way to measure pressure within a microfluidic channel is to measure the deformation induced by this pressure using optical microscopy *(Alric et al., 2022; Delarue et al., 2016)*. As PDMS can be approximated as an elastic material for a wide range of mechanical stresses, one can easily infer the actual pressure applied on the walls by measuring the induced deformation and using the stress-strain equation: stress = E * strain, with E (in kPa) being the Young's modulus of the chip material, such as PDMS. The Young's modulus can be inferred by calibrating the chip deformability in response to a known pressure (applied with a pressure controller for instance) after each experiment, or through rheological measurements. As an order of magnitude, the Young's modulus has been estimated to 2MPa for classical PDMS (ratio base/curing agent = 10:1) *(Delarue et al., 2016)*.
Another related way to measure bulk deformation that has been used in hydrogels is to track the displacement of 100nm-wide fluorescent particles embedded inside the hydrogel. This allows to reconstruct the deformation field and to further infer the stress field, by using the known (non-linear) strain-stress curve of the hydrogel obtained using a rheometer *(Mark et al., 2020; Raghuraman et al., 2022)*.

## 4.2 Membrane deformation-based pressure measurements

A second method, related to the previous one but more sensitive, consists in measuring the deformation of a (PDMS) membrane, rather than the one of the bulk. In practice, such a membrane is often fabricated by adding an empty channel on top of the microcompartment where the pressure will be measured *(Chu et al., 2018; Delarue et al., 2016)*. Similarly, the pressure applied on the membrane can be estimated by measuring its deformation together with its Young's modulus. This method is especially useful in cases where the pressure to measure is too low to induce measurable bulk deformations. Very recently, an even more sensitive method has been developed to measure the low pressure applied by confined spheroids in the kPa range, by monitoring the deformation of a suspended membrane, that is anchored to the channel on one edge only *(BenMeriem et al., 2023)*.

## 4.3 Deformation-based local pressure measurements

While the previous methods allow to measure pressure at the global scale, other methods have also been developed so far to perform local pressure measurements, by using:

- **Deformable micropillars** positioned within the microcompartment where the pressure will be assessed. This method has been used to measure the pressure applied by eukaryotic cells (~ 1 kPa) *(Velve-Casquillas et al., 2010)*.
- **Deformable beads** of known size and rigidities, that can be introduced within the microcompartment where local pressures will be measured. This method has been used to measure the low pressure (~ 100 Pa) applied by macrophages during phagocytic engulfment *(Vorselen et al., 2020)*. Similarly, deformable droplets have been used to probe the mechanical environment during embryonic development *(Mongera et al., 2023)*.
- **The displacement of fluorescent particles** embedded within hydrogels or polyacrylamide gels as a way to infer stress using traction force microscopy. This method has been used to measure the pressure applied by a growing biofilm on a substrate (~ 100 kPa) *(Cont et al., 2020)* and also by fibroblasts on cancer cells (~ 100 Pa) *(Barbazan et al., 2021)*.

By taking advantage of microfluidics and the chip material deformability, these methods provide various combinatorial possibilities to measure both global growth-induced pressure over a wide range (from the MPa to the kPa) and local compressive stresses at specific locations within the chip in real-time.

# 5 How to follow bacterial growth?

The change in the picture scientists had of bacteria, from simple bags of enzymes devoid of internal organization to complex cells with an internal dynamic organization was founded on the great technological advances in fluorescence microscopy over the last 30 years. This was mostly due to the small size of bacterial cells that does not allow them to visualize their internal components using classical optical microscopy, contrary to their eukaryotic counterparts. By taking support on the tools developed in eukaryotic cell biology, scientists have developed fluorescent probes and fluorescent fusion proteins of interest to stain specific bacterial proteins and structures during cell growth and division, opening the door to a new understanding of this underappreciated, tiny but mighty world, called the new microbiology *(Cambré and Aertsen, 2020; Schneider and Basler, 2016; Yao and Carballido-López, 2014)*.
Today, the combination of these chemical and genetic tools with fluorescence spinning-disk high-resolution microscopy is still a method of choice to monitor bacterial growth over time and follow the expression, localization, and dynamics of specific proteins of interest in real-time. In particular, the improvement of spinning-disk microscopy with additional super-resolution modules provides a convenient way to increase the resolution, while limiting phototoxicity side-effects, often considered as a major drawback of classical super-resolution methods.

## 5.1 Fluorescent dyes

Belonging to the chemical labeling approach, these molecules are non-fluorescent compounds that become fluorescent once they bind to a target protein. Many fluorescent dyes are available on the market as they provide an easy way to follow bacterial components over time, without requiring any genetic manipulation. Among these dyes, one can find the classical DAPI and Hoechst, which are DNA intercalating agents. Similarly, SYTOX Green is also a fluorescent DNA intercalating agent yet mostly impermeable to live cells, used as a readout of membrane permeability and cell death *(Harhala et al., 2021; Roth et al., 1997)*. One major limitation of these fluorescent probes is that their amount, and hence the corresponding fluorescence, decreases over time in the absence of a continuous perfusion, upon cell growth and new protein synthesis. In addition, continuous perfusion of fluorescent dyes can sometimes increase the autofluorescence of the background and hence reduce the signal-to-noise ratio. Also, when used in PDMS chips, these dyes adsorb on the PDMS surface and force the use of high concentration, thereby becoming rapidly expensive. Thus, fluorescence dyes are rather optimized for single timepoint imaging rather than for long-term timelapse.

## 5.2 Fluorescent fusion proteins

Part of the genetic labelling approach, fluorescent fusion proteins are the method of choice to fluorescently stain a protein of interest. Yet, this method requires to manipulate the bacterial genome to encode the synthesis of any protein of interest linked to the desired fluorescence protein, ultimately leading to the generation of a genetically modified bacterial strain with specific fluorescence features. As well as being limitless, this method is very convenient as it provides a meaningful and relatively stable fluorescent signal, whose intensity depends on the level of expression of the targeted protein, and whose localization corresponds to the one of the targeted protein. Among the many possibilities of fusion proteins, one can cite the fusion protein HU-GFP, which results from the fusion between the nucleoid-associated protein HU and the GFP fluorophore *(Marceau et al., 2011; Pelletier et al., 2012)*. Another fusion protein used in this PhD research work is the TM-ZipA-mCherry fusion between the terminal domain of the ZipA inner membrane protein and the mCherry fluorophore *(Yao et al., 2012)*.

In sum, live high-resolution microscopy combined with fluorescence labeling strategies provide a powerful way to vivisect bacterial growth in real time at the subcellular scale.

# 6 How to extract quantitative data at the single-cell level under confinement?

Quantitative characterization of the bacterial world at the single cell level has been possible thanks to increasingly improving high-resolution microscopy techniques together with the development of image analysis softwares.

## 6.1 Available image analysis softwares at the beginning of my PhD

High throughput image analysis of bacterial cells at the single cell level has long been a particularly difficult task, once again due to their small size and various shapes. Indeed, for a long time, bacterial bodies on images were composed of few pixels only, making any detection of their contour unprecise and subcellular detection a dream. However, the development of high-resolution microscopy has overcome this problem, thereby opening the door to the new field of quantitative microbiology.

Quantitative image analysis at the single cell level first requires detecting or isolating each bacterial body by drawing its contour, in a process called segmentation. At the beginning of my Ph.D., cell segmentation was a general issue in the field, and was mostly performed on phase-contrast images using various softwares, each of them being specific to a given bacterial shape *(Raaphorst et al., 2019)*.

## 6.2 Why are these image analysis softwares not sufficient for us?

In my Ph.D., in order to quantify how self-induced confinement (1) impacts bacterial physiology (2) (see Thesis Objectives), we needed an image analysis pipeline that allows to:

- (1) Segment and track individual bacteria over time within confined, highly dense aggregates. Indeed, as bacteria fill up a limited space and reach confinement, they are by definition in tight contact with their neighbors. While phase-contrast imaging is well appropriate to image isolated objects characterized by a refractive index different from the background, it does not allow to identify single tightly packed objects, with a similar refractive index, within an aggregate.
- (2) Work with various bacterial species with various shapes and envelopes ideally. Indeed, by confining various bacterial species, we would be able to determine which bacterial response is general to the bacterial kingdom, which one is specific to a given bacterial species and which fitness advantage it provides in the infectious context.

Based on these requirements, it appears that none of the existing image analysis softwares at that time allowed to quantify bacterial growth upon confinement. To overcome this issue, we have worked in collaboration with J.-Y. Tinevez (Image Analysis Hub, Institut Pasteur, Paris, France) to develop an image analysis pipeline that suits our requirements *(Ershov et al., 2022)*.

In the meantime, a plethora of segmentation softwares mostly based on artificial intelligence have been published over the past 3 years, underscoring the tremendous need for more general segmentation tools for the microbiological community *(Cutler et al., 2022; Hartmann et al., 2021; Jelli et al., 2023; Ollion et al., 2019; Pachitariu and Stringer, 2022; Spahn et al., 2018; Stringer et al., 2020; Zhang et al., 2020)*.

# Thesis objectives

Within multicellular aggregates, bacterial proliferation occurs in a limited space. In such environment, bacterial growth has been shown to generate internal mechanical stresses, despite previous studies do not agree on their order of magnitude. While few studies have characterized bacterial behavior at the global scale under internal mechanical stresses, others have focused on bacterial physiology at the single-cell level under externally applied compressive stresses. However, how internal mechanical constraints impact bacterial physiology at the single-cell level within multicellular aggregates remains largely unexplored, despite its ubiquity and potential relevance in the infectious context.

In this context, the main objective of my PhD was to investigate how bacterial growth in a limited space impacts bacterial physiology, and thereafter disease progression. For this, we hypothesized that bacterial proliferation in a limited space ultimately leads to a lack of space, which is a hallmark of confinement. Upon confinement, bacterial proliferation could generate large compressive forces onto the microenvironment. On the bacterial side, these self-generated mechanical constraints could induce bacterial physiological changes, potentially leading to the emergence of antibiotic tolerance. On the host side, these mechanical constraints could damage host cellular structures and barriers, potentially favoring bacterial dissemination (**Figure 17**).

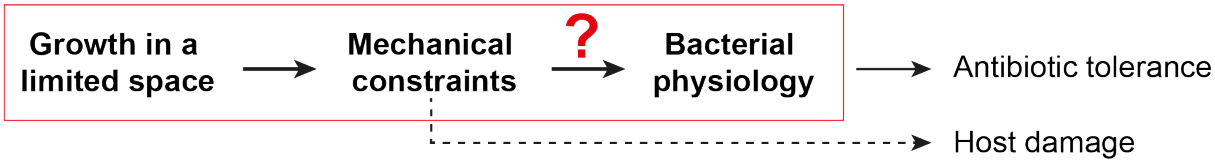


**Figure 17: Hypotheses of this PhD work**

In sum, this PhD work investigated the following question:

### How growth-induced mechanical confinement impacts bacterial physiology?

To address this question, we have used the bacterium *Escherichia coli* as a referring model organism and unraveled the following objectives:

- Develop an experimental set-up to confine various bacterial species
- Develop an image analysis pipeline to quantify single-cell properties in time and space
- Measure growth-induced pressure
- Correlate pressure build-up with bacterial physiological changes
- Dissect the mechanism(s) leading to bacterial adaptation upon confinement

# Results

# 1 The Bacterial Confiner: Development of a microfluidic set-up with nanometric features to study bacterial confinement

To investigate the impact of confinement on bacterial physiology, the first aim of my PhD was to develop a simplified system that mimics the spatial confinement encountered by bacteria during infection, independently of the host. To this aim, we have worked in tight collaboration with Morgan Delarue (LAAS-CNRS, Toulouse, France) to develop a microfluidic device that allows to confine bacteria in a controlled chemical and mechanical environment *(Holt et al., 2018)*, taking support on the chip he developed to confine yeast cells *(Delarue et al., 2016)*. In the original device, yeast proliferates within space-limited growth chambers. These chambers are connected to 1µm-wide microchannels, that ensure a broad control of medium renewal while hindering yeast passage. The continuous flow of nutrients favors yeast proliferation for hours even after the chamber reaches confluency, leading to the formation of a highly packed, confined aggregate. The key point in this device lies in the dimensions of the microchannels, which are small enough to prevent yeast passage. Therefore, to adapt this microfluidic device to bacterial size, typically 1µm wide (*i.e.* 5 times smaller than yeast), we need to produce nanometric/submicrometric channels (~400-300nm).

Designing fluidic devices with nanometric features represents a non-trivial challenge to undertake. Indeed, as its name suggests, microfluidics is defined by the science and the technologies that manipulate small volumes using channels whose critical dimension is at least in the order of the micrometer *(Whitesides, 2006)*. At the micrometer scale, microfluidic channels are easily produced using classical soft-lithography techniques, by molding an elastomer against a silicon master with positive reliefs of the desired design. The patterned elastomer is then bonded by surface oxidation to a glass coverslip to ensure the closure of the chip *(Duffy et al., 1998)*. The commonly used elastomer is the poly(dimethylsiloxane) (written PDMS), whose widespread utility lies, beyond its ease-of-use and low cost, to its material properties, including transparency, deformability, gas permeability and biocompatibility *(Banik et al., 2023)*. However, to our knowledge, only one study has used PDMS so far to produce nanometric channels with a size in our range of interest (300 to 800nm - *(Moolman et al., 2013)*. This rare use of PDMS in nanofluidics is linked to the dimensional instability of this relatively soft material after bonding, that leads to nanochannels collapse at this length scale *(Xu, 2018)*.

## 1.1 Development of a silicon-based microfluidic set-up to confine bacteria

We have fabricated the first version of the nano/microfluidic chip in silicon, a very stiff material that allows to build nanochannels with a high aspect ratio while avoiding collapse, unlike PDMS. In this part, I describe all the steps that led from the conceptualization to the implementation of the experimental set-up, in addition to its biological application.

### 1.1.1 Chip design

We came up with two chip designs to study the impact of confinement on bacteria. The first design, called chemostat, enables to study bacterial aggregation without confinement while controlling chemical exchanges. It consists in a central channel for bacterial loading, connected to an array of nanochannels that allows nutrient diffusion while hindering bacterial passage (Figure 18A, left). The second design, called mechano-chemostat, enables bacterial confinement similarly to Morgan's work *(Delarue et al., 2016; Holt et al., 2018)*. This device consists of a growth chamber of a fixed volume for bacterial proliferation in a limited space. This chamber is connected to an array of nanochannels allowing nutrient diffusion, and to a geometric valve through a constriction favoring confinement (Figure 18A, right).

### 1.1.2 Chip fabrication

The fabrication of the nanochips was done in the LAAS-CNRS clean room, during 2 weeks missions. This work was initiated by Thierry Leichle (LAAS-CNRS), who wrote the first version of the protocol taking support on microelectromechanical systems. The chips were directly fabricated on a silicon wafer in a 2-layer process, using standard photolithography to define the nano/microstructures and etching to excavate the channels. The dimensions of the nano/microchannels were characterized using a mechanical profilometer together with scanning electron microscopy (height: 300nm, width: 5µm). Millimeter-sized holes were drilled on the silicon substrate to enable liquid injection. The channels were then encapsulated by anodic bonding of the patterned silicon wafer to a thick transparent borofloat 33 glass wafer. Finally, the silicon wafer was cut to obtain individual chips (Figure 18B).

### 1.1.3 Chip loading

The loading of silicon-based microfluidic chips is not as easy as PDMS-based ones. Since silicon is a hard, non-deformable material, pressure pump connections cannot be introduced in the chip as simply as in classical PDMS chips. For this reason, the design of a custom-made 3D printed holder was required to connect the chip to the pressure pumps and observe bacteria within channels by reflection microscopy, up to 40X objective. Also, since silicon is a hydrophobic material, the silicon-based chips were hydrophilically activated using plasma before loading to minimize air bubble

formation, the latter being detrimental to the experiment as they cannot be removed from gas non-permeable silicon-based channels. To validate the experimental setup, we monitored dynamic medium perfusion in real-time (Figure 18C, top) and observed that medium renewal through the central channel occurs in less than 1 second (Figure 18C, bottom). Based on these results, we confirmed the feasibility of the experimental setup, opening the way to the study of bacterial proliferation in a controlled environment.

### 1.1.4 Application to bacterial confinement

This system has been validated and optimized using two bacterial species of similar size and various morphologies, the rod-shaped *Escherichia coli* (written *E. coli*) and the diplococcus *Neisseria meningitidis* (written *N. meningitidis)*.

#### *1.1.4.1 Escherichia coli*

We have first tested the silicon-based nanochips with a non-pathogenic strain of *E. coli* to facilitate the optimization process. Using this bacterium, we were able to observe its proliferation within the nanochip central channel without passing through the array of perpendicular nanochannels used for culture medium renewal (Figure 18D). This experimentally validates the design of the nanochip, and especially the appropriate size of the feeding nanochannels that allow nutrient diffusion while hindering bacterial passage. However, we noticed that bacteria tended to be flushed out from the field of view during the course of the experiment, probably because of residual flows coming from the bacteria-injection inlet port. For this reason, no visible aggregate was formed after 3 hours of proliferation despite bacterial proliferation (Figure 18D). We thus optimized the fluidic paths to minimize the parallel flow within the central channel, i.e. the flow that pushed bacteria forward, and to increase the perpendicular flow, hence immobilizing bacteria against the central channel wall. This allowed a better renewal of the culture medium within the central channel, and most importantly to look at bacterial proliferation over time without observing a major drift in bacterial position. Therefore, after optimizing both the loading strategy and the flow within the chips, silicon-based nanochips are a suitable tool to study the proliferation of bacteria in a well-perfused environment.

### *1.1.4.2 Neisseria meningitidis*

We then used this device to monitor the proliferation of the pathogenic bacterium *N.meningitidis*, which requires more stringent physiological conditions to grow in a classical medium (5% $CO_2$, 37°C). At first glance, the use of silicon chips - a gas non-permeable material - seems incompatible with the study of such bacterial species whose proliferation requires controlled $CO_2$ levels. Therefore, finding alternative culture conditions to support bacterial growth in the absence of $CO_2$ was a prerequisite to further experiments. To this end, we compared bacterial growth in various culture media over time by monitoring the $OD_{600}$ of the liquid broth culture using an automatic plate reader, while controlling the percentage of $CO_2$ injected in the plate atmosphere. Strikingly, we noticed that *N.meningitidis* growth at 37°C in GCB medium in the absence of $CO_2$ was as good as in the presence of $CO_2$ in the usual culture medium, RPMI+10% Fetal Bovine Serum. Interestingly, it has been reported for a closely related bacterium, *N.gonorrhoeae*, that bacteria metabolically self-produce the $CO_2$ levels required to support proliferation when this is present in a sufficient amount in a bacterial suspension *(Spence et al., 2008)*. Based on these results, we loaded first a chemostat with an exponentially growing *N.meningitidis* suspension in pre-heated GCB medium supplemented with 0.1 mg/ml fluorescent Dextran for proper visualization of the channels. After bacterial loading, we rapidly established the optimal flow allowing bacterial immobilization onto the wall of the central channel, and monitored bacterial proliferation by live imaging. In these conditions, *N.meningitidis* proliferates for more than 3 hours (Figure 18E). To induce confinement, we loaded bacteria into a mechano-chemostat in a similar manner, and monitored their proliferation upon spatial confinement. We noticed that bacteria proliferate during a few hours until filling up the chamber, but as soon as the chamber is full, they rapidly start to die as indicated by the accumulation of Dextran over bacterial fluorescence (Figure 18F). Whether bacterial death is a direct consequence of the emergence of spatial confinement, or whether this is related to a lack of local $CO_2$ concentration in the bacterial aggregate was unclear to us. At this point, the non-permeability of silicon to gas was a major issue that made us unsure about the relevance of our observations. To eliminate a potential side effect of $CO_2$ depletion, we finally decided to overcome the challenge of producing our nano/microfluidic chips in PDMS.

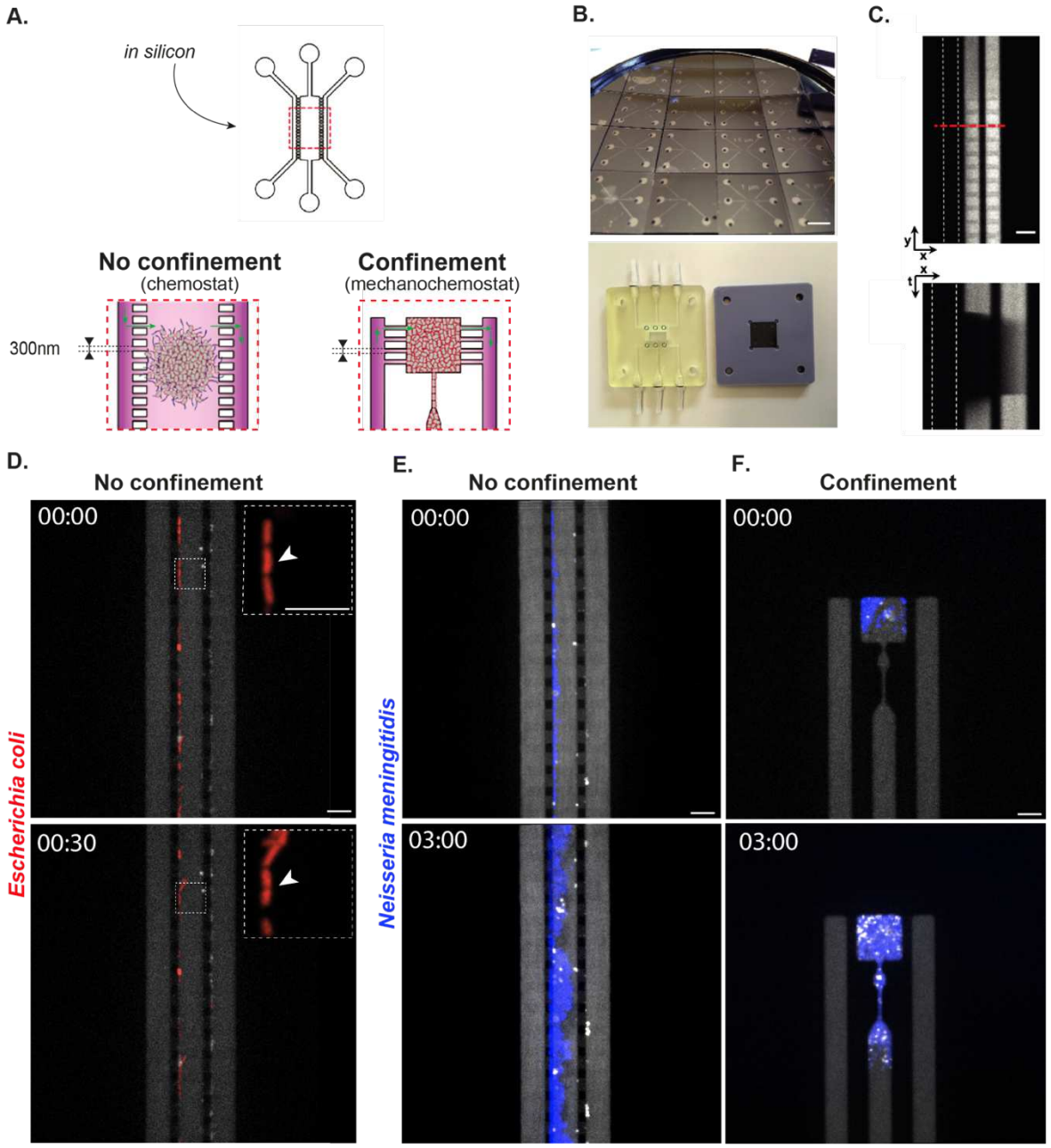


**Figure 18: A silicon-based microfluidic chip with nanometric features to study bacterial proliferation in spatially-constrained environments**. A) Two chip designs were used to study the impact of confinement on bacteria. The chemostat design (left) allows bacterial proliferation in presence of a continuous medium renewal. The mechanochemostat design (right) additionally limits space available for bacterial proliferation. Flow lines are depicted in green. B) Chips were produced in silicon (top) and inserted into a 3D printed holder (bottom) for chip loading and imaging. C) Characterization of medium renewal in real time in a chemostat. Image of the chip at time 0 (left). Kymograph along the red dashed line (right). Intensity profile along the central channel (bottom). D) *Escherichia coli* bacteria (red) proliferate within the central channel of a chemostat, in absence of confinement. The culture medium has been supplemented with fluorescent Dextran (gray) for channel visualization. Zoom on one bacterium that is dividing. E) *Neisseria meningitidis* bacteria proliferate within both a chemostat, F) and a mechanochemostat. Bacteria rapidly fill up the chamber and become confined. *Time: hh :mm. Scale bars : 10µm.*

## 1.2 The bacterial confiner: development of a versatile PDMS-based microfluidic set-up with nanometric features to confine bacteria in a controlled mechanical environment

In this part, I describe the successful development of the bacterial confiner, *i.e.* the PDMS version of our microfluidic chip with nanometric features, its application to various bacterial species, and its optimization to precisely measure mechanical constraints that arise from bacterial proliferation in a limited space.

### 1.2.1 Chip design

We have taken advantage of our first experience with silicon chips to adjust the chip design. In previous experiments, we have noticed that, even in the chemostat design, bacteria ultimately become confined after a longer time. In addition, due to variations in nanochannel arrangement, the chemical environment is not comparable in the two designs for the same applied flows, thus making any comparison difficult. Therefore, we first choose to rely only on the mechano-chemostat design to characterize both bacterial proliferation with and without confinement. Indeed, these 2 conditions occur sequentially within the chambers in the same experiment: at early stages, bacterial proliferation takes place before the growth chamber reaches confluency, while later on the chamber is filled up and confinement is achieved. To increase the experimental throughput, 32 mechano-chemostats (Figure 19A) were organized along one common culture medium channel (Figure 19B) in arborescence (Figure 19C), similar to what has been done to confine yeast *(Alric, 2021)*. The chip design was split into two layers of two different heights, one for the nanostructures (height: 400nm) and the other for the microstructures (height: 2.5µm). These two designs were then printed on two photomasks characterized by transparent and opaque regions allowing light transmission or not.

### 1.2.2 Master fabrication

In the scope of this project, the development of the master fabrication process has been done at the LAAS-CNRS by Baptiste Alric, a former Ph.D. student in Morgan's team, and Laurent Mazenq, a specialist engineer in lithography. Again, I went to the LAAS-CNRS during several missions to optimize this process and fabricate new masters, while working in pairs with Baptiste. To fabricate the 2-layer master, we first built the critical nanostructures, before printing over the micrometer ones. The first layer was fabricated by patterning a light-sensitive resist, using high-resolution photolithography. By using a stepper device (Canon), we were able to obtain the nanostructures in polymerized resist, by patterning a photoresist using light transmission through the projection of a photomask. Compared to classical photolithography, stepper-based high-resolution photolithography uses additional lenses to focus the UV light on the resist, thereby patterning smaller features. As an order of magnitude, the resolution limit (i.e. the minimum distance between two

points at which they are seen separated by the optical system) in classical photolithography is dictated by diffraction (~1µm), while it is only dependent on the UV wavelength (~200nm) in stepper-based photolithography. The patterned silicon wafer was then etched over a depth close to nanochannels width to get positive nanochannels characterized by an aspect ratio equal to 1. To this end, we precisely measured the width and the height of the nanochannels, using both scanning electron microscopy and a mechanical profilometer (width: 400nm, height: 400nm). The second layer was fabricated by following similar steps, except that we used the photoresist to directly produce the microstructures on the nanotextured silicon substrate (no etching).

### 1.2.3 Chip fabrication

As in classical microfluidics, the silicon master was then used to mold PDMS bulks, using soft-lithography techniques. Chip production and bonding was done at the BMcf microfluidic platform at Institut Pasteur, as an autonomous user. One key advantage of this process is that I was fully independent on chip production, by contrast with single-use silicon chips (part 1.1) whose production requires to be at the LAAS-CNRS. This was an important step in the chip development, that has greatly facilitated the optimization process.

### 1.2.4 Chip loading

In addition to the advantages in terms of chip fabrication, PDMS chips were easily loaded under the spinning-disk microscope in the host lab with classical microfluidics setups, in contrast with silicon chips (part 1.1). Indeed, due to PDMS deformability, pressure pump connections were easily inserted into the chip, allowing liquid injection in the channels without leakage. Due to PDMS optical transparency, nano/microstructures were easily visualized using white light only, without adding any fluorescent dye in the medium in contrast with part 1.1. Also, due to PDMS gas permeability, air bubbles were easily removed from PDMS chips. Therefore, PDMS material properties have clearly facilitated chip usage compared to silicon, thus improving the chance of success of each experiment.

### 1.2.5 Application to bacterial confinement

The bacterial confiner has been validated on multiple relevant bacterial species, that proliferate in the form of dense spatially-constrained aggregates in the infectious context. In the following, I detail the use of this device with two Gram-negative bacteria: *E. coli*, a bacterium forming dense intracellular aggregates during urinary tract infections *(Wright et al., 2007);* and *N.meningitidis*, a bacterium that forms dense aggregates occluding the lumen of infected vessels *(Bonazzi et al., 2018; Melican and Dumenil, 2012)*. Of note, this setup has also been used to confine the Gram-positive bacterium *Staphylococcus aureus* (written *S.aureus*) (see Discussion - 2.2.1). In all the

experiments, bacteria were imaged in the focal plane of the nanochannels, at the bottom of the chambers to optimize image quality.

#### 1.2.5.1 *Escherichia coli*

First, I loaded both a non-pathogenic and a uropathogenic strain of *E. coli* within the microfluidic chambers and monitored their proliferation using live imaging while continuously renewing the culture medium. I observed that these rod-shaped Gram-negative bacteria proliferate well within the growth chambers without passing through the 400nm-wide nanochannels (Figure 19B - left). In a few cell cycles, bacteria reach confluency and ultimately become confined (Figure 19B - right). Interestingly, bacteria continue to proliferate upon confinement despite the lack of space, suggesting that the bacterial confiner is a suitable tool to study the impact of confinement on *E. coli* physiology. Similar experiments were conducted to confine the Gram-negative *S.aureus* (see Discussion – 2.2.1).

#### 1.2.5.2 *Neisseria meningitidis*

Similarly, I loaded the sepsis-causing *N.meningitidis* bacterium and monitored its proliferation within the microfluidic chambers. I observed that this Gram-negative diplococcus ultimately passes through the 400nm-wide nanochannels, reaches the culture medium channel, proliferates there, and consumes all the nutrients, hence preventing bacterial proliferation within the space-limited growth chambers. Therefore, we have adjusted the chip fabrication process to reduce nanochannels width around 300nm, while conserving a channel aspect ratio close to 1. This was sufficient to prevent bacterial passage through the nanochannels. In these conditions, bacteria proliferate within the growth chambers in the presence of a continuous medium renewal. Surprisingly, bacteria were rapidly flushed out of the chambers, and never reached confinement, differently from the case of *Ec* (Figure 19C - left). This bacterial escape could be favored by a combination of effects, including:

- **Bacterial size and shape,** that is quasi-isotropic compared to rod bacteria and hence not easily trapped in geometrical constrictions.
- **Bacterial surface properties**, including the bacterial capsule that is responsible maybe the PDMS substrate, and bacterial pili that make the aggregates weakly cohesive due to intermittent interactions *(Bonazzi et al., 2018).* Because of this, these bacteria could be more sensitive to flow lines induced by the medium supply.

Interestingly, by using a PilT mutant strain with defects in pili-mediated intermittent interactions, I observed that bacteria were able to fill the chambers in contrast with the wild-type strain (Figure 19C - middle), suggesting that this bacterial escape might mostly depend on bacterial properties.

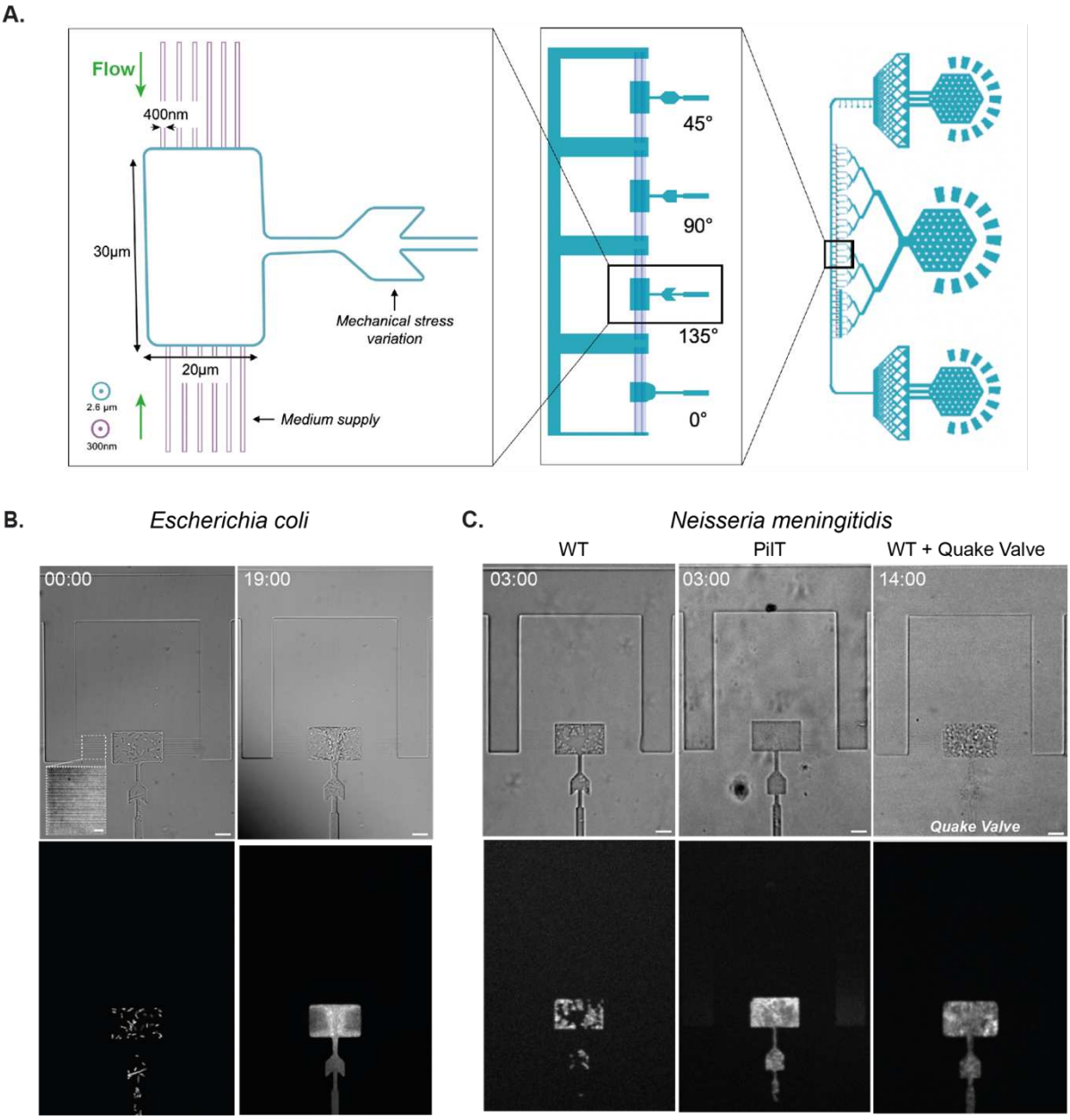


**Figure 19 : The bacterial confiner, a PDMS-based microfluidic chip with nanometric features to study bacterial proliferation in spatially-constrained environments.** A) Design of an individual mechano-chemostat (left). 32 mechano-chemostats are organized in parallel along one common culture medium channel (middle). Global view of the chip design (right). B. *Escherichia coli* fluorescently labeled bacteria were loaded in the growth chamber (time 0, left). These bacteria proliferate in the chamber until filling it up 19 hours later (right). C. *Neisseria meningitidis* fluorescently labeled wild-type bacteria never fill the growth chamber (left), in contrast to the PilT strain (middle). Thanks to the addition of a quake valve at the outlet of the chamber (outside the field of view), WT *Neisseria meningitidis* bacteria (right) fill the chamber even after 14 hours. *Time hh:mm. Scale bars: 10µm.*

As a comment, this "negative" result is potentially meaningful and points out that these bacterial aggregates have an intrinsic ability to avoid specific environments, probably related to their viscous liquid behavior *(Bonazzi et al., 2018).*

Nevertheless, *N.meningitidis* bacteria still form dense aggregates during vascular infections, concurrently with blood flow drop and coagulation *(Corre et al., 2022).* Therefore, we decided to improve the microfluidic system to force bacterial confinement, by adding a quake valve at the outlet of the chamber. This pneumatic valve allows to deform the PDMS layer at the top of the outlet channel upon pressure activation *(Unger et al., 2000),* which artificially closes the chambers, thereby preventing bacterial escape out of the field of view of the experiment. The idea was to partially close the valve to hinder bacterial escape while allowing liquid flows to favor medium renewal in the chambers. Closing this active valve as such, in a reproducible manner, has required the calibration of its deformability for each batch of chips. To do so, I added fluorescent Dextran in the culture medium, and used fluorescence exclusion to relate the actual height of the outlet channel to the pressure applied in the quake valve. By using a pressure around 4000mbar in the quake valve, I was able to sufficiently close the outlet channel to prevent bacterial escape while allowing medium renewal to sustain bacterial growth. In these conditions, after being flushed out of the chambers and trapped by the valve, *N.meningitidis* bacteria were able to proliferate in the channels, ultimately filling up the growth chambers and becoming confined (Figure 19C - right).

Together, these results show that the bacterial confiner allows to reproduce highly dense aggregates as those encountered during infection for a wide range of bacterial species with various envelopes and morphologies.

## 1.3 Optimization of the bacterial confiner to characterize the mechanical environment encountered by bacteria upon confinement

To characterize the mechanical environment encountered by bacteria upon confinement, we took advantage of the PDMS deformability to infer the global force at play during bacterial confinement. To this end, we optimized the following procedure:

a. **Tracking of the deformation of the chambers in real-time:** By tuning the PDMS stiffness, I was able to monitor the deformation of the growth chambers upon bacterial proliferation under confinement. The deformations are measured at the top of the chambers to maximize the extent of the deformation and hence the precision of the force measurement. Indeed, the deformation is lower at the bottom than at the top of the chamber due to chip bonding to the glass coverslip.
   To track the deformation of the chamber by using a semi-automatic analysis, I searched for a way to fluorescently stain the chamber edges. Since PDMS is a hydrophobic material, I tried to:

   - **Mix a fluorescent hydrophobic dye (Nile-Red) in the PDMS base**: This approach was not optimal as the fluorescence signal was dim for concentrations lower than 100µg/ml, while the PDMS almost instantaneously polymerized for higher concentrations even before being entirely degassed.

   - **Covalently link a fluorophore to the PDMS base**: I tried to covalently link Rhodamine B to the PDMS base through a hydrosilylation reaction similar to the one at play during PDMS reticulation *(Souchaud et al., 2020)*. Although the fluorescent staining was promising (Figure 20A), this process erodes the nanochannel features on the silicon master, leading to their collapse and thus preventing any further loading of the chips.

   - **Perfuse a culture medium supplemented with an amphiphilic dye**: Finally, I tried to perfuse the chips with a culture medium supplemented with a small amount of the amphiphilic dye FM1-43, generally used as a membrane probe. Interestingly, the dye was quite rapidly adsorbed on the PDMS surface, resulting in a homogeneous fluorescent staining of the chamber edges (Figure 20A). It was surprising to find out that in these conditions, the dye was majorly sequestered by the PDMS and did not stain well bacterial membrane as in the case of liquid culture or agar pad. To verify that the addition of this dye in the culture medium does not affect bacterial growth, I monitored the $OD_{600}$ of a liquid broth

culture using an automatic plate reader in the presence or not of the dye. As expected, in the presence of the dye, bacteria proliferate as well as in the
control condition. Based on this result, I perfused a culture medium supplemented with FM1-43 at a concentration of 2µg/ml to fluorescently stain the PDMS edges, which facilitates the semi-automatic measurement of chamber deformation over the whole course of the experiment.

b. **Calibration of the PDMS deformability**: To relate the deformation of the growth chamber to the actual mechanical constraints applied by bacteria, the PDMS deformability was calibrated at the end of each experiment. To do so, I applied a range of known pressures at the entrance of the culture medium channel using a pressure controller, while keeping close all the outlets of the chip. For pressures ranging from 200mbar (*i.e.* 20kPa) to 4000mbar (i.e. 400kPa), I measured the deformation at the top of the channel with respect to its initial size without being pressurized (Figure 20B). Then, the known pressures were plotted as a function of the measured deformations. Using a linear regression fit, we obtained a calibration equation that will further be used to infer mechanical constraints applied by bacterial proliferation upon confinement (Figure 20C).

In sum, the bacterial confiner is a convenient tool to provide a characterization of confinement-induced bacterial physiological changes occurring in response to a controlled mechanical environment, in the presence of a continuous medium supply.

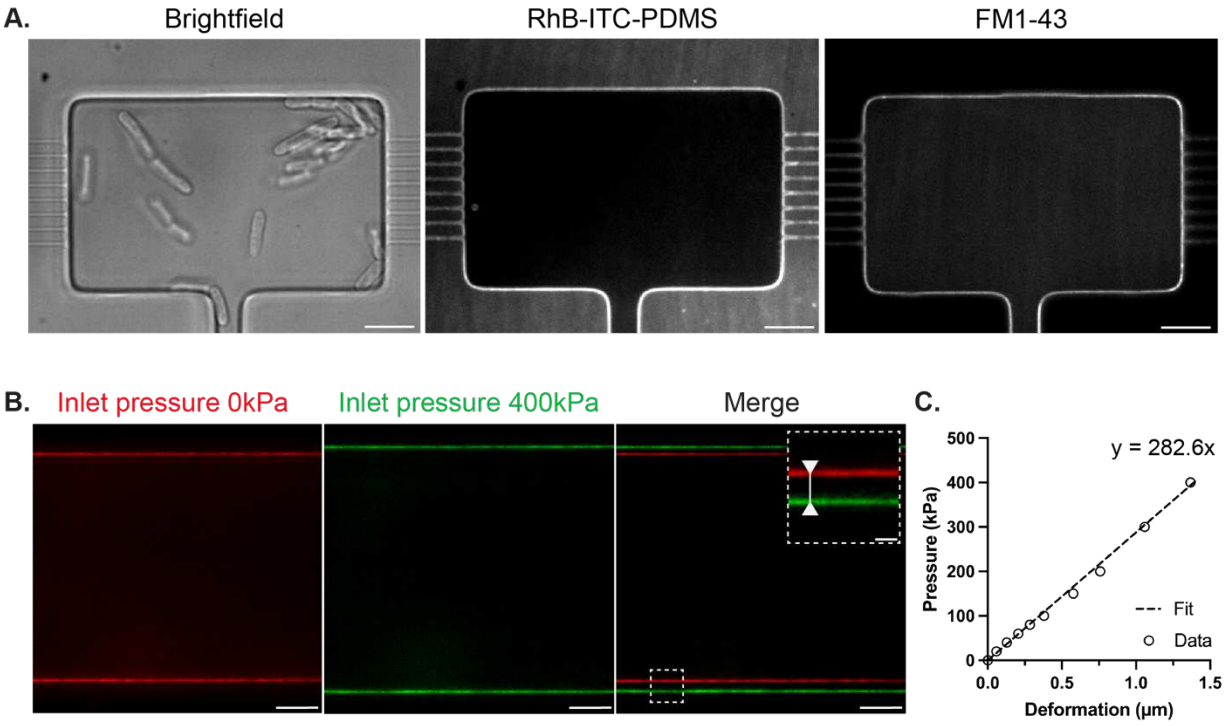


**Figure 20 : Optimization of the bacterial confiner to facilitate the characterization of the mechanical environment encountered by bacteria.** A. The PDMS growth chambers were visualized in brightfield (left) and in fluorescence using a 100X objective. Fluorescence labelling was obtained either by covalently binding a Rhodamine to the PDMS base (middle), or by adding FM1-43, an amphiphilic fluorescent dye directly the culture medium (right). B. The PDMS deformability was assessed by measuring the width of the central channel for a range of pressures applied by a pressure controller (0kPa: left, 400kPa: middle). The corresponding deformation with respect to the non-pressurized state was measured (right). Scale bar inset: 1µm. C. The calibration curve that relates the deformation to the applied pressure was obtained by a linear regression fit (y = 282.6x, R2 = 0.99). The slope is proportional to the Young modulus of the chip material. *Scale bars: 5µm.*

## 1.4 Silicon and PDMS-based microfluidic chips are two complementary systems to study bacterial growth upon confinement (technical discussion)

Here, we have described the technical development of two microfluidic devices with nanometric features, one in silicon (see part 1.1), and the other in PDMS (see part 1.2). Based on the different properties of these materials, these two experimental devices are inherently complementary, in particular on the following points illustrated in Figure 21:

### 1.4.1 Chip deformability

PDMS is an elastomer whose stiffness is easily tunable, while silicon is a hard non deformable material. While the PDMS deformability is useful to measure global forces that arise from bacterial proliferation upon confinement, the silicon non-deformability has also several advantages. As mentioned previously, silicon enables the fabrication of high aspect ratio channels by contrast with PDMS. Also, the non-deformability of silicon can be used in a second step to induce situations of extreme confinement.

### 1.4.2 Chip permeability

Another intrinsic difference between silicon and PDMS relies on gas permeability. As mentioned above, while PDMS is permeable to gas, silicon is not. Thus, PDMS is more appropriate for a first understanding of the impact of confinement on bacterial physiology, to prevent potential side effects of oxygen or $CO_2$ starvation. However, silicon chips could be used in a second step to investigate hypoxia conditions, in combination with a fluorescent indicator of oxygen or $CO_2$ concentrations in the culture medium. Also, a tunable mixture of gases could be potentially injected into the perfusable medium during the experiment with a proper gas controller.

### 1.4.3 Chip porosity

Last but not least, one key difference between the two devices relies on the material porosity. Indeed, PDMS is a porous material known to absorb on its surface small hydrophobic molecules, such as antibiotics, thereby strongly decreasing the available concentration in the culture medium *(Toepke and Beebe, 2006)*. Thus, PDMS microfluidic chips are not the most adapted experimental system to easily perform predictive drug response assays. Although few coatings have been proposed to reduce PDMS absorption, they are not always easy to use in practice *(Gomez-Sjoberg et al., 2010; Mair et al., 2022; Meer et al., 2017)*. By contrast, silicon non-porous microfluidic chips are an alternative experimental system allowing to address this question with accuracy. Thus, silicon chips could represent a complementary assay to verify bacterial phenotypes at specific drug concentrations.

## 1.5 Conclusion

To conclude, in this chapter:

1. **We have developed a versatile microfluidic chip with nanometric features to study bacterial proliferation in a spatially-constrained environment.** The first version of the chip was produced in silicon for technical simplicity but its production and daily use with biological samples was complicated. As a solution, we finally produced this microfluidic chip in PDMS. This has required to unravel the technical challenge of producing nanochannels in PDMS. Although the silicon and PDMS devices are complementary, all the experiments performed in the next chapters focus on the PDMS version of the chip (Figure 21).

2. **This PDMS-based microfluidic device, called the bacterial confiner, allows to reproduce highly dense aggregates as those encountered during infection for a wide range of bacterial species with various envelopes and morphologies.**

3. **The bacterial confiner is a suitable and convenient tool to provide a complete characterization of confinement-induced bacterial physiological changes occurring in response to a controlled mechanochemical environment.**

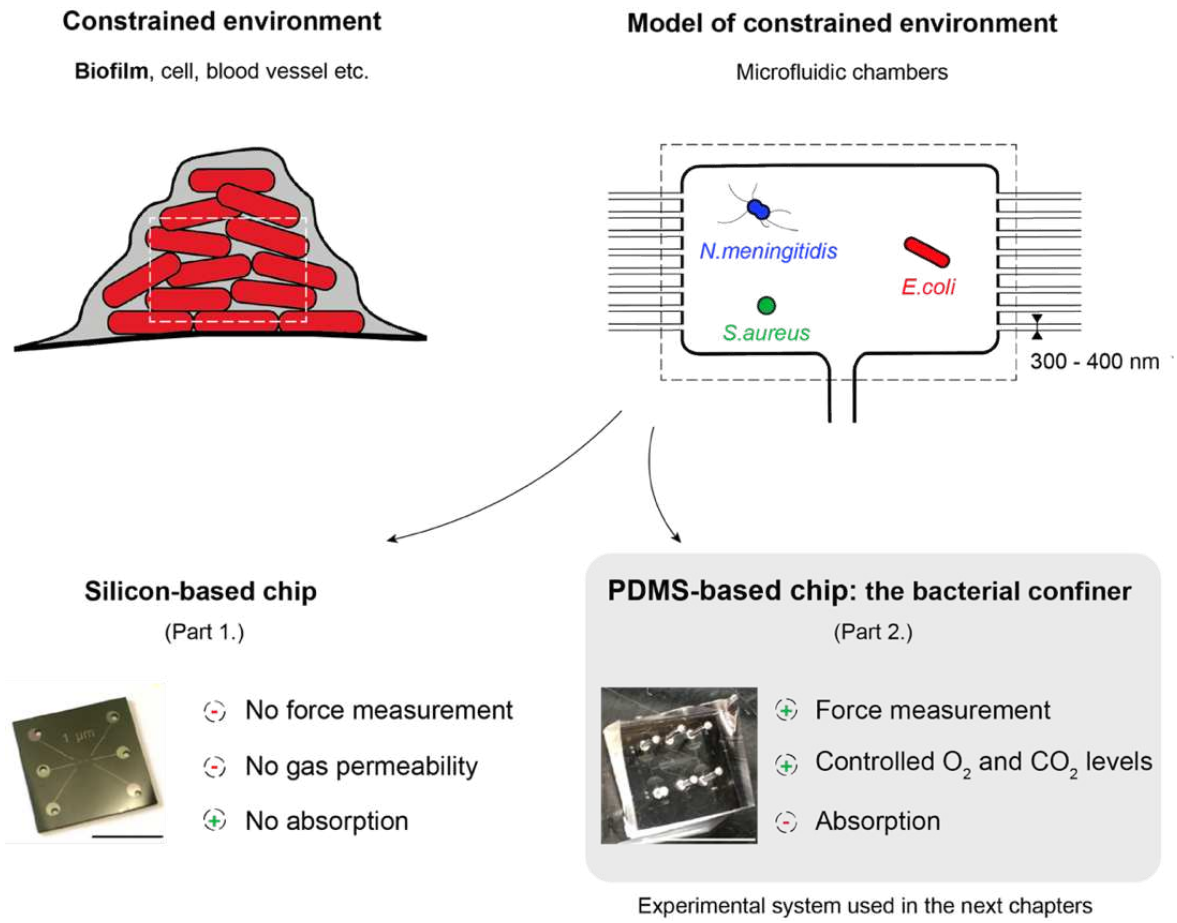


**Figure 21: Summary of the microfabrication developments that have been performed in this PhD work to study bacterial confinement.** Bacteria often proliferate in spatially-constrained environments, such as biofilms (top, left). We have developed a general model system to study bacterial proliferation in such confined environments, that has been validated on various bacterial species, including pathogens (top, right). Two complementary versions of the chip have been fabricated: a first one in silicon, a second more convenient one in PDMS, called the bacterial confiner. All the next experiments are carried out using the bacterial confiner. *Scale bars: 1cm.*

## 2 Development of an image analysis workflow to quantify bacterial growth under confinement at the single-cell level

Deciphering how bacterial physiology is impacted by growth in a spatially constrained environment requires to quantitatively characterize bacterial behavior within a highly dense aggregate, ideally at the single-cell level. Quantitative characterization of bacteria by using optical microscopy has long been challenging, because of their typical size (~1µm) close to the diffraction-limited resolution of a classical epifluorescence microscope. However, great improvements in confocal microscopy applied to live samples (in particular with the spinning-disk technology and the arrival of accessible Super-Resolution modules) together with cutting-edge image analysis methods based on artificial intelligence have recently opened the way to single-cell quantitative approaches on bacterial cells. The emergence of this new quantitative microbiology will shed light on this fascinating world invisible to the naked eye *(Schneider and Basler, 2016; Yao and Carballido-López, 2014)*.

To quantify bacterial physiology upon confinement at the single-cell level, we:

- **Improved the resolution of our confocal spinning-disk microscope**, through the addition of a Structured Illumination Microscopy-like module (Live-SR module, Gataca Systems) coupled to a 95b Prime CMOS camera with high quantum efficiency. This module allows to perform live imaging of bacteria, as easy and fast as in spinning-disk microscopy and with low phototoxicity, while increasing the resolution by 50%. For instance, a 1µm-wide object will be composed of 10 pixels using the 100X objective, and 15 pixels using the 100X objective together with the Live-SR module. This technically means pushing the resolution limit of light microscopy over the diffraction barrier to simultaneously monitor the dynamics of several subcellular components in bacteria and infer their respective functions.

- **Developed a general image analysis workflow** based on the synergy of the machine-learning-based segmentation software Ilastik *(Berg et al., 2019)* and the Fiji tracking plugin TrackMate *(Ershov et al., 2022))*. Thanks to this pipeline, we can identify each individual bacterium by drawing its boundaries (segmentation process) and eventually follow its evolution over time (tracking process) even within extremely dense environments.

This work has been done in collaboration with Jean-Yves TINEVEZ, head of the Image Analysis Hub (Institut Pasteur, Paris, France).

## 2.1 Establishment of a semi-automatic image analysis workflow to quantify bacterial growth under 2D confinement (agar pad)

In search of simplicity, we started by focusing on bacterial growth in one single plane, *i.e.* under 2D confinement. For this, I ran agar pad experiments as a simple assay to monitor bacterial growth using live imaging. In these experiments, bacteria are trapped between a coverslip and a gel, which constrains bacterial growth in the (x,y) plane while preventing growth in the z direction. Using high-resolution time-lapse microscopy, I can follow bacterial growth over multiple cell cycles. To facilitate the detection of bacterial cell shape even in extremely dense environments, I chose to rely on genetically encoded membrane stainings, that are more stable in time and homogeneous over the bacterial contour compared to chemically-based fluorescent probes (Table 3). These experiments have been carried out on two Gram-negative bacterial species with various morphologies, the rod-shaped bacterium *E. coli* and the diplococcus *N.meningitidis*. In the case of *E. coli*, we used the strain MG1655 TM-ZipA-mCherry whose fluorescence is induced by the fusion of the N-terminal domain of the ZipA inner membrane protein to the fluorophore mCherry (original TB28 strain kindly provided by T.Bernhardt (Harvard Medical School, USA) – see Materials & Methods - part 1.2.1) *(Yao et al., 2012)*. Of note, this fusion protein lacks the FtsZ interaction domain of the ZipA protein, so that its localization is dispersed throughout the membrane, with no specific enrichment at the septum. For *N. meningitidis*, we used for the first time the strain 2C43 PilQ-mCherry whose fluorescence is induced by the fusion of the PilQ outer membrane protein to the fluorophore mCherry.

| *Stainings* | *Type* | *Observation* |
|---|---|---|
| ***FM dyes*** | Dye (1-5µg/ml) | No membrane staining / Dye absorbed on PDMS |
| ***WGA dyes*** | Dye (5 – 50 – 100 µg/ml) | Very heterogeneous, no staining at the edges |
| ***MscS-sfGFP*** | Genetically-encoded IPTG inducible | Fluorescent aggregates at the rod tip |
| ***LepB-sfGFP*** | Genetically-encoded IPTG inducible | Fluorescent aggregates at the rod tip |
| ***PBP5-mCherry*** | Genetically-encoded IPTG inducible | Fluorescent aggregates at the rod tip |
| ***TM-ZipA-mCherry*** | Genetically encoded | Homogenous in time and space |

**Table 3 : Overview of the fluorescent membrane stainings tested with *Escherichia coli* in the bacterial confiner**

To quantify bacterial growth, I first tested both a homemade segmentation script in Python, and available segmentation programs *(Raaphorst et al., 2019)*, including Cellpose *(Stringer et al., 2020)*. At that time, none of these programs was optimized to accurately segment bacteria of various morphologies, including both rods and cocci, based on a fluorescent membrane signal. For this reason, we have developed a new image analysis pipeline as described in the following (Figure 22A).

Our workflow uses three open-source softwares:

- **Ilastik: an interactive machine-learning-based segmentation software** *(Berg et al., 2019)*

Segmentation is the most critical part of the analysis. It consists of partitioning the image into different regions of interest, called classes. In Ilastik, these regions are defined based on two morphology-independent criteria: the pixel value and the presence of gradients in the local pixel environment. The Ilastik-based image partition is performed by a machine-learning model, that needs to be trained before becoming predictive. The training is supervised and is done through user annotations of the dataset. In practice, to train a model for bacterial membrane segmentation, I used the images described above and I defined two classes: a "Membrane" class by drawing over the membrane signal, and a "Background" class by drawing over the background signal. These annotations were then used by a pixel classifier to predict to which class each pixel value has the highest probability to belong to (Figure 22B). On average, a dataset of less than 50 independent annotated images was required to properly train a predictive model, which takes approximately 1-2 days. All the segmented datasets were checked and manually corrected if needed. A similar approach can be adopted to segment any fluorescent marker of key cellular components, such as the bacterial membrane, the cytoplasm, the DNA, or even subcellular structures.

- **TrackMate 7: a tracking Fiji plugin interacting with external segmentation softwares** *(Ershov et al., 2022)*

Tracking is a second part of the analysis, that could be of interest to extract cell lineages, *i.e.* to relate the state of a given bacterium at a given time with its state in the past. In TrackMate 7, images that have been segmented by a Fiji-independent software, such as Ilastik, can now be loaded and tracked using various trackers. In practice, we use the Linear Assignment Problem (LAP) Tracker to track bacteria with an isotropic shape (*e.g. N. meningitidis*) (Figure 22B) and the Overlap Tracker to track bacteria with an anisotropic shape (*e.g. E. coli*). Beyond tracking, TrackMate is also useful to interactively display key parameters in time and space, such as the area or the fluorescence intensity of the segmented objects.

- **Python: home-made scripts to post-process and compute additional data**

In the third part of the pipeline, data generated by TrackMate are post-processed using homemade scripts in Python. This allows us to visualize the evolution of many parameters over multiple cell cycles, such as the area of the bacterial body (Figure 22C). If necessary, additional parameters can be computed to strengthen the analysis. For instance, this is what we have done to investigate morphological parameters such as bacterial length and width, each of these parameters being not initially present in the analysis (see Material and Methods, part 7.4 for more details). This post-processing part is now at the heart of the Ph.D. project of Laura Xénard, initially recruited as a M2 student under my supervision, and will give rise to a new open-source software called *Pycellin*.

Together, we describe here a semi-automatic image analysis pipeline that allows bacterial segmentation and tracking at the single-cell level in bacterial aggregates growing under 2D confinement. This workflow was initially developed on the diplococcus *N. meningitidis* (Figure 22E) and easily expanded to other bacteria with various morphologies, such as the rod-shaped *E. coli* (Figure 22F), paving the way to the quantitative characterization of bacterial growth regulation in spatially constrained environments.

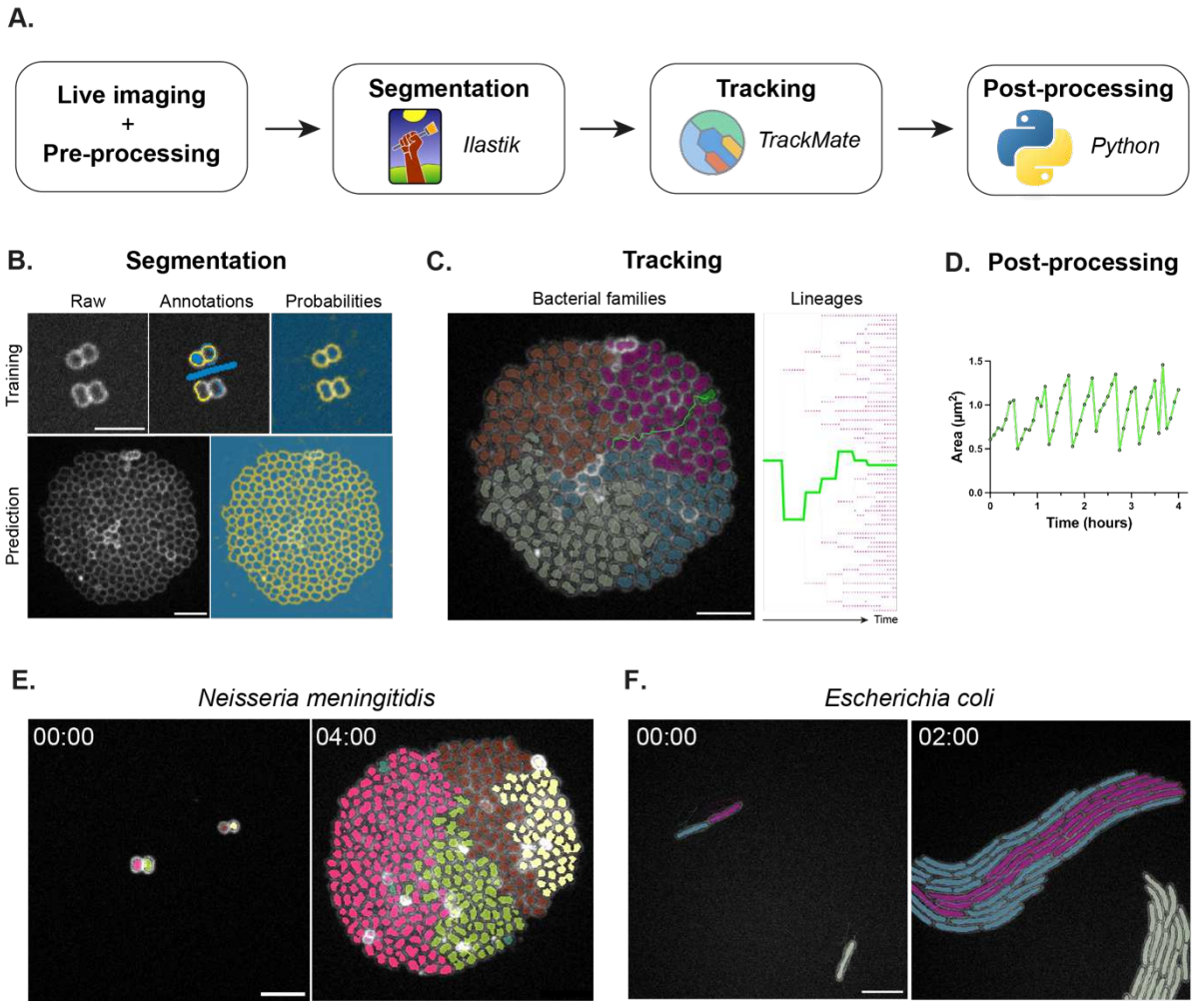


**Figure 22: Development of an image analysis workflow to quantify bacterial growth under 2D confinement at the single-cell level.** A. Image analysis pipeline. Raw images were cropped and rotated before being processed. Individual bacteria were segmented using a machine-learning based segmentation software Ilastik, and eventually tracked using the Fiji plugin TrackMate. Data were then post-processed using Python. B. Ilastik-based segmentation process. A machine-learning model was first trained to identify the cellular component of interest (eg. membrane) on raw images (top, left), by drawing annotations (top, middle) over the membrane (yellow) and over the background (blue). These annotations trained a pixel classifier that determines whether a given pixel value has the highest probability to belong to the membrane signal or to the background one (top, right). After the training, the model is used on a new dataset to predict whether the pixels belong to the membrane signal or background one, resulting in the generation of a binary image of the individual bacteria. C. Tracking process. Individual segmented bacteria were tracked over the duration of the experiment, to reconstruct bacterial families (left), depicted in various colors. The tracking is done by linking one bacterium (green) on the image at time t with the same bacterium on the image at time t+1, leading to the reconstruction of cell lineages (right). D. Data are then post-processed to visualize the evolution of the parameters of interest during time, such as the change in area of the bacterial body over the time course of the experiment. E. Application of the image analysis pipeline to quantify the growth of few individual *Neisseria meningitidis* bacteria (left) during 4 hours (right) on agar pad. F. Application of the pipeline to quantify the growth of few *Escherichia coli* bacteria (left) during 2 hours (right). *Scale bars: 5µm.*

## 2.2 Extension to bacterial growth under 3D confinement (bacterial confiner)

The pipeline described above allows a quantitative analysis of bacterial growth in an unconstrained space. Could we expand this work to quantify bacterial growth in a limited, crowded environment?
The adaptation of the image analysis pipeline to growth upon confinement was done by Laura Xénard during her M2 internship. Similarly, for each bacterial species, a new Ilastik model has been trained to segment individual bacteria based on their fluorescent staining while keeping the other steps of the analysis unchanged. Importantly, the segmentation at the single-cell level in an extremely dense environment requires to use of genetically encoded fluorescent membrane stainings, rather than cytoplasmic ones. Indeed, we found that in the case of *E. coli* forming highly compact aggregates upon confinement, models relying on contour-based signals were crucial to obtain precise and predictive detection of single cells (Figure 23A, top), while cytoplasmic signals gave poor predictive segmentation that needs to be extensively manually corrected to obtain acceptable quantitative outcomes (Figure 23A, bottom). Indeed, when bacteria are tightly packed together, the distance between two bacterial bodies is lower than the resolution of the microscope. This tight proximity leads to a poor signal/noise ratio in the case of bacteria fluorescently stained in the cytoplasm (full objects), while this ratio is not impacted by increased density if bacteria are fluorescently stained at their boundaries (empty objects). For this reason, fluorescently labeled bacteria were segmented using a membrane fluorescence signal (TM-ZipA-mCherry - *(Yao et al., 2012)*), further added in all the bacterial strains of interest to favor quantification (see Materials & Methods – part 1.2.1). Interestingly, the requirement of a membrane signal was less evident in the case of *N.meningitidis*, where confined cells roughly maintain their spherical shape with a lower packing index (Figure 23B).

In summary, the general image analysis pipeline described here allows us to segment and track individual bacteria, no matter their species and morphology, in the presence or not of confinement. While a manual analysis would have been complicated in the bacterial confiner over the time course of the experiments that lasted approximately 15 hours, this semi-automatic workflow allows to extract all information with high reproducibility, both in time and space, in a unified manner.

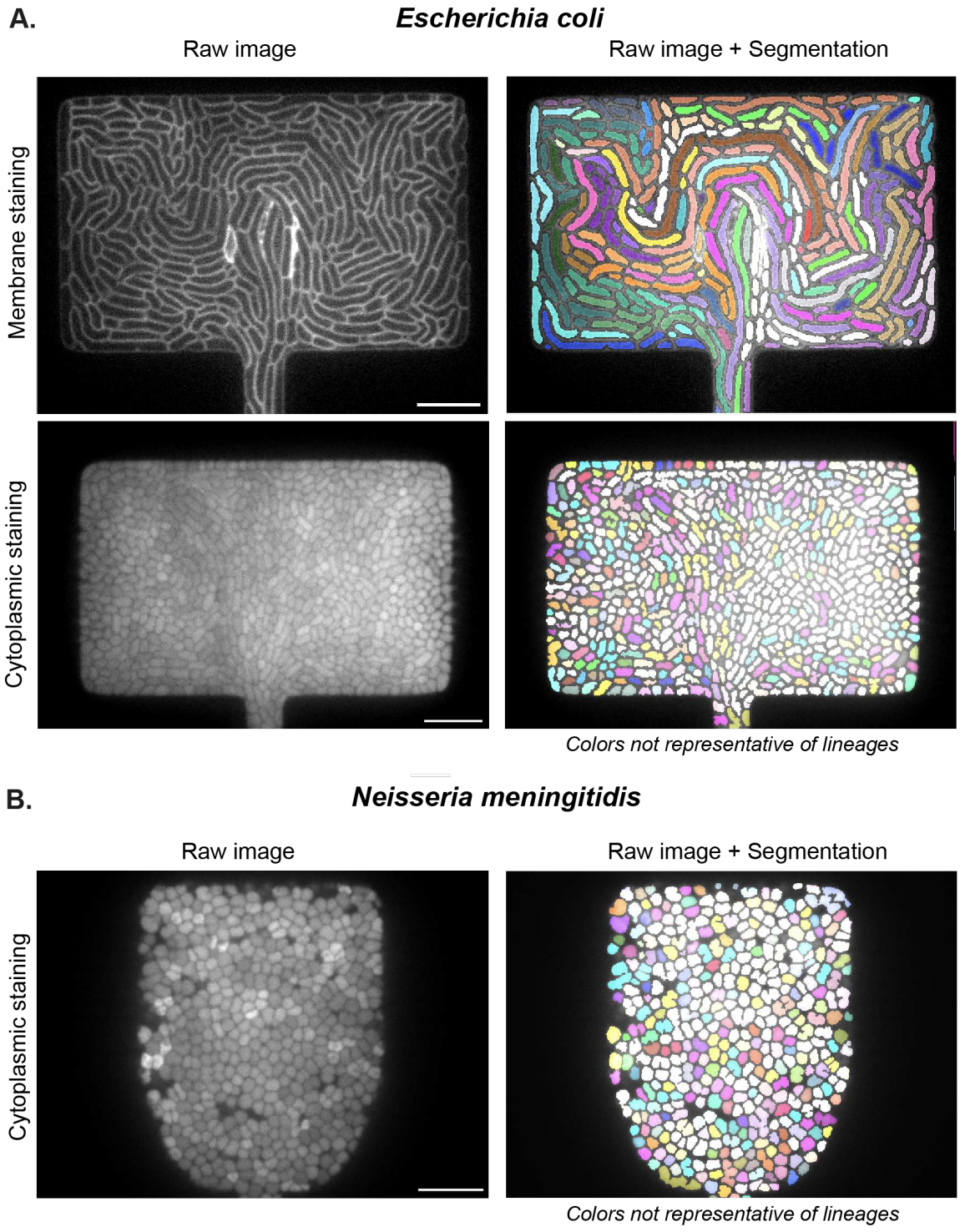


**Figure 23 : Application of the presented image analysis pipeline to quantify bacterial growth in the bacterial confiner.** A. Top: *Escherichia coli* bacteria fluorescently labeled at the membrane were imaged in the bacterial confiner (left), segmented and tracked (right). For the segmented image at the top only, one color represents one bacterial lineage. Bottom: *Escherichia coli* bacteria fluorescently labeled in the cytoplasm were imaged in the bacterial confiner (left) and segmented (right). This segmentation has required many manual corrections, no tracking has been performed so that the colors have no meaning. C. *Neisseria meningitidis* bacteria fluorescently labeled in the cytoplasm were imaged in the bacterial confiner (left, chamber with a glass shape) and segmented (right). Since no tracking have been performed, the colors have no meaning. *Scale bars: 5µm.*

## 2.3 Comparison of the present pipeline with state-of-the-art segmentation approaches

Cell segmentation in microbiological research is a general issue, that has led to the development of a plethora of segmentation softwares during the time course of my PhD *(Cutler et al., 2022; Hartmann et al., 2021; Jelli et al., 2023; Ollion et al., 2019; Pachitariu and Stringer, 2022; Spahn et al., 2022; Stringer et al., 2020; Zhang et al., 2020)*. As a proof of concept, we decided to compare Ilastik-based segmentation with the one provided by Omnipose, one of the most powerful segmentation tools for bacteria currently accessible.

First, using the *N. meningitidis* datasets, we observed that Omnipose bacterial detection was as good as the one provided by Ilastik. However, bacterial morphology was quite imprecise, especially during division completion. More specifically, detection of subtle changes in cell shape that characterize coccus-to-diplococcus transition over the cell cycle, membrane invagination, and septation were not robustly detected over time. Using *E. coli* datasets, bacterial detection was strikingly much better in Ilastik, notably when the bacterial population is highly heterogeneous in shape. Even though more work is needed to quantitatively compare Omnipose and Ilastik segmentations, our image analysis pipeline still achieves similar or even better segmentation quality compared to other state-of-the-art segmentation softwares. In the long term, these segmented data could be used to provide a high throughput classification of bacterial phenotypes throughout the cell cycle for various bacterial species *(Saraiva et al., 2021)*.

## 2.4 Application of the image analysis pipeline to the description of the diplococcus cell cycle: present work and outlooks

The quantification of bacterial growth under 2D confinement (see part 2.1) has been presented here as a validation step for the development of the analysis workflow. Beyond this aspect, this morphology-independent image analysis pipeline also opens the way to the quantitative characterization of bacterial growth for many under-studied bacterial species, such as diplococci. Indeed, while growth regulation has been mostly investigated for rods (*e.g. E. coli, B. subtilis (Haeusser and Levin, 2008)* and cocci (*e.g. S. aureus (Monteiro et al., 2015), S. cystis (Yu et al., 2017), D. radiodurans (Floc'h et al., 2019)*), how diplococci grow and divide remains much more elusive. Yet, few pathogenic bacteria have evolved from rods to adopt this intriguing shape, such as the *Neisseria* family *(Veyrier et al., 2015; Westling-Häggström et al., 1977)*. Therefore, as a side project, I took advantage of this image analysis pipeline to provide a more quantitative description of diplococcus cell cycle, by using the pathogenic bacteria *N. meningitidis* as a model organism.

Here, we use the meningococcal 2D growth dataset (see part 2.1) to visualize cell shape changes that occur during the cell cycle (Figure 24A). We chose to focus on two morphological parameters to quantify diplococcus growth: the area of the bacterial body and its circularity, the latter being a readout of bacterial shape isotropy. We noticed that the meningococcal cell cycle lasts approximately 40 minutes and is characterized by a linear increase in cytoplasmic area (Figure 24B, left). Interestingly, during the first 30 minutes, bacterial circularity remains constant and close to 1, while it drops during the last 5-10 minutes of the cell cycle, differently from what has been shown in the case of the Gram-positive coccus *S. aureus (Monteiro et al., 2015)* (Figure 24B, middle). This suggests that the cell cycle can be decoupled in two phases. During the first phase, diplococci bacteria exhibit a cocci-like shape and grow isotropically. In the second phase, bacteria transition to a mature diplococcus by growing preferentially in one direction at a faster rate to conserve a global linear increase in area (Figure 23B, right), differently from linear changes in volume during the cell cycle of the Gram-positive cocci *S. aureus* and *D. radiodurans (Floc'h et al., 2019; Monteiro et al., 2015).* To date, the mechanisms at play in Gram-negative diplococci, in particular how morphological changes are coordinated with DNA replication and septum formation remain largely unexplored.

To go further and explore this question, we have engineered meningococcal strains with fluorescent reporters of key cellular components, including the outer membrane, the inner membrane, and the DNA, and monitored their proliferation by live imaging (Figure 24C). This quantitative work will be continued by Laura Xénard during her PhD, whose goal is to provide a complete quantitative description of meningococcal growth in the absence of environmental stresses.
In particular, she will:

- Investigate how DNA segregation, membrane remodeling, peptidoglycan synthesis and hydrolysis are regulated to shape septum formation and meningococcal division (Aim 1)

- Address the physical mechanisms of cell size regulation by testing different theoretical models, including recently published *(Harris and Theriot, 2016; Willis and Huang, 2017)* and new ones in collaboration with theoretical physicists (M. Lagomarsino, IBPS, Paris, France) (Aim 2)

As a preliminary basis for the first aim, I have identified potential regulators of division in Gram-negative diplococci by comparing the proteins involved in the regulation of bacterial division for three bacterial species: *N. gonorrhoeae, D. radiodurans* a Gram-positive coccus, and *E. coli*, a Gram-negative rod *(Pinho et al., 2013).* Preliminary experiments on *N. meningitidis* have shown that DNA arrangement is characterized by various morphologies, from ball to banana shape, similar to those observed in *D. radiodurans (Floc'h et al., 2019)* (Figure 24C). These similarities indicate that nucleoid

organization is greatly influenced by cell shape and suggest a similar regulation between cocci and diplococci. Thus, by comparing specifically *N.gonorrhoeae* and *D.radiodurans*, I propose that efficient chromosome segregation and positioning in diplococci could be mediated by the recruitment of the conserved chromosome partitioning system ParABS system, together with the SMC complex, known to actively segregate and position DNA throughout the cell body for a wide range of bacterial species *(Adams et al., 2014; Jalal and Le, 2020; Thanbichler and Shapiro, 2008)*.
In addition, bacteria tightly regulate DNA localization and septum positioning using two different defense mechanisms: nucleoid occlusion that prevents the chromosome from being cut by the septum, and the Min system that prevents septum formation near the poles *(Adams and Errington, 2009)*, thus preventing the birth of anucleate non-viable daughter cells. Yet, cocci bacteria do not have nucleoid occlusion-related proteins (SlmA, Noc), indicating that the proper positioning of the division plane is mostly mediated by the Min system in such bacterial family. This is in agreement with previous experiments performed in the lab, in which *N.meningitidis* Δ*minD* fails to divide symmetrically, resulting in the formation of daughter cells with heterogeneous sizes (Figure 24D).
Then, diplococci cell separation in two daughter cells is a slower and progressive process compared to other bacteria such as *S.aureus*, suggesting an enzymatic process rather than a mechanical one *(Zhou et al., 2015)*. Thus, cell separation is mostly influenced by the bacterial envelope architecture that varies between Gram-negative and Gram-positive bacteria, rather than the bacterial shape *(Adams and Errington, 2009)*. Previous experiments on *N.meningitidis* have shown that inner membrane invagination happens in a first step, followed then by invagination of the outer membrane (Figure 24C). It is reasonable to think that the first event leading to diplococci division is the formation of a well-conserved FtsZ ring, anchored at the inner membrane through conserved membrane-anchored proteins such as FtsA *(Morrison et al., 2022; Pinho et al., 2013; Zou et al., 2017)*. As in the wide majority of bacteria, this polymeric ring probably serves as a scaffold to recruit the divisome, *i.e.* the bacterial-cell-division apparatus that orchestrates nascent cell pole morphogenesis through envelope invagination together with cell wall remodeling by coordinating septal peptidoglycan synthesis and hydrolysis. Based on a previous study, I hypothesize that *N.meningitidis* cell separation is mediated by a septation process, during which septal peptidoglycan synthesis occurs at a faster rate than its hydrolysis, leading to a temporal delay between inner membrane and outer membrane invaginations *(Navarro et al., 2022)*. To verify this hypothesis, peptidoglycan fluorescent pulse labeling using two compatible fluorescent dyes (*e.g.* YADA and HADA) could be a fruitful assay to determine and compare septal peptidoglycan synthesis and degradation rates. The temporal separation between the inner membrane and the outer membrane invagination could also be related to the time required to recruit at the division site linker proteins that stabilize the outer membrane.

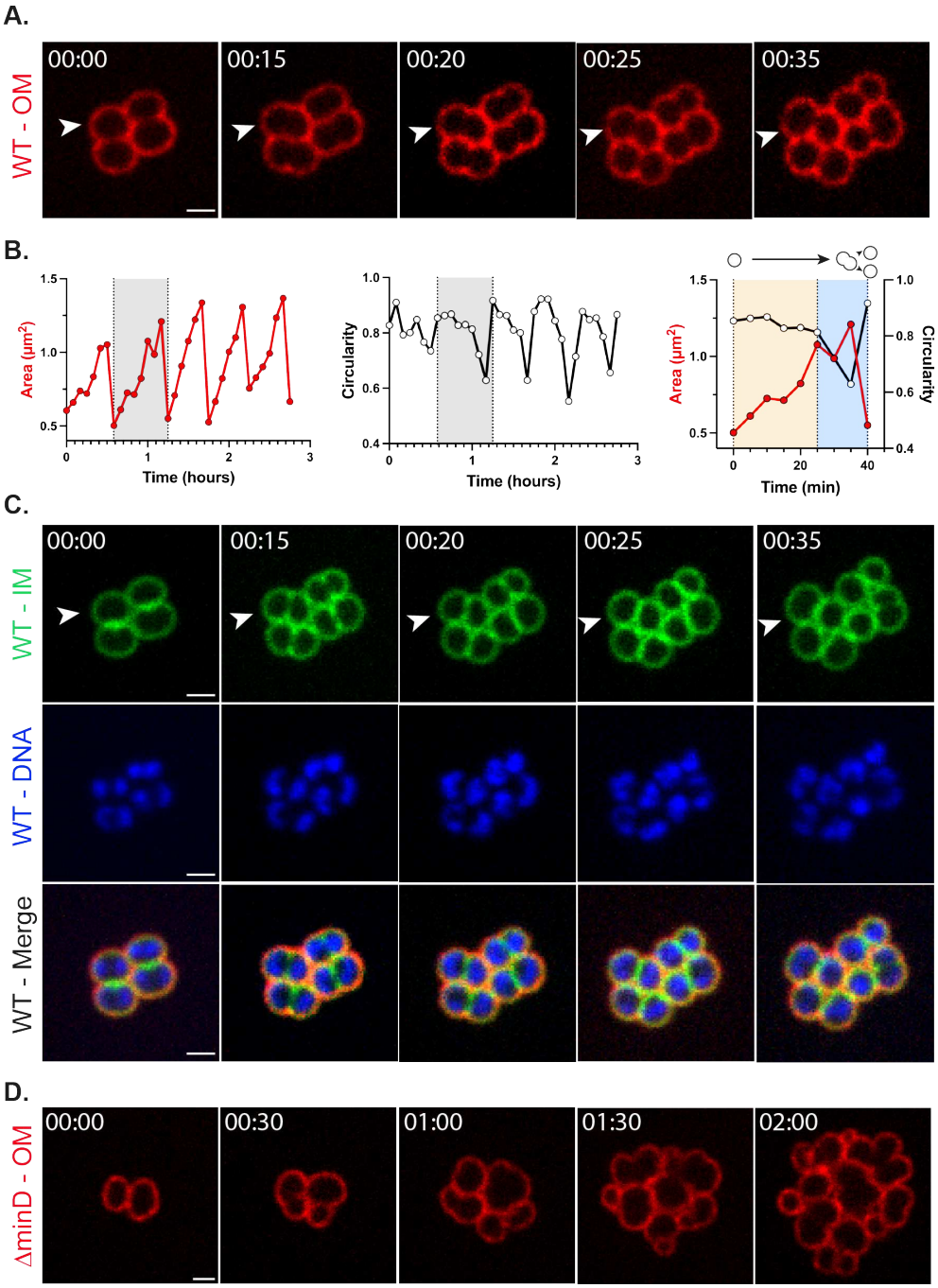


**Figure 24: Characterization of *Neisseria meningitidis* diplococci growth on agar pads.** A. *N. meningitidis* WT bacteria fluorescently labeled at the outer membrane (PilQ-mCherry) were imaged during multiple cell cycles to follow morphological changes. B. Quantification of morphological changes occurring during bacterial growth of the WT *N. meningitidis* strain. Quantification of changes in area (left) and circularity (middle) of the bacterial body over five successive cell cycles. The gray region depicts one cell cycle. Bacterial growth during one cell cycle occurs in two phases (right). In the first one, circularity of the bacterial body is almost constant while the area increases linearly (yellow region). In the second phase, the circularity drops while the area still increases linearly before the bacterium separates in two daughter cells (blue region). C. Corresponding morphological changes of the inner membrane (LepB-sfGFP, top) and the DNA (Hup-mRhubarb, middle). Morphological changes of these three key cellular structures during one cell cycle are overlayed (bottom). D. Morphological changes of a *N. meningitidis* ΔminD strain over multiple cell cycles. *Scale bars: 1µm.*

In *E. coli*, the recruitment of the Tol-Pal system at the division site is an active process that favors the fast stabilization of the outer membrane during outer membrane constriction *(Szczepaniak et al., 2020)*, which occurs at a similar rate than the inner membrane one *(Navarro et al., 2022)*. Interestingly, deletion of this system causes delayed outer membrane invagination and outer membrane vesicle production *(Gerding et al., 2007)*. In line with this observation, *N. meningitidis* does not have a Tol-Pal system and is known to produce outer membrane vesicles *(Schwechheimer and Kuehn, 2015)*. Yet, *N. meningitidis* bacteria have alternative strategies to link the outer membrane to the cell wall, such as the protein RmpM *(Maharjan et al., 2016; Waterbeemd et al., 2010)*. Interestingly, preliminary data in the lab suggest that indeed RmpM deletion in meningococci leads to an increased production of extracellular vesicles and higher probability of cell lysis upon septation. Even if it is unknown whether the recruitment of RmpM at the division site is an active or diffusive process, one can speculate that outer membrane constriction is slower in the case of a diffusive process, potentially leading to a temporal delay between inner and outer membrane constrictions. A large delay between inner and outer membrane constrictions in diplococci than in cocci could ultimately provide a key explanation to distinguish these two closely related phenotypes.

Altogether, we propose here a model for diplococci division, that is recapitulated in Figure 25. This starting Ph.D. work will serve as a first basis to further understand how meningococcal growth is impacted by growth in a limited space, as it is the case at the late stage of meningococcal infection.

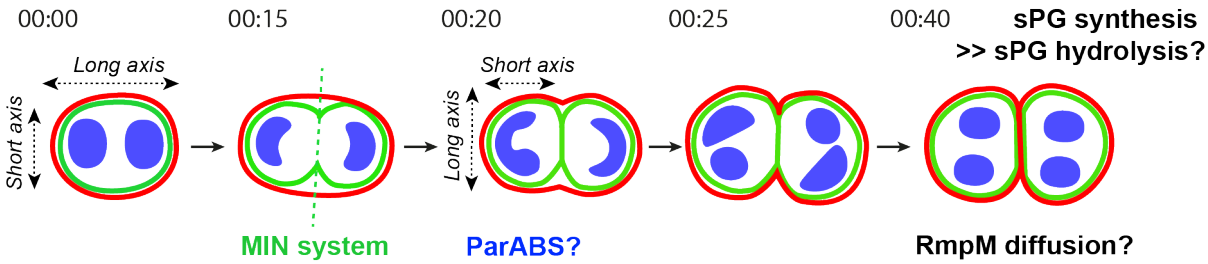


**Figure 25 : Proposed model for diplococci growth.** A single coccus is initially defined by a short and a long axis, and two segregated pools of DNA. During the first 15 minutes of the cell cycle, the Min system positions the division plane at equal distance of the poles, leading to the invagination of the inner membrane. 5 minutes later, an inner membrane septum is formed and DNA starts to segregate along the newly defined long axis, perpendicular to the initial one. Active segregation and positioning of the genetic information could be mediated by the ParABS system, conserved in *Neisseria* species. After DNA segregation, the outer membrane starts to invaginate. Inner membrane constriction is a long process that occurs during the last 15 minutes of the cell cycle. The delay between inner and outer membrane invagination, that lasts approximately 10 minutes, could provide a hint regarding the molecular basis of diplococci cell separation. This long temporal delay between inner and outer membrane constriction could be either related to differential rates of septal peptidoglycan (sPG) synthesis and hydrolysis, or to a diffusive recruitment of the linker protein that mediates the outer membrane stabilization to the cell wall, potentially providing a key difference between cocci and diplococci bacterial families.

## 2.5 Conclusion

In this chapter, we have described the development of a new semi-automatic image analysis pipeline, that is based on the synergy of the machine-learning-based segmentation software Ilastik and the Fiji plugin TrackMate *(Ershov et al., 2022) – in appendix).*
Importantly, we have used this image analysis pipeline to quantitatively characterize the growth of several bacterial species with different morphologies and in various environments. As a proof of concept, we first used this pipeline to quantify bacterial growth in normal growth conditions, by using classical agar pad assays. Notably, by using this tool, we provide a first quantitative description of the cell cycle of the diplococcus *N.meningitidis*, which will be continued by Laura Xénard during her Ph.D. We then extended the scope of this pipeline to bacterial growth in extremely dense environments within the bacterial confiner. Together, the new image analysis workflow presented in this chapter provides us a way to quantify, with high reproducibility and in a unified manner, bacterial growth under self-generated mechanical constraints, both in time and space.

# 3 Quantitative characterization of bacterial physiology upon confinement

We are now in position to address the main question of my Ph.D.: How does growth-induced mechanical confinement impacts bacterial physiology?
To address this question, I took advantage of the newly developed bacterial confiner together with the machine-learning-based image analysis pipeline, both presented in the previous chapters, to provide a quantitative characterization of bacterial physiology upon confinement at the single-cell level.
In the following, I focus on the model organism *E. coli*. All the *E. coli* genetically modified strains used in this part of the work have a MG1655 genetic background, unless stated otherwise. Bacteria were fed with LB Miller for all the experiments.

## 3.1 In the bacterial confiner, bacteria proliferate in the form of tightly packed aggregates and survive in the presence of a controlled chemical environment

To decipher how *E. coli* behaves under spatial confinement, I loaded a suspension of exponentially growing bacteria in the bacterial confiner and monitored their proliferation in the presence of a continuous medium supply, using brightfield high-resolution spinning-disk confocal microscopy coupled to a super-resolution SIM-like module. I observed that bacteria proliferate well in the chambers, ultimately leading to the formation of a tightly packed, confined aggregate (Figure 26A - left). To determine to which extent bacteria survive in this dense environment, I perfused the chamber over time with culture medium supplemented with SYTOX Green, a DNA counterstain that becomes fluorescent once it binds to chromosomes (Figure 26A - right). By quantifying the death index, meaning the ratio between the surface fluorescently stained to estimate the surface fraction occupied by dead bacteria and the one occupied by bacteria using the brightfield image, I found very low values around 2% for both confined and not confined bacterial populations (Figure 26B). This means that bacteria survive upon confinement, as they continue growing over several hours once the entire chamber is filled up, with cell death remaining minimal.

In the bacterial confiner, bacterial survival and proliferation are favored thanks to a continuous medium supply. Indeed, we have optimized both the chip design and the loading strategy to maximize medium renewal within the growth chambers. To verify the perfusability of the aggregate even at different stages of confinement, I injected culture medium supplemented with fluorescent Dextran (molecular weight: 10kDa, hydrodynamic diameter: 2.3nm) once the bacteria had proliferated in the chambers (Figure 26C). In this way, I was able to monitor the diffusion of the fluorescent signal throughout bacterial aggregates.

As expected, after 20 minutes, the total fluorescence of the growth chamber was lower for confined vs. not confined aggregates (Figure 26D - top). Indeed, as more space is occupied by negatively stained bacteria in confined chambers, less space is available for the fluorescent culture medium. However, by normalizing the fluorescent signal between 0 and 1 to get rid of the occupancy level and compare the diffusion kinetics, I observed that the profiles follow the same trend for both confined and unconfined chambers (Figure 26D - bottom), showing that bacterial aggregates are well perfused in even upon confinement.

Therefore, in the bacterial confiner, *E. coli* bacteria proliferate in a limited space in the presence of a strong continuous medium supply, leading to the formation of a confined aggregate in which bacteria survive.

## 3.2 Bacterial growth under confinement leads to the generation of large compressive forces

### 3.2.1 Characterization of the mechanical environment

Next, we wanted to determine whether confinement induces a change in the mechanical environment encountered by bacteria, as it has been previously reported for yeasts *(Delarue et al., 2016)*. To this end, I monitored the proliferation of the *E. coli* MG1655 WT strain over time at 30 minutes frame rate in growth chambers with fluorescently labeled edges in Z-stacks (Figure 27A - left). Using a homemade script in Python, I was able to automatically segment the chamber contour at the top (Figure 27A - right) and measure the corresponding deformation with respect to the chamber's initial size (Figure 27B - top). By using the calibration curve of the chip deformability, I inferred the actual pressure applied by the bacteria over time. Interestingly, I found that as soon as bacteria fill up the chambers, their proliferation generates a large pressure similar to the one in a car tire (~300 kPa) in a few hours only (Figure 27B - bottom)!

In other words:

Bacterial proliferation before confluency ➔ GIP = 0 : "Before Confinement"
Bacteria proliferation after confluency ➔ GIP increases over time : "Confinement"

Interestingly, similar pressures were also generated by the proliferation of other *E. coli* strains, including the TM-ZipA-mCherry one used for single-cell analysis in the following paragraph, and the uropathogenic UTI89 strain responsible for urinary tract infections (Figure 27B - bottom).

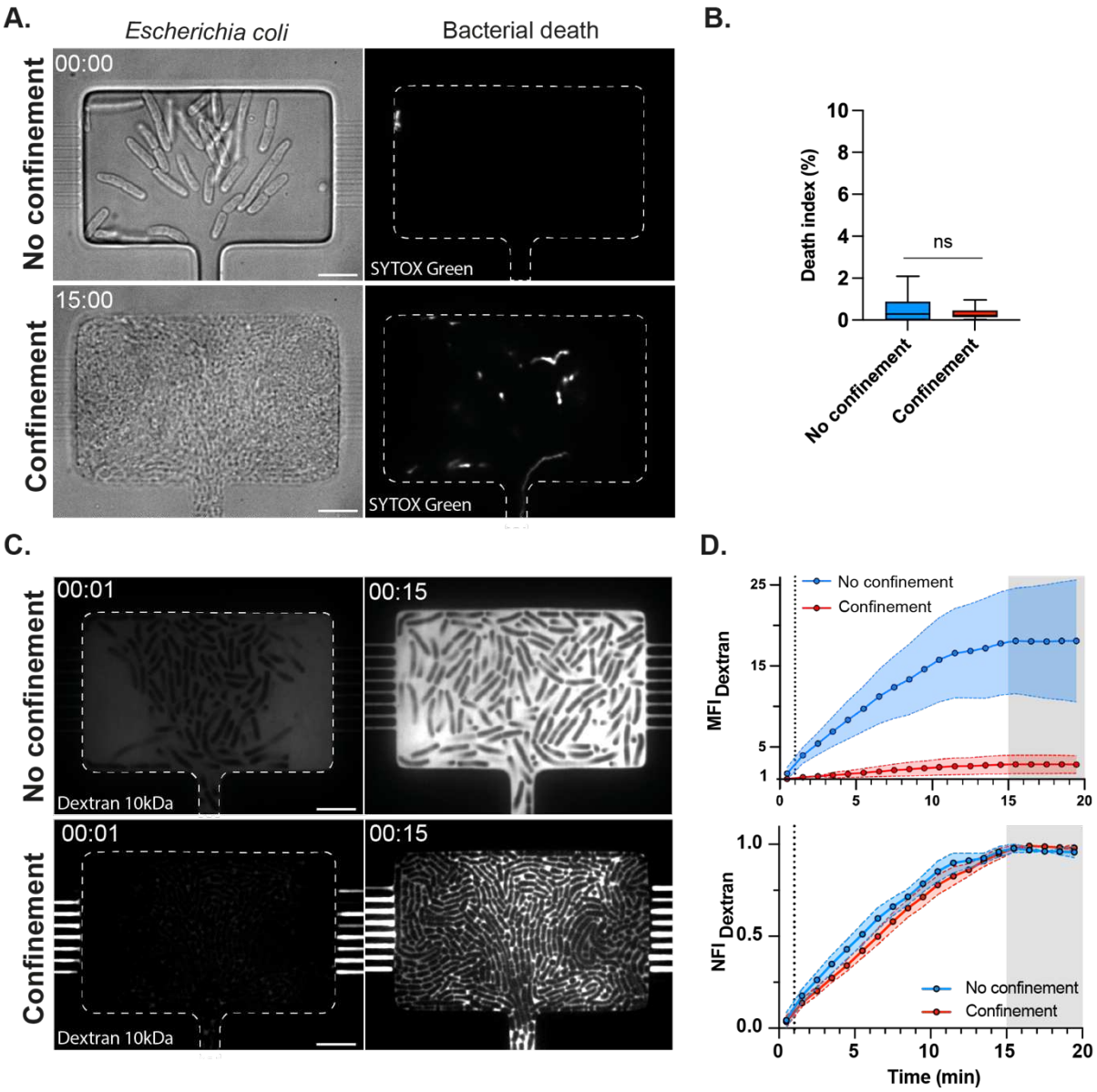


**Figure 26 : In the bacterial confiner, *Escherichia coli* bacteria proliferate in the form of tightly packed aggregates and survive in presence of a strong medium supply.** A. *Escherichia coli* bacteria were initially loaded in the bacterial confiner in presence of SYTOX Green, a DNA counterstain that fluorescently labels permeabilized dead bacteria (top). After 15 hours of proliferation, bacteria form a confined, tightly-packed aggregate without substantial bacterial death (bottom). B. Quantification of the death index in not confined (n = 48, N = 1) and confined chambers (n = 199, N = 1). Statistical analysis: Mann-Whitney test (p = 0.59). C. Fluorescent medium perfusion 1 minute (left) and 15 minutes (right) after fluorescence medium injection, in not confined (n = 3, N = 1) and confined aggregates (n = 2, N = 1). D. Quantification of medium renewal in not confined (blue) and confined (red) aggregates. Quantification of the mean fluorescence increase (fold change) in the chambers over time (top). Quantification of the normalized fluorescence increase in the chambers over time (bottom). *Time: hh:mm, Scale bars: 5µm.*

### 3.2.2 The number of bacteria as a readout of the growth-induced pressure

The image acquisition required to quantify growth-induced pressure over time does not allow us to image several fluorescent markers of key cellular structures at the same time (same wavelength than the fluorescent probe used to stain the PDMS walls and track their deformation), limiting our characterization of bacterial growth upon confinement. Therefore, I wondered whether we could use the number of bacteria as a readout of the growth-induced pressure.

By using the *E. coli* strain expressing the terminal domain of the ZipA protein fused to mCherry as a marker of the inner membrane, I was able to compute in the same experiment both the generated growth-induced pressure and the number of bacteria, the latter being a measurement of bacterial proliferation. We found that the onset of pressure build-up corresponds to an exponential increase in bacterial cell number within the chamber, which saturates to a plateau within 3 hours after confinement.

The temporal evolution of bacterial proliferation upon confinement can hence be described by three regimes in a highly reproducible manner (Figure 27C). In the first one, the number of bacteria increases exponentially due to proliferation in an unconstrained space. Around confluency, it deviates from the exponential growth curve because of the influence of the constrained environment (Figure 27C). More precisely, the number of bacteria still increases in the second regime, before reaching a plateau in the third one. To determine the two critical time points that mark out these regimes, I fitted the mean number of bacteria with a sigmoid curve classically used in population growth modeling (Figure 27C) *(Vandermeer, 2010)*and calculated the intersections of the tangent at the inflection point and the two asymptotes. The first critical time point ($t_1$) corresponds to the time at which the pressure builds up, and the second one ($t_2$) corresponds to the time around which the number of bacteria starts to plateau. This can be reformulated in the following way, with N being the number of bacteria in the chambers:

$$\begin{cases} N < N(t_1) : \text{Regime « Before confinement »} \\ N(t_1) < N < N(t_2) : \text{Regime « Early confinement »} \\ N > N(t_2) : \text{Regime « Late confinement »} \end{cases}$$

Thus, this analysis pipeline allows us to determine in which regime a bacterial aggregate at a given time point is, based only on the number of bacteria in it, providing us a simple way to interpret all our data.

A convenient way to relate the number of bacteria in the chambers with the pressure applied by bacterial proliferation is to plot the growth-induced pressure as a function of bacterial surface density, defined as the number of bacteria per unit area (Figure 27E). This curve is also characterized by three regimes, whose transitions are determined by the previous critical numbers of bacteria ($N(t_1) = 100$ and $N(t_2) = 500$).

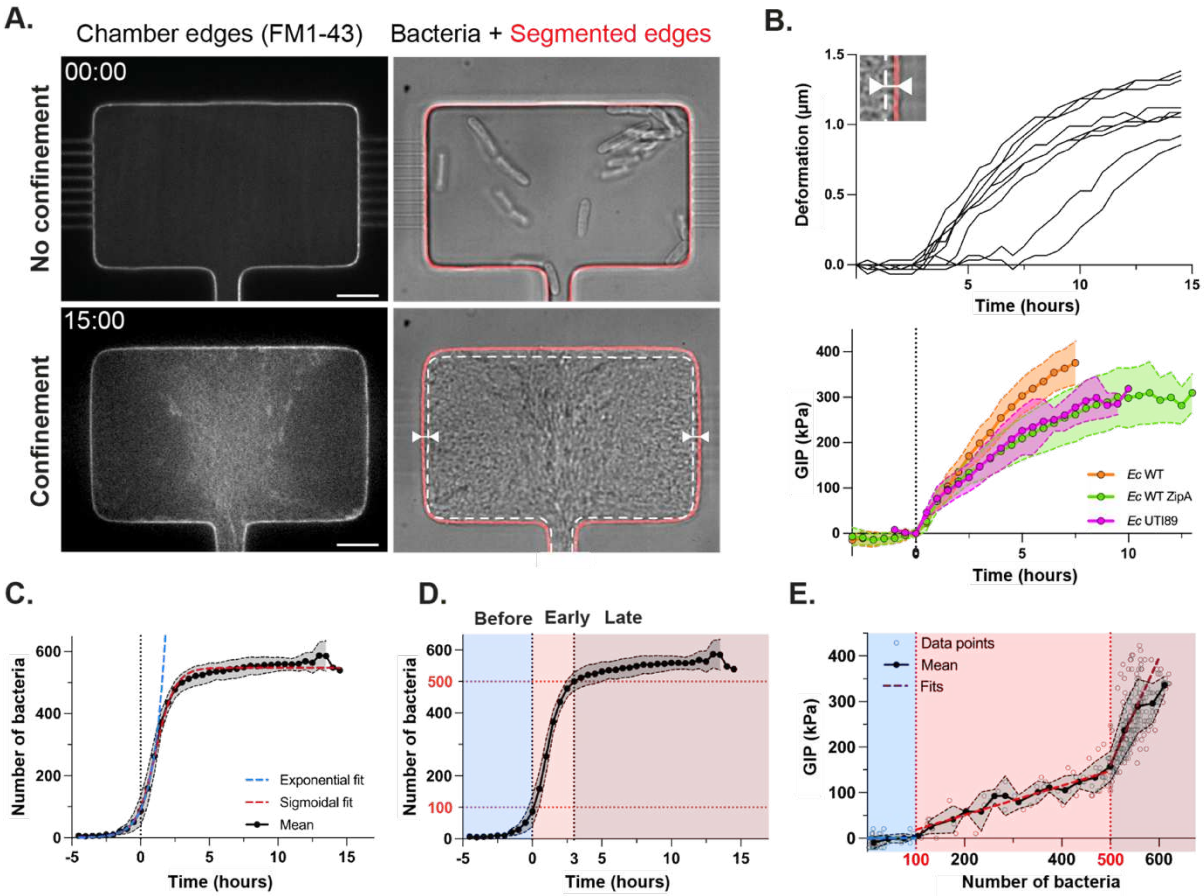


**Figure 27 : *Escherichia coli* proliferation upon confinement generates large forces.** A. Bacterial proliferation deforms the edges of the chambers, fluorescently stained with FM1-43 to facilitate the contour detection (red) over time. After 15 hours, the initial chamber contour is depicted in dashed white line and the corresponding deformation is represented by white arrows. *Time: hh:mm, Scale bars: 5µm.* B. Quantification of the chamber deformation over time (top) induced by the proliferation of *E. coli* MG1655 WT (n = 9, N = 1). Quantification of the growth-induced pressure (GIP, bottom) over time for three *E. coli* strains: MG1655 WT (n = 9, N = 1), MG1655 TM-ZipA-mCherry (n = 13, N = 3), and UTI89 WT (n = 5, N = 2). C. Quantification of the number of *E. coli* TM-ZipA-mCherry bacteria in the chambers over time (n = 13, N = 3). The vertical dashed line at time 0 corresponds to the time at which the GIP builds-up in the chambers. The mean number of bacteria is fitted with an exponential (dashed blue line) and a sigmoidal (dashed red line) curves. D. Definition of the three regimes "Before confinement" (blue), "Early confinement" (red) and "Late confinement" (dark red) based on the two critical numbers of bacteria determined by using the sigmoidal fit. E. GIP in function of the number of bacteria in the chambers. For each regime, a linear regression fit provides an equation that predicts the GIP generated by the aggregate using the number of bacteria as the sole input: GIP = 0 (N < 100), GIP = 0.3321N-13.59 (100 < N < 500, R2 = 0.93), GIP = 2.351N-1015 (N > 500, R2 = 0.99)

Using three linear regression fits, we get the equations that allow us to predict the growth-induced pressure in the chambers by using the number of bacteria as the sole input, which is a measurement easily doable in all the experiments without requiring additional fluorescent dye. For this reason, we used in the following the number of bacteria as a readout of the pressure applied in the chamber.

In sum, we showed that *E. coli* proliferation in the bacterial confiner generates a large pressure on the microenvironment and provided a simple way to investigate the emergence of physiological changes in regard to growth-induced pressure build-up by using the number of bacteria as a readout.

## 3.3 Bacterial adaptation to this new mechanical environment is characterized by a major morphological transition, leading to tiny cells

Next, we investigate how *E. coli* bacteria adapt their physiology to survive to the large forces exerted by their proliferation in a limited space.

### 3.3.1 Bacteria undergo strong cell shape changes upon confinement

#### 3.3.1.1 Characterization of bacterial morphology upon confinement

First, we wondered how bacterial shape is influenced by the new mechanical environment encountered by bacteria upon confinement. To this aim, I monitored the proliferation of the *E. coli* TM-ZipA-mCherry strain in the bacterial confiner over time using high-resolution microscopy (100X + Live-SR module) at 30 minutes frame rate and performed segmentation and tracking of single bacteria. I observed that once bacteria reach confluency in the chamber, they rapidly undergo multiple fast septation events, leading to the formation of tiny cells (Figure 28A). Yet, are these bacteria smaller than initially in the absence of confinement or do they orient in the vertical axis of the chamber as it has been reported in the case of biofilm growth *(Beroz et al., 2018; Nijjer et al., 2021; Zhang et al., 2021)*? To determine whether bacteria were verticalized or not upon confinement in the chambers, we imaged confined aggregates in Z-stack ($z_{step}$ = 0.1µm) using 3D Structured Illumination Microscopy (written SIM3D) and confirmed that confinement does not induce any preferential alignment of bacterial cells in the axial direction. Based on that, we decided to image and analyze one single bacterial layer, thereby limiting photobleaching and phototoxicity side effects (Figure 28B). By using the image analysis pipeline presented in the previous chapter, we were able to quantify changes in bacterial area over time, both in the absence and in the presence of confinement. In the absence of confinement, we noticed that the bacterial area is stable over time (Figure 28C).

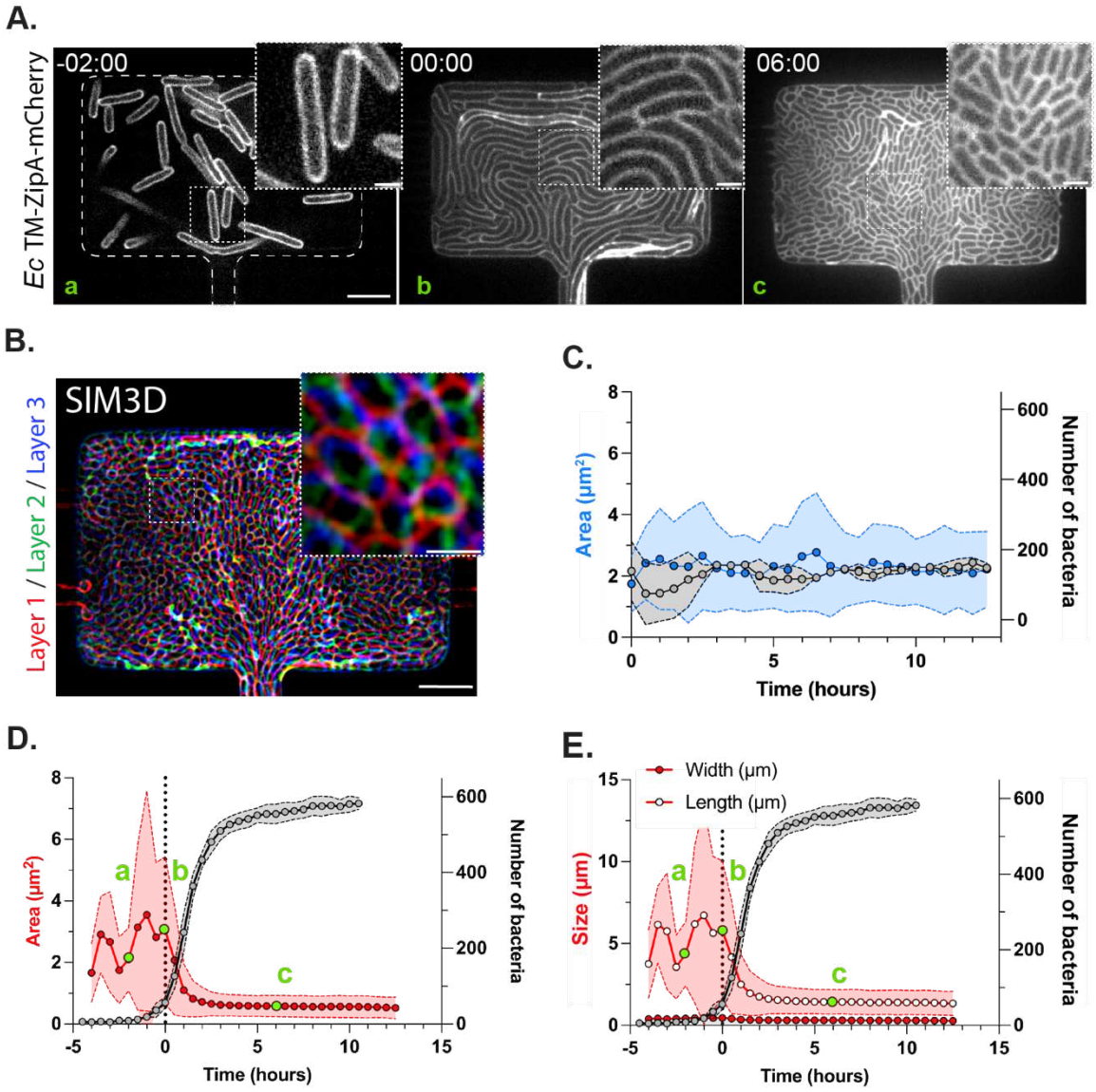


**Figure 28 : Bacterial physiology upon confinement is characterized by strong morphological changes.** A. Representative images of *E. coli* TM-ZipA-mCherry morphological changes upon confinement (a: before confinement, b: pressure build-up, c: 6 hours after pressure build-up). B. Overlay of the three first bacterial layers in the bacterial confiner imaged by SIM 3D. Inset: the first bacterial layer (red) does not superpose to the second (green) and third (blue) ones, meaning that bacteria in the focal plane (layer 1) are mostly not verticalized in the chambers. Pearson correlation coefficient between the first and second layer < 0.2. C. Quantification of bacterial area (blue) in absence of confinement in regard to the number of bacteria (grey)in the chambers (n = 2, N = 1). D. Quantification of bacterial area (red) over time in regard to the number of bacteria (grey) in the chambers (n = 4, N = 2). The vertical dashed line at time 0 represents the time at which the pressure builds-up in the chamber. The three representative images of *E. coli* TM-ZipA-mCherry morphological changes shown in A. are represented in green. E. Quantification of bacterial length (white dots) and width (red dots) over time in regard to the number of bacteria (grey) in the chambers (n = 4, N = 2). *Time: hh:mm. Scale bars insets: 1µm. Scale bars chambers: 5µm.*

By contrast, upon confinement, we surprisingly found that, as soon as the pressure builds up, bacterial area drops until reaching a highly stable minimal size in 3 hours only! On average, these tiny cells are characterized by an area 5 times smaller than their mean area in the absence of confinement in the chambers (Figure 28D). Of note, the bacterial area decreases only by a factor of 3 with respect to the bacterial initial size, just after the chip loading. Indeed, I noticed that bacteria progressively increase in size before the chamber reaches confluency, probably due to the flow.
By looking more specifically at changes in length and width, we found that cell length is the major contributor to this morphological transition (Figure 28E), meaning that compressive stresses induce bacterial synchronization and shortening but still conserve their rod shape under confinement.

#### 3.3.1.2 Confinement-induced morphological changes from the one occurring during the stationary phase

Next, we wondered whether other *E. coli* strains also undergo similar morphological changes during growth upon confinement. To this end, I used two other *E. coli* strains, including a MG1655 strain with a cytoplasmic staining and the UTI89 uropathogenic one, and monitored their proliferation in the bacterial confiner. I observed that similar morphological changes also occur upon confinement for both the MG1655 strain (Figure 29A) and the uropathogenic one (Figure 29B), showing that this is a general feature of *Escherichia coli* growth upon confinement. By manually segmenting the cytoplasmic signal, we noticed that bacterial area decrease upon confinement is slightly more pronounced for the WT and UTI89 bacterial strains than the TM-ZipA-mCherry one (Figure 29C), suggesting that the TM-ZipA-mCherry strain is slightly deficient with regard to bacterial division. Yet, since the TM-ZipA-mCherry bacterial strain is required to semi-automatically quantify bacterial adaptation to confinement, I chose to still rely on this strain for the following experiments, while keeping in mind that our observations are likely even more pronounced during infection.

To better understand the origin of these morphological changes, we compared the area of confined *E. coli* TM-ZipA-mCherry bacteria with the one of bacteria in exponential and stationary phases on agar pads, as a classical assay to characterize bacterial morphology in standard growth conditions. Interestingly, we found that, while the TM-ZipA-mCherry bacteria loaded in the chamber have an area similar to the one in the exponential phase, their area under confinement is much lower than the one in stationary phase (Figure 29C), showing that the morphological changes we described are distinct from those occurring upon entry into stationary phase.

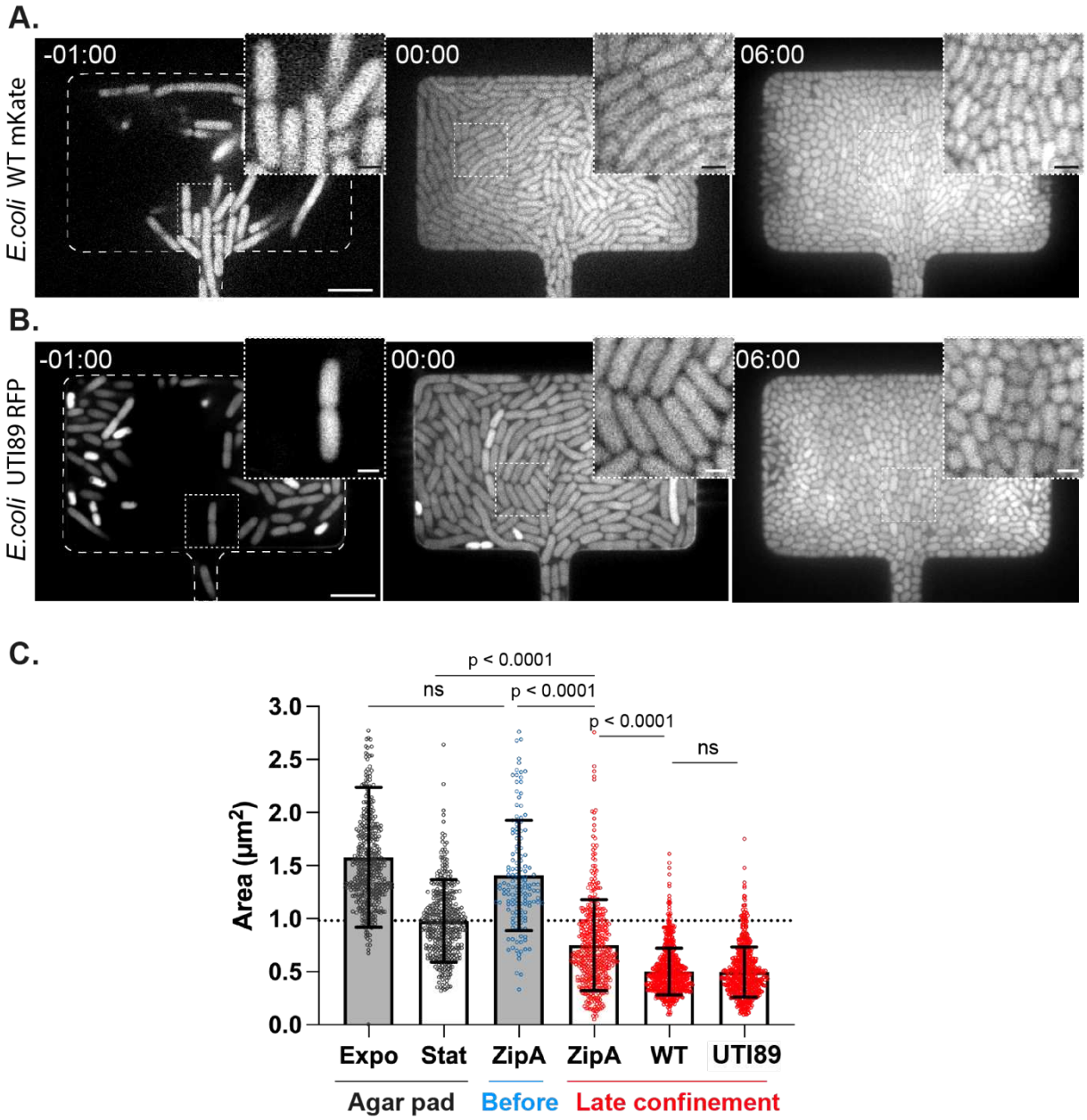


**Figure 29 : *Escherichia coli* bacteria generally adapt to confinement through morphological changes**. A. Representative images of Escherichia coli WT mKate morphological changes upon confinement. B. Representative images of uropathogenic Escherichia coli morphological changes upon confinement. C. Area distribution of single Escherichia coli ZipA-mCherry bacteria in exponential and stationary phases on agar pad (grey), before confinement in the bacterial confiner (blue) and upon confinement in the bacterial confiner (red – ZipA). Escherichia coli ZipA-mCherry bacterial area upon confinement is compared to Escherichia coli WT mKate (red – WT) and Escherichia coli UTI89 RFP area (red – UPEC). Statistical analysis: Kruskal-Wallis tests (Expo vs. Stat: $p = 0.77$, WT vs. UTI89: $p > 0.99$, other: $p > 0.0001$). *Time: hh:mm. Scale bars insets: 1µm. Scale bars chambers: 5µm.*

#### 3.3.1.3 A reversible morphological transition upon pressure release

To further confirm that these morphological changes were induced by the mechanical environment, I monitored bacterial morphology when the bacterial aggregate was destabilized and slipped out from the chambers. Interestingly, I observed that, as soon as the pressure is released, bacteria rapidly regrow (Figure 30A) for 2 hours until they almost recover their initial size (Figure 30B), which highlights a reversible morphological transition.

Together, we showed here that *E. coli* bacteria adapt to mechanical confinement through reversible morphological changes, mainly characterized by a strong shortening of the rods. These results raise the question of how this transition occurs, whether it is via a compression-mediated loss of bacterial volume or an active remodeling of bacterial shape mediated by growth and division.

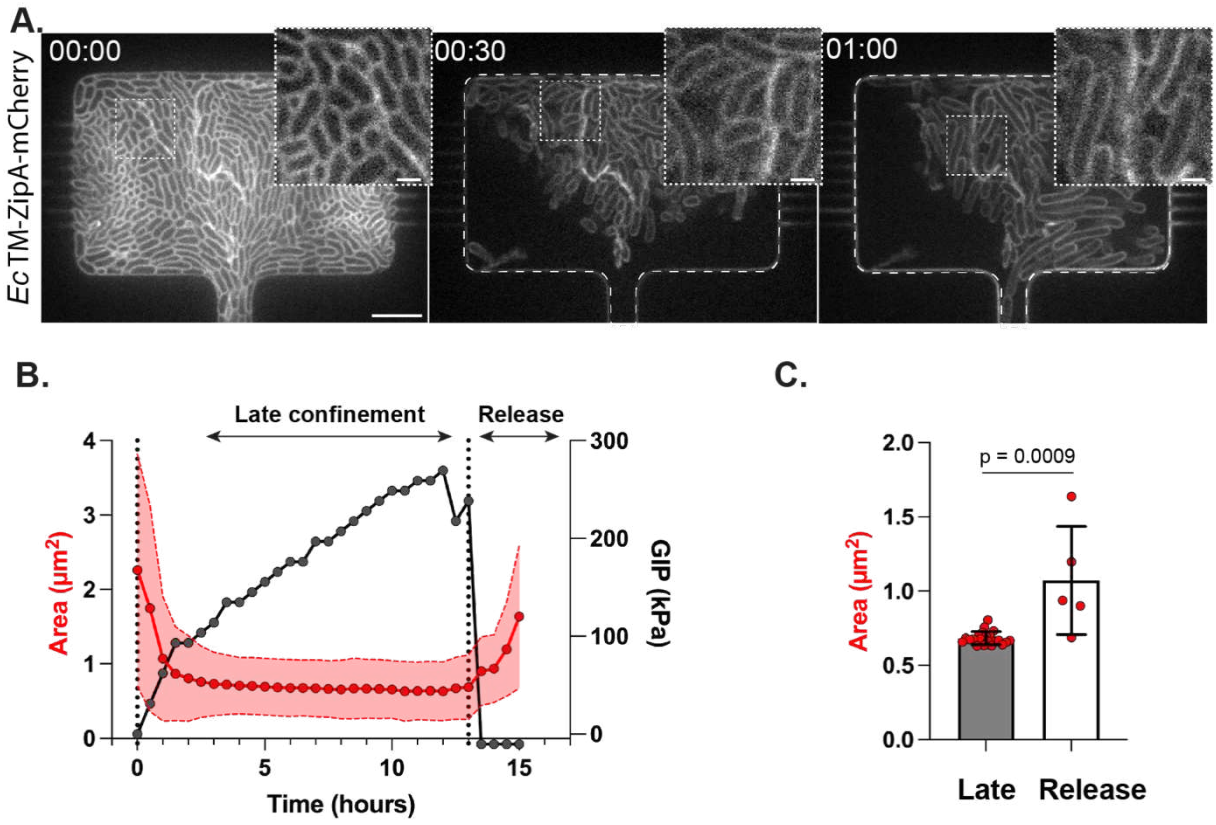


**Figure 30 : Confinement-induced morphological changes are reversible upon pressure release**. A. Representative images of *Escherichia coli* TM-ZipA-mCherry morphological changes upon confinement release. Time 0 corresponds to the last time point at which the aggregate is confined. B. Quantification of bacterial are and growth-induced pressure over time, upon confinement release (n = 1, N = 1). The dashed line at time 0 (resp. 13) corresponds to pressure build-up (resp. release). C. Mean area distributions during late confinement, and confinement release. Statistical analysis: Mann-Whitney test (p = 0.0009). *Time: hh:mm. Scale bars insets: 1µm. Scale bars chamber: 5µm.*

## 3.4 Mechanical confinement induces an uncoupling between growth and division, leading to growth and division arrest

In this part, we define growth as the process during which a bacterium increases in size, and division as the process during which a bacterium physically separates into two daughter cells.

### 3.4.1 Relation between growth and division upon confinement

To query how mechanical confinement induces such morphological changes, I wondered how growth and division are regulated in this peculiar mechanical environment. Indeed, while *E. coli* growth and division are coupled in normal conditions through a cell size control of division *(Campos et al., 2014; Robert et al., 2014; Si et al., 2019; Taheri-Araghi et al., 2014; Willis and Huang, 2017)*, I hypothesized that a division rate exceeding the growth rate would instead lead to smaller cells. To verify this hypothesis, I monitored the proliferation of *E. coli* TM-ZipA-mCherry bacteria at 5 minutes frame rate in the bacterial confiner. I used a shorter timestep to have a larger sampling of bacterial fate, allowing single-cell tracking over time. For each bacterial lineage, I defined the division time as the duration required from birth to division completion, the division rate as the inverse of the division time, and the growth rate as the increase in bacterial area between bacterial birth and division completion. This can be reformulated in the following way, with t being a given timestep:

$$\begin{cases} \text{Division time (in minute)} = \mathrm{t(division)} - \mathrm{t(birth)} \\ \text{Division rate (number of divisions per minute)} = \dfrac{1}{\text{division time}} = \dfrac{1}{\mathrm{t(division)-t(birth)}} \\ \text{Growth rate (area increase per minute)} = \dfrac{\mathrm{Area(division)-Area(birth)}}{\mathrm{t(division)-t(birth)}} = \dfrac{\mathrm{Area(division)} - \mathrm{Area(birth)}}{\text{division time}} \end{cases}$$

Using these parameters, I characterized bacterial growth in the bacterial confiner and compared the values before confinement to growth in normal conditions on agar pads, as a control to verify the consistency of the results. By plotting these parameters over time in regard to the growth-induced pressure build-up in the chamber, I observed that, while the division time before confinement is in agreement with the control on agar pad, it slightly decreases at the onset of confinement for half an hour, before suddenly increasing (Figure 31A). This corresponds to a sudden increase in the fraction of non-dividing bacteria in the chambers (Figure 31A), meaning that once the pressure builds up, bacteria divide for a while and then suddenly stop dividing.
To further understand how this change in cell cycle duration could result in morphological changes, we compared the growth and division rates. Strikingly, by contrast with growth before confinement (Figure 31B), I found that growth and division rates do not follow the same trend upon confinement (Figure 31C).

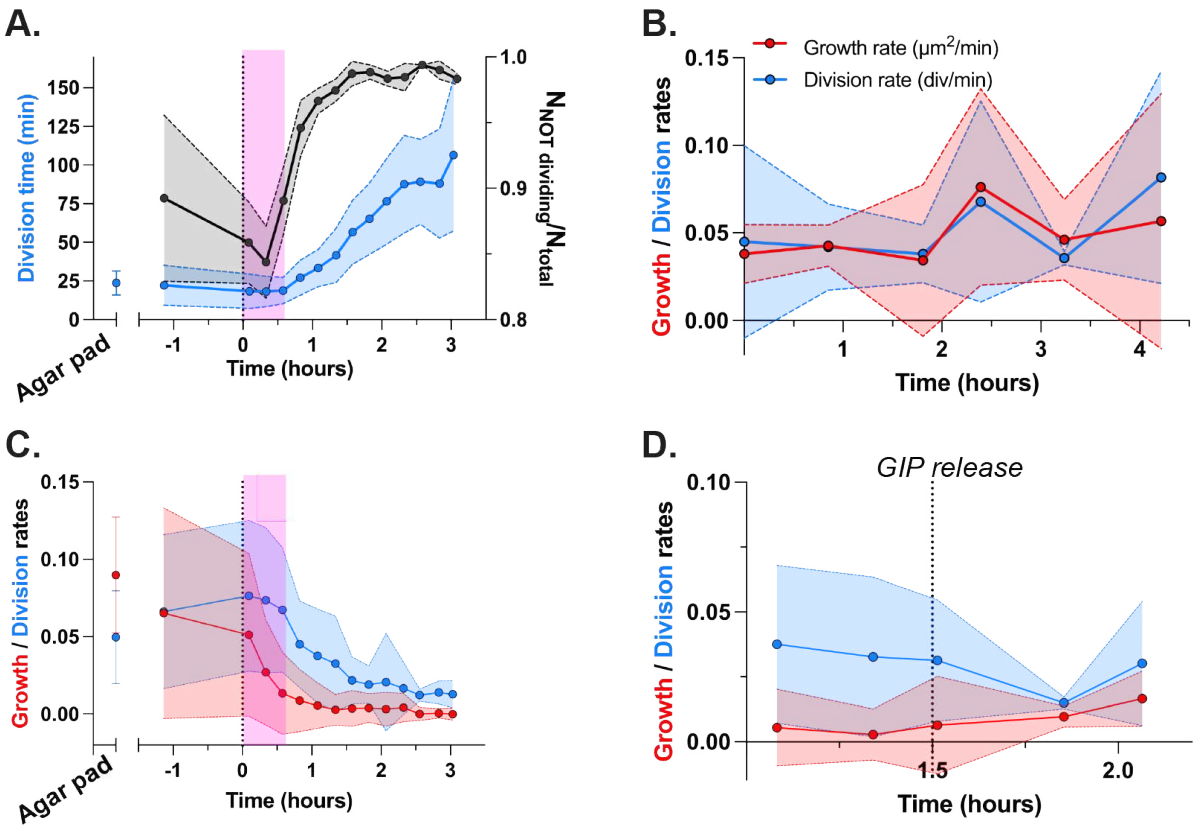


**Figure 31 : Mechanical confinement uncouples growth and division, leading to reversible growth and division arrests.** A. Quantification of the division time in the bacterial confiner over time (n = 3, N = 2). The mean value before confinement is compared to the one on agar pad as a control. Quantification of the fraction of not dividing bacteria in the chambers (n = 3, N = 2). B. Quantification of growth (red) and division (blue) rates in absence of confinement over time (n = 3, N = 2). C. Quantification of growth (red) and division (blue) rates upon confinement over time (n = 3, N = 2). The mean values before confinement are compared to the ones on agar pad as a control. The magenta area depicts the time at which the division time is stable in A. D. Quantifications of growth (red) and division (blue) rates upon pressure release in the bacterial confiner (n = 1, N = 1).

More precisely, at the onset of confinement, the division rate increases, while the growth rate decreases due to the lack of space. After pressure builds up, the division rate remains high for half an hour, while the growth rate drops. Then, both rates decrease until reaching values close to zero although the division rate stays higher than the growth one. Consequently, after the pressure builds up in the chamber, bacteria divide more rapidly while growing less in size due to the lack of space, leading to the formation of non-dividing and non-growing tiny cells.

To confirm that these growth and division arrests were induced by mechanical constraints, we computed the growth and division rates upon pressure release. I observed that the growth rate immediately starts to increase after the pressure drops while it takes half an hour more for the division rate to increase (Figure 31D). This shows that bacteria rapidly start to regrow and then progressively divide upon confinement release, allowing bacteria to progressively recover their homeostatic size.

### 3.4.2 Dynamics of the divisome machinery upon confinement

To better understand the uncoupling between growth and division, in particular how confinement induces a fast synchronization of division events within the bacterial community followed by growth and division arrest, I wondered how compressive forces impact the divisome machinery. I noticed that the division time exhibits an intriguing evolution upon confinement, characterized by a first slight decrease during half an hour, followed by a sharp increase reminiscent of division arrest (Figure 31A). Since the formation of a FtsZ ring at the division site is the earliest event leading to bacterial division *(Harry et al., 2006)*, I first hypothesized that this transition could be mediated by the incapacity of the bacteria to assemble the FtsZ ring. To address this question, I used an *E. coli* TM-ZipA-mCherry strain expressing a FtsZ-GFP fusion under the lac promoter (see Materials & Methods, part 1.1 - original strain from Margolin's lab kindly provided by J.Bos). I monitored the proliferation of this strain under confinement at 5 minutes frame rate and followed FtsZ rings assembly over time (Figure 32A). Interestingly, I observed the presence of numerous division rings upon confinement (Figure 32A), showing that FtsZ filaments still assemble into division rings upon confinement.

So, if Z-rings still assemble upon confinement, why do bacteria rapidly stop dividing? By taking a closer look at the raw images, I noticed that, although some FtsZ ring assemblies lead to bacterial septation (Figure 32B - top), others do not (Figure 32B - bottom). In this case, the FtsZ rings seem to be destabilized before membrane constriction, either by slipping or ring depolymerization, suggesting the presence of a mechanism preventing bacterial division. Of note, these experiments will be replicated by using a strain expressing an endogenous FtsZ fusion protein to confirm these observations.

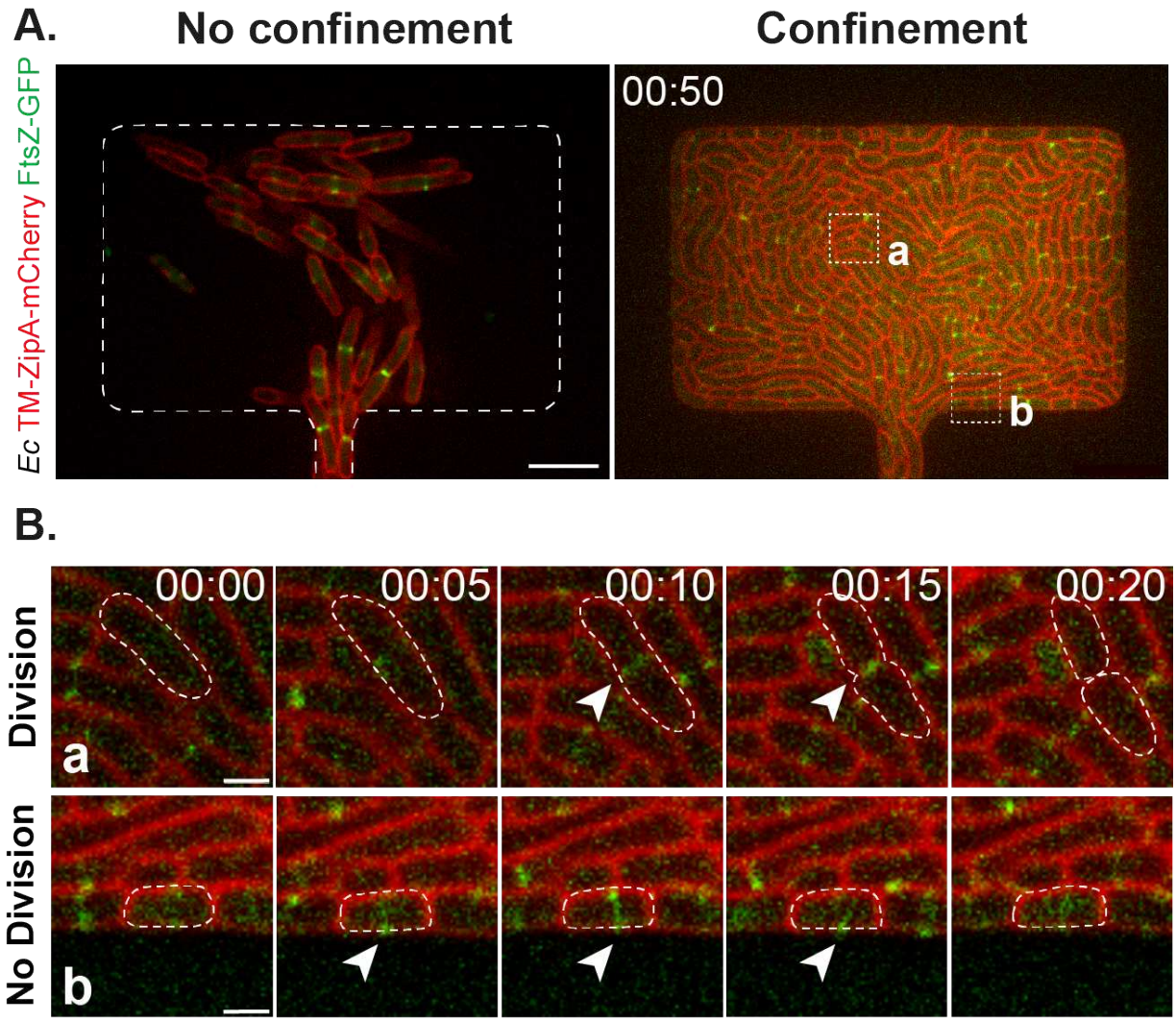


**Figure 32 : Mechanical confinement often impairs bacterial division by hindering Z-ring constriction.** A. Representative image of *Escherichia coli* TM-ZipA-mCherry (red) FtsZ-GFP (green) before confinement (left) and upon confinement, 50 minutes after pressure build-up (right). Two regions of interest (a and b) are depicted by squares in white dashed lines. *Scale bar: 5µm.* B. Dynamics of FtsZ ring formation upon confinement over 20 minutes for the two regions of interest (a and b) depicted in A. The bacterium of interest is depicted by a white dashed line. FtsZ rings are identified with white arrows. *Scale bars: 1µm.*

Altogether, we showed here that mechanical confinement leads to strong morphological changes by uncoupling growth and division. While the lack of space hinders bacterial growth, it seems on the contrary to accelerate bacterial division before arresting it reversibly, raising the question of the mechanism(s) regulating bacterial division upon confinement.

## 3.5 Which mechanisms regulate bacterial division upon confinement?

In this part of the study, we dissected the mechanism(s) that regulate(s) bacterial division during growth in a limited space.

### 3.5.1 Bacterial stress mapping

A potential mechanism used by bacteria to detect compressive mechanical signals is via the activation of a specific stress response. To test this hypothesis, we confined bacteria expressing a series of transcriptional reporters as stress readouts at the level of key subcellular structures, as recapitulated in Table 4 (Figure 33A). Fluorescence induction of each reporter was first verified upon chemical stress at the population level using an automatic plate reader (see Materials & Methods - 1.4).

| *Reporter* | *Stress* | *Expression* | *Chemical inducer* |
|---|---|---|---|
| $P_{rcsA}$-*GFP* | OM | Plasmidic | Cephalexin |
| $P_{cpxP}$-*mEGFP* | IM / Periplasm | Chromosomic | Cephalexin |
| $P_{ibpA}$-*YFP* | Protein misfolding | Chromosomic | Streptomycin |
| $P_{recA}$-*YFP* | DNA damage | Chromosomic | Ciprofloxacin |
| $P_{yiaG}$-*YFP* | Growth arrest | Chromosomic | - |

**Table 4 : Overview of the transcriptional reporters tested upon chemical and mechanical stresses.**

To determine whether these stress responses are activated upon confinement, I monitored the eventual fluorescence induction of *E. coli* TM-ZipA-mCherry bacterial strains expressing the stress reporters during growth in the bacterial confiner. To quantify these experiments, we computed, for each stress, the fluorescence histogram of all the individual bacteria in not confined chambers, fitted the histogram with a Gaussian curve (characterized by a mean $\mu$ and a standard deviation $\sigma$) and defined a fluorescence threshold at $\mu + 2.5\sigma$. This threshold represents the fluorescence value above which the stress is considered as activated, i.e. the bacteria are positive to the targeted stress. Then, we used this threshold value to calculate the number of bacteria that are positive to the targeted stress over time upon confinement (Figure 33B). Interestingly, I found that all the stress responses are activated upon confinement (Figure 33C, D, E, F), except DNA damage (Figure 33G). Of note, each transcriptional response is characterized by a highly reproducible spatial pattern and temporal kinetics, reminiscent of a global reprogramming of a multicellular assembly.

This is similar to the process of cell differentiation during embryo development, and raises the question of how this complex, heterogeneous stress induction impacts bacterial adaptation and survival to confinement.
In particular, I noticed that the Rcs-mediated envelope stress response is activated as soon as the pressure is generated in the chambers (Figure 33C), while the other ones are activated 30 minutes after (Figure 33D, E, F). This points out that the Rcs stress response could be an upstream sensor favoring bacterial adaptation to pressure build-up in agreement with recent unpublished works *(Mason and Rojas, 2022; Zietek et al., 2022)*.

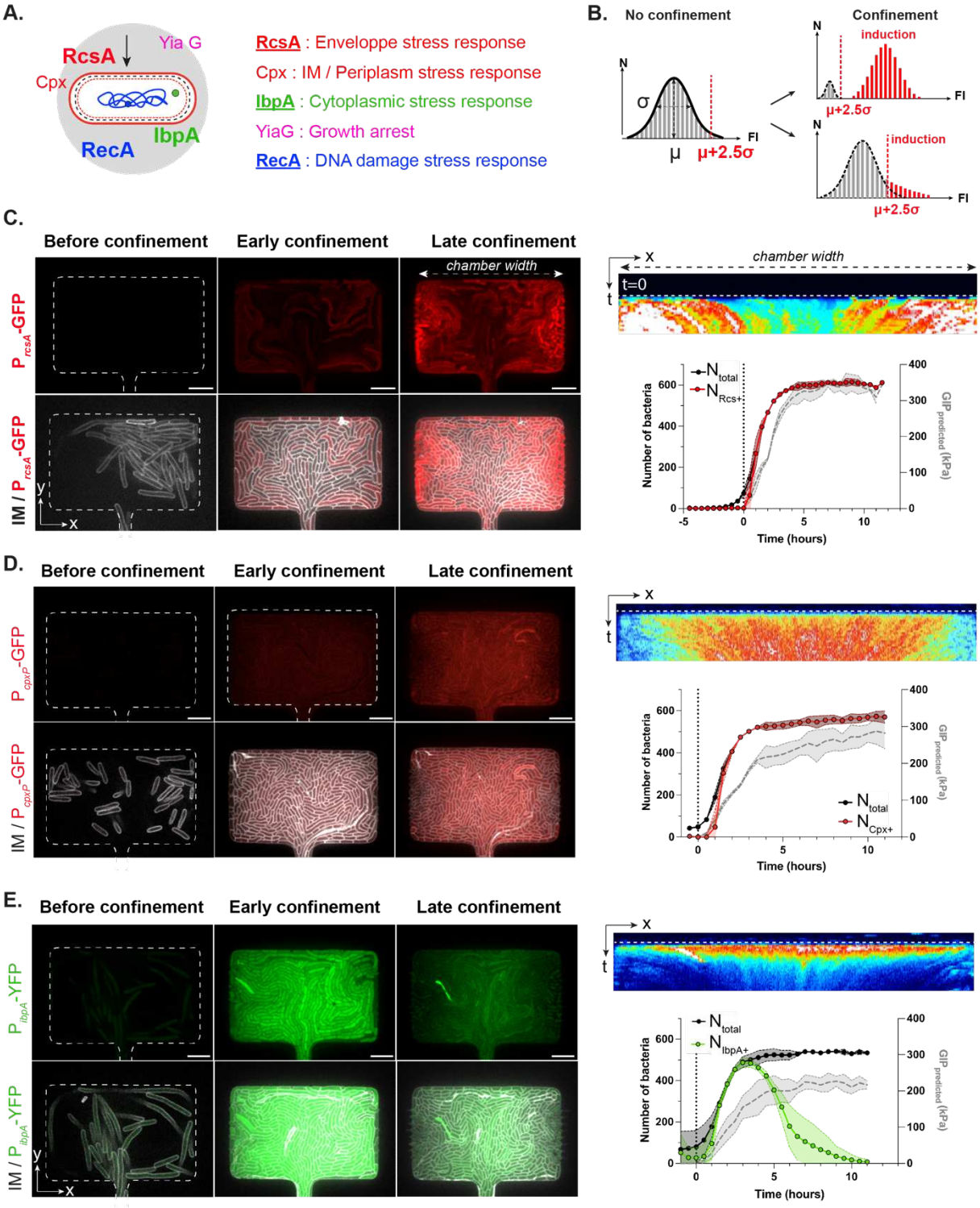
A.
RcsA
Yia G
Cpx
IbpA
RecA
RcsA : Enveloppe stress response
Cpx : IM / Periplasm stress response
IbpA : Cytoplasmic stress response
YiaG : Growth arrest
RecA : DNA damage stress response
B.
No confinement
Confinement
induction
μ+2.5σ
C.
Before confinement
Early confinement
Late confinement
chamber width
t=0
Number of bacteria
Time (hours)
D.
E.

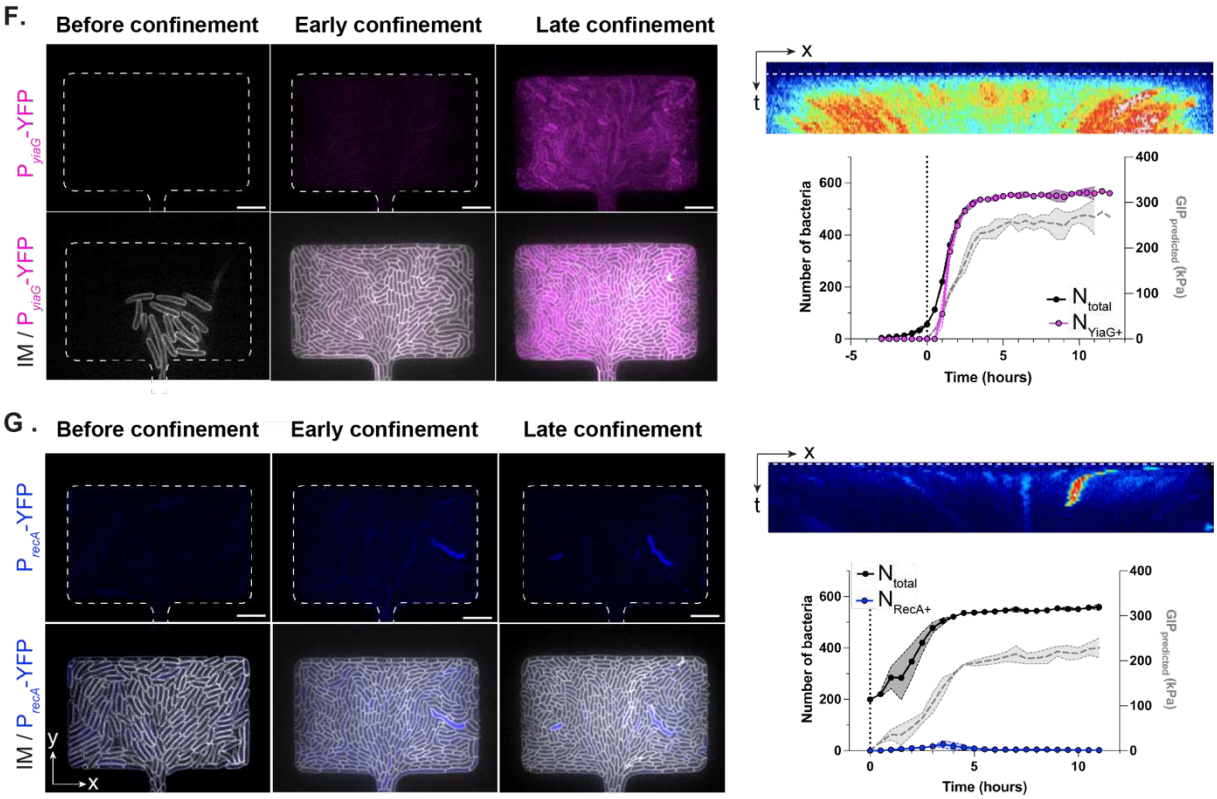


**Figure 33 : Bacterial physiology upon confinement is characterized by a strong transcriptional reprogramming.** A. Overview of the transcriptional reporters used to assess stress responses activation at various levels of the envelope architecture. B. Quantification pipeline used to quantify the number of bacteria that are positive to a targeted stress. Mean fluorescence distribution in absence of confinement is fitted with a gaussian curve, characterized by a mean μ and a standard deviation sigma. The threshold value is defined at μ + 2.5 sigma. Upon confinement, the mean fluorescence intensity distribution either exhibit a two separated gaussian shape, or a single prolonged one. In these two cases, bacteria that have a mean fluorescence intensity higher than the threshold value are considered as positive to the targeted stress. C. Representative images of Rcs-mediated fluorescence intensity (top, left - red) together with the overlay signal with the bacterial membrane (top, bottom - grey) before confinement (left), and upon early (middle) and late (right) confinement. Kymograph of the Rcs-mediated fluorescence induction over the width of the chamber (horizontal axis) and over time (vertical axis). The white dashed line corresponds to the time at which the pressure builds up (Time 0) in the chamber (top, right). Quantification of the number of bacteria that are positive to the Rcs stress (red) in regard to the total number of bacteria in the chamber (black) and the predicted growth-induced pressure (dashed grey) (n = 3, N = 1). D, Same than C. for the Cpx-mediated cytoplasmic stress response (n = 3, N = 1). E. Same than C. for the IbpA-mediated DNA damage stress response (n = 3, N = 1). F. Same than C. for the YiaG-mediated inner membrane and periplasmic stress response (n = 3, N = 1). G. Same than C. for the RecA-mediated growth arrest stress response (n = 3, N = 1). *Scale bars: 5μm.*

### 3.5.2 A role for the Rcs envelope stress response?

Based on the previous results, we first hypothesized that the Rcs envelope stress response could mediate bacterial adaptation to confinement as a first line of defense, by positively regulating bacterial division, as it has previously been reported *(Carballès et al., 1999)*. To explore this question, I used in this part *E. coli* Δ*rcsB* strains. First, I characterized the proliferation upon confinement of a Δ*rcsB* mutant by quantifying the growth-induced pressure build-up and the death index. I found that the Δ*rcsB* mutant generates a similar growth-induced pressure to the WT strain (Figure 34A), yet with a defect in bacterial survival mostly at the edges of the chamber (Figure 34B).

Then, to decipher whether the Rcs phosphorelay plays a role in the regulation of bacterial division upon confinement, I constructed an *E. coli* TM-ZipA-mCherry Δ*rcsB* strain (see Material & Methods - 1.2.2), monitored its proliferation in the bacterial confiner. I noticed that while bacteria grow in the absence of confinement without substantial changes in cell size, they exhibit abnormal blebbing shapes upon confinement, at the edges of the chambers, near the feeding nanochannels (Figure 34C). I then quantified the average changes in bacterial area in regard to pressure build-up. At the population level, I found that, once the pressure builds up in the chamber, the mean area follows the same trend from the mutant and the WT strain, while the dispersion of the values increases upon confinement (Figure 34D).

To go further, I quantified the heterogeneities in bacterial number (Figure 34E) and bacterial area within the chambers (Figure 34F). To this end, we defined one region "center" and one region "edges" based on the Rcs induction pattern, which is mostly located at the chamber boundaries, close to the nanochannel entries (Figure 33C). This heterogeneity analysis was motivated by the following observation: at the edges of the chamber (*i.e.* where Rcs is the most expressed), the Δ*rcsB* mutant exhibits blebbing shapes with large areas, whereas at the center of the chamber (*i.e.* where Rcs is less expressed), bacteria maintain their rod shape characterized by small areas (Figure 34C). These observations were confirmed by quantifications. We found that, while the bacterial number follows the same trend between the WT and the Δ*rcsB* strains at the center than at the edges, this is not the case for the bacterial mean area. In the WT strain, the bacterial mean area is small and similar both at the edges and at the center, whereas in the Δ*rcsB* strain, the bacterial mean area is small at the center but large at the edges. This shows that, while the Rcs pathway is important for bacterial survival and shape maintenance at the edges of the chambers where bacteria are the most proliferative, it is not responsible for triggering bacterial division in the center of the aggregate, thereby emphasizing the idea that the Rcs pathway cannot be the only player responsible for triggering division upon pressure build-up.

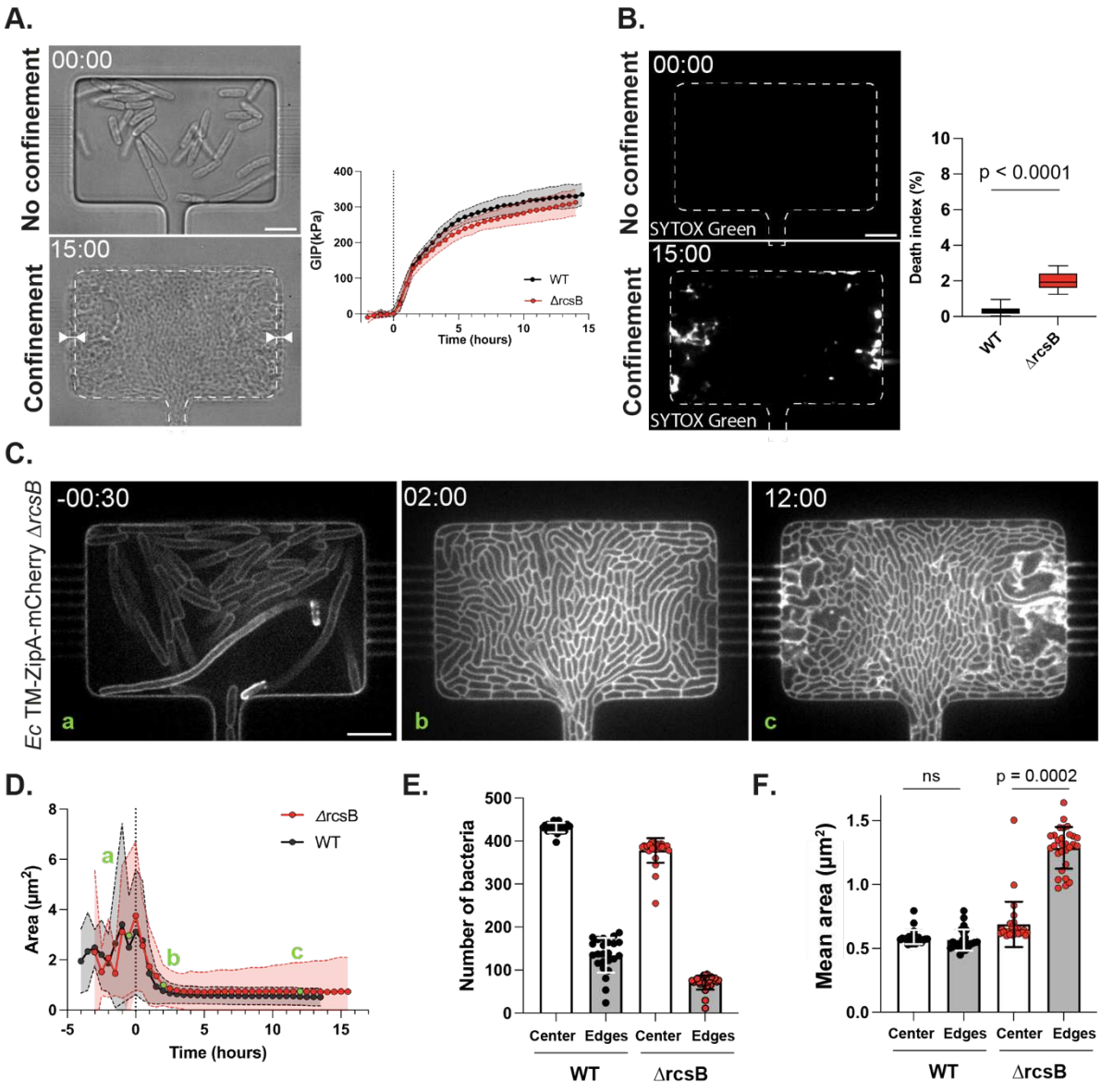


**Figure 34: The Rcs envelope stress response favors bacterial survival and shape maintenance upon confinement at the edges of the chamber, where bacteria are much more proliferative, but not in the center.** A. *Escherichia coli* Δ*rcsB* strain deforms the chambers during their growth upon confinement over 15 hours (left, depicted by a white arrow). This deformation corresponds to the build-up of growth-induced pressure (n = 25, N = 1), which is slightly lower than the WT strain (right) (n = 17, N = 1). B. Upon confinement, *Escherichia coli* Δ*rcsB* strain is permeable to the DNA intercalant SYTOX Green at the edges of the chamber, meaning that bacterial viability is compromised at the edges (left). Quantification of the death index at the population level for the WT and the Δ*rcsB* strains (right) (n = 12, N = 1). C. Proliferation of the *Escherichia coli* TM-ZipA-mCherry Δ*rcsB* strain in the bacterial confiner. D. Quantification of *Escherichia coli* TM-ZipA-mCherry Δ*rcsB* (n = 2, N = 1) and WT (n = 4, N = 2) area over the whole chamber over time. Time 0 corresponds to the time at which the pressure builds-up. E. Quantification of the number of bacteria at the center vs. at the edges of the chambers for the WT and the ΔrcsB strains (n = 2, N = 1). F. Quantification of the mean bacterial area at the center vs. at the edges of the chambers for the WT and the Δ*rcsB* strains (n = 2, N = 1). Statistical analyses: Kruskal-Wallis tests. *Time hh:mm. Scale bars: 5μm.*

### 3.5.3 A role for cytoplasmic crowding?

In search of another mechanism used by bacteria to regulate division, we hypothesized that an increase in cytoplasmic crowding, resulting from an uncoupling between growth and protein synthesis, could also perturb bacterial division in two ways. First, an increase in crowding could increase cytoplasmic protein concentrations, including FtsZ, potentially triggering bacterial division. Second, a further increment in crowding could also perturb protein folding and/or diffusion in the cytoplasm, thereby delaying or even preventing divisome recruitment at the division site.

To explore this hypothesis, we have expressed the 40nm-wide Genetically Encoded Multimeric nanoparticles (written GEMs) *(Delarue et al., 2018)* into *Escherichia coli* cytoplasm and used their diffusive motion as a readout of cytoplasmic crowding. These nanoparticles have a size close to the one of a ribosome, so that their diffusive motion also gives us a quantification of protein dynamics within the cytoplasm. First, I have characterized GEMs diffusion in *E. coli* in normal growth conditions. To this end, I performed agar pad experiments and imaged GEMs diffusion using stream high-resolution acquisitions (100X + Live-SR module) with a stream time of 50ms during 2.5s. Then, I tracked GEMs trajectories using the Fiji plugin MOSAIC (Figure 35A), computed the mean-squared displacements, and estimated the corresponding distribution of diffusive coefficients (Figure 35B), using a MATLAB script previously developed by Morgan Delarue during his post-doc. By using this pipeline, I found a median diffusion coefficient value equal to 0.05µm$^2$/s (Figure 35C), which is, as expected, lower than the one computed for yeasts (D ~ 0.3 µm$^2$/s - *(Delarue et al., 2018)* and mammalian cells (D ~ 0.5 µm$^2$/s - *Delarue et al., 2018*) *(Mika and Poolman, 2011)*. To better understand the meaning of this value, I performed hyperosmotic shocks to artificially crowd the bacterial cytoplasm of the *E. coli* XL1Blue strain by increasing the osmolarity of the medium. Interestingly, the diffusion coefficient decreases the more the bacteria are crowded (i.e. the more the osmolarity of the medium increases) until reaching a plateau around 0.025 µm$^2$/s (Figure 35D), showing that GEMs are a suitable tool to study changes in cytoplasmic crowding and their influence on proteins dynamics.

I then took advantage of this tool to quantify changes in cytoplasmic crowding upon confinement. To this end, I loaded the *E. coli* TM-ZipA-mCherry GEM40 strain in the bacterial confiner and imaged GEMs diffusion at three time points (30 minutes after the loading, 5 hours later, and 7 hours later) to avoid phototoxicity side effects. By using the number of bacteria in the chambers, I was able to quantify the distribution of diffusive coefficient for the three regimes "Before confinement", "Early confinement" (*i.e.* from the onset of confinement to 3 hours after pressure build-up), and "Late confinement" (*i.e.* more than 3 hours after pressure build-up) (Figure 36A).

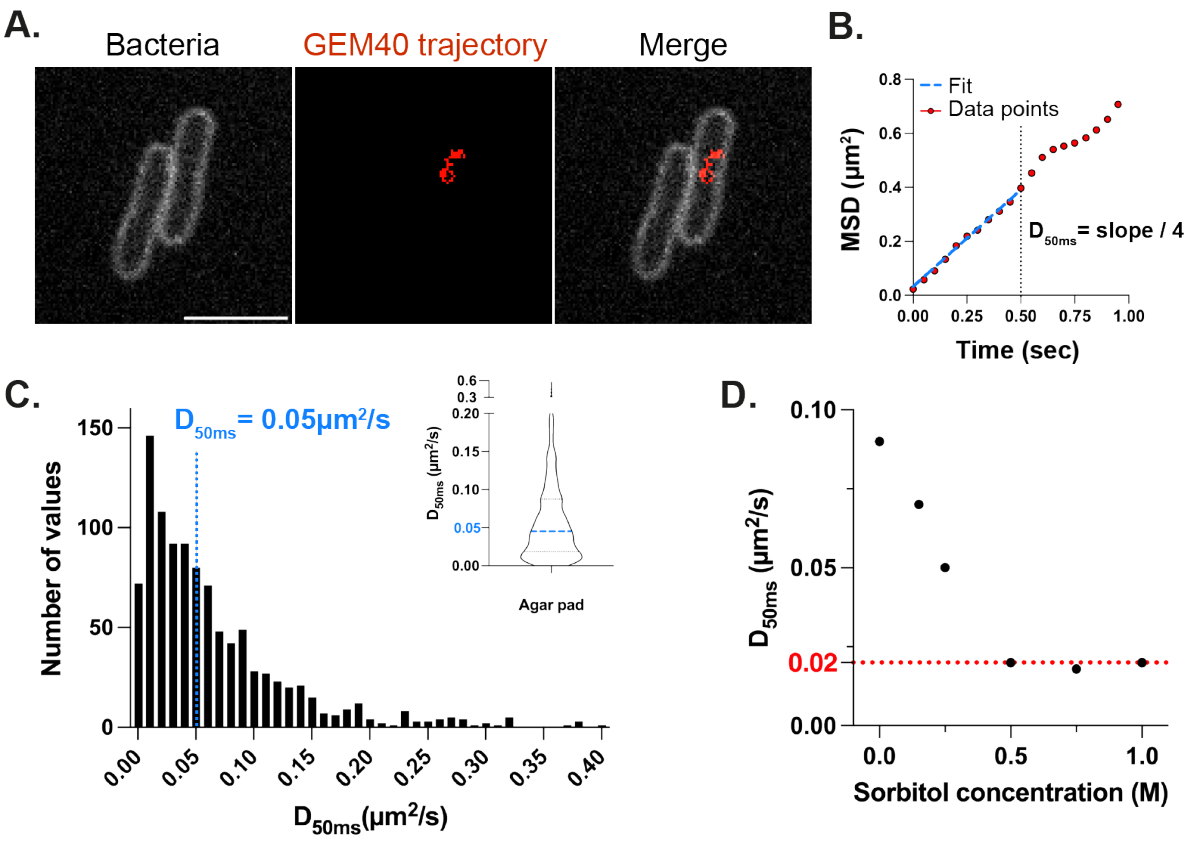


**Figure 35: Characterization of GEM40 diffusion within the cytoplasm as a way to assess change in cytoplasmic crowding.** A. *Escherichia coli* TM-ZipA-mCherry GEM40 are imaged with a 50ms stream time under agar pad (left) to facilitate GEM trajectory detection (middle) within the cytoplasm (overlay – right). *Scale bar: 5µm*. B. Analysis pipeline used to compute GEM40 diffusion coefficient. For each single trajectories, GEM40 diffusive motion is characterized by calculating the Mean Squared Displacement (MSD), from which the corresponding diffusion coefficient is inferred. C. Distribution of diffusion coefficient measured with a 50ms stream time ($n_{tracks}$ = 1020, N = 2). The median value is depicted in blue. Inset: Violin representation of the diffusion coefficient distribution. D. GEM40 diffusion coefficient as a function of the concentration of sorbitol added in the culture medium (0M: n = 818, N = 3 / 0.15M: n = 160, N = 7 / 0.25M: n = 217, N = 7 / 0.5M: n = 142, N = 7 / 0.75M: n = 152, N = 7 / 1M: n = 125, N = 3) In D. only: experiments and analysis have been performed with the *Escherichia coli* XL1Blue GEM40 strain.

I found that, while the distribution of diffusive coefficients before confinement is close to the control on agar pad, the distribution is already flattened in "Early confinement" without substantial changes in "Late confinement" (Figure 36B). Interestingly, the median diffusion coefficient drops to 0.015μm$^2$/s upon confinement, which corresponds to the plateau value reached upon large osmotic shocks. This shows that cytoplasmic crowding increases at the onset of confinement and rapidly becomes so high that 40nm-wide proteins get frozen.

Another way to assess a change in cytoplasmic crowding that arises from an uncoupling between growth and division is to monitor the cytoplasmic mean fluorescence intensity of a fluorophore constitutively expressed in the cytoplasm. Indeed, if cytoplasmic crowding is due to protein synthesis in the absence of cell growth, this would lead to an increase in protein concentration, which could be measured by its mean cytoplasmic fluorescence intensity. To this end, I used an *E. coli* TM-ZipA-mCherry strain expressing GFP under the pR promoter in a constitutive manner (meaning that GFP expression level is constant throughout the cell cycle in normal growth conditions) and monitored GFP fluorescence intensity over time as a function of the growth-induced pressure build-up. In agreement with GEMs diffusion measurements, I found that cytoplasmic GFP mean fluorescence intensity increases progressively upon confinement (Figure 36C), emphasizing that the bacterial cytoplasm becomes more crowded at the onset of confinement due to an imbalance between growth and division. We reason that a similar increase in mean fluorescence intensity, which is used as a readout of protein concentration, could also happen in the case of FtsZ. If this holds to be true, we envision that this could trigger bacterial division much faster at the onset of confinement than in normal growth conditions *(Si et al., 2019)*. Preliminary data suggest that this is the case, but we are planning to validate this by using an endogenous FtsZ protein fusion (current search of the corresponding strain in numerous labs and experiments planned in the following months).

Yet, whether such an increase in cytoplasmic crowding could prevent complete divisome recruitment at the division site by hindering protein diffusion remains elusive. Indeed, most of the proteins recruited at the divisome are smaller in size than GEMs, meaning that their diffusion motion is less impaired by confinement than GEMs one. From our observations, we can say that, at least, cytoplasmic crowding alone does not prevent Z ring assembly and that it does not explain Z ring destabilization (Figure 32D), suggesting the presence of an active mechanism leading to division blockage.

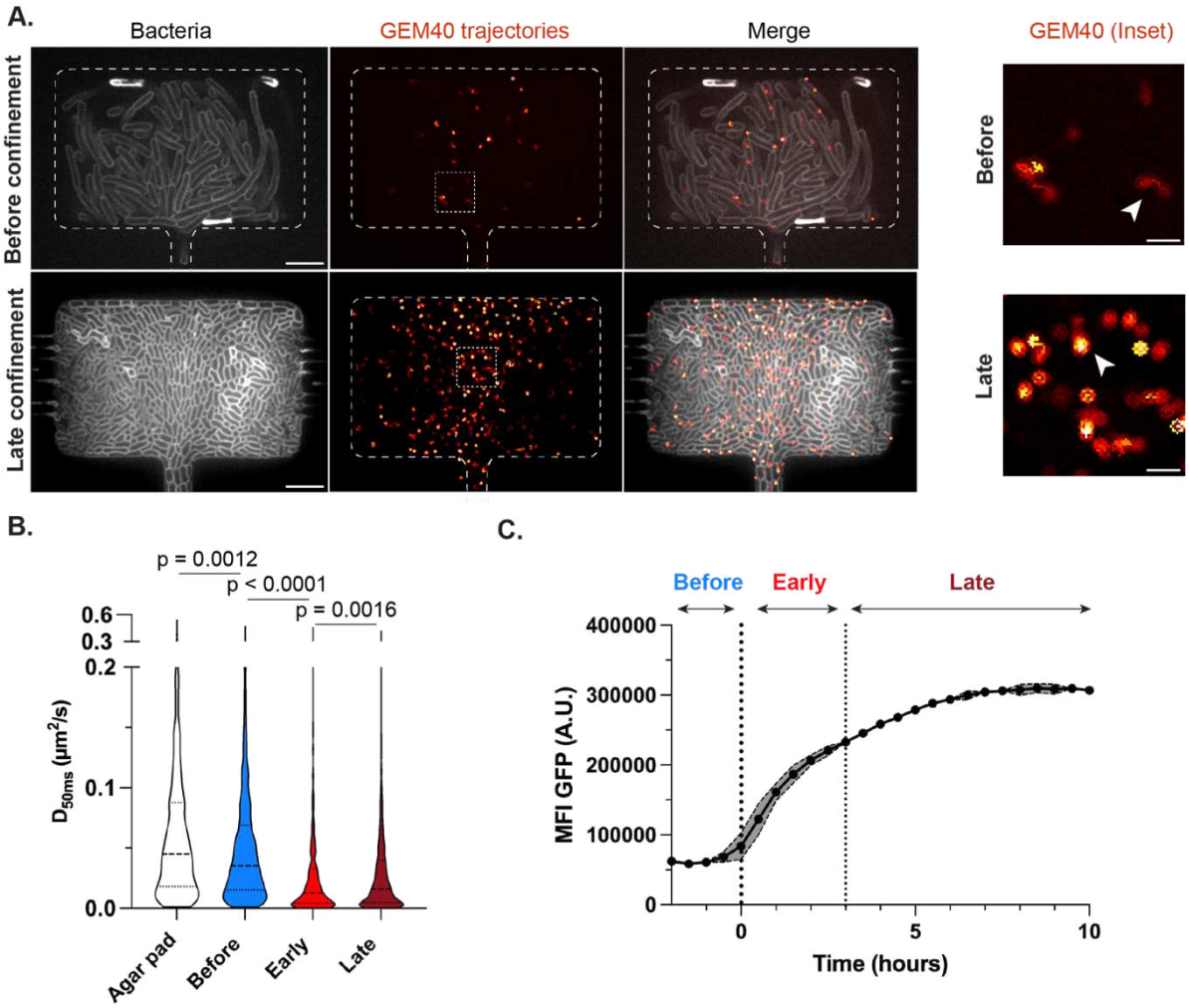


**Figure 36 : Bacterial physiology upon confinement is characterized by an increase in cytoplasmic crowding.** A. *Escherichia coli* TM-ZipA-mCherry GEM40 were imaged in the bacterial confiner at various time points, both in absence (top) or in presence (bottom) of confinement. Bacteria were imaged (left) and GEM trajectories were tracked (middle) to quantify GEM40 diffusive motion within the cytoplasm (overlay – right). Insets: zoom on typical GEM40 trajectories depicted by a white arrow, in absence (top) and in presence (bottom) of confinement. Scale bars inset: 1µm. Scale bars chambers: 5µm. B. Distributions of diffusion coefficient acquired at a 50ms stream time in agar pad, before confinement (n = 1120, N = 2), and upon early (n = 1875, N = 2) and late confinement (n = 2531, N = 1). Statistical analysis: Kruskal-Wallis tests. C. Quantification of the GFP cytoplasmic mean fluorescence intensity upon confinement of *Escherichia coli* TM-ZipA-mCherry GFP (n = 4, N =1).

### 3.5.4 A role for nucleoid occlusion?

In search of a mechanism that could actively block bacterial division, I decided to zoom in by visualizing DNA, which is one of the most important crowding agents of the bacterial cytoplasm. To this end, I used an *E. coli* TM-ZipA-mCherry expressing a functional fusion HU-GFP as the endogenous copy of the DNA binding protein HU (see Materials & Methods – part 1.2.1 - *(Marceau et al., 2011)*, and monitored its proliferation in the bacterial confiner. Strikingly, I observed that while DNA is organized in isolated pools in the cytoplasm before confinement, it forms a single pool filling up the cytoplasm rapidly after pressure build-up (Figure 37A). To quantify this observation, we built up an Ilastik model to segment the DNA signal and used it to calculate the nucleoid-to-cytoplasmic ratio (written N:C ratio), meaning the ratio of the area occupied by the DNA with respect to the area of the bacterial cytoplasm. We found that, as soon as the pressure build-up in the chamber, the nucleoid-to-cytoplasmic ratio increases strongly for 2 hours and then reaches a plateau around 0.8 on average (Figure 37B). By contrast, it stays constant around 0.6 in non-confined chambers (Figure 37B). By plotting the average N:C ratio over the three regimes (Figure 37C), I noticed that it exhibits a similar trend to GEMs diffusion coefficient, both being characterized by a rapid change during the early phase of confinement, suggesting that change in cytoplasmic crowding upon confinement is mainly due to DNA occupancy.

Considering these results, I took a closer look at the raw images and observed that bacteria usually stop dividing when their cytoplasm is filled up by DNA. To quantify this observation, we quantified the fraction of not-dividing bacteria in regard to changes in the nuclear-to-cytoplasmic ratio. We found that these two parameters follow the same trend (Figure 37D), strongly suggesting that DNA occupancy could be the factor limiting bacterial division. We conclude that these changes in nuclear size and shape are sufficient to interpret the measurements in molecular crowding and could impact cell division regulation. Currently, we are exploring whether division arrest is mediated by the action of the nucleoid occlusion factor SlmA, which has been shown to induce depolymerization of FtsZ filaments *(Cho et al., 2011).* Another possibility is that steric hindrance of the nucleoid within the bacterial cytoplasm physically blocks Z-ring assembly.

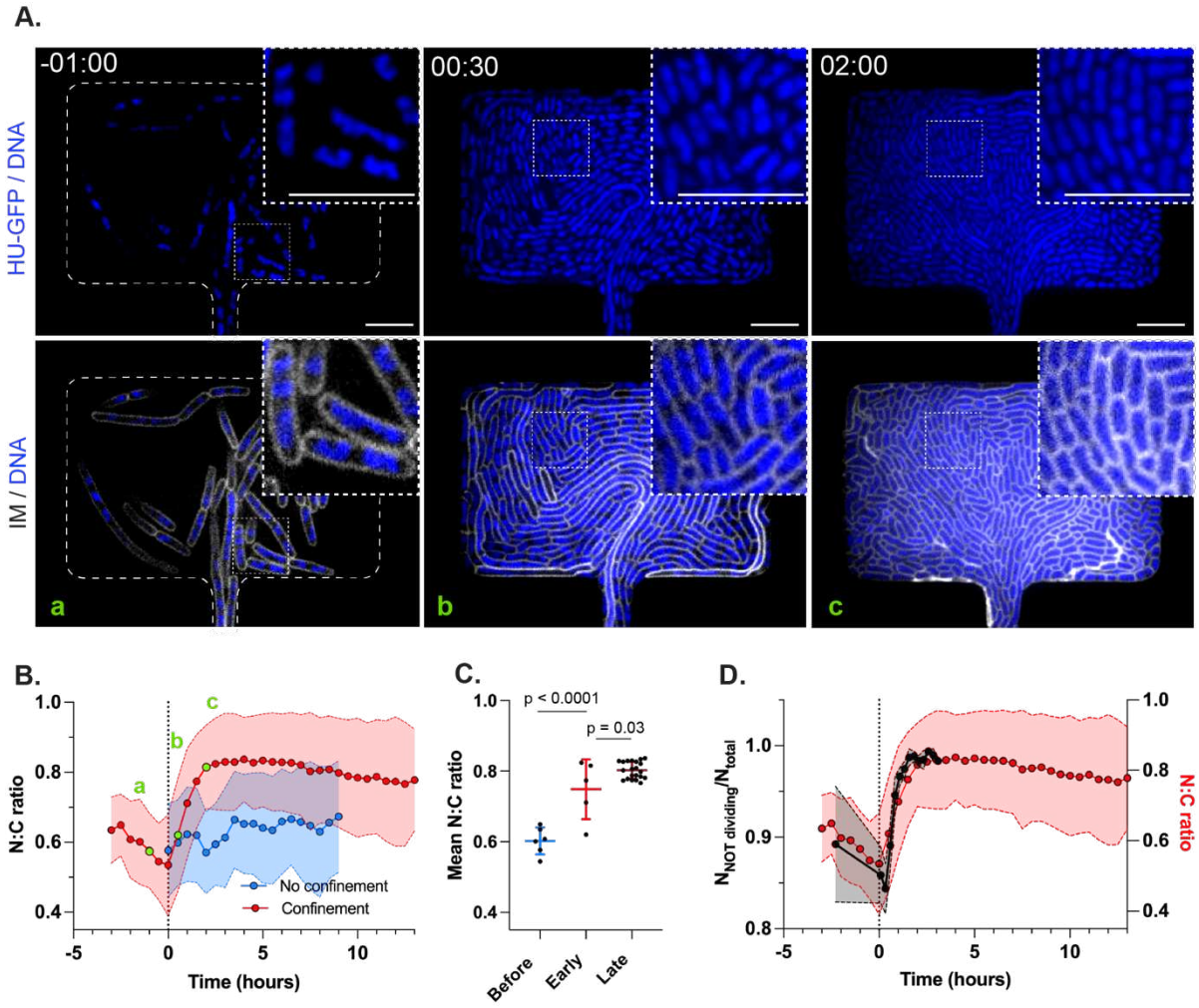


**Figure 37: Bacterial physiology upon confinement is characterized by change in nucleoid-to-cytoplasmic ratio.** A. Representative images of *Escherichia coli* TM-ZipA-mCherry (grey) HU-GFP (blue) proliferation in the bacterial confiner at three different time points, before (left, a) and upon confinement (middle, b and right, c). DNA only is represented (top) in addition to the overlay with bacterial membrane (bottom). Scale bars: 5µm. B. Quantification of the nucleoid-to-cytoplasmic ratio over time both in absence (blue) and in presence (red) of confinement (n = 2, N = 1). The three representative images of DNA changes shown in A. are represented with a green letter. C. Quantification of the nucleoid-to-cytoplasmic ratio in the three regimes "Before confinement", "Early confinement" and "Late confinement" (n = 2, N = 1). Statistical analysis : one-way ANOVA tests (Before vs. Early: $p < 0.0001$, Early vs. Late: $p = 0.03$) D. Quantification of the fraction of non-dividing bacteria (black) over time ) (n = 3, N = 2) in regards to the nucleoid-to-cytoplasmic ratio (red) (n = 2, N = 1).

## 3.6 Conclusion

In this chapter, by using *E. coli* as a referring organism, we have characterized bacterial adaptation at the single-cell level to the large mechanical constraints, that arise from proliferation in a limited space. By taking advantage of the tools described in the previous chapters, i.e. the bacterial confiner and the machine-learning-based image analysis pipeline, we show that bacteria undergo strong morphological changes upon confinement. These morphological changes are induced by an uncoupling between growth and division at the onset of confinement. Specifically, while growth is rapidly arrested after pressure build-up, division persists for a while before being arrested suddenly.

Then, we try to identify which mechanisms regulate bacterial division upon confinement. First, based on previous studies, we hypothesize that the Rcs stress response could trigger division upon confinement. We show that this envelope stress response, which is activated as soon as the pressure builds up, triggers division at the edges of the chambers but not in the center. Second, we hypothesize that the uncoupling between growth and division could induce an increase in cytoplasmic crowding. Indeed, we show that cytoplasmic crowding increases upon confinement using two different readouts: diffusive nanoparticles and the mean fluorescent intensity of a constitutive GFP. These experiments suggest that, in the case of FtsZ, crowding-mediated increase in intracellular protein concentration could trigger bacterial division at the onset of confinement.

Finally, we try to decipher which mechanism mediates division arrest upon confinement. We show that FtsZ rings still form upon confinement, but often fail to constrict. Interestingly, in some cases, we notice that these rings were destabilized upon confinement by an unknown mechanism. So far, we show that division arrest correlates with increasing DNA occupancy, which suggests that nucleoid occlusion could mediate division arrest, potentially in a SlmA-dependent process.

# Discussion

Mechanical constraints are ubiquitous to bacterial life, at the single cell level (surface contact, flow-induced shear stress) but also at the multicellular level where bacteria proliferate in a limited space (growth-induced pressure, cell-cell interactions) (Persat et al., 2015b). It is therefore crucial to understand how bacteria behave in physiological conditions and realistic mechanical environments. To date, mechano-microbiological studies have mostly focused on the single-cell level, in particular on the impact of extrinsic forces (Persat et al., 2015a; Rodesney et al., 2017), or at the multicellular level in the context of biofilm mechanics (Chu et al., 2018; Cont et al., 2020; Douarche et al., 2015; Hartmann et al., 2021; Yan et al., 2018)and internal organization (Beroz et al., 2018; Hartmann et al., 2018; Zhang et al., 2021). However, the impact of mechanics on bacterial physiology within bacterial communities remains largely unexplored.
In this context, my Ph.D. work provides a novel approach and understanding of how growth-induced mechanical constraints, that arise from proliferation in a limited space, influence bacterial physiology. In the following, the results of this work will be discussed around three major questions:

i) What is the complex mechanism at play for *E. coli* adaptation to confinement?
ii) Can bacteria teach us something about a universal response to confinement?
iii) How could confinement determine infection outcome?

## 1 What is the complex mechanism at play for E. coli adaptation to confinement?

Confinement is a general situation that *E. coli* encounters in its natural environment. This can be summarized in two situations: first, when it grows as a biofilm by proliferating in a space limited by the extracellular matrix and physical obstacles commonly present in the wild; second, during infection for example of the urinary tract, when it invades uroepithelial cells and forms dense aggregates constrained by host subcellular structures, called Intracellular Bacterial Colonies (IBCs) *(Eto et al., 2006; Mulvey et al., 2001; Wright et al., 2007).* In these contexts, bacterial confinement could lead to the emergence of new bacterial features important for survival and disease progression. To decipher how confinement impacts bacterial physiology, we have developed cutting-edge microfluidic growth chambers with nanometric features as a model of a constrained environment, where bacteria proliferate in a controlled chemical and mechanical environment.

## 1.1 Measurement of bacterial growth-induced pressure

Using this experimental device, we show that bacterial proliferation in a limited space ultimately leads to the generation of large growth-induced compressive stresses onto the microenvironment (~ 300 kPa) (Figure 27B). Is this measurement in agreement with other estimations of growth-induced mechanical stresses available in the literature?
This order of magnitude is similar to the internal pressure estimated by Cont and colleagues within *Vibrio cholerae* and *Pseudomonas aeruginosa* biofilms, after 12 hours of proliferation (~ 100 kPa, (Cont et al., 2020). However, this measurement is not in agreement with the measurement performed by Chu and coworkers upon *E. coli* confinement (~ 20 kPa) within related microfluidic chambers, yet with higher dimensions (width: 100 – 200µm, length: 200µm, feeding channels width: 10µm, feeding channels height: 650nm) *(Chu et al., 2018)*.

To provide an explanation to this discrepancy, we first wondered whether growth-induced pressure measurement is sensitive to medium renewal. To test this hypothesis, I stopped medium perfusion ($P_{inlet}$ = 0 mbar) before and after the bacteria reach confluency, while monitoring pressure build-up. I observed that indeed it is the case, bacteria stop growing rapidly upon flow arrest before reaching confluency in the chambers, showing that medium renewal is necessary for bacterial growth (Figure 38A). However, when medium renewal was stopped just after confluency and pressure build-up, bacteria were still able to generate a growth-induced pressure around 200kPa, yet not as fast as in the presence of flow (Figure 38B). Therefore, medium renewal cannot entirely explain the variation in GIP measurements.
Then, we wondered whether this discrepancy could be related to the size of the chambers. We reasoned that in the case of much larger colonies, the impact of nutrient access and chemical gradients could limit the ability of bacteria to grow and therefore exert pushing forces on the microenvironment. As *E. coli* intracellular bacterial colonies formed during urinary tract infections have been reported to be about 30µm wide *(Sharma et al., 2021)*, we believe our chamber size (20µm x 30µm) is closer to physiological conditions encountered by bacteria during infection.
Another explanation could rely on the size of the feeding channels. In our case, we designed dimensions in the nanometer scale (width, height = 400nm) to prevent bacterial passage, while Chu and colleagues used larger channels (width = 10µm, height = 650nm) that limit but do not hinder bacterial escape (Chu et al., 2018). Based on this, we propose that this discrepancy in GIP measurement is likely mostly related to the amount of confinement imposed on the bacterial population. While Chu and colleagues provide an estimation of the minimal pressure exerted by bacterial growth, we provide an estimation of the maximal pressure exerted in case of more intense confinement, still physiological in the infectious context *(Cont et al., 2020)*.

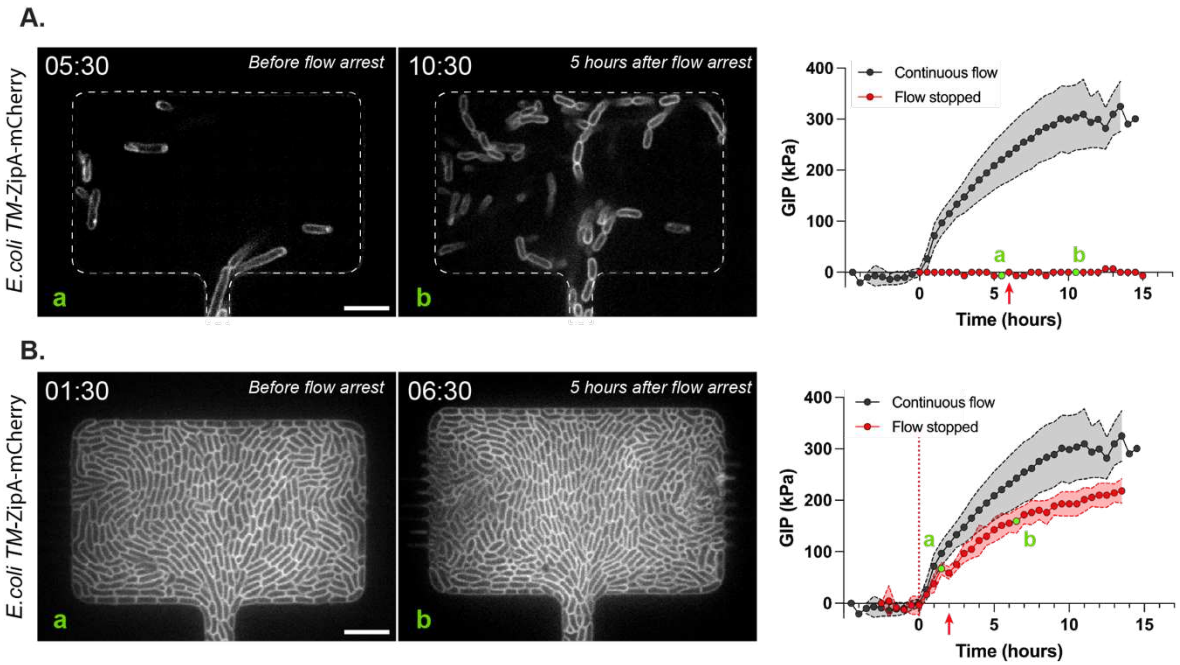


**Figure 38: Impact of culture medium perfusion on growth-induced pressure build-up**. A. When medium perfusion is arrested before bacteria reach confluency in the chamber (left), bacteria do not proliferate enough to fill up the chambers (middle: 5 hours after flow arrest). As a result, bacteria never reach confinement, so that no growth-induced pressure is generated in absence of flow (right). The time at which medium perfusion was arrested is depicted by a red arrow. The two images are represented on the graph by green letters. B. When medium perfusion is arrested after bacteria reach confluency (left) and start to generate pressure, bacteria still continue to grow (middle) and to generate pressure yet in a slower and lower manner than in presence of a continuous medium supply (right). Bacteria ultimately exert a growth-induced pressure about 200kPa. The time at which medium perfusion was arrested is depicted by a red arrow. The two images are represented on the graph by green letters. *Time hh:mm. Scale bars: 5µm.*

## 1.2 Confinement induces a morphological transition by uncoupling growth and division

### 1.2.1 Bacteria undergo major morphological changes upon confinement

Next, we characterized bacterial morphology in regard to growth-induced pressure build-up. We show that, as soon as the pressure builds up in the chambers, bacteria synchronize and rapidly decrease in area until reaching a constant minimal size 2 hours later (Figure 28D). These morphological changes are mostly due to changes in bacterial length (Figure 28E), underscoring that confinement induces a major shortening of the rods. Importantly, we show that the confinement-induced minimal size is significantly different from the one adopted by bacteria upon stationary phase (Figure 29C), suggesting that these morphological changes are part of a unique adaptation process used by bacteria to cope with mechanical confinement.

To my knowledge, such morphological changes induced by (self-generated) mechanical stress have never been observed. Indeed, few studies have rather described a transition to a pancake-like morphology in response to an externally applied 2D compressive stress *(Si et al., 2015; Zietek et al., 2022)*. We believe this difference is because self-generated compression is isotropic, while 2D compression is anisotropic and unidirectional, potentially leading to different responses in bacteria. Interestingly, these cell shape changes have also been reported to be reversible upon pressure release, like in our case (Figure 30) *(Si et al., 2015)*.

### 1.2.2 On the path to identify the mechanisms involved in confinement-induced morphological adaptation

#### 1.2.2.1 Uncoupling between growth and division

We found that the onset of confinement induces an uncoupling between bacterial growth and division. More precisely, we show that confinement induces bacterial growth arrest as soon as the pressure builds up in the chambers. Strikingly, growth arrest is followed by a sudden division arrest with a delay of 30 minutes, during which bacterial division persists (Figure 31). In other words, even though the lack of space limits bacterial growth, bacteria still divide without increasing in size for half an hour, which ultimately leads to the formation of non-growing and non-dividing tiny cells.

#### 1.2.2.2 Which mechanisms trigger bacterial division upon confinement?

Next, we search for potential sensors that could trigger bacterial division upon confinement. The first candidate we identify is the Rcs envelope stress response, which is activated as soon as the pressure builds up in the chamber. Thus, it is a good candidate for confinement sensing (Figure 33C), in agreement with recent unpublished works *(Mason and Rojas, 2022; Zietek et al., 2022)*, 2D compression). By

using a *rcsB* mutant, we show that the Rcs pathway is responsible for division at the edges of the chambers, but not in the center, emphasizing the presence of another mechanism that triggers bacterial division upon mechanical confinement (Figure 34F). The second sensor we identified is cytoplasmic crowding. We show that confinement induces an increase in crowding using two different readouts, the diffusive motion of nanoparticles within the cytoplasm, and the mean fluorescence intensity of a constitutive GFP (Figure 36B, C). Our results strongly suggest that at a short timescale, an increase in molecular crowding due to sudden space limitation could be sufficient to enrich intracellular protein concentration, as shown with GFP (Figure 36C). We envision that this could also happen with FtsZ (experiment planned in the fall), similar to what has been shown during hyperosmotic shock *(Sun et al., 2021b)* (detailed in the following paragraph). This could in turn mediate the attainment of an absolute threshold number of FtsZ molecules to trigger Z-ring formation and subsequent cell division, as proposed in recent work *(Si et al., 2019)*. In addition, at a long timescale, the activation of Rcs transcriptional stress response could further promote active FtsZ synthesis in a second phase *(Carballès et al., 1999; Miguel et al., 2022)*, as part of a whole bacterial adaptation response. We suspect that crowding-mediated bacterial division at a short timescale is probably one explanation for the synchronization of the bacterial morphological state observed in this work. Indeed, bacterial division acceleration occurs at the onset of confinement within 15 minutes (Figure 31A). Although crowding increase is almost instantaneous, we reason that DNA replication and segregation state could be a limiting factor for bacterial division, potentially delaying crowding-mediated bacterial division for a few minutes.

#### 1.2.2.3 Insights from bacterial response to osmotic stress

This situation is reminiscent of the one encountered during hyperosmotic shocks. Although confinement-induced mechanical stress and hyperosmotic stress are different due to their nature, timing, and effect on turgor pressure, both are characterized by the induction of the Rcs envelope stress response *(Meng et al., 2021; Sledjeski and Gottesman, 1996)* and by an increase in cytoplasmic crowding *(Bremer and Kramer, 2019; Cayley et al., 1991)*. Thus, the knowledge of bacterial division upon hyperosmotic stress can potentially provide insights into the role of crowding in division acceleration upon confinement. One study of particular interest has shown that hyperosmotic stress leads to an instantaneous increase in constriction rate *(Sun et al., 2021b)*. The authors have proposed that this could be mediated by an increase in FtsZ intracellular concentration together with a decrease in turgor pressure *(Sun et al., 2021b)*. In our case, we observe a similar acceleration of bacterial division, in a slightly different situation. Upon confinement, bacteria are characterized by both an activation of the Rcs pathway and an increase in crowding, which might both lead to an increase in FtsZ intracellular concentration, but not by a decrease in turgor pressure. Thus, the short timescale of the bacterial response in both situations strengthens our hypothesis that a crowding-mediated increase in FtsZ concentration,

from a biophysical origin, could be responsible for instantaneous division. Specifically, in both situations, an increase in crowding could induce osmotic water effluxes through mechanosensitive channels, that have been shown to influence FtsZ proteins positioning by interacting with their cytoplasmic domain *(Koprowski et al., 2015)*, thereby potentially favoring Z-ring assembly.
Therefore, to demonstrate that crowding is the main trigger of bacterial division at the onset of confinement, we need to decouple Rcs activation and crowding increase. To this end, we plan to perform hyperosmotic shocks using the *rcsB* mutant vs. a WT strain, and to compare the time needed for division in this situation with respect to the one occurring at the onset of confinement.

In sum, we propose that crowding is the main trigger of bacterial division at the onset of confinement, leading to a first round of instantaneous divisions, while the Rcs pathway is a second trigger that promotes division in a second phase, as part of a bacterial adaptation strategy.

#### 1.2.2.4 Which mechanisms induce division arrest upon confinement?

Next, we search for a mechanism that could lead to division arrest 30 minutes after the onset of confinement (Figure 31A). We first hypothesize that a large increase in crowding could prevent divisome function. Yet, we still observe FtsZ rings forming under confinement (Figure 32). Even though crowding probably impacts the timing of recruitment of the proteins involved in the later steps, it does not seem to hinder the capacity to initiate and form a division ring, suggesting that other players could be responsible for sudden division arrest.

Then, we zoom in and wonder whether the nucleoid could play a role in this process. We show that the nucleoid-to-cytoplasmic ratio increases suddenly at the onset of confinement for 2 hours, before reaching a plateau (Figure 37B). Interestingly, these changes in the nucleoid-to-cytoplasmic ratio are anticorrelated to the changes in bacterial area (Figure 39). Based on these results, we propose that bacteria reach a minimal size upon confinement that is determined by the nucleoid. This hypothesis is in agreement with a previous study, in which smaller bacteria are reported to be characterized by a higher N:C ratio *(Gray et al., 2019)*, and reviews that have questioned bacterial minimal size *(Koch, 1996; Levin and Angert, 2015)*.

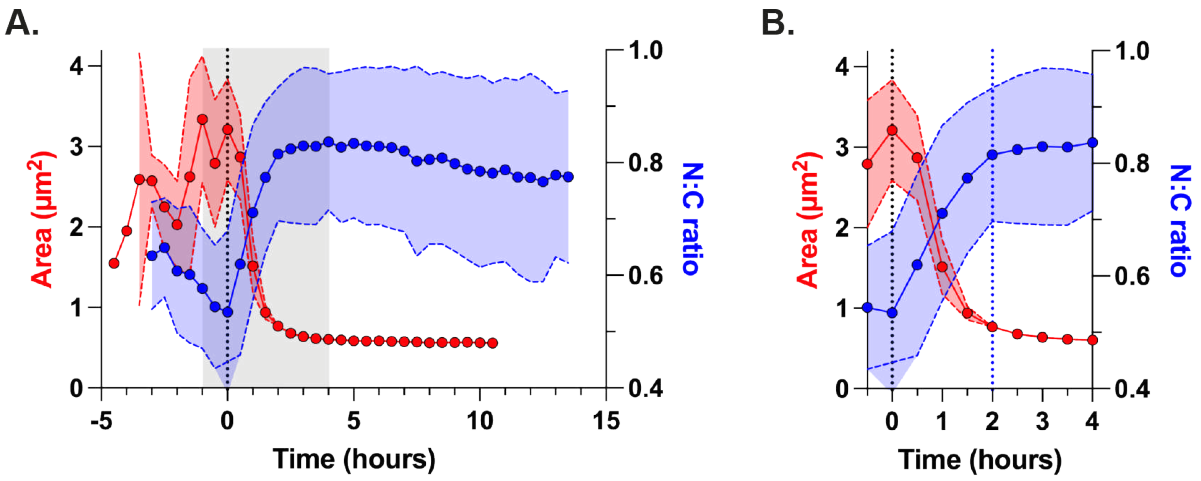


**Figure 39: Confinement-induced morphological changes correlate with changes in DNA occupancy.** A. Quantification of bacterial area (red) and nucleocytoplasmic ratio (blue) over time. The vertical dotted line represents the time at which pressure builds-up. The gray region identifies the region of interest, represented in B. B. Quantification of bacterial area (red) and nucleocytoplasmic ratio (blue) during the first 4 hours after the onset of confinement (black vertical dotted line). The blue vertical dotted line represent the time at which the nucleocytoplasmic ratio reaches a plateau. This corresponds to time at which bacteria reaches their minimal size.

To go further, we also show that nucleoid-to-cytoplasmic ratio increase correlates with changes in the fraction of non-dividing bacteria (Figure 37D), suggesting a potential link between DNA occupancy and division arrest. Based on the literature, we propose that nucleoid occlusion ultimately inhibits division upon confinement, as a protective mechanism that prevents DNA bisection *(Wu and Errington, 2012)*, and subsequent lethal DNA damage (Figure 33G).

In Gram-negative bacteria, nucleoid occlusion has been reported to be mediated by the FtsZ polymerization antagonist SlmA *(Bernhardt and Boer, 2005; Cho et al., 2011)*. Such SlmA-mediated inhibition mechanism of bacterial division could perfectly suit our observations regarding division arrest (Figure 31), FtsZ dynamics (Figure 32), and DNA occupancy (Figure 37), potentially providing a molecular explanation for division arrest upon confinement (experiment planned before the PhD defense). Another possibility is that steric hindrance of the nucleoid within the bacterial cytoplasm physically blocks Z-ring constriction *(Männik et al., 2012; Tiruvadi-Krishnan et al., 2022)*.

## 1.3 Working model

Altogether, based on these results, we propose the following model to characterize *E. coli* morphological adaptation upon confinement (Figure 40).
When bacteria proliferate in a limited space, they fill up the available space and ultimately face a lack of space (depicted by a gray area), which is a hallmark of confinement. In this context, bacteria push on their neighbors to accommodate some space for their growth, which results in the generation of a growth-induced pressure on the microenvironment, and a slow-down in growth rate ultimately leading to growth arrest. While mechanical forces lead to the activation of the Rcs envelope stress response, sudden growth arrest results in an increase in cytoplasmic crowding. These two parameters are thought to favor bacterial division while growth is arrested. As a result, this uncoupling between growth and division leads to major morphological changes, characterized by a strong shortening of the rods. Division is ultimately arrested near a minimal size set by DNA, potentially in a SlmA-mediated nucleoid occlusion process.

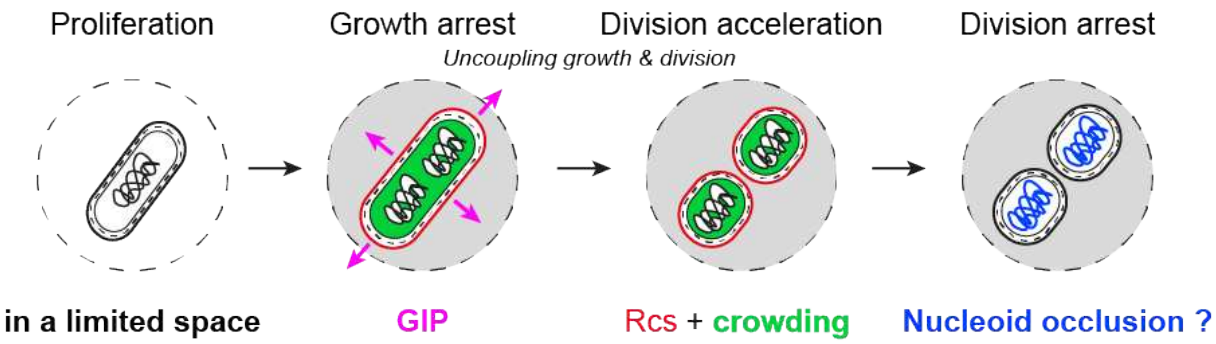


**Figure 40: Proposed model for *Escherichia coli* morphological adaptation to mechanical confinement.**

# 2 Can bacteria teach us something about a universal response to confinement?

In this section, we discuss general principles of growth-induced pressure build-up and how this work can be extended to other bacterial species, that encounter confinement during infection. To this end, we use two case studies:

- *Neisseria meningitidis*, a Gram-negative bacterium with another shape that occludes the lumen of infected vessels *(Melican and Dumenil, 2012)*

- *Staphylococcus aureus*, a Gram-positive bacterium with a different envelope and turgor pressure, which proliferates in the form of abscesses during skin and bone infections *(Gimza and Cassat, 2021; Kobayashi et al., 2015)*.

Finally, we provide a global comparison between prokaryotes and eukaryotes, and the different strategies used by cells to adapt to confinement.

## 2.1 What is the origin of growth-induced pressure?

In this work, we show that *E. coli* proliferation upon confinement generates large growth-induced pressures. Would it be true for any bacterial species? If yes, to which extent? To address these questions, we confined the Gram-positive bacterium *S. aureus*. We observe that this bacterium deforms much more the chambers than *E. coli* (Figure 41A), by generating pressure in the MPa range (Figure 41B). Interestingly, for both bacterial species, growth-induced pressures correlate in order of magnitude with turgor pressures, which differ between Gram-negative and Gram-positive bacterial species *(Rojas and Huang, 2018)*. Conceivably, this suggests that turgor pressure, which drives bacterial growth, is at the origin of growth-induced pressure at the multicellular level.

As mentioned in the introduction, turgor pressure arises from the high solute concentration of the bacterial cytoplasm together with the inner membrane semi-permeability, and is thus a common trait between bacteria. Therefore, in theory, any bacterial species should be able to exert growth-induced pressure onto the microenvironment upon confinement, as noticed by Cont and colleagues, to an extent similar to their internal turgor pressure *(Cont et al., 2020)*. More generally, beyond the bacterial kingdom, yeasts and mammal cells also generate substantial growth-induced pressure on their microenvironment to an extent that correlates with their internal pressure *(BenMeriem et al., 2023; Delarue et al., 2016)*. Together, this shows that growth-induced pressure generation is a general trait of cell proliferation in a limited space, which is shared across the different kingdoms of life.

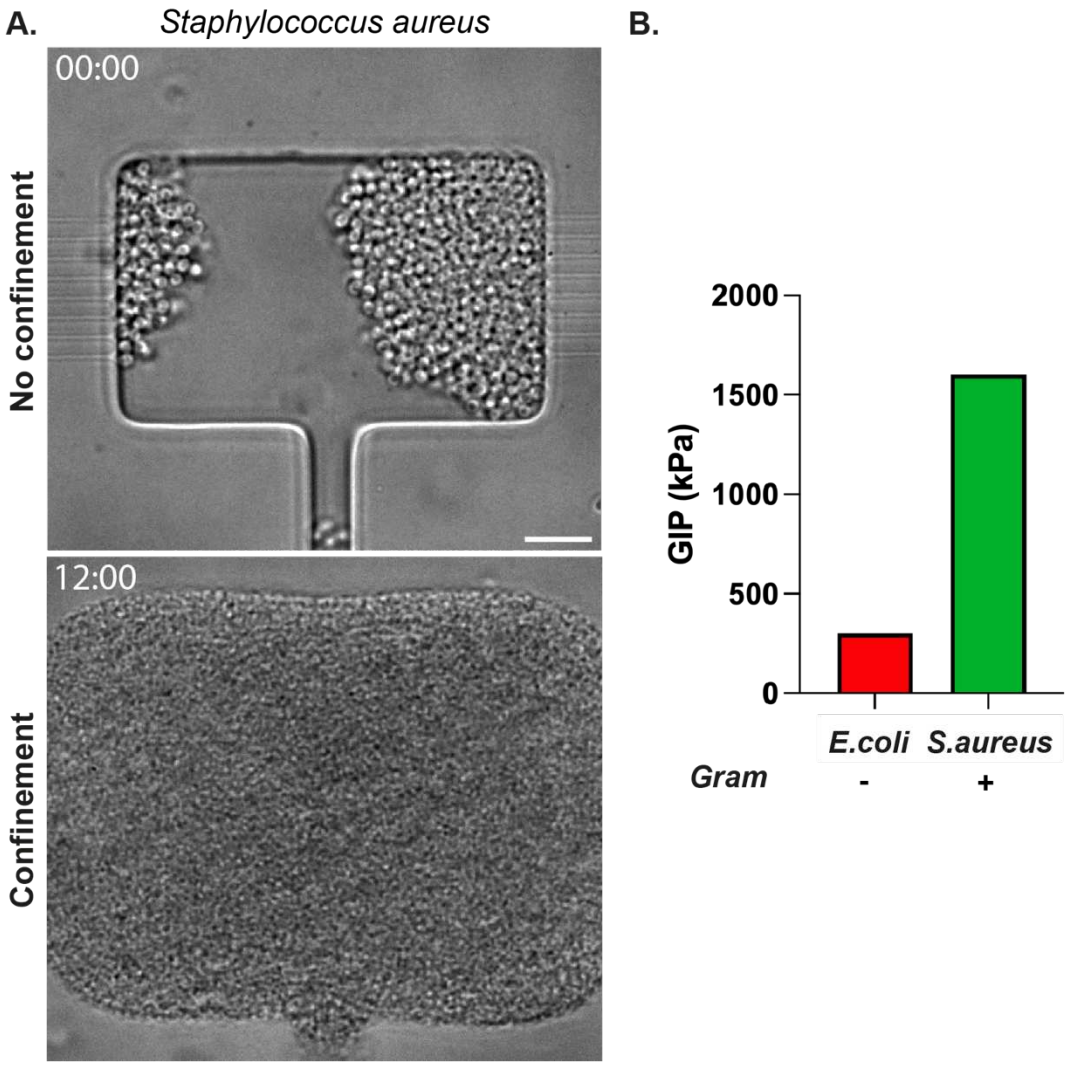


**Figure 41: The Gram-positive *Staphylococcus aureus* generates higher growth-induced pressure upon confinement than the Gram-negative *Escherichia coli***. A. *Staphylococcus aureus* bacteria proliferation induces striking deformation of the chamber upon confinement (top: time 0, bottom: after 12 hours). The deformation is so large that the entire chamber does not fit in the field of view. *Time hh:mm. Scale bar: 5µm. B.* Estimation of the maximal growth-induced pressure generated by *Escherichia coli* (red) and *Staphylococcus aureus* (green).

## 2.2 Which strategies are used by bacteria to sustain growth-induced pressure?

In this section, we investigate which parameters are used by bacteria to sustain the growth-induced pressure generated by their proliferation in a limited space.

### 2.2.1 Role of the bacterial cell envelope

In this work, we show that *E. coli* adaptation to confinement is characterized by the activation of the Rcs and Cpx envelope stress responses (Figure 33C, D). In the literature, these two stress pathways are known to maintain envelope homeostasis and importantly to participate in peptidoglycan remodeling *(Delhaye et al., 2019; Mitchell and Silhavy, 2019)*. Notably, Cpx activation has been reported to increase peptidoglycan cross-linking *(Bernal-Cabas et al., 2014; Cava and Pedro, 2014)*, which in turn increases envelope stiffness *(Auer and Weibel, 2017)*. Therefore, it is likely that upon confinement, activation of both Rcs and Cpx stress responses induces remodeling of the envelope, which could increase its stiffness together with its load-bearing capacity *(Rojas et al., 2018)*.

To determine whether Rcs and Cpx-mediated adaptations are crucial for Escherichia coli survival under confinement, we assessed the bacterial viability of *rcsB* and *cpxR* mutants upon confinement. We find that both mutants were less viable than the WT strain upon confinement (Figure 42), showing that envelope stress response-mediated adaptation improves bacterial fitness under high growth-induced pressure. Of note, the effect on bacterial viability is probably underestimated as the various envelope stress responses are known to cross-talk *(Bury-Moné et al., 2009)*. Yet, beyond this work, we still lack a general understanding of the molecular mechanisms at play during Rcs and Cpx-mediated bacterial adaptation, which would require to characterize the envelope composition in WT vs. in different mutants of key proteins involved in these pathways.

### 2.2.2 Role of the bacterial cell shape

In this work, we show that *E. coli* undergoes a major morphological transition upon confinement. Interestingly, bacterial shape adaptation in response to an external stress has been reported in several cases, in a process called morphological plasticity *(Justice et al., 2008; Ultee et al., 2019; Yang et al., 2016; Young, 2007)*. In line with these studies, we suppose that changes in morphology and size upon confinement could represent an adaptation strategy used by bacteria to better sustain mechanical stress. To assess the role of bacterial shape in adaptation to confinement, we confined the Gram-negative diplococcus *N. meningitidis* and quantified bacterial morphology. We observed that these bacteria conserve their overall isotropic shape (Figure 43A) and that bacterial area is significantly reduced, yet to a lesser extent than *E. coli* (Figure 43B).

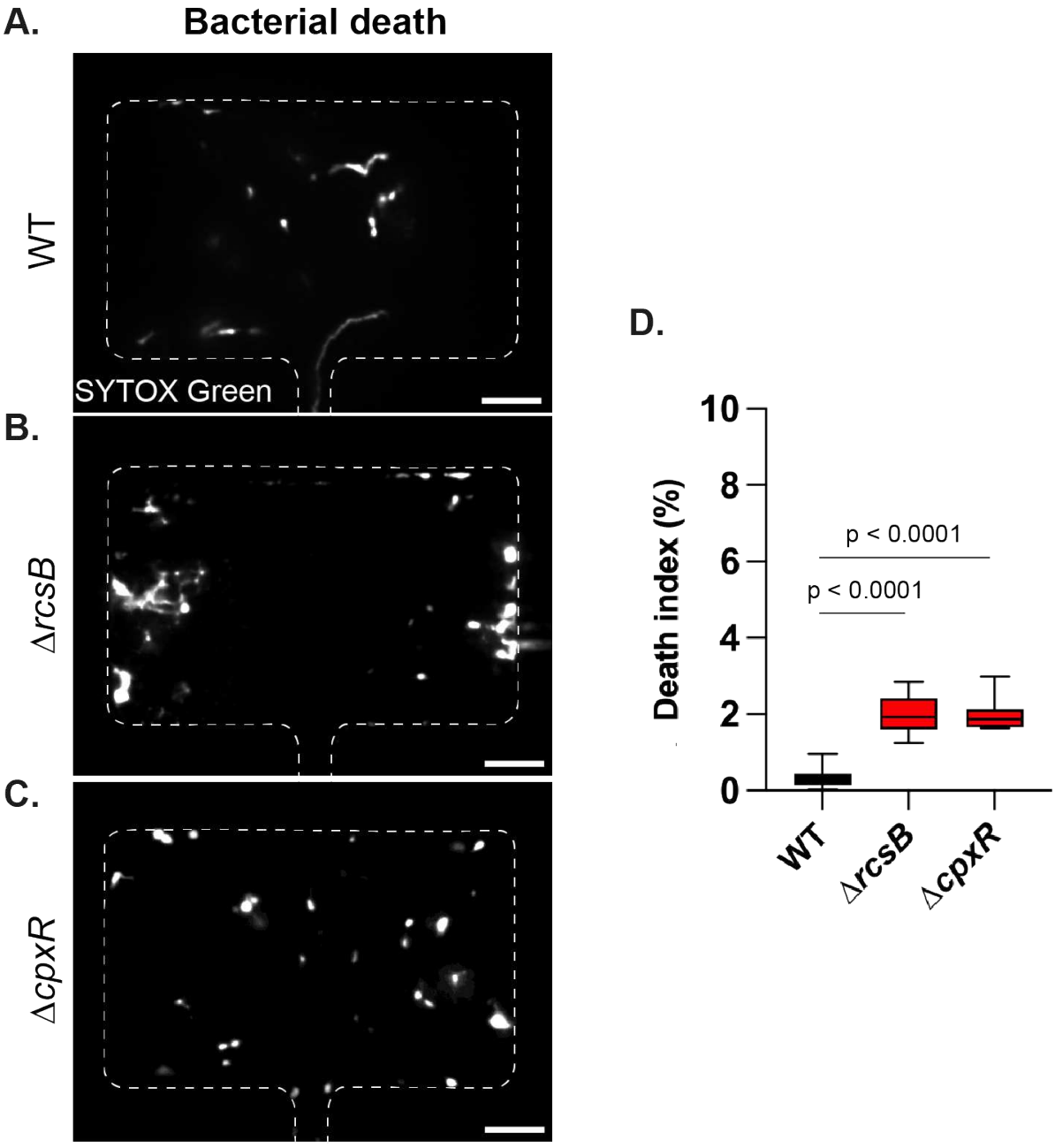


**Figure 42: Bacterial viability upon confinement for *Escherichia coli* WT, Δ*rcsB* and Δ*cpxR* mutants strains.** Dead bacteria are stained with SYTOX Green upon late confinement for *Escherichia coli*: A. WT, B. Δ*rcsB*, and C. Δ*cpxR* strains. D. Quantification of the death index for the WT, Δ*rcsB* and Δ*cpxR* strains. Statistical analysis: Kruskal-Wallis test. Scale bars: 5µm.

By looking at the shape of the area distribution, we noticed that bacterial area in the absence of confinement is characterized by two peaks, one with a smaller area corresponding to the coccus population, and another one corresponding to the diplococcus population. Interestingly, upon confinement, the area distribution is mostly dominated by the peak at smaller areas, suggesting that confinement favors the coccus shape rather than the diplococcus one (Figure 43B).

*N. meningitidis* morphological transition from diplococci to cocci is reminiscent of the one observed in *E. coli*, which could be approximated as a rod-to-cocci transition. Given this similarity in two unrelated bacterial species, we propose that the coccoid shape provides a fitness advantage to sustain large mechanical stresses, by minimizing the force experienced by bacteria and increasing bacterial mechanical strength. Indeed, in the case of *E. coli*, the coccoid shape has been proposed to favor nutrient consumption and bacterial packing *(Justice et al., 2014)*. In addition, as a spherical shape minimizes the surface area of an object, it also results in a lower force experienced by the bacteria at a given pressure, compared to the rod one.
In the case of *N. meningitidis*, we reason that the enrichment in cocci upon confinement could be explained by two different scenarios. First, similarly to *E. coli*, confinement could induce division arrest and impair the transition from cocci to diplococci. Second, bacteria could continue to grow and divide upon confinement while diplococci could have a higher probability of dying upon confinement-induced mechanical constraints, due to the weak mechanical strength conferred by the diplococcus shape. So far, our preliminary results rather tend to support the second hypothesis, in which the coccus shape could provide higher mechanical strength to the bacteria. Indeed, the coccus state is characterized by a uniform envelope made of three layers: the inner membrane, the cell wall and the outer membrane. By contrast, we have seen that the diplococcus state is characterized by two compartments delimited by the inner membrane (and probably by the cell wall *(Navarro et al., 2022)*, while the outer membrane is not invaginated yet (Figure 24). Taking support on what is known about *E. coli*, we assume that mechanical strength is conferred by the assembly of the outer membrane and the cell wall, mechanically linked with various proteins *(Rojas et al., 2018)*. Based on this, we propose that the coccus state is likely characterized by a higher mechanical strength compared to the diplococcus one, which exhibits a weak point at mid-cell. In line with this idea, *N. gonorrhoeae* bacteria have been shown to rupture at the neck between the two cocci most often, *i.e.* at the division site *(Elmros et al., 1976)*.

In sum, these two case studies exemplify that the coccus shape provides a fitness advantage to sustain large mechanical stresses.

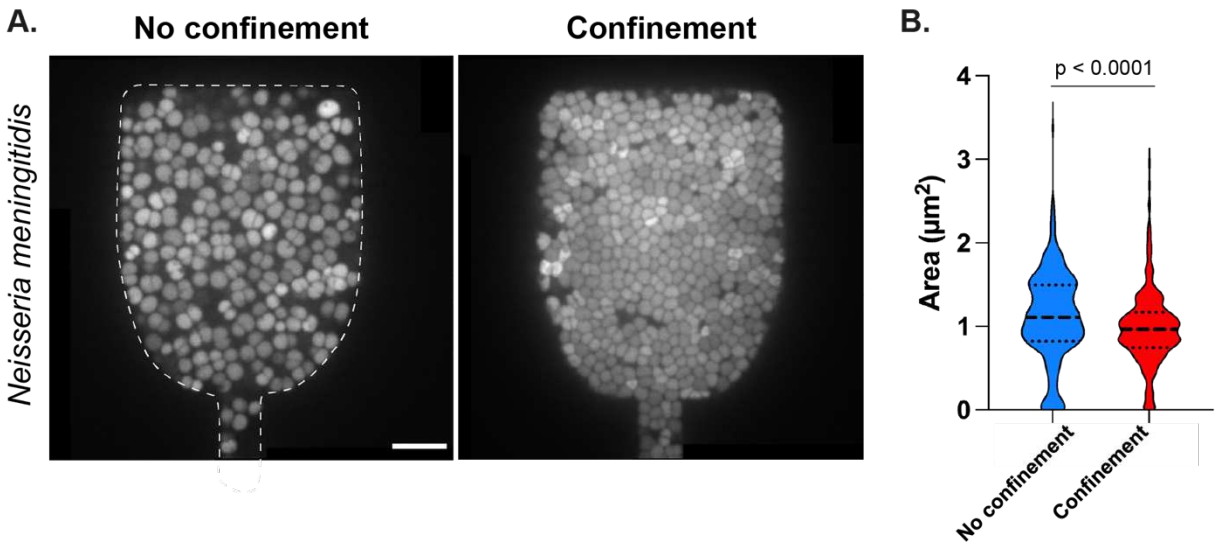


**Figure 43: Morphological changes occurring during *Neisseria meningitidis* confinement**. A. *Neisseria meningitidis* bacteria are characterized by their diplococcus shape in absence of confinement (left). By proliferating in the chamber (closed with a quake valve), these bacteria ultimately become confined (right). Scale bar: 5µm. B. Quantification of the bacterial area in absence (blue) and in presence of confinement (red). The mean values are represented in dashed lines, and the quartiles in dotted lines. Statistical analysis: Mann-Whitney test.

### 2.2.3 Role of bacterial cell death

In this work, we show that *E. coli* bacteria proliferate under confinement in the form of tightly packed aggregates by generating important mechanical constraints, to which they adapt to survive. We also show that this strategy induces a bacterial vegetative state, where growth and division are both arrested. Intriguingly, another strategy seems to be adopted by the bacterium *N. meningitidis*. In preliminary experiments, I observed that these bacteria continue growing and dividing but have a higher rate of autolysis upon confinement (Figure 44A). In addition, we have measured a lower growth-induced pressure for this bacterial specie (~100kPa, preliminary data). Inspired by a previous study on eukaryotic cells, we propose that bacterial death could be a strategy used by bacteria to release mechanical stress *(Ranft et al., 2010)*. Like so, by tuning bacterial death, bacteria could be able to monitor growth-induced pressure in a range that is beneficial for bacterial physiology. Notably, I suspect that, by releasing free space, bacterial death enables the growth and division of the neighboring cells (Figure 44B). Indeed, isolated bacterial sacrifice could provide a fitness advantage to the bacterial population, by releasing nutrients and DNA as previously reported *(Claverys and Håvarstein, 2007; Popp and Mascher, 2019)*, but also by releasing free space, thereby favoring the growth and division of the neighbors even at late infection stages, and dissemination to other tissues and organs within the host.

In sum, various adaptation strategies seem to be adopted by different bacterial species to cope with confinement, including envelope remodeling, morphological changes, and isolated bacterial death. In the future, the implementation of a theoretical framework based on the quantitative approaches developed in this work will allow us to build a physico-chemical model for bacterial adaptation to confinement.

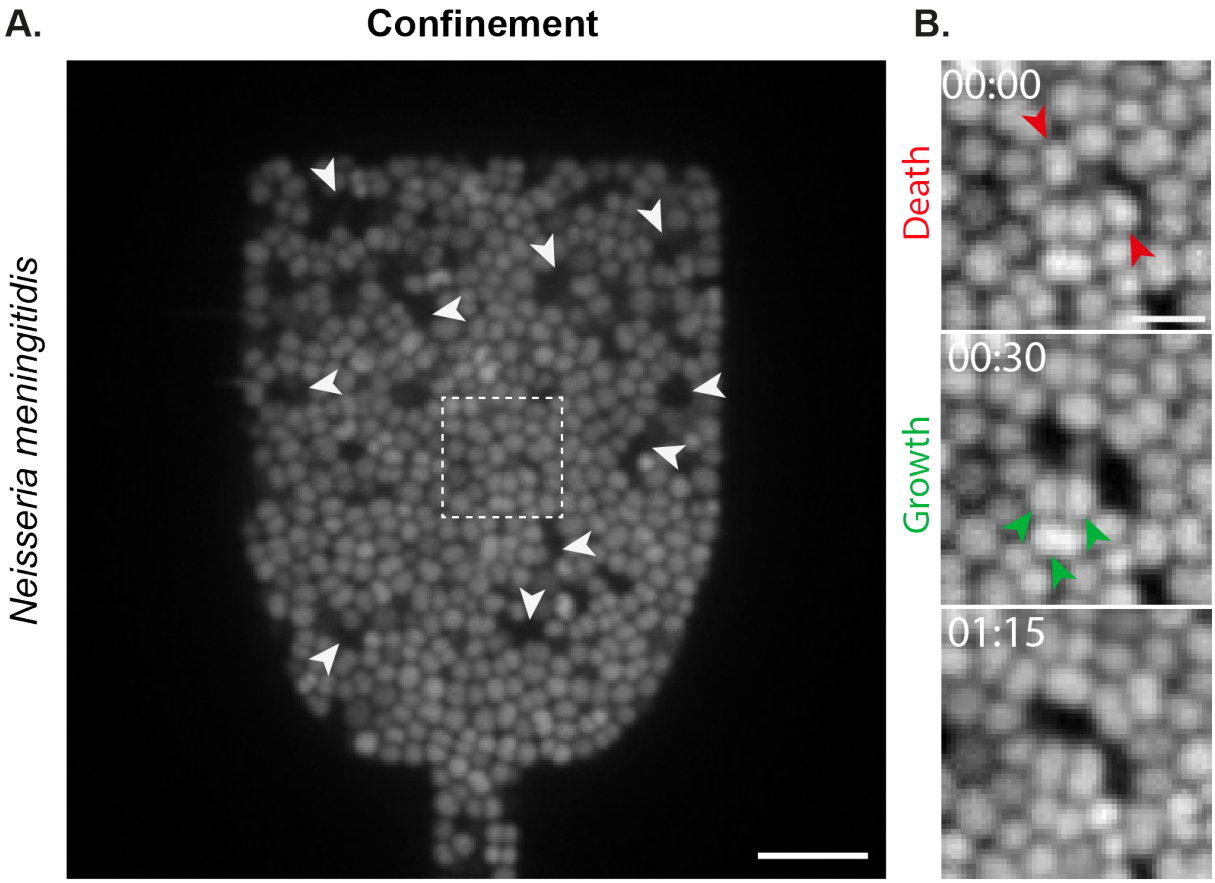


**Figure 44: *Neisseria meningitidis* adaptation to confinement is characterized by a higher rate of autolysis.** A. By looking at a confined chamber, one can see that *Neisseria meningitidis* confinement is characterized by the presence of many dark islands, depicted by white arrows. Scale bar: 5µm. B. Evolution in time of the inset depicted in A. Two confined bacteria depicted by a red arrow (top) die (middle), leading to the apparition of a dark island (middle). In the meantime, their neighbors depicted by a green arrow grow (bottom). *Scale bar: 1µm. Time hh:mm.*

## 2.3 Towards a universal response to mechanical confinement?

In this section, we compare our results to the eukaryotic response to confinement to identify and discuss potentially conserved and/or specific adaptation strategies among the different kingdoms.

### 2.3.1 Similarities between prokaryotic and mammal cells

This section has been motivated by a very recent publication, that describes epithelial cell response upon tissue confinement with a special interest in size and division regulation *(Devany et al., 2023)*. In this work, Devany and colleagues show that epithelial tissue confinement induces cell growth arrest at the onset of confinement, while division is progressively inhibited. This uncoupling between growth and division leads to a decrease in cellular volume, through successive slow division events in the absence of cell growth, until the cell cycle is arrested near a minimal size. This minimal size is set by the genome, and corresponds to the minimal size to which the nucleus is able to pack DNA while preventing its damage *(Devany et al., 2023)*. These findings are strikingly similar to the results described in this PhD work. Despite eukaryotic systems are characterized by various complex molecular regulatory mechanisms that are absent in the bacterial world, these similarities suggest the underlying presence of common, conserved mechanisms to respond to confinement.
On the one hand, Devany and colleagues propose that cell division is regulated solely by cell volume upon confinement, the smaller cells having the lower division rate, as we show in bacteria *(Devany et al., 2023)* (Figure 28D, 31A). Taken together, this suggests that division regulation is governed by a conserved biophysical parameter that relates cell volume to cellular function, such as cytoplasmic *crowding (Mourão et al., 2014)* despite not mentioned in Devany's work).
On the other hand, similar to bacteria, eukaryotic mammal cells reach a minimal size upon confinement *(Devany et al., 2023)*. The authors show that cell divisions stop near a minimal cell size before inducing DNA damage, in a cyclin D1-dependent process. Similarly, in our case, we suspect that bacterial division arrests to protect the DNA from bisection, in a SlmA-mediated process. This suggests that while division under confinement is potentially regulated by a common physical mechanism across the different kingdoms, division arrest is rather mediated by organism-dependent molecular mechanisms, that act as checkpoints to protect genome integrity.

### 2.3.2 Similarities between prokaryotic and yeast cells

In this work, we show that bacterial growth upon confinement is characterized by an increase in crowding at the onset of confinement, which results from an uncoupling between growth and division (Figure 36). Similarly, an increase in crowding upon confinement has also been described by M.Delarue and his former Ph.D. student in the budding yeast *Saccharomyces cerevisiae*, which has been shown to ultimately limit growth under pressure *(Alric et al., 2022)*. In this line, a previous work on bacteria has

reported that the formation of protein misfolding condensates (that are part of the protein misfolding stress response studied in this work – Figure 33E), which are a hallmark of aging, correlates with a decrease in growth rate *(Lindner et al., 2008)*. As crowding is known to impair protein folding *(Zhou et al., 2008)*, we suspect that a similar mechanism mediating growth arrest could also happen in bacteria.

In this work, we also show that confinement-induced morphological changes are reversible. More precisely, we observe that bacteria start to regrow as soon as the pressure is released, and tend to reach their homeostatic size in a few hours only (Figure 30). Interestingly, a similar phenomenon, referred to as supergrowth, has been reported in fission yeast *Schizosaccharomyces pombe (Knapp et al., 2019).* In particular, Knapp and colleagues have shown that, after a period of increase in crowding, induced by abnormal growth rate reduction through osmotic shocks, yeast cells transiently regrow much faster than in homeostatic conditions, in a process called "supergrowth" which depends on their cell-wall biosynthetic machinery. Ultimately, this transient increase in growth rate dilutes the excess in proteins and allows yeast to recover homeostatic cytoplasmic protein concentration *(Knapp et al., 2019).* Given the similarity, we propose that supergrowth could also drive bacterial growth recovery upon pressure release, in the context of bacterial confinement.

### 2.3.3 Differences between prokaryotic and eukaryotic cells: impact of crowding

This work suggests that a confinement-mediated increase in molecular crowding is the main trigger of bacterial division upon confinement. Strikingly, a previous study from our collaborator M.Delarue shows on the contrary that a pressure-mediated increase in crowding leads to a coordinated slow-down between cell growth and division, without any uncoupling between the two processes and no major changes in cell size *(Alric et al., 2022).* Yet, how do changes in crowding impact bacterial and eukaryotic physiology to such a different extent?

In this work, we express GEMs nanoparticles in bacteria and quantify their diffusion within the cytoplasm, as a readout of crowding, in *E. coli* (and *N. meningitidis* – not shown) and find a mean value ($D_{bacteria\text{-}GEM40}$ = 0.07 $\mu m^2/s$ – Figure 35) about 7 times smaller than the one measured in eukaryotic cells using the same tool ($D_{HeLa\text{-}GEM40}$ = 0.5$\mu m^2/s$ - *(Delarue et al., 2018)*, showing that, in homeostatic conditions, bacteria are much more crowded than eukaryotic cells, in agreement with previous studies *(Berg et al., 2017; Swaminathan et al., 1997).*

Beyond the level of crowding, the impact of crowding on cell physiology is also highly dependent on cell types as the mechanisms used to perform a given task are different. For instance, trafficking is only mediated by diffusion in bacteria, while eukaryotic cells have evolved active transport systems to carry proteins between their various

compartments *(Pedrero, 2013).* Because of this key difference, bacteria have to tightly regulate their level of homeostatic crowding to maintain protein trafficking and key cellular processes essential to their proliferation *(Berg et al., 2017; Neurohr and Amon, 2020).*
Another main difference between prokaryotic and eukaryotic cells relies on the control of cell division. While the division is triggered at a threshold of FtsZ number in *bacteria (Si et al., 2019),* the division is rather dependent on a relative concentration between an activator protein and an inhibitor one in yeasts *(Delarue et al., 2017; Schmoller et al., 2015).*
In sum, this suggests that even though crowding is a highly conserved phenomenon across the different kingdoms, its impact on cell physiology is cell-type specific. Nevertheless, it seems more stringent in bacteria than in eukaryotic cells, as exemplified by cell division in this project.

Altogether, the similarities between bacteria and eukaryotic cells support the idea that cell response to confinement is essentially driven by a universal biophysical parameter (such as cytoplasmic crowding), that emerges from the slow-down of growth and its uncoupling from protein synthesis. Yet, to which extent cell physiology is impacted by this parameter depends on the organism of interest through organism-specific molecular mechanisms. In the future, modeling could help to provide a better understanding of the crosstalk between crowding and cell physiology in various organisms by exploring the impact of crowding fluctuations *in silico*.

# 3 How could confinement determine infection outcome?

In this section, I discuss the relevance and the functional consequences of confinement during infection.

## 3.1 Is confinement relevant in the infectious context?

In this work, we show that *E. coli* proliferation in space-limited PDMS chambers generates large mechanical forces onto the microenvironment, in the range of 100kPa. This result has been obtained for various *E. coli* strains, including a lab strain and an uropathogenic one, responsible for urinary tract infections in humans (Mora-Bau et al., 2015)(Figure 27B). Yet, is this relevant in the infectious context?
During urinary tract infections, *E. coli* bacteria have been reported to infect uroepithelial cells in the form of bacterial factories, which are dense intracellular bacterial colonies (written IBCs), both *in vivo* and *in vitro (Mulvey et al., 2001; Sharma et al., 2021).* IBCs have been also observed in clinical samples from human patients and their formation is a key step of the infection cycle *(Rosen et al., 2007).* Interestingly, the formation of these bacterial factories is inhibited by the use of the bacteriostatic agent TMP-SMZ, which blocks bacterial proliferation *(Mulvey et al., 2001)*, showing that bacterial proliferation within the host cytoplasm is responsible for the formation of these IBCs. More importantly, 6 hours after bacterial inoculation, infected cells exhibit a bump shape, while the non-infected ones remain flat *(Anderson et al., 2003; Mulvey et al., 2001).* Using a bladder-on-chip, Sharma and colleagues have also shown that these IBCs eventually explode, leading to bacterial shedding *(Sharma et al., 2021).* Collectively, these observations strongly suggest that bacterial proliferation within IBCs could exert pressure on the host membrane, eventually triggering cell bursts.
To determine which intracellular pressure a eukaryotic cell could sustain before bursting, we make an analogy with hypoosmotic shock, during which a cell inflates due to an osmotic imbalance between the external environment and the cytoplasm. As an order of magnitude, a hypoosmotic shock of about 50 mOsm/L is sufficient to trigger cell burst *(Božič et al., 2020)*, which roughly corresponds to an osmotic pressure of 100kPa. Altogether, this suggests that bacterial IBCs form during urinary tract infections are indeed able to generate pressures similar to the one exerted in the bacterial confiner.

Another supporting factor relies on the emergence of force-induced morphological changes. Indeed, 6 to 8 hours after infection, *E. coli* bacteria within tightly-packed IBCs have been previously characterized by their striking small length, around 0.7µm$^2$, giving them the appearance of cocci *(Justice et al., 2004).* Yet, this measurement was done on poor-quality epifluorescence images. Also, very little is known on the mechanisms involved in this morphological transition when bacteria proliferate within

IBCs *(Flores-Mireles et al., 2015)*. To better characterize bacterial cell shape in IBCs at high resolution, we are currently trying to reproduce these IBCs in vitro and ex vivo in collaboration with M.Ingersoll (Institut Cochin, Paris, France). In any case, this measurement is in close agreement with the one we measured (0.55 $\mu m^2$ at 300kPa, 0.7$\mu m^2$ at 125kPa – Figures 27B, 28D), underscoring the relevance of our experimental model.

Nevertheless, the reason behind the bacterial morphological transition observed during urinary tract infections was so far unknown. In this work, we show that bacterial proliferation in a limited space is sufficient to reproduce the key physiological features observed during these infections. Therefore, we propose that mechanical confinement drives bacterial morphological changes and adaptation within dense bacterial aggregates encountered in the infectious context, such as within IBCs during urinary tract infections.

## 3.2 What are the functional benefits provided by confinement during infection?

In this section, I discuss how confinement could participate in disease progression and infection outcome, focusing on bacterial dissemination, escape from the immune response, and the emergence of antibiotic tolerance.

### 3.2.1 A way to increase bacterial dissemination during infection?

In this work, we show that confinement increases the number of bacteria packed within a limited space (by a factor 3 of to 5 - Figure 27C), by triggering divisions in the absence of growth. Also, we show that confinement-induced morphological transition is reversible as soon as the pressure is released (Figure 30). Based on these results, we posit that confinement favors bacterial dissemination by increasing the amount of bacteria that are likely to further infect the host. For instance, when *E. coli* cocci are released from uroepithelial cells (due to cell exfoliation or burst), their large amount could increase the chances to further spread and invade new host cells, in a robust cycle that alternates "hidden", intracellular bacterial proliferation and extracellular dissemination. This could in turn favor the observed resurgence of urinary tract infections *(Mulvey et al., 2001)*.

We also show that bacterial proliferation upon confinement generates a large pressure on the microenvironment (~ 300 kPa) (Figure 27B), which is much higher than common mechanical stresses encountered in host tissues in homeostatic conditions.
As mentioned previously, we suppose that this force is sufficient to disrupt the cell membrane during urinary tract infections, thereby allowing bacterial shedding and further dissemination before exfoliation.

Beyond physically disrupting the host cell, we posit that growth-induced pressure is also sufficient to weaken or even fracture tissue barriers such as epithelia and endothelia, in line with a previous study *(Cont et al., 2020)*. Indeed, the maximal stress sustained at cell-cell junctions in these tissues is in the order of 20kPa only *(Charras and Yap, 2018)*! As an illustrative example, *N. meningitidis* is known to form confined aggregates filling up the lumen of infected vessels from 6 to 16 hours post-infection. At similar timescales, this bacterium is also known to induce vascular damage and breaching *(Manriquez et al., 2021; Melican and Dumenil, 2012)*. Thus, it is tempting to speculate that confinement could, in this case, could provide an explanation for endothelium disruption, thereby favoring bacterial dissemination in other regions of the body.

In sum, we propose that confinement favors bacterial dissemination over the course of infection, by increasing the number of bacteria encased in a limited space and/or by generating large forces, that could potentially disrupt biological barriers.

### 3.2.2 A way to escape the immune response?

During meningitis, *N. meningitidis* bacteria rapidly fill up the lumen of infected vessels, preferentially capillaries (Mairey et al., 2006), which correlates with poor clearance by immune cells (Manriquez et al., 2021). In this part, we envision that several features of bacterial growth upon confinement could reduce the efficiency of bacterial clearance by immune cells during infection, for two different reasons. First, the tight packing of bacteria within confined aggregates might prevent immune cells access within the infection site. Second, the mechanical properties of confined aggregates might reduce the ability of immune cells to engulf them (Stewart, 2014). Indeed, in case the bacterial aggregate is bigger than immune cells, cells have to break it into small pieces to clear it. However, immune cells have been reported to exert pressures in the order of 1kPa on their target (Kovach et al., 2017; Vorselen et al., 2020; Yan and Bassler, 2019), which is by far lower than the pressure exerted by bacteria upon confinement (~100 kPa), suggesting that immune cells cannot easily crumble confined aggregates. Collectively, this suggests that confinement could provide another piece of information regarding bacterial escape from the immune system, as exemplified by *N. meningitidis* fulminant disease progression *(Manriquez et al., 2021; Melican and Dumenil, 2012)*.

### 3.2.3 A way to tolerate antibiotic treatment?

During both urinary tract and *N. meningitidis*-caused infections, bacteria are known to become less susceptible to antibiotics *(Deuren et al., 1993; Hunstad and Justice, 2010)*. In the case of urinary tract infections, this phenomenon has long been associated with *E. coli* intracellular lifestyle shielded from the external environment by the host membrane *(Mulvey et al., 2001)*. Yet, in a recent study, Sharma et al. have shown that most of the intracellular bacteria die after antibiotic treatment, but some

eventually regrow afterward *(Sharma et al., 2021)*. Taken together, we posit that confinement-induced physiological changes could also mediate the emergence of antibiotic tolerance.

Confinement could mediate the emergence of antibiotic tolerance in two ways, either by preventing antibiotic access to the core of the aggregate due to a lower permeability, or by inducing force-induced bacterial physiological changes. To investigate whether confinement leads to the emergence of antibiotic resistance and if yes, for which reason, we assess bacterial response in the presence or not of confinement to ciprofloxacin (40x MIC), an antibiotic clinically used to treat this infection *(Krcmery et al., 1999)*, by using a strain expressing a RecA fluorescent stress reporter, which is turned on by ciprofloxacin (see Materials & Methods – part 1.4) but not by confinement (Figure 33G). In other words, in this experiment, we use the fluorescence of the RecA stress reporter as an indicator of the presence of ciprofloxacin in close proximity of individual bacteria. Interestingly, we observe that bacteria die in the presence of ciprofloxacin in about 1.5 hours in the absence of confinement, as reported by the decrease in RecA-mediated fluorescence (Figure 45). By contrast, upon confinement, bacteria respond at longer timescales and heterogeneously depending on their location within the chambers (Figure 46). More precisely, while bacteria located at the edges of the chambers die quite rapidly after triggering the antibiotic perfusion, the ones located in the center start to die after about 10 hours of treatment, even if they are rapidly in contact with the antibiotic (Figure 46). Also, I noticed that bacteria located in the center of the chamber respond heterogeneously to the antibiotic. After 10 hours of treatment, while most of them are dying, some of them are very bright, suggesting that they are stressed but alive (Figure 46). To determine whether these bacteria could regrow after the treatment, I perfused fresh culture medium within the chambers and monitored the bacterial state for 5 hours. I observed that very few bacteria regrow after 10 hours of treatment, yet without dividing (Figure 47). Despite preliminary, this promising experiment shows that bacteria are indeed much less susceptible to antibiotics upon confinement than in normal growth conditions.

The force-induced physiological changes described in this work that could provide a fitness advantage to the bacteria to tolerate treatments can be separated into two categories: morphological and transcriptional changes. First, morphological changes from a rod to a cocci-like shape have been shown through modeling to increase the tolerance of bacteria in response to not membrane-bound antibiotics, such as ciprofloxacin, by decreasing the surface-to-volume ratio *(Ojkic et al., 2022)*. Second, transcriptional reprogramming can also participate in antibiotic tolerance by favoring the entry into a slow-growth quiescent state characterized by low metabolic activity *(Morrison et al., 2023)*. Yet, whether the potential fitness advantage provided by confinement is either related to the first hypothesis, the second one, or a combination

of the two is not clear so far. To go further, it would be interesting to assess the response to antibiotics of various mutants of interest (shape, or metabolism) in the bacterial confiner to identify key regulators of antibiotic tolerance upon confinement.

In sum, confinement is likely to provide key advantages to the bacterial population by favoring bacterial dissemination and the emergence of antibiotic tolerance. Confinement also protects the bacteria located in the core of the aggregate by providing them a hard-to-reach hiding place, which potentially serves as a shield against the immune response and antibiotic treatments.

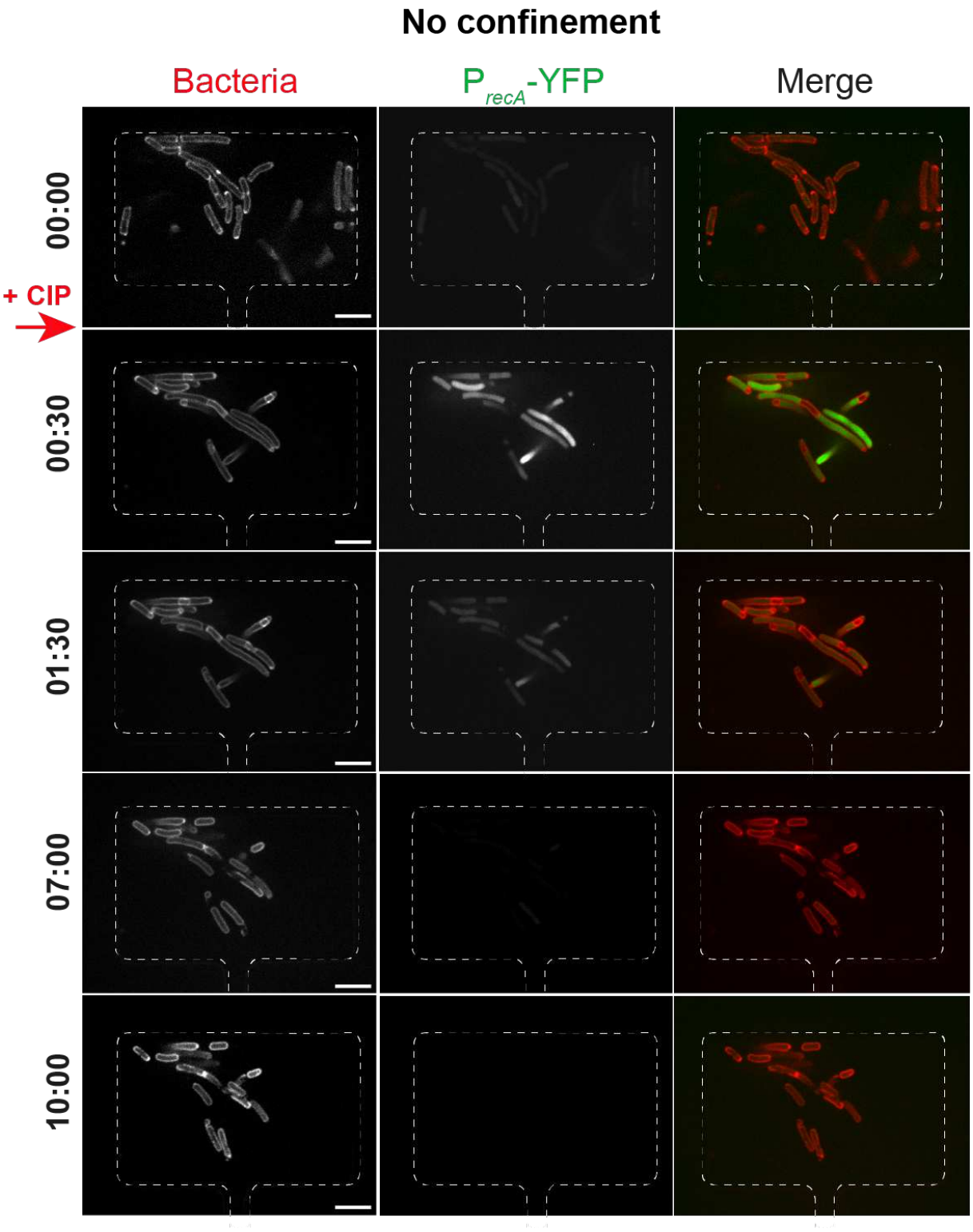


**Figure 45 : In absence of confinement, *Escherichia coli* bacteria rapidly die in presence of ciprofloxacin (CIP).** *Escherichia coli* bacteria (left) expressing $P_{recA}$-YFP (middle) were loaded in the chamber (Time 0). About one minute after, unconfined bacteria were submitted to ciprofloxacin at a concentration of 40x MIC until the end of the experiment. Bacterial state in the chambers was then monitored over 10 hours. RecA-mediated green fluorescence is used as an indicator of the presence of ciprofloxacin in proximity to individual bacteria. *Scale bars: 5µm. Time hh:mm.*

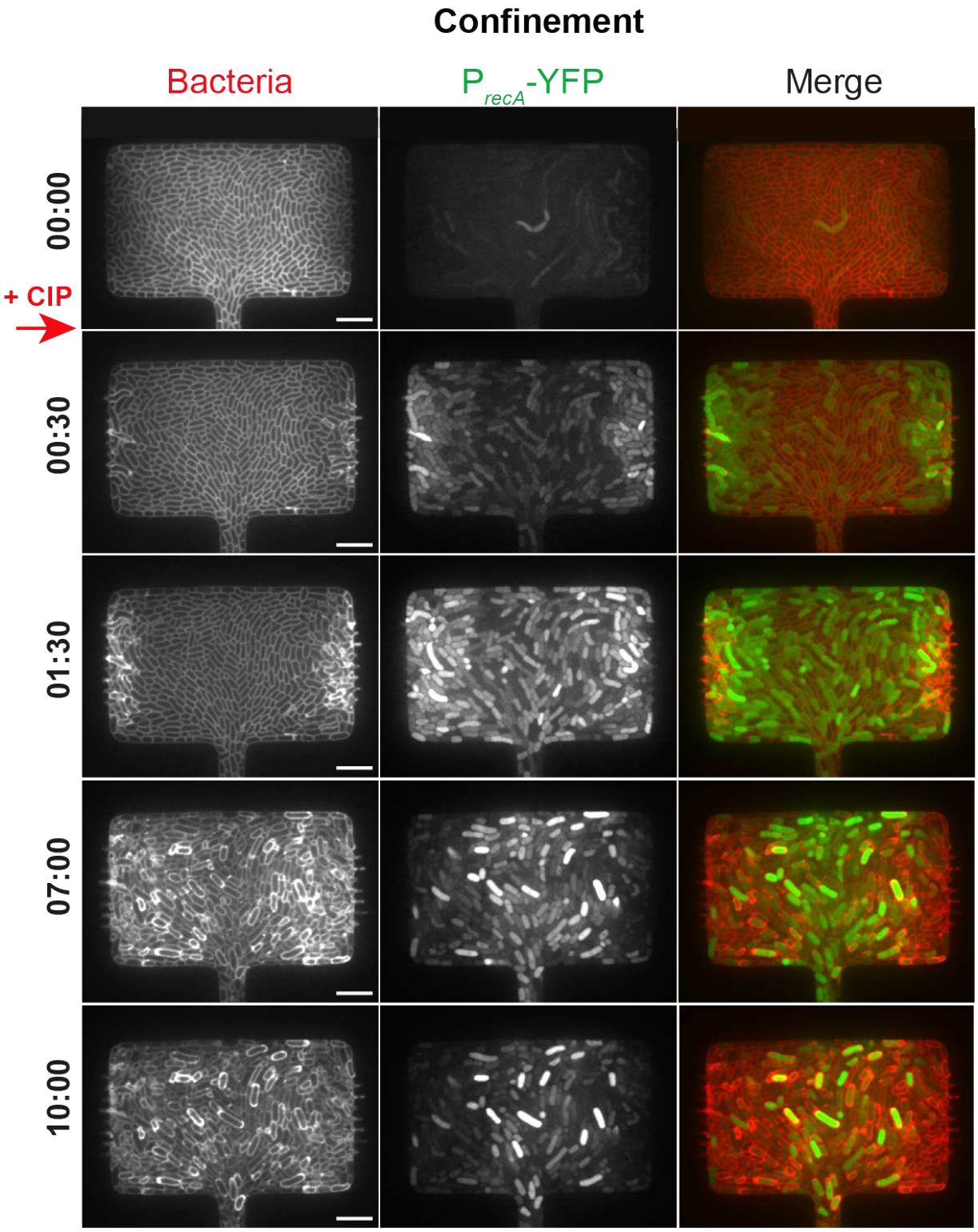


**Figure 46: Upon confinement, *Escherichia coli* bacteria survive much longer to ciprofloxacin (CIP).** *Escherichia coli* bacteria (left) expressing PrecA-YFP (middle) proliferate in the chamber, ultimately reaching confinement (Time 0). About one minute after, confined bacteria were submitted to ciprofloxacin at a concentration of 40x MIC until the end of the experiment. Bacterial state in the chambers was then monitored over 10 hours. RecA-mediated green fluorescence is used as an indicator of the presence of ciprofloxacin in proximity to individual bacteria. *Scale bars: 5µm. Time hh:mm.*

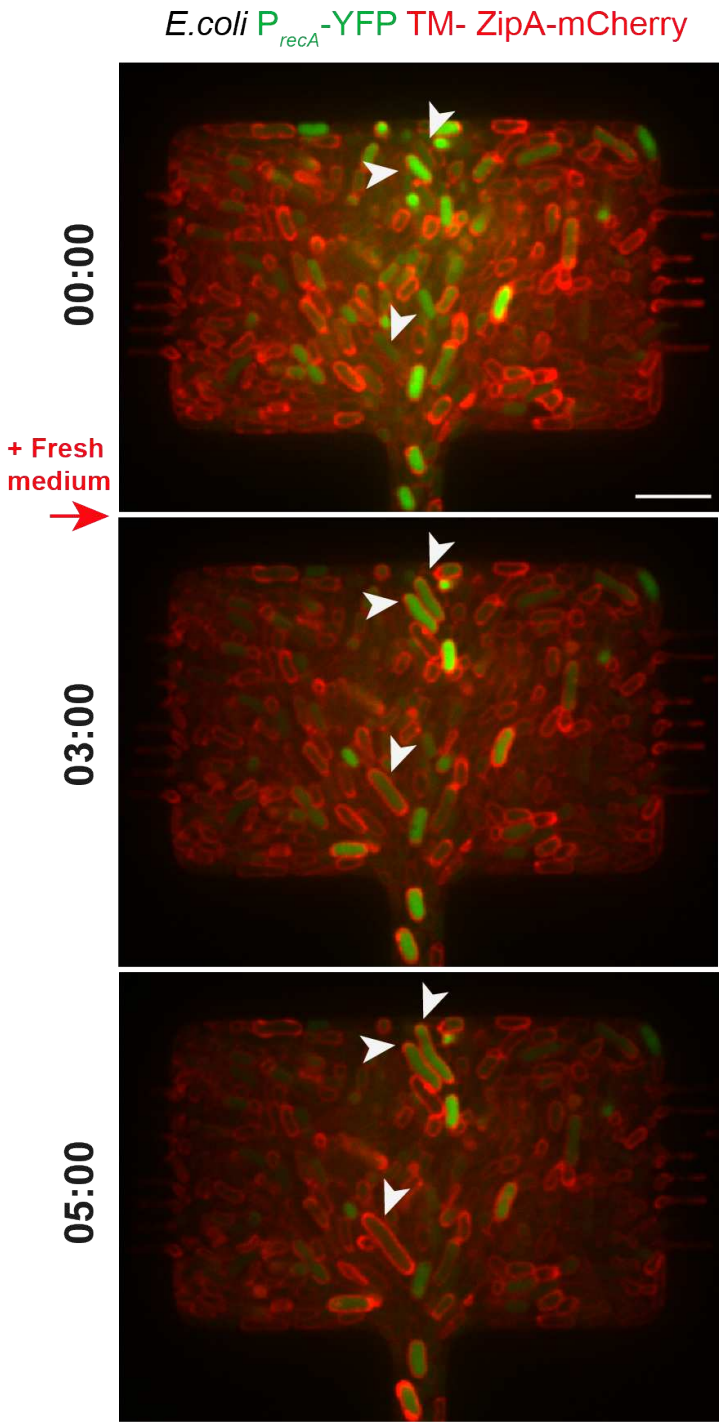


**Figure 47 : After 10 hours of antibiotic treatment, confined bacteria eventually regrow, yet without dividing.** After the treatment, bacteria were submitted to fresh culture medium, about one minute after the first image. Few bacteria regrow in presence of fresh medium as indicated by the white arrows, but no division was observed in the course of the experiment. *Scale bar: 5µm. Time: hh:mm.*

# General conclusion & Outlook

Bacteria frequently proliferate in the form of dense multicellular aggregates or communities, such as the so-called biofilms, which are often associated with complicated diseases. Within these communities, bacteria grow in a constrained environment, limited by their neighbors and eventually by extracellular structures such as the extracellular matrix. Despite it is now well appreciated that bacteria face mechanical constraints within such communities, how they adapt to these mechanical constraints at the single cell level remains elusive, despite its ubiquity in the infectious context.

To address this question, we have developed cutting-edge microfluidic growth chambers with nanometric features as a model of confinement, where bacteria proliferate in a controlled mechano-chemical environment. By using the bacterium *Escherichia coli* as a biofilm-forming model organism, we have shown that bacterial proliferation upon confinement exerts a large growth-induced pressure onto the microenvironment, thereby generating a new mechanical environment. By combining high-resolution time-lapse optical microscopy with a novel machine-learning-based image analysis pipeline, we have characterized for the first time bacterial adaptation in real time in regards to pressure build-up at the single-cell level. We have found that, as soon as the pressure builds up in the chamber, bacteria undergo major reversible morphological changes due to an uncoupling between growth and division. Specifically, whereas growth is arrested at the onset of confinement, division persists for a while in a process mediated by both the Rcs envelope stress response and probably by a crowding-mediated increase in cytoplasmic protein concentration. Division is then arrested near a minimal size, that seems to be determined by DNA content. We also found that these bacteria are characterized by strong transcriptional reprogramming. Together, we show that confinement induces the emergence of a unique bacterial phenotype, characterized by both a peculiar morphology and transcriptional profile.

Importantly, we propose that confinement is relevant in the infectious context. Indeed, thanks to the bacterial confiner, we were able to reproduce bacterial morphological changes observed during urinary tract infections, which were unexplained so far. We can thus hypothesize that mechanical confinement is the main driver of this morphological transition during infection, potentially leading to bacterial adaptation within biofilm-like intracellular bacterial colonies and higher survival rates. In addition, beyond *E. coli*, I believe that all the development performed in this project, in terms of microfabrication and image analysis, will pave the way to the study of confinement in other bacterial species and infectious contexts.

To sum up, this study has proven that bacterial confinement is a novel important feature in the process of host invasion and dissemination by using *Escherichia coli* as a model organism. It has also raised several open questions that need to be addressed in the future. For instance, what is the exact molecular mechanism used by bacteria to sense confinement? How is bacterial physiology affected by confinement at different time and length scales? Is there a molecular sensor acting as a master regulator of pressure build-up? How do confinement-induced physiological changes impact the expression of virulence factors? Also, by favoring the emergence of a unique transient vegetative bacterial state, confinement might play a role in infection outcome, by increasing bacterial dissemination and potentially favoring antibiotic tolerance. So, what are the functional benefits provided by confinement in terms of bacterial survival? By which mechanisms? I would love to answer these questions.
Although the current experimental setup can be used to address some of these questions, additional improvements could further facilitate the investigation of these questions in the future. Among them, here are three key examples:

- The use of deformable hydrogel beads as precise local force sensors (collaboration with D.Vorselen (Wageningen University, The Netherlands - (Vorselen et al., 2020)). In preliminary experiments, we show that these beads can be used in the bacterial confiner to measure local forces that arise from the proliferation of *E. coli* at the onset of confinement, slightly before being measurable through chamber deformation (**Figure 48**). In addition, another preliminary experiment suggests that, after functionalization, these beads can serve as force sensors within an in vivo model of Nm-caused infections,

- The fixation and cutting of the chips to perform FIB-SEM and cryo-ET to reach nanometer resolution,

- The improvement of the chip design to recover bacteria from the chambers for RNA sequencing, transcriptomics, and mass spectrometry analyses to get both genetic and molecular insights.

Overall, these technical improvements promise to open new doors in the knowledge of the impact of confinement on bacterial physiology and disease progression, at the cellular, subcellular, and molecular level.

As a last comment, I truly believe that bacterial confinement has many important implications for infection outcome, to which this study has just scratched the surface.

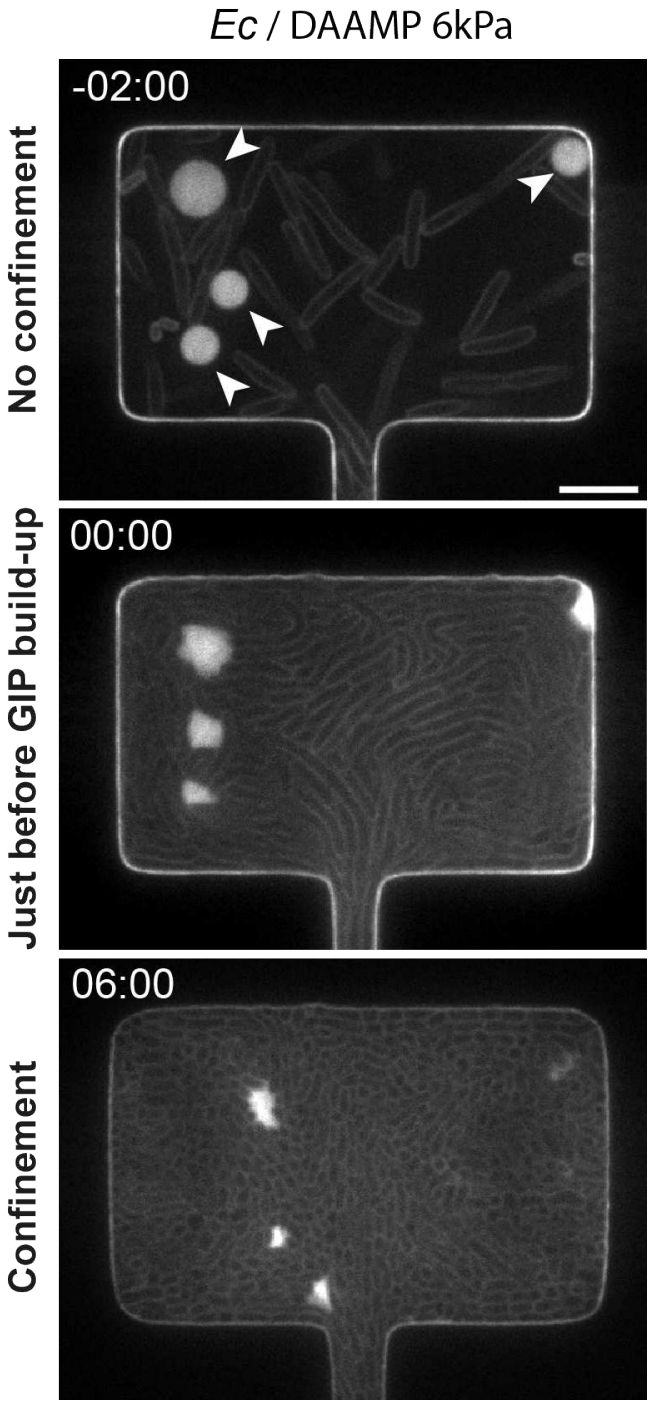


**Figure 48: Deformable hydrogel beads can be used as local force sensors within the bacterial confiner.** *E. coli* bacteria were initially loaded in the bacterial confiner in the presence of DAAMP hydrogel beads characterized by a Young modulus of 6kPa (depicted with white arrows, top). Once bacteria reach confluency, at the time at which pressure builds up in the chamber (Time 0), hydrogel beads are deformed, showing that bacteria already exert forces, despite being non-detectable through chamber deformation (middle). Upon confinement, the hydrogel beads are even more squeezed by the bacteria, which exert large pressure onto the microenvironment, sufficient to deform the chambers (bottom). Time hh:mm. Scale bar: 5µm.

# Materials & Methods

In this chapter, I describe the methods that have been used to carry out this work.

# 1 Bacterial culture

All bacterial cultures and experiments were performed in a laboratory of safety level 2 in the host lab at Institut Pasteur (Paris, France).

## 1.1 Bacterial strains and growth conditions

The bacterial strains used in this study are listed in Tables 5, 6.

*Escherichia coli*

Genetically modified *E. coli* strains used in this study (Table 5) were derived from an *E. coli* MG1655 K12 wild-type strain obtained from *(Guyer et al., 1981)*. Bacteria were grown in liquid or solid Luria-Bertani medium (LB, BD Difco) at 37°C or 30°C when grown to perform allelic exchange experiments. Antibiotics were used at the following concentrations: carbenicillin (Cb), 100 µg/ml, chloramphenicol (Cm), 25 µg/ml, kanamycin (Km), 25 µg/ml, tetracyclin (Tc), 2.5µg/ml.

*Neisseria meningitidis*

Genetically modified *N. meningitidis* strains used in this study (Table 6) were derived from the 8013 /clone 12 (2C43) strain expressing the SB pilin variant *(Nassif et al., 1993)*. Bacteria were grown on Gonococcal Medium Base (GCB, BD Difco) agar plates supplemented with Kellogg's supplements *(Kellogg et al., 2014)* and, when required, 100 µg/ml kanamycin, 5 µg/ml chloramphenicol, or 2 µg/ml erythromycin at 37°C in a moist atmosphere containing 5% $CO_2$.

| *Strains* | *Description/Genotype* | *Origin (Original strain)* | *Origin* |
|---|---|---|---|
| Ec XL1Blue GFP | Ec XL1Blue pGCC2 $P_{pilE}$-GFP | Stratagene | - |
| Ec MG1655 GFP | Ec MG1655 intC::pR-mEGFP (CHN 128) | I.Matic's lab | M.-F. Bredeche |
| Ec MG1655 mKate | Ec MG1655 intC::pR-mKate (CHN 129) | I.Matic's lab | M.-F. Bredeche |
| Ec UTI89 RFP | Ec UTI89 attB::aphA-marsRFP | (Mora-Bau et al., 2015) | - |
| Ec MG1655 TM-ZipA-mCherry | Ec MG1655 $P_{zapA}$ ::TM-ZipA-mCherry2 | (Yao et al., 2012) | this work |
| Ec MG1655 FtsZ-GFP TM-ZipA-mCherry | Ec MG1655 $P_{lac}$::ftsZ-GFP $P_{zapA}$ ::TM-ZipA-mCherry2 | (Si et al., 2013) | this work |
| Ec MG1655 $pP_{rcsA}$-GFP TM-ZipA-mCherry | Ec MG1655 $P_{zapA}$ ::TM-ZipA-mCherry2 prcsA-GFP | (Zaslaver et al., 2006) | this work |
| Ec MG1655 $P_{cpxP}$-mEGFP TM-ZipA-mCherry | Ec MG1655 galK::$P_{cpxP}$-mEGFP $P_{zapA}$ ::TM-ZipA-mCherry2 | I.Matic's lab | this work |
| Ec MG1655 $P_{ibpA}$-YFP TM-ZipA-mCherry | Ec MG1655 galK::$P_{ibpA}$-YFP $P_{zapA}$ ::TM-ZipA-mCherry2 | I.Matic's lab | this work |
| Ec MG1655 $P_{yiaG}$-YFP TM-ZipA-mCherry | Ec MG1655 yiaG::$P_{yiaG}$-YFP $P_{zapA}$ ::TM-ZipA-mCherry2 | I.Matic's lab | this work |
| Ec MG1655 $P_{recA}$-YFP TM-ZipA-mCherry | Ec MG1655 recA::$P_{recA}$-YFP $P_{zapA}$ ::TM-ZipA-mCherry2 | I.Matic's lab | this work |
| Ec MG1655 ΔrcsB TM-ZipA-mCherry | Ec MG1655 ΔrcsB $P_{zapA}$ ::TM-ZipA-mCherry2 | (Baba et al., 2006) | this work |
| Ec MG1655 GEM40 pREP4 | Ec MG1655 GEM40 pREP4 | Addgene | this work |
| Ec MG1655 HU-GFP TM-ZipA-mCherry | Ec MG1655 hupA-GFP $P_{zapA}$ ::TM-ZipA-mCherry2 | (Marceau et al., 2011) | this work |

**Table 5: List of the *Escherichia coli* strains used in this study**

| *Strains* | *Description/Genotype* | *Origin (Original strain)* | *Origin* |
|---|---|---|---|
| Nm WT iRFP | Nm 8013 $P_{pilE}$-iRFP | (Bonazzi et al., 2018) | - |
| Nm WT mScarlet | Nm 8013 $P_{pilE}$-mScarlet | - | host lab |
| Nm WT pilQ-mCherry | Nm 8013 pilQ-mCherry | - | host lab |
| Nm WT lepB-sfGFP HU-mRhubarb | Nm 8013 $P_{tac}$::lepB-sfGFP pilQ-mCherry HU-mRhubarb | - | host lab |
| Nm ΔpilT iRFP | Nm 8013 ΔpilT $P_{pilE}$-iRFP | (Bonazzi et al., 2018) | |
| Nm ΔminD pilQ-mCherry | Nm 8013 ΔminD pilQ-mCherry | - | host lab |

**Table 6 : List of the *Neisseria meningitidis* strains used in this study**

## 1.2 Strains construction

In the following, the protocols used to construct the strains are detailed. Most of the *Escherichia coli* strains used in this study have been constructed by lambda-red recombination by Sylvie Goussard (UPIV, Institut Pasteur, Paris, France), and few of them have been constructed by myself by plasmid transformation or P1 phage transduction, essentially to learn the methods.

### 1.2.1 Lambda-red recombination

PCR products (detailed below) were transferred by lambda-red recombination method into *E. coli* K-12 MG1655 or derivatives transformed with the pKOBEGA or pKOBEG plasmids *(Chaveroche et al., 2000)*, which contains the **λ**-Red operon under the control of the arabinose-inducible araBAD promoter. They were dialyzed on a 0.025-µm-porosity filter and bacteria were electroporated after expression of the **λ**-Red genes obtained with 0.2 % of arabinose. The bacteria were spread on LB plates with the appropriate antibiotic and incubated overnight at 37°C. Transformants were checked by PCR and then tested for carbenicillin resistance to test loss of pKOBEGA/pKOBEG.

The PCR products that have been generated as described below:

- **hupA-GFP-Km$^R$** : A fragment hupA-GFP containing a Km$^R$ cassette was amplified from E. coli SJ156 *(Pelletier et al., 2012)* with primers ATGAACAAGACTCAACTGATTGAT (hupA-F) and GAAGAGTTATGACTACAGGCAGTG (yjaH-R).

- **zipA(TM)-mCherry2-Tc$^R$:** A fragment zipA(TM)-mCherry2 containing a Tc$^R$ cassette was created in two steps. First, the Tc$^R$ cassette was amplified from pBR322 vector *(Bolivar et al., 1977)* with primers HK022-att-Tc-F/ Tc-R, and the zipA(TM)-mCherry2 fusion was amplified from E. coli TB28(attHKpHC503) (Yao et al., 2012) with Tc-PzapA-F/HK022-att-mCherry-R. The latter PCR product plus the amplified Tc$^R$ cassette were used for a two-way overlap PCR with primers HK022-att-Tc-F and HK022-att-mCherry-R. The tet gene is oriented in the direction opposite that of zipA(TM)-mCherry2. Primers HK022-att-Tc-F and HK022-att-mCherry-R carried 50 bp of homology with the insertion region at each end (HK022 att site). The expected chromosome structure in the HK022 att site was confirmed with primers GGAATCAATGCCTGAGTG (P1) and GGCATCAACAGCACATTC (P4*) (Haldimann and Wanner, 2001).*

- **GEM40-Cm$^R$ :** The sequence encoded for the 40 nm GEM was amplified using GEM40-XhoI-F/GEM40-PmeI-R primers from the plasmid pCDNA3.1-pCMV-PfV-GS-Sapphire (Addgene #116933) (Delarue et al., 2018) and cloned into pMGC10 vector *(Ershov et al., 2022)* with XhoI and PmeI restriction sites. It contains the open reading frame encoding the *Pyrococcus furiosus* encapsulin

fused with the T-Sapphire fluorophore under the control of the inducible $P_{tac}$ promoter. Then a fragment 40nm GEM containing a $Cm^R$ cassette was created in two steps. First, the $Cm^R$ cassette was PCR amplified from *E. coli* UGB2670 (kind gift from C.Beloin) with lambda-att-Cm-F/Cm-UGB1479-R, and the 40nm GEM was amplified from the previously constructed pMGC10 plasmid with Cm-UGB1479-F/lambda-att-Sapphire-R. The latter PCR product plus the amplified $Cm^R$ cassette were used for a two-way overlap PCR with lambda-att-Cm-F/lambda-att-Sapphire-R. The cat gene is oriented in the direction opposite that of 40 nm GEM. Primers lambda-att-Cm-F/lambda-att-Sapphire-R carried 41 bp of homology with the insertion region at each end (lambda att site). The expected chromosome structure in the lambda att site was confirmed with primers lambda-att-ext5-F and lambda-att-ext3-R. The low-copy plasmid pREP4 (Qiagen) was transferred into E. coli strain expressing GEM40, it constitutively expresses the LacI repressor protein and tightly regulates recombinant protein.

### 1.2.2 Phage transduction

The strain *E. coli* ΔrcsB TM-ZipA-mCherry was constructed by P1 allelic transduction from the Keio collection *(Baba et al., 2006)* to the *E. coli* MG1655 TM-ZipA-mCherry strain *(Moore, 2011).* Transductants were verified by PCR and sequencing, with the following primers: CTTAAAGGCGTATTTGCCAT (rcsB_fwd) and GATAAAACAGACGCTGACGTTA (rcsB_rev).

## 1.3 Bacterial culture

### 1.3.1 Bacterial stocks

A few µl of bacterial suspension were diluted in 100µl of sterile water and spread on a fresh agar plate supplemented with the appropriate antibiotics. After overnight incubation, bacteria were scratched and resuspended in 1.5mL of the appropriate culture medium supplemented with 20% glycerol. Bacterial stocks were kept at -80°C.

### 1.3.2 Bacterial preculture

*Escherichia coli*

Bacteria from the frozen stock were streaked on fresh agar plates with the appropriate antibiotics and incubated overnight at 37°C. On the day of the experiment, early in the morning, bacteria from plates (maximum two weeks old) were resuspended in 5mL of filtered LB Miller culture medium, and incubated at 37°C, 180RPM over about 5 hours. Bacteria were then resuspended in 5mL of fresh filtered LB medium at an optical density at 600nm (written $OD_{600nm}$) of 0.01, and incubated at 37°C, 180RPM over 2 hours, eventually in the presence of antibiotics. After 2 hours, the $OD_{600nm}$ of the liquid broth was measured around 0.3-0.4, meaning that the bacteria reached the

exponential phase. A similar protocol was followed to get Staphylococcus aureus bacteria in the exponential phase.

*Neisseria meningitidis*

The day of the experiment, bacteria from the frozen stock were streaked on fresh agar plates with the appropriate antibiotics and incubated over 7 hours at 37°C, 5% $CO_2$. 2 hours before the beginning of the experiment, bacteria were resuspended in 5mL of fresh filtered RPMI medium supplemented with 10% Fetal Bovine Serum (written FBS) at an $OD_{600nm}$ equal to 0.05, and incubated at 37°C, 5% $CO_2$, 140RPM over 2 hours. After 2 hours, the $OD_{600nm}$ of the liquid broth reached 0.2-0.3 and the bacteria were in exponential phase.

## 1.4 Experimental validation of *Escherichia coli* stress reporters

Upon reception of the original strains and after final cloning, the fluorescence induction of the transcriptional reporters was verified upon chemical stress. In a glass bottom multiwell plate (Greiner bio one), exponentially growing bacteria were diluted at $OD_{600nm}$ of 0.01 eventually in the presence of antibiotics at various concentrations (Table 7). Green fluorescence (excitation wavelength: 485 ± 10nm, emission wavelength: 520 ± 10nm) was recorded by using an automatic plate reader (Cytation, Biotek intruments) over 18 hours under agitation at 37°C. All the strains were validated upon chemical stress before further experiments (Figure 49).

| *Stress response* | *Reporter* | *Origin* | *Inducer* | *Concentrations (µg/ml)* | *Mode of action* |
|---|---|---|---|---|---|
| *Outer membrane* | $pP_{rcsA}$-GFP | C.Beloin | Cephalexin | 0, 5, 15, 20 | Inhibit peptidoglycan synthesis (PBP3) |
| *Inner membrane Periplasm* | $P_{cpxP}$-mEGFP | I.Matic | Cephalexin | 0 5, 15, 20 | Inhibit peptidoglycan synthesis (PBP3) |
| *Protein misfolding* | $P_{ibpA}$-YvFP | I.Matic | Streptomycin | 0, 0.1, 1, 5, 10 | Inhibit protein synthesis (ribosome) |
| *Stationary phase* | $P_{yiaG}$-YFP | I.Matic | Stationary phase | - | - |
| *DNA damage* | $P_{recA}$-YFP | I.Matic | Ciprofloxacin | 0, 0.01, 0.1, 0.5, 1, 10 | Inhibit DNA replication (topoisomerase and gyrase) |

**Table 7 : Experimental conditions used to verify *E. coli* stress reporters induction upon chemical stress**

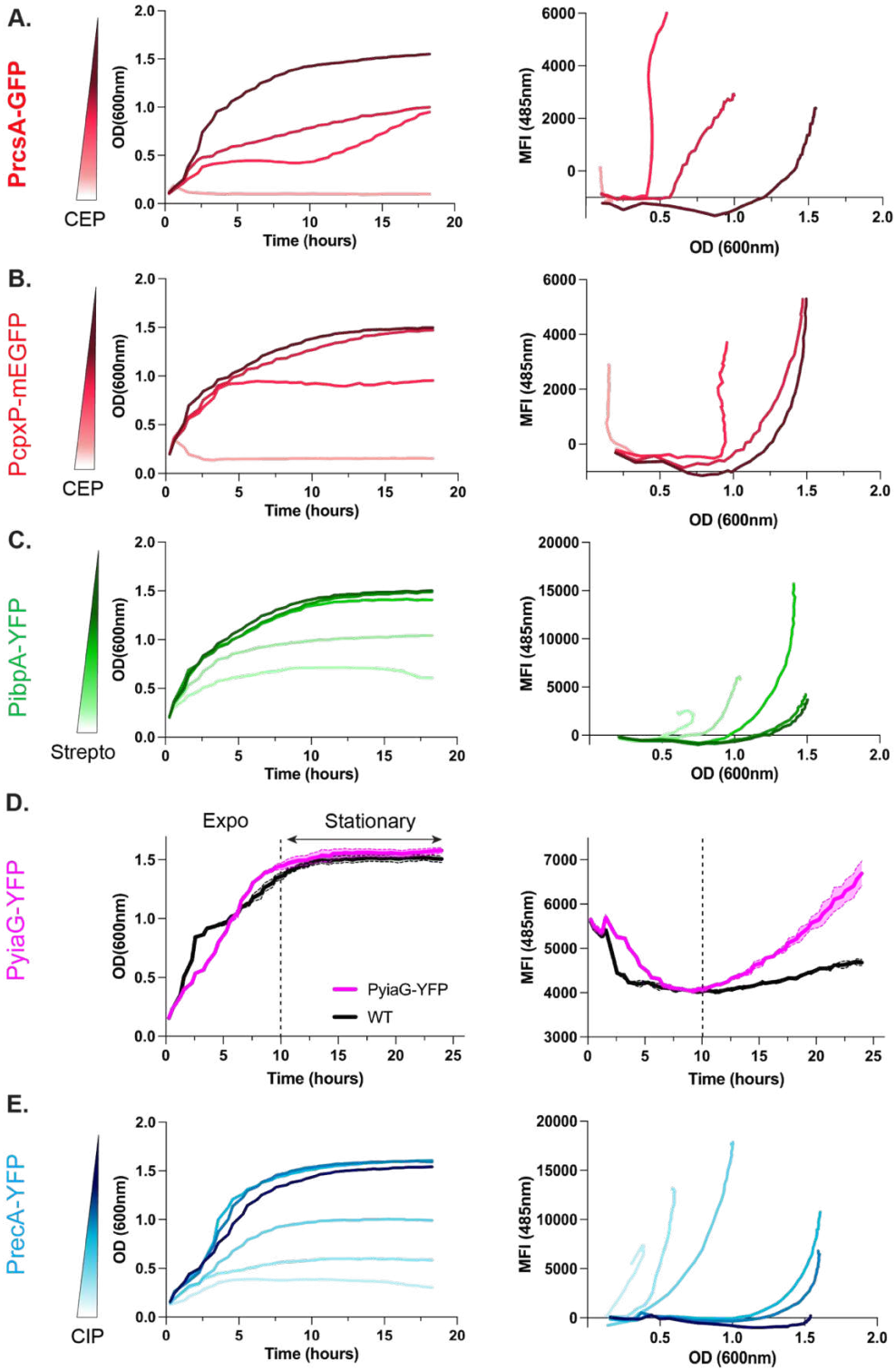


**Figure 49: Validation of the fluorescent stress reporters induction upon chemical stress.** The growth of each transcriptional stress reporter (A: $P_{rcsA}$-GFP, B: $P_{cpxP}$-meEGFP, C: $P_{ibpA}$-YFP, D: $P_{yiaG}$-YFP, E: $P_{recA}$-YFP) was assessed eventually in presence of inducers (A, B: cephalexin, C: streptomycin, E: ciprofloxacin). For each condition, the darker curve represents the control condition without chemical stress. The fluorescence was recorded and plotted as a function of the OD(600nm) to visualize fluorescence induction. At a given OD(600nm), the higher the inducer concentration, the higher the fluorescence induction.

# 2 Microfabrication

All the microfabrication work, from the chip design to the chip production, has been done in tight collaboration with M. Delarue and his former Ph.D. student B.Alric (LAAS-CNRS, Toulouse, France). In the following, I describe the protocols used to fabricate the bacterial confiner.

## 2.1 Chip design

The chip design was drawn on Clewin software, by rescaling the dimensions of the chips that are used in M. Delarue's team to confine yeasts cells. It is composed of two layers, characterized by the following dimensions:

- **Feeding nanochannels:** width = height = 300 – 400nm, length = 25 µm (**Layer 1**)
- **Growth chambers:** width = 20µm, length = 30µm, height = 2.5µm (**Layer 2**)

These two layers were then printed at the LAAS-CNRS on chromium masks adapted to the photolithography technique we used in the next part.

## 2.2 Master fabrication

This work was done in the LAAS-CNRS clean room, during 8 missions of two weeks, with the help of B.Alric and L.Mazenq, expert in photolithography. The silicon master was fabricated in a two-layer process by using stepper-based photolithography (Figure 50).

*Layer 1*

First, a 4-inch silicon wafer was cleaned using oxygen plasma. A layer of the adhesion promoter BARC was deposited and baked at 200°C during 1 minute. This was followed by the deposition of the ECI photoresist, baked at 105°C for 1 minute. The coated wafer was then introduced into the stepper and insolated using a dose of 700J/m$^2$. After a post-exposure bake and the development of the resist, the dimensions of the nanochannels (patterned positively with the resist) were measured using a scanning electron microscope (in x, y) and a mechanical profilometer (in z). Once the dimensions were in agreement with the expected ones, the coated wafer was etched for 2 minutes, although this duration was slightly adjusted on a daily basis. Indeed, the etching time was precisely estimated after a daily calibration to get a height as close as possible to the measured channels' width. Nanochannels having an aspect ratio close to 1 were a prerequisite in order to ensure their fabrication in PDMS without collapse. The resist was then removed using acetone and a cleaning plasma. The nanochannels dimensions were then properly characterized in (x, y, z).

*Layer 2*

The micrometric layer was fabricated following a similar process, except that a negative photoresist was used to directly pattern the growth chambers instead of etching. To this end, a SU8 photoresist was deposited onto the silicon wafer previously etched, and baked for 3 minutes at 95°C. The coated wafer was reintroduced into the stepper, aligned with respect to the first layer, and insolated using a dose of 3000 $J/m^2$. After a post-exposure bake of less than 3 minutes at 95°C and a development, the final dimensions of the silicon features were precisely measured using both scanning electron microscopy (in x, y) and a mechanical profilometer (in z). After a hard bake of 125°C for 2 minutes, the patterned wafer was then silanized with perfluorodecyltrichlorosilane (also known as FDTS) for 5 minutes.

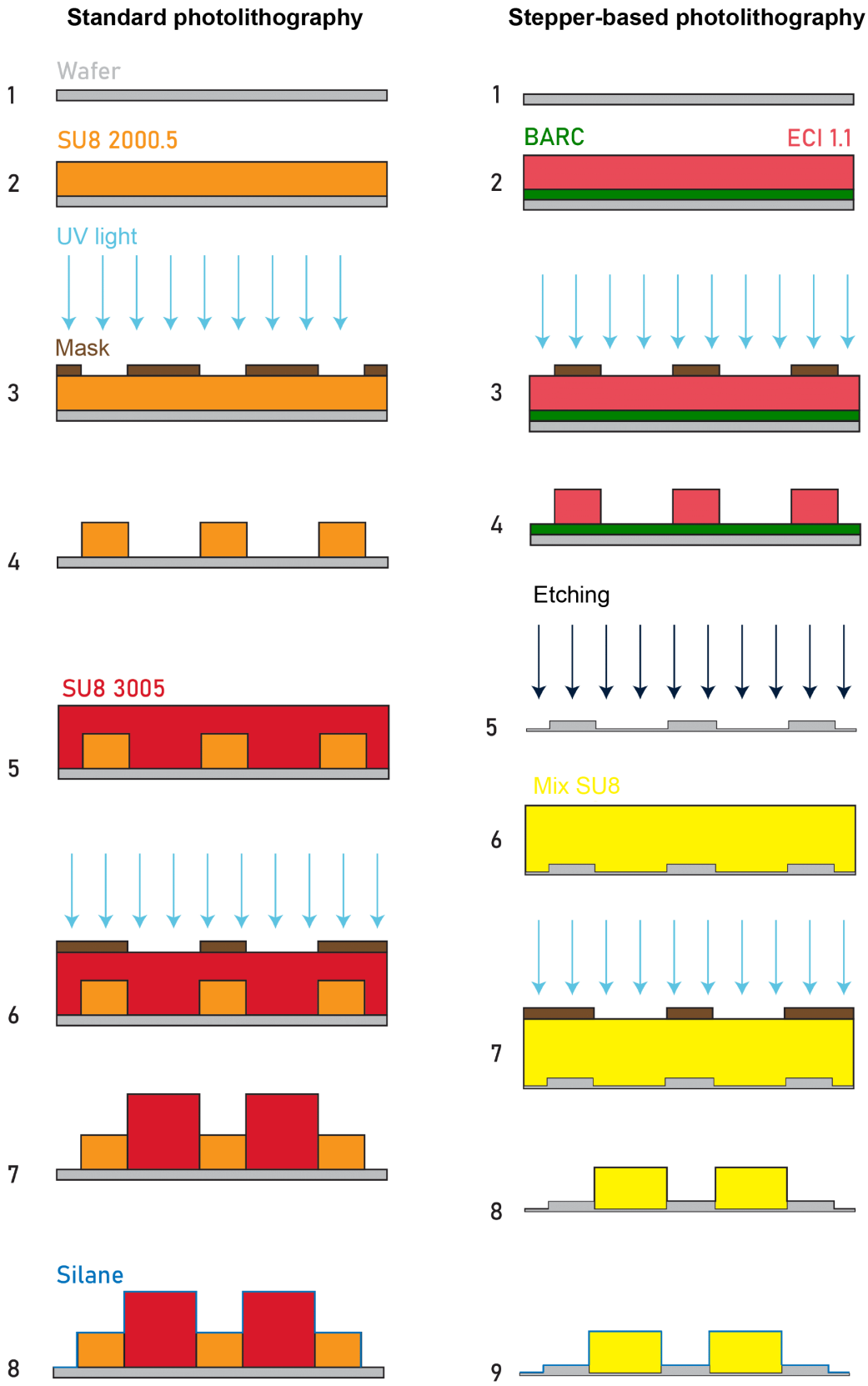


**Figure 50: Description of the microfabrication process developed in this work, which uses stepper-based photolithography (right), by comparison with standard photolithography (left).** Adapted from *(Alric, 2021)*.

## 2.3 Chip production

The chips were produced in PDMS (Sylgard 184, Dow corning) at the Biomaterial and Microfluidics plateform at Institut Pasteur as an autonomous user. To this end, a droplet of soft degassed PDMS (ratio base : curing agent = 15 : 1) was placed over the features on the silicon master and baked at 65°C during 30 minutes. A bulk of classical PDMS (ratio base : curing agent = 10 : 1) was casted, degassed and cured at 65°C overnight.
The next morning, individual chips were cut using a razor blade and holes were bored using a 0.75mm punch (Robbins Instruments). The chips were cleaned with isopropanol and air dried. In the meantime, glass coverslips (Marienfeld, 25mm round, No 1.5) were cleaned by using an ultrasonic bath during 30 minutes in deionized water supplemented with soap, 30 minutes in ethanol and finally washed in deionized water. After cleaning, the chips and the coverslips were activated using oxygen plasma (Femto Science) for 4 seconds at 60W, and rapidly bound to each other. Then, the chips were cured at 65°C for 5 hours, sterilized by using a UV ozone cleaner for 30 minutes, and further cured at 65°C for 30 minutes.

## 2.4 Adaptation of the fabrication process to confine *Neisseria meningitidis*

The process described above allows the fabrication of microfluidic chips that are suitable to confine most of the bacterial species, including *E. coli* and *S. aureus*. However, this was not sufficient to confine *N. meningitidis* bacteria that were flushed out of the chambers before reaching confinement.
To force confinement, I have improved the experimental set-up by adding a quake valve at the outlet of the chambers, that allows to artificially close them once inflated by pressure (written $P_{QV}$).

### 2.4.1 Quake valve master fabrication

The quake valves were designed as 40µm-wide straight channels on Clewin software. The fabrication of the quake valve master was performed using dry film (Vulto et al., 2004). The dry film process is similar to classical photolithography (Figure 50), except that it uses a dry film made of epoxy photoresist of well-controlled thickness (> 5 µm) instead of a liquid photoresist. In practice, a fresh 25µm thick dry film was laminated over the wafer, insolated, baked, and developed in cyclohexane. The dimensions of the channels were measured using optical microscopy. Finally, a hard-bake was performed and the silicon master was silanized.

### 2.4.2 Chip production

The quake valve-mediated closure of the chambers relies on the deformation of the 2.5µm high outlet channel roof upon pressure activation. Such deformation can be achieved only if the PDMS roof is sufficiently deformable, which depends on its stiffness and thickness. I did not change chip stiffness to keep a similar chip deformability compared with the initial experimental set-up. Rather, I chose to adjust the thickness of the chamber layer. In the following, I detail the fabrication process.

*Chambers preparation*

To get a thin chamber roof, I spin-coated 5g of soft PDMS (ratio base : curing agent = 15 : 1) on the chamber's silicon master at 7000RPM during 1 minute. The PDMS layer (~10µm thick) was cured at 65°C during 1 hour.

*Quake valve preparation*

A bulk of PDMS (ratio base : curing agent = 10 : 1) was cast over the quake valve master, degassed, and cured overnight. The next morning, the chips were cut and punched using a puncher of 0.75mm.

*Chambers – quake valve assembly*

After cleaning with isopropanol, both the spin-coated chambers master and the cut quake valve chips were activated using oxygen plasma (Femto Science) for 40 seconds at 60W. Then, the quake valve chips were manually aligned over the chamber features under the microscope. After bonding, the chamber master was cured overnight at 65°C.

*Chips preparation*

The next morning, chips were cut from the silicon master. Holes were made at the inlets/outlets of the chambers using a punch of 0.75mm. Then, the chips were bound to glass coverslips using oxygen plasma, cured during 5 hours, and sterilized.

### 2.4.3 Quake valve calibration

For each batch of chips, the deformation of the quake valve was calibrated to determine the optimal pressure $P_{QV}$ at which the quake valve closure hinders bacterial passage while allowing medium renewal. To this end, the chambers were filled with culture medium supplemented with 1mg/ml Dextran FITC 10kPa, and the quake valves were filled with (incompressible) water. The fluorescence signal below the quake valve was monitored as a function of the pressure applied in the quake valve. By plotting the mean fluorescence profile along the quake valve, I determined the optimal pressure to use: $P_{QV}$ = 4000mbar (Figure 51).

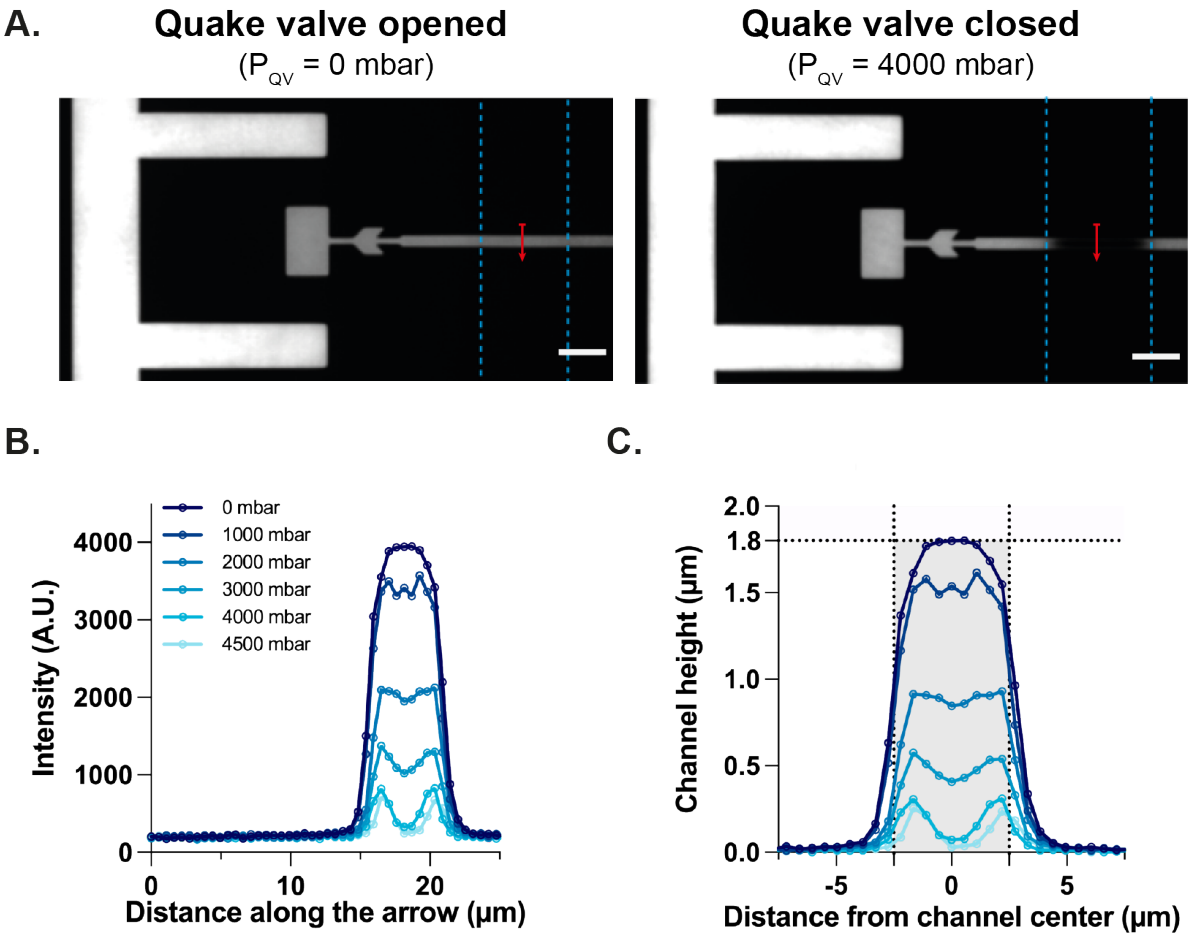


**Figure 51 : Quake valve calibration process.** A. Culture medium supplemented with Dextran 10kDa at 1mg/ml was injected into the chambers. The fluorescence intensity was monitored below the quake valve (depicted by a blue dashed line) along the red arrow. Two representative images are shown: without pressure in the quake valve ($P_{QV}$ = 0 mbar, left), and after applying a pressure of 4000mbar in the quake valve ($P_{QV}$ = 4000mbar, right). Scale bars: 20µm. B. Fluorescence intensity profile along the red arrow for a wide range of pressures applied in the quake valve, $P_{QV}$, ranging from 0 to 4500mbar. C. Corresponding height of the chamber outlet channel upon quake valve closure, as a function of the distance to the channel center.

# 3 Bacterial proliferation assays

## 3.1 Agar pads

To assess the proliferation of bacterial strains in a classical way, exponentially growing bacteria were trapped between a glass coverslip and a 2% agarose gel made of rich culture medium.

A 2% agarose gel was prepared in an erlenmeyer of 50 ml, by adding 0.2 g of agarose powder (Dutscher Scientific) into 10 ml of rich culture medium and heated in the microwave until it started to boil twice. Under the cell culture hood in the P2 lab, 2 ml of the melted agarose gel was added without bubbles on parafilm and a glass coverslip was put on top to flatten it. Once the gel had polymerized, the coverslip was removed and a slice of approximately $1cm^2$, called agar pad, was cut. Then, 2 µl of the bacterial suspension at an $OD_{600\ nm}$ around 0.015 for proliferation assay, and 0.05 otherwise, were dropped on the flat agar pad. Once the droplet dried up, meaning that bacteria had been absorbed, the agar pad was put in a fluorodish (Ibidi, 60 µ-Dish, 35 mm high Glass bottom) by flipping the surface containing bacteria on top of the glass bottom. The sample was then imaged under the microscope.

## 3.2 The bacterial confiner

To assess the proliferation of bacterial strains upon confinement, bacterial proliferation was monitored within the microfluidic chip we have developed in this work, called bacterial confiner.

### 3.2.1 Experimental set-up

Prior to the experiments, all the materials needed (tubings, connectors, needles, holder) were autoclaved at the Material Plateform (Institut Pasteur, Paris, France). The experimental set-up was put in place directly on the microscope stage, whose temperature was set at 37°C. Additionally, during Neisseria meningitidis experiments, the $CO_2$ level was set at 5%.

The experimental setup consists in:

- A microfluidic chip is placed within a screwed metal holder (Attofluor chamber, Thermo Fisher). The chip contains two independent sides which can be used to perform a control and a perturbation condition (mutant, antibiotic). Each side has one inlet for culture medium, one inlet for bacterial broth, and one culture medium outlet.
- The medium culture inlet is connected through a TYGON tubing (IN: 0.020 in, OD: 0.06 in, wall: 0.020 in, Saint Gobain) and a steel connector, to a medium

reservoir tightly closed with a P-cap (P-cap 15mL, Fluigent). This P-cap allows to connect the reservoir to the pressure controller (MFCS-EZ 7 bars 4 ports, Fluigent), and to maintain the liquid at a constant pressure fixed at $P_M$ = 1000 mbar.

- The bacterial inlet is connected to a 1ml syringe with a needle of gauge 23 (LS23, Phymep) through a TYGON tubing and a steel connector.
- The culture medium inlet is closed with a steel plug after the chip loading.

The pressure controller was connected to a computer by using the MAESFLO software (Fluigent), in order to control the pressure supply over the course of the experiments.

### 3.2.2 Chip loading

The chip loading was done in 5 steps:

- **Step 1: Tubing connections**
  - Bacterial inlet: 1mL of the exponentially growing bacteria were introduced within the syringe. After removing all the bubbles and the air contained in the syringe, the needle was connected to a TYGON tubing and a steel connector. The tubing was filled with the bacterial suspension before being inserted into the bacterial inlet of the chip.
  - Medium inlet: The tubing connected to medium reservoir was filled with liquid before being inserted into the medium inlet of the chip.
- **Step 2: Bacteria loading**
  - Bacteria were introduced in the chambers by gently pushing on the syringe.
- **Step 3: Culture medium loading**
  - The medium reservoir was pressurized at 2000mbar to fill the central channel with culture medium until all the bubbles were removed, while pushing a bit on the syringe to prevent bacterial escape from the chambers.
- **Step 4: Closure of the medium channel**
  - Once the bubbles were removed, the pressure at the medium inlet was set to 0 mbar, and a steel plug was introduced into the culture medium outlet.
- **Step 5: Definition of the new outlet of the chip**
  - Then, the tubing which connects the bacterial syringe to the chip was cut using scissors. Now, the bacterial inlet is the new outlet of the chip, thereby forcing liquid flows through the growth chambers.

- Finally, the pressure of the medium channel was set at $P_M$ = 1000mbar and monitored over the whole course of the experiment using MAESFLO software.

### 3.2.3 Calibration of the chip deformability

To control the mechanical environment encountered by bacteria upon proliferation, I calibrated the chip deformability after each experiment where a force measurement was performed. In these experiments, channel contours were stained using FM1-43 dye (AAT Bioquest). The chip calibration was done in 5 steps:

- **Step 1: Setting the pressure at the medium inlet to 0 mbar**
- **Step 2: Closure of the bacterial inlet**
  - The tubing and the steel connector at the bacterial inlet were removed and replaced by a steel plug. The medium outlet was kept closed.
- **Step 3: Assessing the deformation of the central channel in response to a range of inlet pressures**
  - The non-pressurized channel was first imaged using both the white light and the 491nm laser, in Z-stacks every 0.1µm over 5µm, at 4 different positions along the array of growth chambers.
  - Then, the medium inlet was pressurized at various pressures (200, 400, 600, 800, 1000, 2000, 3000, 4000mbar) and the deformation of the central channel was imaged in Z-stacks using the same imaging parameters. The acquisition was done 5 minutes after setting the pressure at the pressure controller to ensure equilibrium conditions.
- **Step 4: Measuring the deformation at the top of the central channel** (see part 7.1)
  - This was done for every position at each pressure.
- **Step 5: Relationship between deformation and pressure**
  - On Python, the applied pressure was plotted as a function of the mean deformation measured over the 4 positions. A linear regression fit was then performed to get the equation that relates a given deformation with the corresponding pressure.

### 3.2.4 Validation of growth-induced pressure measurement

The protocol presented in the previous part allowed us to measure the growth-induced pressure applied by bacteria upon confinement, whose maximum value is about 300 kPa (Figure 27B). To validate this measurement, we checked that the deformation measured upon bacterial proliferation was in agreement with the deformation of the chambers pressurized at 300kPa (*i.e.* 3000mbar) using the pressure controller (Figure 52).

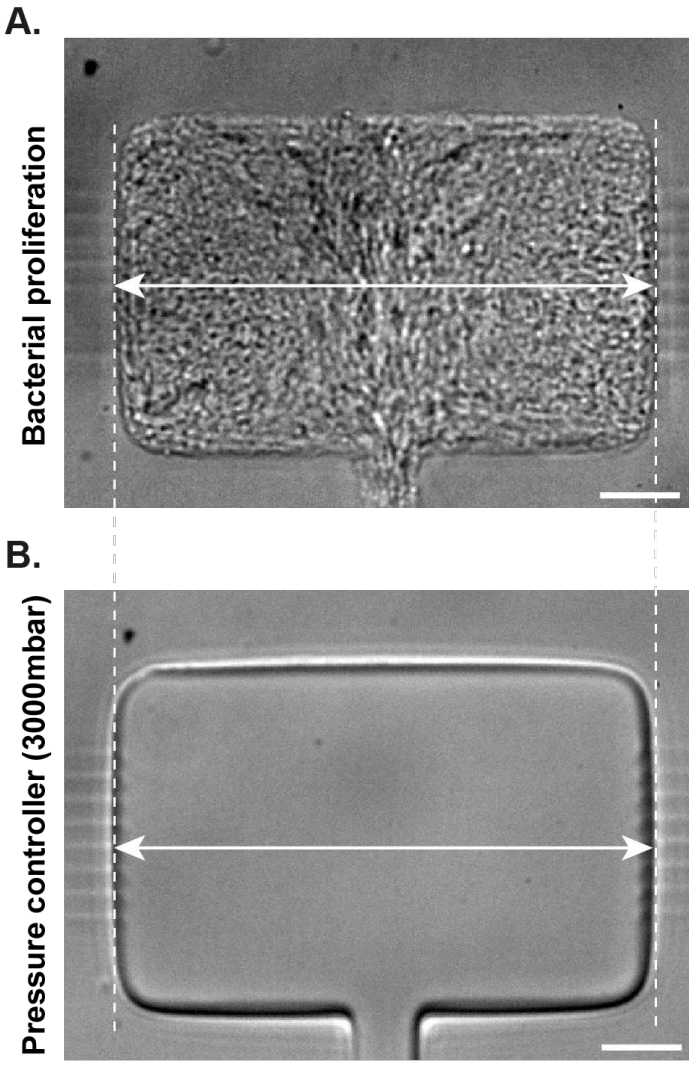


**Figure 52: Validation of growth-induced pressure measurement.** A. Chamber deformation upon bacterial proliferation after 10 hours after pressure build-up (late confinement), upon 300kPa. B. Chamber deformation induced by the pressure controller, connected at the outlet of the chamber, and set at 3000mbar (i.e. 300kPa). The white arrows represent the width of the chambers. The white dashed lines highlight the similar width of the two chambers. Scale bars: 5µm.

### 3.2.5 Chip perfusion experiments

To characterize the chemical environment encountered by bacteria upon confinement, I quantified the diffusion of culture medium supplemented with Dextran-FITC 10kDa at 1 mg/ml within the chambers, once bacteria have proliferated and eventually reached confinement.
In such experiments, instead of using a steel connector to connect the TYGON tubing to the chip, I preferred to use a short PTFE tubing (#24 AWG thin wall tubing natural, Cole Parmer) that serves as an adaptor between TYGON and the chip. Like so, tubings can be easily removed from the chip without generating important backflows, potentially destabilizing bacterial aggregates.

The characterization of medium perfusion was done in 5 steps:

- **Step 1: Closure of the bacterial channel**
  - First, I closed the bacterial inlet with a PTFE plug to prevent bacterial escape from the chamber upon medium renewal.

- **Step 2: Medium renewal within the central channel**
  - Then, I disconnected the previous medium reservoir and replaced it by a new reservoir filled with culture medium supplemented with Dextran-FITC 10kDa at 1 mg/ml.
  - After filling the tubing, I connected the new reservoir to the chip and set the pressure at $P_M$ = 1000mbar for 5 minutes. In the meantime, I imaged the fluorescence signal within the central channel during X minutes, to verify that the culture medium was well renewed.

- **Step 3: Closure of the medium channel and opening of the outlet**
  - Once the medium was well renewed, I set the pressure at 0 mbar. Also, I closed the medium channel and removed the plug from the bacterial inlet, which is now the new outlet of the chip.

- **Step 4: Medium diffusion acquisition**
  - Then, I launched an acquisition to monitor diffusion within the chip taking an image every minute for 20 minutes. The fluorescent medium was pressurized at $P_M$ = 1000mbar starting at the second timestep.

- **Step 5: Fluorescence measurements**
  - The fluorescence of the whole chamber was measured on Fiji over time. A homemade script in Python was written to compute the Mean Fluorescence Intensity (written MFI) and the Normalized Fluorescence Intensity (written NFI), defined as:

$$\left[ \text{MFI} = \frac{\text{Fluorescence Intensity}}{\text{Fluorescence Intensity (t0)}} \right.$$

$$NFI = \frac{\text{Fluorescence Intensity (t)} - \min(\text{Fluorescence Intensity})}{\max(\text{Fluorescence Intensity}) - \min(\text{Fluorescence Intensity})}$$

This protocol allows to follow the diffusion of a fluorescent medium within confined and unconfined aggregates. A similar pipeline can be used to perfuse culture medium supplemented with antibiotics within the aggregates both in the presence and in the absence of confinement.

# 4 Hyperosmotic shocks

Glass coverslips for Ibidi sticky slides (Ibidi) were treated with (3-Aminopropyl)triethoxysilane (APTES, Sigma-Aldrich) at 2% in ethanol for 15 minutes, rinsed 3 times in sterile water, and air dried. Coverslips were then stuck to Ibidi chips (sticky-slide VI 0.4, Ibidi). Exponentially growing bacteria were introduced slowly within the channels at $OD_{600nm}$ 0.2 and incubated for 10 minutes in the microscope chamber. Then, LB medium was rinsed out 5 times and replaced with fresh medium supplemented with sorbitol at various concentrations (0.25, 0.5, 0.75, and 1M). Image acquisition was launched 30 seconds after changing the medium.

# 5 In vitro infection assay

In this part, I described the protocol we are still optimizing in order to reproduce in vitro *E. coli* intracellular bacterial communities within uroepithelial cells. This work is done in collaboration with M.Ingersoll's lab (Institut Cochin, Paris, France).

## 5.1 Gel preparation

2 days before the experiment, polyacrylamide gels (written PAA) of 5kPa were prepared within fluorodishes using a protocol similar to those used for traction force microscopy (Pérez-González et al., 2019).

## 5.2 Cell seeding

The day before the experiment, G/G immortalized murine uroepithelial cells (ACC224, DMCZ) cultured on Dulbecco's Modified Eagle Medium (written DMEM) were seeded on PAA gels at a density of 400 000 cells per wells.

## 5.3 Infection

The day of the experiment, we infected the cells with stationary *E. coli* UTI89 RFP, cultured overnight in LB Miller in standing conditions, at a multiplicity of infection of

10, during 2 hours at 37°C, 5% $CO_2$. After 2 hours, gentamycin at 10µg/ml was added in each fluorodish to kill extracellular bacteria, and incubated during 1 hour at 37°C, 5% CO2. The medium was rinsed out 3 times with PBS to remove extracellular dead bacteria. At the last washing, PBS was replaced by DMEM supplemented with gentamycin at 1 or 10µg/ml. Finally, intracellular bacterial proliferation was monitored in live using the same microscope used for microfluidic chip experiments (see part 6.1).

# 6 Microscopy

All the experiments performed in this work were imaged in live, using spinning-disk microscopy, except for one experiment where 3D-SIM microscopy was used.

## 6.1 Spinning-disk acquisitions

### 6.1.1 Microscope settings

Most of the experiments were imaged using the host lab's confocal microscope (Nikon, Ti Eclipse) equipped with a spinning module (CSU-X1, Yokogawa). Images were acquired using either a 20X objective (Plan Apo, NA = 0.75) or a 100X oil objective (Plan Fluor, NA = 0.5 - 1.3) coupled to a Live-SR SIM-like module (Gataca Systems). The microscope stage was kept at 37°C using a temperature controller (The Cube), and when required at 5% $CO_2$ (Okolab). Fluorescence was recorded using a CMOS camera (95BPrime, Photometrics). For all the experiments, the laser power was set at 30% and the focus was maintained thanks to the Perfect Focus System (PFS, Nikon). Image acquisitions were computer-controlled using MetaMorph software (Molecular Devices).

### 6.1.2 Timelapse acquisition

Most of the experiments were performed in timelapse, whose settings slightly depend on the analysis that will be performed, including whether bacteria will be tracked or not and whether forces will be measured.

### 6.1.3 Timelapse parameters without tracking analysis

Most of the time, bacterial proliferation was acquired in Z-stacks every 0.1µm over 1 µm centered around the focal plane to not lose it, at a 30 minutes frame rate during 17 hours, with an exposure time of 300ms. Such a low frame rate allows to image bacteria overnight without photobleaching side effects.

### 6.1.4 Timelapse parameters for tracking analysis

When tracking was required to compute parameters of interest (growth rate, division rate, division time – see part 7.4), similar settings were used except that bacterial proliferation was acquired at a 5 minutes frame rate, for 5 to 6 hours. Such a high frame rate is not compatible with long time-lapse imaging, for example to follow bacterial proliferation overnight due to photobleaching side effects, but it allows to follow and track single bacteria over a shorter time period (5 hours).

### 6.1.5 Timelapse parameters for force measurements

To perform force measurements, images were acquired every 30 minutes during 17 hours. A MetaMorph script written by Marie-George Côme (ImageXcell) was used to perform Z-stacks in 2 colors with different parameters at each timepoints. The chamber deformation was imaged using the 491nm laser in Z-stack every 0.2µm over 4µm, while the bacteria where imaged in Z-stack every 0.1µm over 1µm centered around the focal plane using the 561nm laser.

### 6.1.6 GEMs acquisition

GEMs diffusion was imaged in stream mode over 5 s every 50 ms, using a 491nm laser power set at 95%. The stream mode enables to image fast moving particles with a reduced time step but with a lower signal-noise ratio.

## 6.2 3D-SIM acquisition

One chip was imaged in 3D-SIM (Zeiss Elyra 7 Lattice SIM) to visualize 3D bacterial arrangement over several layers with higher precision than with our spinning-disk microscope. 3D-SIM acquisition was performed by Audrey Salles (Photonic BioImaging Plateform, Institut Pasteur, Paris, France) using a 63X objective (Plan-Apochromat NA = 1.4 oil DIC M27), in Z-stacks every 0.1µm over 4µm, at one timepoint only.

# 7 Image analysis

In this section, I describe the image analysis pipelines used to quantify the experiments. For all of them, the mean and standard deviation are represented on graphes.

## 7.1 Measurement of the chamber deformation

The workflow presented below enables us to measure the deformation at the top of PDMS channels/chambers fluorescently labeled at the edges, by using the fluorescence images as inputs.
It was used to:

- Calibrate the deformability of the PDMS material in response to a known pressure
- Measure the deformation induced by bacterial proliferation and estimate the corresponding growth-induced pressure

The workflow can be decomposed in the following steps:

- **Step 1: Binarization of the raw images (Fiji macro)**

First, I defined the z slice corresponding to the top of the chamber for each position and extracted the corresponding stack. The fluorescence contour at the top of the channel was binarized over time using the Otsu auto threshold. For each position, a binary stack with the same dimensions (x, y, z=1, t) than the input stack, was saved and manually verified.

- **Step 2: Measuring the chamber deformation (Python)**

For each binary stack, the intensity profiles along the channel's width were computed and saved. The distance between the 2 maxima of the intensity profiles was measured, and used to compute the deformation of the chamber over time with respect to its initial (non-pressurized) size.

- **Step 3: Conversion of the deformation in growth-induced pressure (Python)**

The deformation was then used to infer the corresponding growth-induced pressure by using the equation established during the calibration of the PDMS deformability.

## 7.2 Segmentation of bacteria at the single-cell level

The workflow used to segment bacteria at the single-cell level in the bacterial confiner was adapted from the one we have developed in collaboration with J.-Y. Tinevez to quantify bacterial proliferation on agar pads (Image Analysis Hub, Institut Pasteur) *(Ershov et al., 2022)*. This work was done by Laura Xénard, during her M2 internship under my supervision.

To this end, an Ilastik model was trained on 60 images. This model was imported in TrackMate7 and used to segment the cytoplasmic contour defined by the membrane signal, using a threshold probability of 0.6. A minimal area filter was set at 0.05µm$^2$ to remove noise. The segmented stacks were saved, verified, and eventually manually corrected.

## 7.3 Tracking of bacterial lineages

Similarly, taking support from our previous work, segmented bacteria were eventually tracked over the course of the experiments using the TrackMate7 Fiji plugin *(Ershov et al., 2022),* by Laura Xénard. To this end, the Overlap tracker was used to track Escherichia coli bacteria, before being manually corrected on TrackScheme.

## 7.4 Quantification of the parameters of interest

In this section, I detailed how the parameters used to characterize bacterial physiology were measured (Table 8).

| *Parameter* | *Quantification* | *Tracking* | *Figure* |
|---|---|---|---|
| *Death index* | Manually | No | 26B; 34B |
| *Number of bacteria* | Python | No | 27C-D |
| *Area* | TrackMate | No | 28C-D; 29C, 30B-C, 34D-F |
| *Length* | Python | No | 28E |
| *Width* | Python | No | 28E |
| *Division time* | Python | Yes | 31A |
| *Growth rate* | Python | Yes | 31B-C-D |
| *Division rate* | Python | Yes | 31B-C-D |
| *Fluorescence intensities* | TrackMate | No | 33, 36C |
| *N:C ratio* | Python | No | 37 |

**Table 8 : Quantification processes used to measure the parameters of interest**

### 7.4.1 Death index

The death index was measured using the following equation:

$$\text{Death index (\%)} = \frac{\text{SYTOX positive area}}{\text{bacterial area on brightfield image}} \times 100$$

The SYTOX positive area was determined by the Otsu auto threshold on Fiji.
The bacterial area was measured manually on brightfield images.

### 7.4.2 Number of bacteria

The number of bacteria was computed in Python by counting the number of segmented objects per frame.

### 7.4.3 Length & Width

Bacterial length was computed using a homemade script in Python. First, a skeletonization using Zhang implementation *(Zhang and Suen, 1984)* was performed on the binary mask of each segmented bacterium, followed by a distance transform. In case of a branching skeleton, it was pruned so as to keep the longest branch. Bacterial length is defined as the skeleton length plus the value of the distance transform from both tips of the skeleton. In the specific event of a circular or a one pixel skeleton because of a high circularity of the bacterium, bacterial length was defined as the diameter, computed by TrackMate. The mean and the standard deviation values were obtained by binning all the individual values over time.

### 7.4.4 Division time

For each bacterium, the division time (written Δt) was defined as the duration between its birth and its division. A table containing the time at which each bacterium divides and the corresponding division time was saved and binarized to get the mean curve and the standard deviation. The mean and the standard deviation values were obtained by binning all the individual values over time.

### 7.4.5 Growth rate

The growth rate was computed using the following equation:

$$\text{Growth rate } (\mu m^2/\text{min}) = \frac{\text{Area(birth time} + \Delta t) - \text{Area (birth time)}}{\Delta t}$$

A table containing the time at which each bacterium divides and the corresponding growth rate was saved and binarized to get the mean curve and the standard deviation. The mean and the standard deviation values were obtained by binning all the individual values over time.

### 7.4.6 Division rate

The division rate was computed using the following equation:

$$\text{Division rate (doubling / min)} = \frac{1}{\Delta t}$$

A table containing the time at which each bacterium divides and the corresponding division rate was saved and binarized to get the mean curve and the standard

deviation. The mean and the standard deviation values were obtained by binning all the individual values over time.

### 7.4.7 N:C ratio

For each bacterium, the nuclear-to-cytoplasmic ratio was defined as follow:

$$\text{N:C} = \frac{\text{DNA Area}}{\text{Bacterial Area}}$$

Bacterial area is computed by TrackMate from the bacterium segmentation. Segmentation of DNA was done with an Ilastik model trained on 36 images. DNA-occupied area per bacterium was obtained by intersecting bacteria segmentation with DNA segmentation. The mean and the standard deviation values were obtained by binning all the individual values over time.

## 7.5 GEMs diffusion

GEMs diffusion was tracked using the Fiji plugin MOSAIC (Sbalzarini and Koumoutsakos, 2005), with the following parameters: radius = 3 px, link = 1, displacement = 5px. For each position, one table was saved with the coordinates of each trajectories over time. These tables were then used to compute, for every trajectory, the mean squared displacement and the corresponding diffusion coefficient using MATLAB codes previously written by M.Delarue *(Delarue et al., 2018).*

# 8 Statistical analyses

Statistical analysis was performed in GraphPad Prism 9.5.1 (GraphPad, USA) for Mac OS X applying the nonparametric Mann-Whitney test for unpaired data in the case of two group comparisons. In the case of three groups or more comparison, Kruskal-Wallis test was applied, with Dunn's post hoc test to correct for multiple comparisons. All p-values are shown in the figures

# Appendix

nature methods

BRIEF COMMUNICATION

https://doi.org/10.1038/s41592-022-01507-1

Check for updates

# TrackMate 7: integrating state-of-the-art segmentation algorithms into tracking pipelines

Dmitry Ershov[1,2,11], Minh-Son Phan[1,11], Joanna W. Pylvänäinen[3,4,5,11], Stéphane U. Rigaud[1,11], Laure Le Blanc[6], Arthur Charles-Orszag[6], James R. W. Conway[3], Romain F. Laine[7,8,10], Nathan H. Roy[9], Daria Bonazzi[6], Guillaume Duménil[6], Guillaume Jacquemet[3,4,5] ✉ and Jean-Yves Tinevez[1] ✉

**TrackMate is an automated tracking software used to analyze bioimages and is distributed as a Fiji plugin. Here, we introduce a new version of TrackMate. TrackMate 7 is built to address the broad spectrum of modern challenges researchers face by integrating state-of-the-art segmentation algorithms into tracking pipelines. We illustrate qualitatively and quantitatively that these new capabilities function effectively across a wide range of bio-imaging experiments.**

In the life sciences, tracking is used, for instance, to follow single particles, subcellular organelles, bacteria, cells, and whole animals. Owing to the sheer diversity of images, no single software can address every tracking challenge. This has prompted the development of flexible and extensible software tracking platforms[1–5] that enable biologists to build automated tracking pipelines tailored to a specific problem. Most tracking algorithms proceed in two steps. First, a detection algorithm detects or segments individual objects at each time point. Second, a linking algorithm links the detections to build tracks that follow each object over time. Importantly, the accurate detection of objects is crucial for the tracking process[6]. However, the low signal-to-noise ratio (SNR) that is typical of live-cell fluorescence microscopy often makes segmentation challenging. Aberrant object detection then leads to missing links and the generation of tracks that end prematurely, with multiple short tracks representing an individual object over time. Objects at high density can also be challenging to segment owing to overlap or close contact. Most detection algorithms will treat tightly packed objects as a single entity, resulting in breaks in tracks or single tracks linking groups of objects. Modern segmentation algorithms, in particular those based on machine learning (ML) and deep learning (DL) approaches, can address these challenges, because they excel at image-segmentation tasks in low-SNR and high-density images[7]. TrackMate[4] is a user-friendly Fiji[8] plugin for tracking objects in fluorescence microscopy images. TrackMate offers automated and semi-automated tracking algorithms, together with advanced visualization and analysis tools. However, until now, TrackMate detectors were solely based on the Laplacian of Gaussian (LoG) filter that is efficient against sub-resolved particles[9] or other blob-like objects, but performs poorly for textured objects, objects with complex shapes, and imaging modalities other than fluorescence. These detectors are also limited to measuring the objects' position and not their shape.

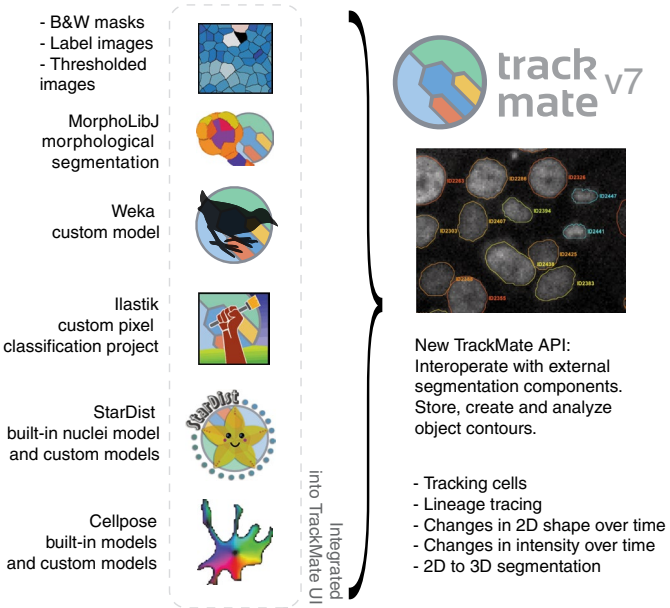


**Fig. 1 | The new capabilities of TrackMate.** TrackMate can now create, use, analyze, and store object contours segmented from 2D images. These contours enable TrackMate to extract morphological features of the tracked objects over time. We also wrote a new application programming interface (API) to allow the integration of external components in TrackMate. We use this API to incorporate popular segmentation tools including ilastik, the Weka Trainable-Segmentation Fiji plugin, cellpose, StarDist, and the morphological segmentation tool MorphoLibJ within TrackMate. TrackMate can also import segmentation results as masks or label images and use them for tracking, making it compatible with any segmentation algorithm. B&W, Black and White.

[1]Institut Pasteur, Université de Paris Cité, Image Analysis Hub, Paris, France. [2]Institut Pasteur, Université de Paris Cité, Biostatistics and Bioinformatic Hub, Paris, France. [3]Turku Bioscience Centre, University of Turku and Åbo Akademi University, Turku, Finland. [4]Åbo Akademi University, Faculty of Science and Engineering, Biosciences, Turku, Finland. [5]Turku Bioimaging, University of Turku and Åbo Akademi University, Turku, Finland. [6]Institut Pasteur, Université Paris Cité, INSERM UMR1225, Pathogenesis of Vascular Infections unit, Paris, France. [7]MRC Laboratory for Molecular Cell Biology, University College London, London, UK. [8]The Francis Crick Institute, London, UK. [9]Department of Microbiology and Immunology, SUNY Upstate Medical University, Syracuse, NY, USA. [10]Present address: Micrographia Bio, Translation and Innovation Hub, London, UK. [11]These authors contributed equally: Dmitry Ershov, Minh-Son Phan, Joanna W. Pylvänäinen, Stéphane U. Rigaud. ✉e-mail: guillaume.jacquemet@abo.fi; jean-yves.tinevez@pasteur.fr

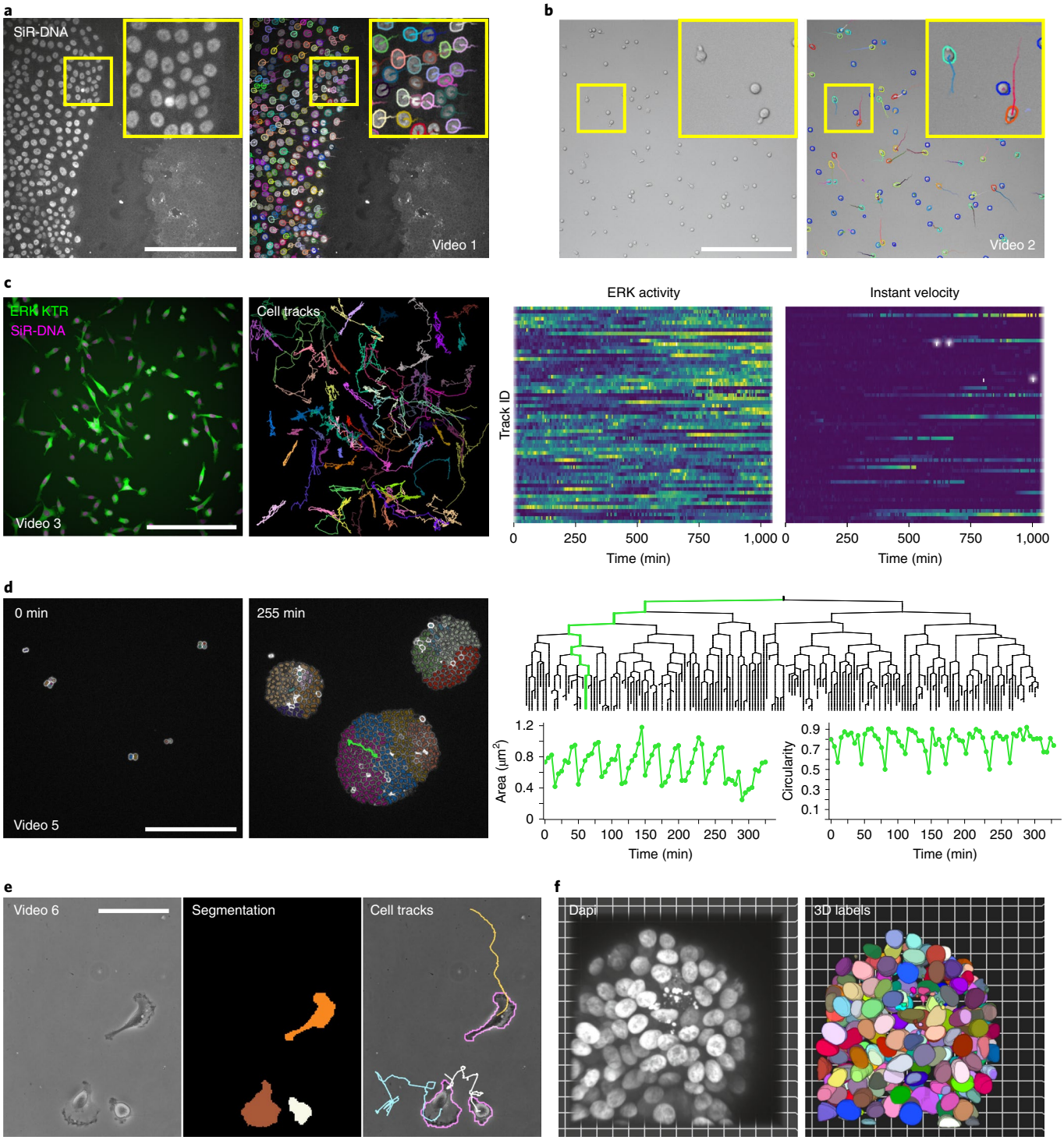


Here, we introduce a new version of TrackMate (TrackMate 7) that has been rewritten to improve performance, usability, and versatility, all of which present several advantages over other available tracking tools (Supplementary Table 1). In particular, we developed a new application programming interface (API) that enables developers to integrate segmentation tools as TrackMate detectors. As examples, we provide detectors based on ilastik[10], Weka[11], cellpose[12], MorphoLibJ[13], and StarDist[14]. While the training of custom ML and DL models must be performed with external tools (using, for example, ilastik or the ZeroCostDL4Mic[15] platform for StarDist and cellpose), popular built-in models are now fully integrated into TrackMate with a user-friendly interface and scripting capabilities. TrackMate can also import segmentation results as mask or label images for tracking, making it possible to perform tracking with any segmentation algorithm. Notably, as TrackMate now detects object contours in every frame, we reconfigured the TrackMate data model to store, display and analyze two-dimensional (2D) morphological features of the tracked objects over time (Fig. 1). The new detectors work for 2D and three-dimensional (3D) images when possible, but the analysis of object contours is currently limited to 2D images.

These new features widely increase the breadth of TrackMate applications and capabilities (Fig. 2, Supplementary Videos 1–11, Extended Data Figs. 1–4, Supplementary Manual, and Supplementary Tutorials) and its tracking performance (Supplementary Table 2).

**Fig. 2 | TrackMate can be used to track objects from a wide variety of bio-imaging experiments. a**, Migration of MCF10DCIS.com cells, labeled with SiR-DNA, recorded using a spinning disk confocal microscope and automatically tracked using a custom StarDist model loaded in TrackMate (see Supplementary Video 1). Detected cells and their local tracks (colors indicate track ID) are displayed. Scale bar, 250 µm. **b**, The migration of activated T cells plated on ICAM-1 was recorded using a brightfield microscope and automatically tracked using a custom StarDist model loaded in TrackMate (see Supplementary Video 2). Detected cells (colors indicate the mean track speed: blue, slow-moving cells; red, fast-moving cells) and their local tracks (colors indicate track ID) are displayed. Scale bar, 250 µm. **c**, MDA-MB-231 cells stably expressing an ERK activity reporter (ERK-KTR-Clover) and labeled using SiR-DNA were recorded live using a widefield fluorescence microscope over 17 hours. Cell nuclei were automatically tracked over time using a StarDist model available in TrackMate (see Supplementary Video 3). For each tracked cell, the average intensity of the ERK reporter was measured in their nucleus over time (directly in TrackMate). Changes in ERK activity and in instant velocity are displayed as heatmaps (blue, high; yellow, low). **d**, The growth of *Neisseria meningitidis* expressing PilQ-mCherry was recorded using a spinning-disk confocal microscope. An ilastik pixel classifier, trained to segment individual bacteria, was loaded into TrackMate to follow bacteria growth. Representative fields of view and the lineage tree of the bacteria highlighted in green are displayed (see Supplementary Video 5). Changes in area and circularity of a bacterium over the tracking period are also highlighted (green track). Cell division events translate into sharp decreases in area, followed by a quasi-linear increase. The circularity roughly plateaus during cell growth then decreases before cell division. Scale bar, 25 µm. **e**, Glioblastoma cells migrating on a polyacrylamide gel were automatically segmented using a custom cellpose model trained in the ZeroCostDL4Mic platform. The resulting label images were automatically tracked using TrackMate (see Supplementary Fig. 1 and Supplementary Video 6). Example raw and label images, as well as cell tracks, are displayed. **f**. MCF10DCIS.com 3D spheroids were stained for DAPI and imaged using a spinning disk confocal microscope. Across the *Z* volume, nuclei were detected at each *Z* plane using StarDist and tracked (all performed in TrackMate). Tracked nuclei were then exported as a label image to create 3D labels (see Supplementary Video 9).

For instance, the StarDist integration offers efficient and versatile nuclei detection in fluorescence images via the built-in model (from image set BBBC038v1 in ref. [16]). Our integration also provides an interface to use custom StarDist models. To illustrate this, we used custom StarDist models trained with the ZeroCostDL4Mic platform[15] to track fluorescently labeled nuclei of collectively migrating breast cancer cells, or rapidly migrating T cells from brightfield images (Fig. 2a,b and Supplementary Videos 1 and 2). Before this integration, fully automated tracking of label-free cells was not possible in TrackMate.

As TrackMate supports multi-dimensional images, users can now track objects using one channel while measuring the changing intensities of the tracked objects in separate channels over time. As an example, we tracked the nuclei of breast cancer cells expressing a kinase translocation reporter, following changes in ERK activity in single cells as they migrated (Fig. 2c, Extended Data Fig. 1, and Supplementary Video 3).

To further showcase the versatility of TrackMate, we used a Weka model (trained using the Weka Fiji plugin) together with the new overlap tracker (linking algorithm based on object overlap between consecutive frames) to follow focal adhesions in endothelial cells (Extended Data Fig. 2 and Supplementary Video 4). We also used an ilastik pixel classifier (trained using ilastik) to follow *Neisseria meningitidis* growth and correlate lineage information to single bacteria morphological measurements (Fig. 2d and Supplementary Video 5). To showcase that TrackMate can now import segmentation results directly, then follow the imported objects, we tracked migrating cancer cells (fluorescent images and brightfield images), and hematopoietic stem cells (ref. [17], brightfield images) previously segmented using cellpose[12] (Fig. 2e, Extended Data Fig. 3, and Supplementary Videos 6–8).

TrackMate's new detectors can also be used to perform 3D segmentation. Indeed, by swapping the *z* dimension of the source image with time, TrackMate can propagate 2D segmentation results across *z* planes and generate a 3D segmentation result from successive annotated 2D planes. This new feature makes the segmentation of 3D objects accessible, flexible, and possible without programming knowledge (Fig. 2f, Extended Data Fig. 4, and Supplementary Videos 9–11).

TrackMate v7 currently offers a choice of ten segmentation detectors (plus the integration of custom models for some of them) and five particle-linking algorithms for tracking the detected objects. To facilitate choosing an optimal combination for a specific dataset, we developed an additional module, the TrackMate helper (Supplementary Manual and Extended Data Fig. 5). This module is a user-friendly application that performs parameter sweeps over any combination of detectors and particle-linking algorithms. Using the ground truth provided by the user, TrackMate helper computes the Cell-Tracking-Challenge (CTC) metrics[18] for each parameter combination and reports the optimal one for each of the CTC metrics (Supplementary Table 2). In a nutshell, TrackMate helper allows the optimization of the tracking parameters for a whole dataset systematically.

Altogether, TrackMate now enables powerful segmentation approaches for tracking purposes directly in Fiji within a user interface already familiar to many. We envision that, by enabling scientists to resolve complex tracking problems more efficiently, this new version of TrackMate will accelerate biological discovery. We expect that TrackMate will continue to evolve in the years to come. In particular, as core libraries handling 3D objects are further developed in Fiji, the analysis of 3D object contours and shapes during tracking could become an invaluable addition. TrackMate was also built as a software platform to be extended by others independently and is documented as such. As DL-based segmentation and tracking algorithms are being developed, we hope contributors will consider TrackMate as a platform to accelerate the dissemination of their work to researchers in the Life Sciences and beyond[18,19].

## Online content

Any methods, additional references, Nature Research reporting summaries, source data, extended data, supplementary information, acknowledgements, peer review information; details of author contributions and competing interests; and statements of data and code availability are available at https://doi.org/10.1038/s41592-022-01507-1.

Received: 20 September 2021; Accepted: 25 April 2022;
Published online: 2 June 2022

## References

1. Sbalzarini, I. F. & Koumoutsakos, P. Feature point tracking and trajectory analysis for video imaging in cell biology. *J. Struct. Biol.* **151**, 182–195 (2005).
2. Chenouard, N., Bloch, I. & Olivo-Marin, J.-C. Multiple hypothesis tracking for cluttered biological image sequences. *IEEE Trans. Pattern Anal. Mach. Intell.* **35**, 2736–3750 (2013).
3. Piccinini, F., Kiss, A. & Horvath, P. CellTracker (not only) for dummies. *Bioinformatics* **32**, 955–957 (2016).
4. Tinevez, J.-Y. et al. TrackMate: an open and extensible platform for single-particle tracking. *Methods* **115**, 80–90 (2017).
5. McQuin, C. et al. CellProfiler 3.0: Next-generation image processing for biology. *PLoS Biol.* **16**, e2005970 (2018).

6. Chenouard, N. et al. Objective comparison of particle tracking methods. *Nat. Methods* **11**, 281–289 (2014).
7. Moen, E. et al. Deep learning for cellular image analysis. *Nat. Methods* **16**, 1233–1246 (2019).
8. Schindelin, J. et al. Fiji: an open-source platform for biological-image analysis. *Nat. Methods* **9**, 676–682 (2012).
9. Sage, D., Neumann, F. R., Hediger, F., Gasser, S. M. & Unser, M. Automatic tracking of individual fluorescence particles: application to the study of chromosome dynamics. *IEEE Trans. Image Process.* **14**, 1372–1383 (2005).
10. Berg, S. et al. ilastik: interactive machine learning for (bio)image analysis. *Nat. Methods* **16**, 1226–1232 (2019).
11. Arganda-Carreras, I. et al. Trainable Weka Segmentation: a machine learning tool for microscopy pixel classification. *Bioinformatics* **33**, 2424–2426 (2017).
12. Stringer, C., Wang, T., Michaelos, M. & Pachitariu, M. Cellpose: a generalist algorithm for cellular segmentation. *Nat. Methods* **18**, 100–106 (2021).
13. Legland, D., Arganda-Carreras, I. & Andrey, P. MorphoLibJ: integrated library and plugins for mathematical morphology with ImageJ. *Bioinformatics* **32**, 3532–3534 (2016).
14. Schmidt, U., Weigert, M., Broaddus, C. & Myers, G. Cell detection with star-convex polygons. in *Medical Image Computing and Computer Assisted Intervention – MICCAI 2018* (eds. Frangi, A. F., Schnabel, J. A., Davatzikos, C., Alberola-López, C. & Fichtinger, G.) 265–273 (Springer International Publishing, 2018).
15. von Chamier, L. et al. Democratising deep learning for microscopy with ZeroCostDL4Mic. *Nat. Commun.* **12**, 2276 (2021).
16. Caicedo, J. C. et al. Nucleus segmentation across imaging experiments: the 2018 Data Science Bowl. *Nat. Methods* **16**, 1247–1253 (2019).
17. Lutolf, M. P., Doyonnas, R., Havenstrite, K., Koleckar, K. & Blau, H. M. Perturbation of single hematopoietic stem cell fates in artificial niches. *Integr. Biol. Quant. Biosci. Nano Macro* **1**, 59–69 (2009).
18. Haase, R. et al. CLIJ: GPU-accelerated image processing for everyone. *Nat. Methods* **17**, 5–6 (2020).
19. Haase, R. *clij/TrackMate-clij2: 2.5.1.3-doi*. (Zenodo, 2022); https://doi.org/10.5281/zenodo.5983244

## Methods

**Cells and reagents.** MDA-MB-231 and U2OS cells were engineered to express ERK-KTR by first producing lentiviral particles in HEK 293FT packaging cells (Thermo Fisher, R70007). Cells were co-transfected with the third-generation lentiviral packaging system composed of pMDLg / pRRE (Addgene plasmid 12251), pRSV-Rev (Addgene plasmid 12253), and pMD2.G (Addgene plasmid 12259), along with the pLentiPGK Puro DEST ERK KTRClover (a kind gift from M. Covert; Addgene plasmid 90227) transfer plasmid, using Lipofectamine 3000 (ThermoFisher) in OptiMEM (Gibco, 31985070), as per the manufacturer's protocol[20,21]. After 24 hours, the medium was replaced with complete growth medium and incubated for 24 hours, at which point the medium was collected and filtered through a 0.45-µm syringe filter. MDA-MB-231 and U2OS cells were transduced with lentivirus for 48 hours in the presence of polybrene (8 µg/ml; Sigma, TR-1003-G), before washing and selection of stable positive cells using puromycin (2 µg/ml). Cells were then sorted by fluorescence-activated cell sorting (FACS) to isolate a population within a similar fluorescence range. MCF10 DCIS.COM cells were cultured in a 1:1 mix of DMEM (Sigma Aldrich) and F12 (Sigma Aldrich) supplemented with 5% horse serum (16050-122; Gibco BRL), 20 ng/ml human EGF (E9644; Sigma Aldrich), 0.5 mg/ml hydrocortisone (H0888-1G; Sigma Aldrich), 100 ng/ml cholera toxin (C8052-1MG; Sigma Aldrich), 10 µg/ml insulin (I9278-5ML; Sigma Aldrich), and 1% (vol/vol) penicillin/streptomycin (P0781-100ML; Sigma Aldrich). All cell lines were regularly checked for mycoplasma contamination, and all cell lines tested negative. MDA-MB-231 triple-negative human breast adenocarcinoma cells were acquired from ATCC (catalog number: HTB-26). U2OS osteosarcoma cells were provided by the Leibniz Institute DSMZ-German Collection of Microorganisms and Cell Cultures (cat. no. ACC 785). MCF10DCIS.COM cells were provided by J. F. Marshall (Barts Cancer Institute, Queen Mary University of London).

**Tracking migrating breast cancer cells.** Migrating MCF10DCIS.com cells were tracked using either StarDist directly implemented within TrackMate or using Cellpose and then TrackMate. To track MCF10DCIS.com cells labeled with sir-DNA using StarDist and TrackMate, a custom StarDist model was generated using the ZeroCostDL4Mic platform[14,15]. This custom StarDist model was trained for 100 epochs on 72 paired image patches (image dimensions: 1024 × 1024, patch size: 1024 × 1024) with a batch size of 2 and a mae loss function, using the StarDist 2D ZeroCostDL4Mic notebook (v1.12.2). The StarDist 'Versatile fluorescent nuclei' model was used as a training starting point. Key python packages used include TensorFlow (v1.15), Keras (v2.3.1), CSBdeep (v0.6.1), NumPy (v1.19.5), and Cuda (v10.1.243). The training was accelerated using a Tesla P100 GPU. This model generated excellent segmentation results on our test dataset (average $F_1$ score > 0.96). This model, the training dataset, and the code used for training are available on Zenodo[22]. In TrackMate, the StarDist detector custom model (score threshold = 0.41 and overlap threshold = 0.5) and the LAP tracker (linking max distance = 30 µm; track segment splitting = 15 µm) were used. Tracks were filtered in the function of their total distance traveled, and tracks shorter than 80 µm were excluded.

To track MCF10DCIS.com cells expressing lifeact-RFP (cell line described in ref. [23]) and labeled with sir-DNA, cells were first segmented using the ZeroCostDL4Mic cellpose 2D notebook (v1.12, refs. [12,15]). The cellpose model Cyto was used for the segmentation and the lifeact staining was used as the main segmentation channel. The Sir-DNA channel was used as the secondary segmentation channel. The following cellpose parameters were used: flow threshold = 0.4, cell probability threshold = 0, object diameter = 50. This approach generated excellent segmentation results on our test dataset (average $F_1$ score > 0.93). In TrackMate, the label image detector and the LAP tracker (linking max distance = 30 µm; track segment gap closing = 15 µm and 2 frames; track segment splitting = 15 µm) were used. Tracks were filtered in the function of the total number of spots detected, and tracks with fewer than 40 spots were excluded. This dataset is available on Zenodo[24,25].

**Tracking migrating T cells.** T cells migrating on ICAM-1 were automatically tracked using StarDist directly implemented within TrackMate. The StarDist model used was described previously[26] and is publicly available on Zenodo[27,28]. This model generated excellent segmentation results on our test dataset ($F_1$ score > 0.99). In TrackMate, the StarDist detector custom model (score threshold = 0.41 and overlap threshold = 0.5) and the Simple LAP tracker (linking max distance = 30 µm; gap closing max distance = 15 µm, gap closing max frame gap = 2 frames) were used. This dataset is available on Zenodo[27].

**Following ERK activity in migrating cells.** MDA-MD-231 or U2OS cells stably expressing clover-ERK-KTR were seeded on fibronectin-coated (1 µg /ml) Ibidi 8-well slides (Ibidi) 1 day before imaging. Four hours before imaging, the medium was supplemented with 250 nM sir-DNA (Cytoskeleton) and 25 mM HEPES (Sigma). Cells were then imaged live (37 °C, 5% $CO_2$) using a Nikon Eclipse Ti2-E microscope (Nikon) equipped with an sCMOS Orca Flash4.0 camera (Hamamatsu) and controlled by the NIS-Elements software (Nikon, v 5.11.01). MDA-MD-231 cells were imaged using a 20× Nikon CFI Plan Apo Lambda objective (NA 0.75), either 1 frame per minute for 2 hours or 1 frame every 5 minutes for 17 hours. In these experiments, a camera binning of 2 × 2 was used. U2OS cells were imaged using a 10× Nikon CFI Plan-Fluor objective (NA 0.3) every 5 minutes for 3 hours. Cell nuclei were automatically tracked over time by using StarDist in TrackMate.

To track the nuclei of U2OS cells, a custom StarDist model was trained using the ZeroCostDL4Mic platform[15]. The training source for the model was generated from 25 manually annotated images (dimensions: 2048 × 2048) using the LOCI plugin in Fiji. The generated training source and target were randomly cropped into size 1024 × 1024, rotated, flipped, and multiplied by 5 using the Augmentor ZeroCostDL4Mic notebook[15,29] to generate a dataset of 120 paired images. The custom StarDist model was trained for 200 epochs on the 120 paired image patches (image dimensions: 1024 × 1024, patch size: 1024 × 1024) with a batch size of 2 and a mae loss function, using the StarDist 2D ZeroCostDL4Mic notebook (v1.12.2)[15]. Key python packages used include TensorFlow (v1.15), Keras (v2.3.1), CSBdeep (v0.6.1), NumPy (v1.19.5), and Cuda (v11). The training was accelerated using a Tesla P100GPU. This model generated excellent segmentation results on our test dataset (average $F_1$ score > 0.918). In TrackMate, the StarDist detector custom model (score threshold = 0.41 and overlap threshold = 0.5) and the LAP tracker (linking max distance = 20 µm; track segment gap closing = 25 µm, gap closing max frame gap = 10 frames) were used. Tracks were filtered in function of their track duration and tracks shorter than 34 frames (2 hours and 40 minutes) were excluded. This dataset is available on Zenodo.

To track the nuclei of MDA-MB-231 cells, the 'Versatile fluorescent nuclei' StarDist model was used. In TrackMate, the StarDist detector (score threshold = 0.41; overlap threshold = 0.5) and the LAP tracker (linking max distance = 40 µm; track segment splitting = 30 µm) were used. Tracks were filtered using their duration, and only the tracks spanning the whole video were considered for further analysis (directly in TrackMate). For each tracked cell, the average intensity of the ERK reporter was measured in their nucleus over time (directly in TrackMate). To visualize the changes in ERK activity over time, results were uploaded to PlotTwist[30], and data were rescaled between 0 and 1 and visualized as heatmaps. This dataset is available on Zenodo[31].

**Tracking mouse hematopoietic stem cells migrating in hydrogel microwells.** Mouse hematopoietic stem cells migrating in a hydrogel microwell[17] were automatically segmented using cellpose (Cyto model) implemented in the ZeroCostDL4Mic platform[12,15]. The following Cellpose parameters were used: flow threshold = 0.4 and cell probability threshold = 0, object diameter = 17. This approach generated excellent segmentation results on our test dataset (average $F_1$ score > 0.93). The resulting label images were automatically tracked using TrackMate. In TrackMate, the label image detector and the LAP tracker (linking max distance = 30 µm; track segment gap closing = 15 µm and 2 frames; track segment splitting = 15 µm) were used. Spots were filtered by their circularity and area. Tracks were filtered by the total distance traveled; tracks shorter than 80 µm were excluded. This dataset is available from the Cell Tracking Challenge website (http://celltrackingchallenge.net/).

**Tracking glioblastoma-astrocytoma cells migrating on a polyacrylamide gel.** Glioblastoma-astrocytoma U373 cells migrating on a polyacrylamide gel were automatically segmented using a custom cellpose trained using the ZeroCostDL4Mic platform[12,15]. This cellpose model was trained for 500 epochs on 214 paired image patches (image dimensions: 520 × 696), with a batch size of 8, using the cellpose ZeroCostDL4Mic notebook (v1.13). The cellpose Cyto2 model was used as a training starting point. The training was accelerated using a Tesla K80 GPU. The following cellpose parameters were used for inference: flow threshold = 0.4 and cell probability threshold = 0, object diameter = 100. This approach generated excellent segmentation results on our test dataset (average $F_1$ score > 0.97). The resulting label images were automatically tracked using TrackMate. In TrackMate, the label image detector and the simple LAP tracker (linking max distance = 100 µm; track segment gap closing = 100 µm and 10 frames) were used. This dataset is available from the Cell Tracking Challenge website (http://celltrackingchallenge.net/) and on Zenodo[32].

***Neisseria meningitidis* sample preparation and imaging.** The *Neisseria meningitidis* strain 2C43 (ref. [33]) *pilQ/pilQ-mCherry*$_{ind}$ was grown on GCB agar plates (Difco) containing Kellog's supplements, 3 µg/ml vancomycin and 5 µg/ml chloramphenicol at 37 °C in a moist atmosphere containing 5% $CO_2$. The pMGC17 plasmid was designed in order to generate the 2C43 *pilQ/pilQ-mCherry*$_{ind}$ strain allowing IPTG-inducible expression of the type IV pilus secretin protein PilQ with a carboxy-terminal fusion to mCherry expressed from the *Neisseria meningitidis* chromosome.

First, *pilQ* was PCR-amplified from *Neisseria meningitidis* chromosomal DNA with primers pilQ-F: TTAATTAAAGGAGTAATTTTATGAATACCAAACTGAC AAAAATCGTCGACTCAATAGCGCAGGCTGTTGC

This PCR fragment was cloned in a pCRII-Blunt-TOPO vector (Invitrogen). Then, the mCherry ORF was PCR-amplified with a forward primer containing a region homologous to the 3' of *pilQ* (minus the stop codon) as well as a Gly-Ser-Gly linker, and a reverse primer containing a SalI restriction site and a region homologous to the TOPO vector (MUTmChCT-F: AGCCTGCGCTATGGTT CCGGTGTGAGCAAGGGC, MUTmChCT-R: CTGCAGAATTCGCCCTTGTC GACTCACTTGTACAG).

This PCR fragment was used as a mutagenesis megaprimer to amplify *pilQ* from the TOPO vector[34]. Finally, this vector was digested with PacI and SalI restriction enzymes and the resulting insert ligated into pMGC10. The pMGC10 plasmid was generated by inserting the *lacI* gene and the *lac* promoter in the pMGC3 plasmid[35]. The fragment of interest was PCR-amplified from the pMMB207 plasmid[36] using primers (LacIF2: GAA TTC GCT AAC TTA CAT TAA TTG CGT TGC, LacIPR: GTC GAC GAT CTT AAT TAT TTC CTG TGT GAA ATT GTT ATC CG) and cloned in pMGC3 using EcoRI and SalI restriction. The pMGC17 plasmid was used to transform *Neisseria meningitidis*, generating an intermediate strain that carries both a native *pilQ* and *pilQ-mCherry*. This strain was then transformed with chromosomal DNA from a *pilQ* mutant strain[37,38].

Bacteria in exponential phase from a 2-hour pre-culture in RPMI + 10% FBS supplemented with 100 µM IPTG at 37 °C and 5% $CO_2$ were diluted to an optical density of 0.015 ($1.5 \times 10^7$ bacteria/ml) and dropped onto a 2% agarose gel supplemented with 100 µM IPTG. Once the bacteria-containing droplet had dried up, the agar pad was flipped down onto a Fluorodish (Ibidi, 60-µm dish, 35-mm-high glass-bottom). Fluorescently labeled proliferating bacteria were acquired using an inverted spinning-disk confocal microscope (Nikon, TI Eclipse) equipped with a 100× immersion objective (Plan-Fluor, NA = 0.5–1.3) at 37 °C in the presence of 5% $CO_2$. Bacterial fluorescence was imaged in time-lapse at a 5-min frame rate with an exposure time of 300 ms for 5.5 hours and recorded with a CMOS Camera (Photometrics, 95BPrime) using Metamorph Imaging Software (Molecular Devices, MetaMorph v7.10.4.407). The focus was maintained with the Perfect Focus System (PFS, Nikon).

We trained an ilastik model using the Pixel Classification workflow using images from these experiments. This model was then used in the TrackMate-Ilastik detector, with a threshold on the probability map of 0.5. Spurious detections larger than 4,000 µm$^2$ were removed prior to linking. We used the LAP tracker for linking, using a max linking distance of 1 µm, with a max gap-closing distance of 2 µm over a maximum of 2 frames, and detecting cell divisions over a maximal distance of 2 µm. We then filtered out tracks that start after 43 minutes. This dataset is available on Zenodo[39].

**Tracking focal adhesions in endothelial cells.** Live imaging of the endothelial cells expressing paxillin-eGFP was described previously[40]. Briefly, human dermal microvascular blood endothelial cells expressing paxillin were imaged using a Marianas spinning disk confocal microscope. This microscope was controlled by SlideBook 6 (Intelligent Imaging Innovations), equipped with a Yokogawa CSU-W1 scanning unit, an inverted Zeiss Axio Observer Z1 body, and a 100×, NA-1.4 oil (Plan-Apochromat, M27) objective. Images were acquired every two minutes using an Orca Flash4 sCMOS camera (chip size 2048 × 2048; 2 × 2 camera binning enabled; Hamamatsu Photonics), at 37 °C and in the presence of 5% $CO_2$. Acquired images were then processed using Fiji to remove background (rolling ball radius: 10 pixels), compensate for bleaching (exponential fit method), and correct drifting (StackReg, Rigid body). A custom Weka pixel classifier was then trained in Fiji to segment the focal adhesions. In TrackMate, the Weka detector (threshold on probability = 0.5) and the overlap tracker (min IoU = 0.3, scale factor = 1) were used. This dataset is available on Zenodo[41].

**3D segmentation based on the association of 2D segmentation results.** To form spheroids, MCF10 DCIS.com cells were seeded as single cells, in standard growth medium, at low density (3,000 cells per well) on growth factor reduced (GFR) Matrigel-coated glass-bottom dishes (coverslip No. 0; MatTek). After 12 h, the medium was replaced by a normal growth medium supplemented with 2% (vol/vol) GFR matrigel. After 6 days, spheroids were fixed with 4% PFA for 10 min at room temperature and labeled using DAPI. Spheroids were then imaged using a spinning-disk confocal microscope ($Z$ step = 0.5 µm). The spinning-disk confocal microscope used was a Marianas spinning disk imaging system with a Yokogawa CSU-W1 scanning unit on an inverted Zeiss Axio Observer Z1 microscope (Intelligent Imaging Innovations) equipped with a 100× (NA 1.4) oil, Plan-Apochromat, M27 (Zeiss). To generate 3D labels, nuclei were detected and tracked across the $Z$ volume using StarDist implemented in TrackMate.

In TrackMate, the StarDist detector (score threshold = 0.41 and overlap threshold = 0.5) and the LAP tracker (linking max distance = 1 µm, track merging and splitting enabled) were used. Detected spots were filtered in function of their mean intensity to exclude spots with weak intensities. Tracks were filtered in function of the number of spots per track, and only the tracks with more than three spots were considered for further analysis (directly in TrackMate). In TrackMate, tracked nuclei were then exported as a label image to create 3D labels. 3D labels were then visualized using the FPBioimage software[42]. The video was also generated using the FPBioimage software. This dataset is available on Zenodo[43].

Confocal images of *Arabidopsis thaliana* floral meristem[44] and light-sheet images of a developing *Drosophila melanogaster* embryo[45,46] were automatically segmented using cellpose (Cyto2 model) implemented in the ZeroCostDL4Mic platform[12,15]. The following cellpose parameters were used: flow threshold = 0.4 and cell probability threshold = 0, object diameter = 0. This approach generated excellent segmentation results on our test datasets (*Arabidopsis thaliana* floral meristem, average $F_1$ score > 0.97; *Drosophila melanogaster* embryo, average $F_1$ score > 0.89). To generate 3D labels, the 2D label images were tracked using TrackMate. In TrackMate, the label image detector and the simple LAP tracker were used. The videos were generated using the FPBioimage software.

**Reporting summary.** Further information on research design is available in the Nature Research Reporting Summary linked to this article.

## Data Availability

All of the new data used in this article are available on Zenodo, under a dedicated collection (https://zenodo.org/communities/trackmate). They are publicly available under the Creative Commons Attribution 4.0 International license.

## Code Availability

TrackMate 7 and TrackMate-Helper introduced and used in this article are open-source software (GNU General Public License v3.0). Their source code is available on GitHub (https://github.com/fiji/TrackMate and https://github.com/tinevez/TrackMate-CTCRunner). TrackMate 7 is directly available in the Fiji software by simply updating it. TrackMate is documented on the ImageJ wiki: https://imagej.net/plugins/trackmate/ and the documentation for the new features can be accessed from https://imagej.net/plugins/trackmate/trackmate-v7-detectors.

## References


20. Regot, S., Hughey, J. J., Bajar, B. T., Carrasco, S. & Covert, M. W. High-sensitivity measurements of multiple kinase activities in live single cells. *Cell* **157**, 1724–1734 (2014).
21. Kudo, T. et al. Live-cell measurements of kinase activity in single cells using translocation reporters. *Nat. Protoc.* **13**, 155–169 (2018).
22. Jacquemet, G. *Combining StarDist and TrackMate Example 1—Breast Cancer Cell Dataset* (2020); https://doi.org/10.5281/zenodo.4034976
23. Jacquemet, G. et al. FiloQuant reveals increased filopodia density during breast cancer progression. *J. Cell Biol.* **216**, 3387–3403 (2017).
24. Jacquemet, G., Pylvänäinen, J. W. & Tinevez, J.-Y. *Tracking Breast Cancer Cells Migrating Collectively and Imaged in Fluorescence with TrackMate-Cellpose* (2022); https://doi.org/10.5281/zenodo.5864646
25. Tinevez, J.-Y., Jacquemet, G. & Pylvänäinen, J. W. *Tracking Label Images with TrackMate* (2021); https://doi.org/10.5281/zenodo.5221424
26. Fazeli, E. et al. Automated cell tracking using StarDist and TrackMate. *F1000Res.* **9**, 1279 (2020).
27. Tinevez, J.-Y., Jacquemet, G. & Roy, N. H. *T cells Migration Followed with TrackMate* (2021); https://doi.org/10.5281/zenodo.5206119
28. Roy, N. H. & Jacquemet, G. *Combining StarDist and TrackMate Example 2—T Cell Dataset* (2020); https://doi.org/10.5281/zenodo.4034929
29. Bloice, M. D., Roth, P. M. & Holzinger, A. Biomedical image augmentation using Augmentor. *Bioinformatics* **35**, 4522–4524 (2019).
30. Goedhart, J. PlotTwist: A web app for plotting and annotating continuous data. *PLoS Biol.* **18**, e3000581 (2020).
31. Tinevez, J.-Y. & Pylvänäinen, J. W. *Cell Migration with ERK Signalling* (2021); https://doi.org/10.5281/zenodo.5205955
32. Jacquemet, G., Pylvänäinen, J. W. & Tinevez, J.-Y. *Tracking Glioblastoma–Astrocytoma Cells Imaged in Brightfield with TrackMate-Cellpose* (2022); https://doi.org/10.5281/zenodo.5863317
33. Nassif, X. et al. Antigenic variation of pilin regulates adhesion of *Neisseria meningitidis* to human epithelial cells. **8**, 719–725 (1993).
34. Ke, S.-H. & Madison, E. L. Rapid and efficient site-directed mutagenesis by single-tube 'megaprimer' PCR method. *Nucleic Acids Res.* **25**, 3371–3372 (1997).
35. Soyer, M. et al. Early sequence of events triggered by the interaction of Neisseria meningitidis with endothelial cells. *Cell. Microbiol.* **16**, 878–895 (2014).
36. Morales, V. M., Bäckman, A. & Bagdasarian, M. A series of wide-host-range low-copy-number vectors that allow direct screening for recombinants. *Gene* **97**, 39–47 (1991).
37. Geoffroy, M.-C., Floquet, S., Métais, A., Nassif, X. & Pelicic, V. Large-scale analysis of the meningococcus genome by gene disruption: resistance to complement-mediated lysis. *Genome Res.* **13**, 391–398 (2003).
38. Georgiadou, M., Castagnini, M., Karimova, G., Ladant, D. & Pelicic, V. Large-scale study of the interactions between proteins involved in type IV pilus biology in *Neisseria meningitidis*: characterization of a subcomplex involved in pilus assembly. *Mol. Microbiol.* **84**, 857–873 (2012).
39. Le Blanc, L., Rigaud, S. & Tinevez, J.-Y. Neisseria meningitidis *Bacterial Growth* (2021); https://doi.org/10.5281/zenodo.5419619
40. Hakanpaa, L. et al. Targeting β1-integrin inhibits vascular leakage in endotoxemia. *Proc. Natl Acad. Sci. USA* **115**, E6467–E6476 (2018).
41. Jacquemet, G., Minh-Son-Phan & Tinevez, J.-Y. *Tracking Focal Adhesions with TrackMate and Weka—Tutorial Dataset 2* (2022); https://doi.org/10.5281/zenodo.5978940
42. Fantham, M. & Kaminski, C. F. A new online tool for visualization of volumetric data. *Nat. Photonics* **11**, 69–69 (2017).

43. Tinevez, J.-Y., Pylvänäinen, J. W. & Jacquemet, G. *Segmenting Cells in a Spheroid in 3D using 2D StarDist within TrackMate* (2021); https://doi.org/10.5281/zenodo.5220610
44. Kar, A. *Original Stacks and Segmented Data* (2021); https://doi.org/10.6084/m9.figshare.14447079.v1
45. Ulman, V. et al. An objective comparison of cell-tracking algorithms. *Nat. Methods* **14**, 1141–1152 (2017).
46. Maška, M. et al. A benchmark for comparison of cell tracking algorithms. *Bioinformatics* **30**, 1609–1617 (2014).

## Acknowledgements

The integration of existing algorithms as new detectors in TrackMate has been made possible thanks to the high quality of the code, documentation, and support provided by their respective authors. In particular, we would like to thank A. Kreshuk, D. Legland, D. Kutra, I. Arganda-Carreras, C. Stringer, M. Pachitariu, M. Weigert, S. Culley, and U. Schmidt. We can only hope for TrackMate to reach such a standard of quality to become a better tool of science. We are also grateful for the support and help of the bioimage analysis community, in particular C. Rueden, J. Eglinger, N. Chiaruttini, R. Guiet, O. Burri, V. Ulman, T. Pietzsch, and P. Tomancak. We thank H. Blau for giving us the permission to use the 'mouse hematopoietic stem cells in hydrogel microwells' dataset made available on the Cell Tracking Challenge website. The authors thank H. Hamidi for her critical reading of the manuscript. This study was supported by France BioImaging (Investissement d'Avenir; ANR-10-INBS-04, J.-Y. T.), the Academy of Finland (338537, G. J.), the Sigrid Juselius Foundation (G. J.), the Cancer Society of Finland (G. J.), the Åbo Akademi University Research Foundation (G. J., CoE CellMech), the Drug Discovery and Diagnostics strategic funding to Åbo Akademi University (G. J.) and the European Union's Horizon 2020 research and innovation program under Marie Sklodowska-Curie grant agreement 841973 (J. R. W. C.). J. W. P. was supported by Health Campus Turku 2.0 funded by the Academy of Finland. R. F. L. was supported by an MRC Skills development fellowship (MR/T027924/1). The Cell Imaging and Cytometry Core facility (Turku Bioscience, University of Turku, Åbo Akademi University, and Biocenter Finland) and Turku Bioimaging are acknowledged for services, instrumentation, and expertise.

## Author contributions

G. J. and J.-Y. T. conceived the project; J.-Y. T. wrote the source code; G. J., J. W. P., N. H. R., and L. L. B. performed the image acquisition of the test and example data; G. J., J. W. P., R. F. L., J.-Y. T., M.-S. P., D. E., and S. U. R. tested the code; J. R. W. C., D. B., G. D. and A. C.-O. provided critical reagents; G. J., J. W. P., J.-Y. T., M.-S. P., D. E., S. U. R., and J.-Y. T. wrote the documentation and tutorials.; G. J. and J.-Y. T. wrote the manuscript with input from all co-authors.

## Competing interests

The authors declare no competing interests.

## Additional information

**Extended data** is available for this paper at https://doi.org/10.1038/s41592-022-01507-1.

**Supplementary information** The online version contains supplementary material available at https://doi.org/10.1038/s41592-022-01507-1.

**Correspondence and requests for materials** should be addressed to Guillaume Jacquemet or Jean-Yves Tinevez.

**Peer review information** *Nature Methods* thanks the anonymous reviewers for their contribution to the peer review of this work. Rita Strack was the primary editor on this article and managed its editorial process and peer review in collaboration with the rest of the editorial team.

# References

Adams DW, Errington J. 2009. Bacterial cell division: assembly, maintenance and disassembly of the Z ring. Nat Rev Microbiol 7:642–653. doi:10.1038/nrmicro2198

Adams DW, Wu LJ, Errington J. 2014. Cell cycle regulation by the bacterial nucleoid. Curr Opin Microbiol 22:94–101. doi:10.1016/j.mib.2014.09.020

Aertsen A, Houdt RV, Vanoirbeek K, Michiels CW. 2004. An SOS Response Induced by High Pressure in Escherichia coli. J Bacteriol 186:6133–6141. doi:10.1128/jb.186.18.6133-6141.2004

Aertsen A, Michiels CW. 2005. Mrr instigates the SOS response after high pressure stress in Escherichia coli. Mol Microbiol 58:1381–1391. doi:10.1111/j.1365-2958.2005.04903.x

Ahn J, Hayes RB. 2021. Environmental Influences on the Human Microbiome and Implications for Noncommunicable Disease. Annu Rev Publ Health 42:277–292. doi:10.1146/annurev-publhealth-012420-105020

Ahn SH, Rath M, Tsao C-Y, Bentley WE, Raghavan SR. 2021. Single-Step Synthesis of Alginate Microgels Enveloped with a Covalent Polymeric Shell: A Simple Way to Protect Encapsulated Cells. Acs Appl Mater Inter 13:18432–18442. doi:10.1021/acsami.0c20613

Alric B. 2021. Impact des contraintes mécaniques sur la physiologie cellulaire. Thèse.

Alric B, Formosa-Dague C, Dague E, Holt LJ, Delarue M. 2022. Macromolecular crowding limits growth under pressure. Nat Phys 18:411–416. doi:10.1038/s41567-022-01506-1

Anderson GG, Palermo JJ, Schilling JD, Roth R, Heuser J, Hultgren SJ. 2003. Intracellular Bacterial Biofilm-Like Pods in Urinary Tract Infections. Science 301:105–107. doi:10.1126/science.1084550

André AAM, Spruijt E. 2020. Liquid–Liquid Phase Separation in Crowded Environments. Int J Mol Sci 21:5908. doi:10.3390/ijms21165908

Asally M, Kittisopikul M, Rué P, Du Y, Hu Z, Çağatay T, Robinson AB, Lu H, Garcia-Ojalvo J, Süel GM. 2012. Localized cell death focuses mechanical forces during 3D patterning in a biofilm. P Natl Acad Sci Usa 109:18891–6. doi:10.1073/pnas.1212429109

Auer GK, Weibel DB. 2017. Bacterial Cell Mechanics. Biochemistry-us 56:3710–3724. doi:10.1021/acs.biochem.7b00346

Baba T, Ara T, Hasegawa M, Takai Y, Okumura Y, Baba M, Datsenko KA, Tomita M, Wanner BL, Mori H. 2006. Construction of Escherichia coli K-12 in-frame, single-gene knockout mutants: the Keio collection. Mol Syst Biol 2:2006.0008-2006.0008. doi:10.1038/msb4100050

Banik S, Uchil A, Kalsang T, Chakrabarty S, Ali MdA, Srisungsitthisunti P, Mahato KK, Surdo S, Mazumder N. 2023. The revolution of PDMS microfluidics in cellular biology. Crit Rev Biotechnol 43:465–483. doi:10.1080/07388551.2022.2034733

Barbazan J, Pérez-González C, Gómez-González M, Dedenon M, Richon S, Latorre E, Serra M, Mariani P, Descroix S, Sens P, Trepat X, Vignjevic DM. 2021. Cancer-associated fibroblasts actively

compress cancer cells and modulate mechanotransduction. bioRxiv 2021.04.05.438443. doi:10.1101/2021.04.05.438443

Battesti A, Majdalani N, Gottesman S. 2011. The RpoS-Mediated General Stress Response in Escherichia coli*. Microbiology+ 65:189–213. doi:10.1146/annurev-micro-090110-102946

Belas R. 2014. Biofilms, flagella, and mechanosensing of surfaces by bacteria. Trends Microbiol 22:517–527. doi:10.1016/j.tim.2014.05.002

Benham CJ, Mielke SP. 2005. DNA MECHANICS. Annu Rev Biomed Eng 7:21–53. doi:10.1146/annurev.bioeng.6.062403.132016

BenMeriem Z, Mateo T, Faccini J, Denais C, Dusfour-Castan R, Guynet C, Merle T, Suzanne M, Di-Luoffo M, Guillermet-Guibert J, Alric B, Landiech S, Malaquin L, Mesnilgrente F, Laborde A, Mazenq L, Courson R, Delarue M. 2023. An easy-to-use microfluidic mechano-chemostat for tissues and organisms reveals that confined growth is accompanied with increased macromolecular crowding. bioRxiv 2023.03.29.534752. doi:10.1101/2023.03.29.534752

Berg S, Kutra D, Kroeger T, Straehle CN, Kausler BX, Haubold C, Schiegg M, Ales J, Beier T, Rudy M, Eren K, Cervantes JI, Xu B, Beuttenmueller F, Wolny A, Zhang C, Koethe U, Hamprecht FA, Kreshuk A. 2019. ilastik: interactive machine learning for (bio)image analysis. Nat Methods 16:1226–1232. doi:10.1038/s41592-019-0582-9

Berg J van den, Boersma AJ, Poolman B. 2017. Microorganisms maintain crowding homeostasis. Nat Rev Microbiol 15:309–318. doi:10.1038/nrmicro.2017.17

Bernal-Cabas M, Ayala JA, Raivio TL. 2014. The Cpx Envelope Stress Response Modifies Peptidoglycan Cross-Linking via the l,d-Transpeptidase LdtD and the Novel Protein YgaU. J Bacteriol 197:603–614. doi:10.1128/jb.02449-14

Bernhardt TG, Boer PAJ de. 2005. SlmA, a Nucleoid-Associated, FtsZ Binding Protein Required for Blocking Septal Ring Assembly over Chromosomes in E. coli. Mol Cell 18:555–564. doi:10.1016/j.molcel.2005.04.012

Beroz F, Yan J, Meir Y, Sabass B, Stone HA, Bassler BL, Wingreen NS. 2018. Verticalization of bacterial biofilms. Nat Phys 14:954–960. doi:10.1038/s41567-018-0170-4

Bertani B, Ruiz N. 2018. Function and Biogenesis of Lipopolysaccharides. Ecosal Plus 8. doi:10.1128/ecosalplus.esp-0001-2018

Biais N, Ladoux B, Higashi D, So M, Sheetz M. 2008. Cooperative retraction of bundled type IV pili enables nanonewton force generation. Plos Biol 6:e87. doi:10.1371/journal.pbio.0060087

Boedicker JQ, Vincent ME, Ismagilov RF. 2009. Microfluidic Confinement of Single Cells of Bacteria in Small Volumes Initiates High-Density Behavior of Quorum Sensing and Growth and Reveals Its Variability. Angew Chem Int Ed 48:5908–5911. doi:10.1002/anie.200901550

Bolivar F, Rodriguez RL, Greene PJ, Betlach MC, Heyneker HL, Boyer HW, Crosa JH, Falkow S. 1977. Construction and characterization of new cloning vehicle. II. A multipurpose cloning system. Gene 2:95–113. doi:10.1016/0378-1119(77)90000-2

Bonazzi D, Schiavo VL, Machata S, Djafer-Cherif I, Nivoit P, Manriquez V, Tanimoto H, Husson J, Henry N, Chaté H, Voituriez R, Duménil G. 2018. Intermittent Pili-Mediated Forces Fluidize Neisseria meningitidis Aggregates Promoting Vascular Colonization. Cell 174:143-155.e16. doi:10.1016/j.cell.2018.04.010

Bowman GR, Lyuksyutova AI, Shapiro L. 2011. Bacterial polarity. Curr Opin Cell Biol 23:71–77. doi:10.1016/j.ceb.2010.10.013

Boye E, Nordström K. 2003. Coupling the cell cycle to cell growth. EMBO Rep 4:757–760. doi:10.1038/sj.embor.embor895

Boye E, Stokke T, Kleckner N, Skarstad K. 1996. Coordinating DNA replication initiation with cell growth: differential roles for DnaA and SeqA proteins. Proc National Acad Sci 93:12206–12211. doi:10.1073/pnas.93.22.12206

Božič B, Jokhadar ŠZ, Kristanc L, Gomišček G. 2020. Cell Volume Changes and Membrane Ruptures Induced by Hypotonic Electrolyte and Sugar Solutions. Front Physiol 11:582781. doi:10.3389/fphys.2020.582781

Bremer E, Kramer R. 2019. Responses of microorganisms to osmotic stress. Annu Rev Microbiol 73:313–334. doi:10.1146/annurev-micro-020518-115504

Brown L, Wolf JM, Prados-Rosales R, Casadevall A. 2015. Through the wall: extracellular vesicles in Gram-positive bacteria, mycobacteria and fungi. Nat Rev Microbiol 13:620–630. doi:10.1038/nrmicro3480

Bury-Moné S, Nomane Y, Reymond N, Barbet R, Jacquet E, Imbeaud S, Jacq A, Bouloc P. 2009. Global analysis of extracytoplasmic stress signaling in Escherichia coli. Plos Genet 5:e1000651. doi:10.1371/journal.pgen.1000651

Cambré A, Aertsen A. 2020. Bacterial Vivisection: How Fluorescence-Based Imaging Techniques Shed a Light on the Inner Workings of Bacteria. Microbiol Mol Biol R 84. doi:10.1128/mmbr.00008-20

Campos M, Surovtsev IV, Kato S, Paintdakhi A, Beltran B, Ebmeier SE, Jacobs-Wagner C. 2014. A Constant Size Extension Drives Bacterial Cell Size Homeostasis. Cell 159:1433–1446. doi:10.1016/j.cell.2014.11.022

Carballès F, Bertrand C, Bouché J, Cam K. 1999. Regulation of Escherichia coli cell division genes ftsA and ftsZ by the two-component system rcsC–rcsB. Mol Microbiol 34:442–450. doi:10.1046/j.1365-2958.1999.01605.x

Cava F, Pedro MA de. 2014. Peptidoglycan plasticity in bacteria: emerging variability of the murein sacculus and their associated biological functions. Curr Opin Microbiol 18:46–53. doi:10.1016/j.mib.2014.01.004

Cayley S, Lewis BA, Guttman HJ, Record MT. 1991. Characterization of the cytoplasm of Escherichia coli K-12 as a function of external osmolarity Implications for protein-DNA interactions in vivo. J Mol Biol 222:281–300. doi:10.1016/0022-2836(91)90212-o

Charras G, Yap AS. 2018. Tensile Forces and Mechanotransduction at Cell–Cell Junctions. Curr Biol 28:R445–R457. doi:10.1016/j.cub.2018.02.003

Chaveroche M-K, Ghigo J-M, d'Enfert C. 2000. A rapid method for efficient gene replacement in the filamentous fungus Aspergillus nidulans. Nucleic Acids Res 28:e97–e97. doi:10.1093/nar/28.22.e97

Chen Y, Harapanahalli AK, Busscher HJ, Norde W, Mei HC van der. 2014. Nanoscale Cell Wall Deformation Impacts Long-Range Bacterial Adhesion Forces on Surfaces. Appl Environ Microbiol 80:637–643. doi:10.1128/aem.02745-13

Chien A-C, Hill NS, Levin PA. 2012. Cell Size Control in Bacteria. Curr Biol 22:R340–R349. doi:10.1016/j.cub.2012.02.032

Chivian D, Brodie EL, Alm EJ, Culley DE, Dehal PS, DeSantis TZ, Gihring TM, Lapidus A, Lin L-H, Lowry SR, Moser DP, Richardson PM, Southam G, Wanger G, Pratt LM, Andersen GL, Hazen TC, Brockman FJ, Arkin AP, Onstott TC. 2008. Environmental Genomics Reveals a Single-Species Ecosystem Deep Within Earth. Science 322:275–278. doi:10.1126/science.1155495

Cho H, McManus HR, Dove SL, Bernhardt TG. 2011. Nucleoid occlusion factor SlmA is a DNA-activated FtsZ polymerization antagonist. Proc National Acad Sci 108:3773–3778. doi:10.1073/pnas.1018674108

Choudhary KS, Kleinmanns JA, Decker K, Sastry AV, Gao Y, Szubin R, Seif Y, Palsson BO. 2020. Elucidation of Regulatory Modes for Five Two-Component Systems in Escherichia coli Reveals Novel Relationships. mSystems 5:e00980-20. doi:10.1128/msystems.00980-20

Chu EK, Kilic O, Cho H, Groisman A, Levchenko A. 2018. Self-induced mechanical stress can trigger biofilm formation in uropathogenic Escherichia coli. Nat Commun 9:4087. doi:10.1038/s41467-018-06552-z

Claverys J-P, Håvarstein LS. 2007. Cannibalism and fratricide: mechanisms and raisons d'être. Nat Rev Microbiol 5:219–229. doi:10.1038/nrmicro1613

Connell JL, Ritschdorff ET, Whiteley M, Shear JB. 2013. 3D printing of microscopic bacterial communities. Proc National Acad Sci 110:18380–18385. doi:10.1073/pnas.1309729110

Connell JL, Wessel AK, Parsek MR, Ellington AD, Whiteley M, Shear JB. 2010. Probing Prokaryotic Social Behaviors with Bacterial "Lobster Traps." mBio 1:e00202-10. doi:10.1128/mbio.00202-10

Cont A, Rossy T, Al-Mayyah Z, Persat A. 2020. Biofilms deform soft surfaces and disrupt epithelia. Elife 9:e56533. doi:10.7554/elife.56533

Corre J-P, Obino D, Nivoit P, Yatim A, Schmitt T, Duménil G. 2022. Anti-thrombotic treatment enhances antibiotic efficiency in a humanized model of meningococcemia. Biorxiv 2022.01.10.475613. doi:10.1101/2022.01.10.475613

Craig L, Forest KT, Maier B. 2019. Type IV pili: dynamics, biophysics and functional consequences. Nat Rev Microbiol 17:429–440. doi:10.1038/s41579-019-0195-4

Cutler KJ, Stringer C, Lo TW, Rappez L, Stroustrup N, Peterson SB, Wiggins PA, Mougous JD. 2022. Omnipose: a high-precision morphology-independent solution for bacterial cell segmentation. Nat Methods 19:1438–1448. doi:10.1038/s41592-022-01639-4

Dame RT. 2005. The role of nucleoid-associated proteins in the organization and compaction of bacterial chromatin: Organization and compaction of bacterial chromatin. Mol Microbiol 56:858–870. doi:10.1111/j.1365-2958.2005.04598.x

Delarue M, Brittingham GP, Pfeffer S, Surovtsev IV, Pinglay S, Kennedy KJ, Schaffer M, Gutierrez JI, Sang D, Poterewicz G, Chung JK, Plitzko JM, Groves JT, Jacobs-Wagner C, Engel BD, Holt LJ. 2018. mTORC1 Controls Phase Separation and the Biophysical Properties of the Cytoplasm by Tuning Crowding. Cell 174:338-349.e20. doi:10.1016/j.cell.2018.05.042

Delarue M, Hartung J, Schreck C, Gniewek P, Hu L, Herminghaus S, Hallatschek O. 2016. Self-driven jamming in growing microbial populations. Nat Phys 12:762–766. doi:10.1038/nphys3741

Delarue M, Montel F, Vignjevic D, Prost J, Joanny J-F, Cappello G. 2014. Compressive Stress Inhibits Proliferation in Tumor Spheroids through a Volume Limitation. Biophys J 107:1821–1828. doi:10.1016/j.bpj.2014.08.031

Delarue M, Weissman D, Hallatschek O. 2017. A simple molecular mechanism explains multiple patterns of cell-size regulation. Plos One 12:e0182633. doi:10.1371/journal.pone.0182633

Delhaye A, Collet J-F, Laloux G. 2019. A Fly on the Wall: How Stress Response Systems Can Sense and Respond to Damage to Peptidoglycan. Front Cell Infect Mi 9:380. doi:10.3389/fcimb.2019.00380

Delhaye A, Collet J-F, Laloux G. 2016. Fine-Tuning of the Cpx Envelope Stress Response Is Required for Cell Wall Homeostasis in Escherichia coli. Mbio 7:e00047-16. doi:10.1128/mbio.00047-16

Deuren M van, Dijke BJ van, Koopman RJ, Horrevorts AM, Meis JF, Santman FW, Meer JW van der. 1993. Rapid diagnosis of acute meningococcal infections by needle aspiration or biopsy of skin lesions. Bmj 306:1229–1232. doi:10.1136/bmj.306.6887.1229

Devany J, Falk MJ, Holt LJ, Murugan A, Gardel ML. 2023. Epithelial tissue confinement inhibits cell growth and leads to volume-reducing divisions. Dev Cell. doi:10.1016/j.devcel.2023.05.018

Discher DE, Janmey P, Wang Y. 2005. Tissue Cells Feel and Respond to the Stiffness of Their Substrate. Science 310:1139–1143. doi:10.1126/science.1116995

Donachie WD. 1968. Relationship between Cell Size and Time of Initiation of DNA Replication. Nature 219:1077–1079. doi:10.1038/2191077a0

Douarche C, Allain J-M, Raspaud E. 2015. Bacillus subtilis Bacteria Generate an Internal Mechanical Force within a Biofilm. Biophys J 109:2195–2202. doi:10.1016/j.bpj.2015.10.004

Doyle RJ, Marquis RE. 1994. Elastic, flexible peptidoglycan and bacterial cell wall properties. Trends Microbiol 2:57–60. doi:10.1016/0966-842x(94)90127-9

Du S, Lutkenhaus J. 2017. Assembly and activation of the Escherichia coli divisome. Mol Microbiol 105:177–187. doi:10.1111/mmi.13696

Duffy DC, McDonald JC, Schueller OJA, Whitesides GM. 1998. Rapid Prototyping of Microfluidic Systems in Poly(dimethylsiloxane). Anal Chem 70:4974–4984. doi:10.1021/ac980656z

Dufrêne YF, Persat A. 2020. Mechanomicrobiology: how bacteria sense and respond to forces. Nat Rev Microbiol 18:1–14. doi:10.1038/s41579-019-0314-2

Egan AJF, Errington J, Vollmer W. 2020. Regulation of peptidoglycan synthesis and remodelling. Nat Rev Microbiol 18:446–460. doi:10.1038/s41579-020-0366-3

Ellis RJ. 2001. Macromolecular crowding: obvious but underappreciated. Trends Biochem Sci 26:597–604. doi:10.1016/s0968-0004(01)01938-7

Elmros T, Burman LG, Bloom GD. 1976. Autolysis of Neisseria gonorrhoeae. J Bacteriol 126:969–976. doi:10.1128/jb.126.2.969-976.1976

Ent F van den, Amos LA, Löwe J. 2001. Prokaryotic origin of the actin cytoskeleton. Nature 413:39–44. doi:10.1038/35092500

Ershov D, Phan M-S, Pylvänäinen JW, Rigaud SU, Blanc LL, Charles-Orszag A, Conway JRW, Laine RF, Roy NH, Bonazzi D, Duménil G, Jacquemet G, Tinevez J-Y. 2022. TrackMate 7: integrating state-of-the-art segmentation algorithms into tracking pipelines. Nat Methods 19:829–832. doi:10.1038/s41592-022-01507-1

Eto DS, Sundsbak JL, Mulvey MA. 2006. Actin-gated intracellular growth and resurgence of uropathogenic Escherichia coli. Cell Microbiol 8:704–717. doi:10.1111/j.1462-5822.2006.00691.x

Eun Y-J, Utada AS, Copeland MF, Takeuchi S, Weibel DB. 2011. Encapsulating Bacteria in Agarose Microparticles Using Microfluidics for High-Throughput Cell Analysis and Isolation. ACS Chem Biology 6:260–266. doi:10.1021/cb100336p

Fischer-Friedrich E, Hyman AA, Jülicher F, Müller DJ, Helenius J. 2014. Quantification of surface tension and internal pressure generated by single mitotic cells. Sci Rep-uk 4:6213. doi:10.1038/srep06213

Flemming H-C, Wingender J. 2010. The biofilm matrix. Nat Rev Microbiol 8:623–633. doi:10.1038/nrmicro2415

Fletcher DA, Mullins RD. 2010. Cell mechanics and the cytoskeleton. Nature 463:485–492. doi:10.1038/nature08908

Floc'h K, Lacroix F, Servant P, Wong Y-S, Kleman J-P, Bourgeois D, Timmins J. 2019. Cell morphology and nucleoid dynamics in dividing Deinococcus radiodurans. Nat Commun 10:3815. doi:10.1038/s41467-019-11725-5

Flores-Mireles AL, Walker JN, Caparon M, Hultgren SJ. 2015. Urinary tract infections: epidemiology, mechanisms of infection and treatment options. Nat Rev Microbiol 13:269–284. doi:10.1038/nrmicro3432

Gao Z, Zhang W, Chang R, Zhang S, Yang G, Zhao G. 2021. Liquid-Liquid Phase Separation: Unraveling the Enigma of Biomolecular Condensates in Microbial Cells. Frontiers Microbiol 12:751880. doi:10.3389/fmicb.2021.751880

Geersens E, Vuilleumier S, Ryckelynck M. 2022. Growth-Associated Droplet Shrinkage for Bacterial Quantification, Growth Monitoring, and Separation by Ultrahigh-Throughput Microfluidics. Acs Omega 7:12039–12047. doi:10.1021/acsomega.2c00248

Genova LA, Roberts MF, Wong Y-C, Harper CE, Santiago AG, Fu B, Srivastava A, Jung W, Wang LM, Krzemiński Ł, Mao X, Sun X, Hui C-Y, Chen P, Hernandez CJ. 2019. Mechanical stress compromises multicomponent efflux complexes in bacteria. Proc National Acad Sci 116:25462–25467. doi:10.1073/pnas.1909562116

Gerding MA, Ogata Y, Pecora ND, Niki H, Boer PAJD. 2007. The trans-envelope Tol–Pal complex is part of the cell division machinery and required for proper outer-membrane invagination during cell constriction in E. coli. Mol Microbiol 63:1008–1025. doi:10.1111/j.1365-2958.2006.05571.x

Gimza BD, Cassat JE. 2021. Mechanisms of Antibiotic Failure During Staphylococcus aureus Osteomyelitis. Front Immunol 12:638085. doi:10.3389/fimmu.2021.638085

Gomez-Sjoberg R, Leyrat AA, Houseman BT, Shokat K, Quake SR. 2010. Biocompatibility and Reduced Drug Absorption of Sol−Gel-Treated Poly(dimethyl siloxane) for Microfluidic Cell Culture Applications. Anal Chem 82:8954–8960. doi:10.1021/ac101870s

Goodell EW. 1985. Recycling of murein by Escherichia coli. J Bacteriol 163:305–310. doi:10.1128/jb.163.1.305-310.1985

Goodsell DS. 2009. The Machinery of Life. doi:10.1007/978-0-387-84925-6

Gordon VD, Wang L. 2019. Bacterial mechanosensing: the force will be with you, always. J Cell Sci 132:jcs227694. doi:10.1242/jcs.227694

Gottesman S. 2019. Trouble is coming: Signaling pathways that regulate general stress responses in bacteria. J Biol Chem 294:11685–11700. doi:10.1074/jbc.rev119.005593

Gray WT, Govers SK, Xiang Y, Parry BR, Campos M, Kim S, Jacobs-Wagner C. 2019. Nucleoid Size Scaling and Intracellular Organization of Translation across Bacteria. Cell 177:1632-1648.e20. doi:10.1016/j.cell.2019.05.017

Groisman A, Lobo C, Cho H, Campbell JK, Dufour YS, Stevens AM, Levchenko A. 2005. A microfluidic chemostat for experiments with bacterial and yeast cells. Nat Methods 2:685–689. doi:10.1038/nmeth784

Guest RL, Raivio TL. 2016. Role of the Gram-Negative Envelope Stress Response in the Presence of Antimicrobial Agents. Trends Microbiol 24:377–390. doi:10.1016/j.tim.2016.03.001

Guo H, Ryan JC, Song X, Mallet A, Zhang M, Pabst V, Decrulle AL, Ejsmont P, Wintermute EH, Lindner AB. 2022. Spatial engineering of E. coli with addressable phase-separated RNAs. Cell 185:3823-3837.e23. doi:10.1016/j.cell.2022.09.016

Guyer MS, Reed RR, Steitz JA, Low KB. 1981. Identification of a Sex-factor-affinity Site in E. coli as . Cold Spring Harb Symp Quant Biol 45:135–140. doi:10.1101/sqb.1981.045.01.022

Haeusser DP, Levin PA. 2008. The great divide: coordinating cell cycle events during bacterial growth and division. Curr Opin Microbiol 11:94–99. doi:10.1016/j.mib.2008.02.008

Haldimann A, Wanner BL. 2001. Conditional-replication, integration, excision, and retrieval plasmid-host systems for gene structure-function studies of bacteria. J Bacteriol 183:6384–93. doi:10.1128/jb.183.21.6384-6393.2001

Hall-Stoodley L, Costerton JW, Stoodley P. 2004. Bacterial biofilms: from the Natural environment to infectious diseases. Nat Rev Microbiol 2:95–108. doi:10.1038/nrmicro821

Han Y, Jiang N, Xu H, Yuan Z, Xiu J, Mao S, Liu X, Huang J. 2023. Extracellular Matrix Rigidities Regulate the Tricarboxylic Acid Cycle and Antibiotic Resistance of Three-Dimensionally Confined Bacterial Microcolonies. Adv Sci 10:2206153. doi:10.1002/advs.202206153

Harhala M, Gembara K, Miernikiewicz P, Owczarek B, Kaźmierczak Z, Majewska J, Nelson DC, Dąbrowska K. 2021. DNA Dye Sytox Green in Detection of Bacteriolytic Activity: High Speed, Precision and Sensitivity Demonstrated With Endolysins. Frontiers Microbiol 12:752282. doi:10.3389/fmicb.2021.752282

Harper CE, Hernandez CJ. 2020. Cell biomechanics and mechanobiology in bacteria: Challenges and opportunities. Apl Bioeng 4:021501. doi:10.1063/1.5135585

Harris LK, Theriot JA. 2016. Relative Rates of Surface and Volume Synthesis Set Bacterial Cell Size. Cell 165:1479–92. doi:10.1016/j.cell.2016.05.045

Harry E, Monahan L, Thompson L. 2006. Bacterial Cell Division: The Mechanism and Its Precison. Int Rev Cytol 253:27–94. doi:10.1016/s0074-7696(06)53002-5

Hartmann R, Jeckel H, Jelli E, Singh PK, Vaidya S, Bayer M, Rode DKH, Vidakovic L, Díaz-Pascual F, Fong JCN, Dragoš A, Lamprecht O, Thöming JG, Netter N, Häussler S, Nadell CD, Sourjik V, Kovács ÁT, Yildiz FH, Drescher K. 2021. Quantitative image analysis of microbial communities with BiofilmQ. Nat Microbiol 1–6. doi:10.1038/s41564-020-00817-4

Hartmann R, Singh PK, Pearce P, Mok R, Song B, Díaz-Pascual F, Dunkel J, Drescher K. 2018. Emergence of three-dimensional order and structure in growing biofilms. Nat Phys 15:251–256. doi:10.1038/s41567-018-0356-9

Helmann JD. 2019. Where to begin? Sigma factors and the selectivity of transcription initiation in bacteria. Mol Microbiol 112:335–347. doi:10.1111/mmi.14309

Herrmann M, Schneck E, Gutsmann T, Brandenburg K, Tanaka M. 2015. Bacterial lipopolysaccharides form physically cross-linked, two-dimensional gels in the presence of divalent cations. Soft Matter 11:6037–6044. doi:10.1039/c5sm01002k

Hews CL, Cho T, Rowley G, Raivio TL. 2019. Maintaining Integrity Under Stress: Envelope Stress Response Regulation of Pathogenesis in Gram-Negative Bacteria. Front Cell Infect Mi 9:313. doi:10.3389/fcimb.2019.00313

Hill NS, Kadoya R, Chattoraj DK, Levin PA. 2012. Cell Size and the Initiation of DNA Replication in Bacteria. PLoS Genet 8:e1002549. doi:10.1371/journal.pgen.1002549

Ho P-Y, Amir A. 2015. Simultaneous regulation of cell size and chromosome replication in bacteria. Frontiers Microbiol 6:662. doi:10.3389/fmicb.2015.00662

Holt LJ, Hallatschek O, Delarue M. 2018. Mechano-chemostats to study the effects of compressive stress on yeast. Methods Cell Biol 147:215–231. doi:10.1016/bs.mcb.2018.06.010

Ho□ltje J-V. 1998. Growth of the Stress-Bearing and Shape-Maintaining Murein Sacculus of Escherichia coli. Microbiol Mol Biol R 62:181–203. doi:10.1128/mmbr.62.1.181-203.1998

Hostetler Z. 2018. A Genetically Encoded Fluorescent Amino Acid Reveals Protein Dynamics Regulating the Bacterial DNA Damage Response. University of Pennsylvania ProQuest Dissertations Publishing.

Hug I, Deshpande S, Sprecher KS, Pfohl T, Jenal U. 2017. Second messenger–mediated tactile response by a bacterial rotary motor. Science 358:531–534. doi:10.1126/science.aan5353

Humphrey JD, Dufresne ER, Schwartz MA. 2014. Mechanotransduction and extracellular matrix homeostasis. Nat Rev Mol Cell Biology 15:802–12. doi:10.1038/nrm3896

Hunstad DA, Justice SS. 2010. Intracellular Lifestyles and Immune Evasion Strategies of Uropathogenic Escherichia coli. Annu Rev Microbiol 64:203–221. doi:10.1146/annurev.micro.112408.134258

Hyman AA, Weber CA, Jülicher F. 2014. Liquid-liquid phase separation in biology. Annu Rev Cell Dev Bi 30:39–58. doi:10.1146/annurev-cellbio-100913-013325

Irastortza-Olaziregi M, Amster-Choder O. 2021. Coupled Transcription-Translation in Prokaryotes: An Old Couple With New Surprises. Front Microbiol 11:624830. doi:10.3389/fmicb.2020.624830

Iskratsch T, Wolfenson H, Sheetz MP. 2014. Appreciating force and shape — the rise of mechanotransduction in cell biology. Nat Rev Mol Cell Biology 15:825–833. doi:10.1038/nrm3903

Jakiela S, Kaminski TS, Cybulski O, Weibel DB, Garstecki P. 2013. Bacterial Growth and Adaptation in Microdroplet Chemostats. Angew Chem-ger Edit 125:9076–9079. doi:10.1002/ange.201301524

Jalal ASB, Le TBK. 2020. Bacterial chromosome segregation by the ParABS system. Open Biol 10:200097. doi:10.1098/rsob.200097

Jarosławski S, Duquesne K, Sturgis JN, Scheuring S. 2009. High-resolution architecture of the outer membrane of the Gram-negative bacteria Roseobacter denitrificans. Mol Microbiol 74:1211–1222. doi:10.1111/j.1365-2958.2009.06926.x

Jelli E, Ohmura T, Netter N, Abt M, Jiménez-Siebert E, Neuhaus K, Rode DKH, Nadell CD, Drescher K. 2023. Single-cell segmentation in bacterial biofilms with an optimized deep learning method enables tracking of cell lineages and measurements of growth rates. Mol Microbiol. doi:10.1111/mmi.15064

Jeong Y, Kong W, Lu T, Irudayaraj J. 2023. Soft hydrogel-shell confinement systems as bacteria-based bioactuators and biosensors. Biosens Bioelectron 219:114809. doi:10.1016/j.bios.2022.114809

Justice SS, Harrison A, Becknell B, Mason KM. 2014. Bacterial differentiation, development, and disease: mechanisms for survival. Fems Microbiol Lett 360:1–8. doi:10.1111/1574-6968.12602

Justice SS, Hung C, Theriot JA, Fletcher DA, Anderson GG, Footer MJ, Hultgren SJ. 2004. Differentiation and developmental pathways of uropathogenic Escherichia coli in urinary tract pathogenesis. Proc National Acad Sci 101:1333–1338. doi:10.1073/pnas.0308125100

Justice SS, Hunstad DA, Cegelski L, Hultgren SJ. 2008. Morphological plasticity as a bacterial survival strategy. Nat Rev Microbiol 6:162–168. doi:10.1038/nrmicro1820

Kaminski TS, Scheler O, Garstecki P. 2016. Droplet microfluidics for microbiology: techniques, applications and challenges. Lab Chip 16:2168–2187. doi:10.1039/c6lc00367b

Kannaiah S, Livny J, Amster-Choder O. 2019. Spatiotemporal Organization of the E. coli Transcriptome: Translation Independence and Engagement in Regulation. Mol Cell 76:574-589.e7. doi:10.1016/j.molcel.2019.08.013

Kellogg RA, Gómez-Sjöberg R, Leyrat AA, Tay S. 2014. High-throughput microfluidic single-cell analysis pipeline for studies of signaling dynamics. Nat Protoc 9:1713–1726. doi:10.1038/nprot.2014.120

Kimkes TEP, Heinemann M. 2018. Reassessing the role of the Escherichia coli CpxAR system in sensing surface contact. Plos One 13:e0207181. doi:10.1371/journal.pone.0207181

Knapp BD, Odermatt P, Rojas ER, Cheng W, He X, Huang KC, Chang F. 2019. Decoupling of Rates of Protein Synthesis from Cell Expansion Leads to Supergrowth. Cell Syst 9:434-445.e6. doi:10.1016/j.cels.2019.10.001

Kobayashi SD, Malachowa N, DeLeo FR. 2015. Pathogenesis of Staphylococcus aureus Abscesses. Am J Pathol 185:1518–1527. doi:10.1016/j.ajpath.2014.11.030

Koch AL. 1996. WHAT SIZE SHOULD A BACTERIUM BE? A Question of Scale. Annu Rev Microbiol 50:317–348. doi:10.1146/annurev.micro.50.1.317

Koch AL, Lane SL, Miller JA, Nickens DG. 1987. Contraction of filaments of Escherichia coli after disruption of cell membrane by detergent. J Bacteriol 169:1979–1984. doi:10.1128/jb.169.5.1979-1984.1987

Koch AL, Woeste S. 1992. Elasticity of the sacculus of Escherichia coli. J Bacteriol 174:4811–4819. doi:10.1128/jb.174.14.4811-4819.1992

Kong HH, Segre JA. 2012. Skin Microbiome: Looking Back to Move Forward. J Invest Dermatol 132:933–939. doi:10.1038/jid.2011.417

Konovalova A, Mitchell AM, Silhavy TJ. 2016. A lipoprotein/β-barrel complex monitors lipopolysaccharide integrity transducing information across the outer membrane. Elife 5:e15276. doi:10.7554/elife.15276

Koprowski P, Grajkowski W, Balcerzak M, Filipiuk I, Fabczak H, Kubalski A. 2015. Cytoplasmic Domain of MscS Interacts with Cell Division Protein FtsZ: A Possible Non-Channel Function of the

Mechanosensitive Channel in Escherichia Coli. Plos One 10:e0127029. doi:10.1371/journal.pone.0127029

Kovach K, Davis-Fields M, Irie Y, Jain K, Doorwar S, Vuong K, Dhamani N, Mohanty K, Touhami A, Gordon VD. 2017. Evolutionary adaptations of biofilms infecting cystic fibrosis lungs promote mechanical toughness by adjusting polysaccharide production. npj Biofilms Microbiomes 3:1. doi:10.1038/s41522-016-0007-9

Krcmery S, Naber KG, Dietzenbach. GCUSGCUSGKGN Straubing (principal investigator); R Barth, Mallersdorf; W Bischoff, Backnang; M Indig, Trier; KD Lauber, Gießen; H Roth, Breisach; K Schalkhäuser, Dorfen; M Westenfelder, Krefeld; E Wutzke; 1999. Ciprofloxacin once versus twice daily in the treatment of complicated urinary tract infections. Int J Antimicrob Agents 11:133–138. doi:10.1016/s0924-8579(98)00088-0

Kühn MJ, Macmillan H, Talà L, Inclan Y, Patino R, Pierrat X, Al-Mayyah Z, Engel JN, Persat A. 2023. Two antagonistic response regulators control Pseudomonas aeruginosa polarization during mechanotaxis. EMBO J 42:e112165. doi:10.15252/embj.2022112165

Kühn MJ, Talà L, Inclan YF, Patino R, Pierrat X, Vos I, Al-Mayyah Z, Macmillan H, Negrete J, Engel JN, Persat A. 2021. Mechanotaxis directs Pseudomonas aeruginosa twitching motility. Proc Natl Acad Sci 118:e2101759118. doi:10.1073/pnas.2101759118

Kysela DT, Randich AM, Caccamo PD, Brun YV. 2016. Diversity Takes Shape: Understanding the Mechanistic and Adaptive Basis of Bacterial Morphology. Plos Biol 14:e1002565. doi:10.1371/journal.pbio.1002565

Lacour S, Landini P. 2004. **σ** S -Dependent Gene Expression at the Onset of Stationary Phase in Escherichia coli : Function of **σ** S -Dependent Genes and Identification of Their Promoter Sequences. J Bacteriol 186:7186–7195. doi:10.1128/jb.186.21.7186-7195.2004

Ladouceur A-M, Parmar BS, Biedzinski S, Wall J, Tope SG, Cohn D, Kim A, Soubry N, Reyes-Lamothe R, Weber SC. 2020. Clusters of bacterial RNA polymerase are biomolecular condensates that assemble through liquid–liquid phase separation. Proc National Acad Sci 117:18540–18549. doi:10.1073/pnas.2005019117

Laloux G, Jacobs-Wagner C. 2013. How do bacteria localize proteins to the cell pole? J Cell Sci 127:11–19. doi:10.1242/jcs.138628

Lane N. 2015. The unseen world: reflections on Leeuwenhoek (1677) 'Concerning little animals.' Philos Trans R Soc B: Biol Sci 370:20140344. doi:10.1098/rstb.2014.0344

Laub MT, Goulian M. 2007. Specificity in Two-Component Signal Transduction Pathways. Genetics 41:121–145. doi:10.1146/annurev.genet.41.042007.170548

Lederberg J. 1956. BACTERIAL PROTOPLASTS INDUCED BY PENICILLIN*. Proc National Acad Sci 42:574–577. doi:10.1073/pnas.42.9.574

Lee CK, Kim AJ, Santos GS, Lai PY, Lee SY, Qiao DF, Anda JD, Young TD, Chen Y, Rowe AR, Nealson KH, Weiss PS, Wong GCL. 2016. Evolution of Cell Size Homeostasis and Growth Rate Diversity

during Initial Surface Colonization of Shewanella oneidensis. ACS Nano 10:9183–9192. doi:10.1021/acsnano.6b05123

Lele PP, Hosu BG, Berg HC. 2013. Dynamics of mechanosensing in the bacterial flagellar motor. Proc National Acad Sci 110:11839–11844. doi:10.1073/pnas.1305885110

Levin PA, Angert ER. 2015. Small but Mighty: Cell Size and Bacteria. Csh Perspect Biol 7:a019216. doi:10.1101/cshperspect.a019216

Lewis PJ. 2008. Bacterial Physiology, A Molecular Approach 1–42. doi:10.1007/978-3-540-74921-9_1

Lindner AB, Madden R, Demarez A, Stewart EJ, Taddei F. 2008. Asymmetric segregation of protein aggregates is associated with cellular aging and rejuvenation. P Natl Acad Sci Usa 105:3076–81. doi:10.1073/pnas.0708931105

Løbner-Olesen A, Skarstad K, Hansen FG, Meyenburg K von, Boye E. 1989. The DnaA protein determines the initiation mass of Escherichia coli K-12. Cell 57:881–889. doi:10.1016/0092-8674(89)90802-7

Lutkenhaus J. 2007. Assembly Dynamics of the Bacterial MinCDE System and Spatial Regulation of the Z Ring. Biochemistry 76:539–562. doi:10.1146/annurev.biochem.75.103004.142652

Maharjan S, Saleem M, Feavers IM, Wheeler JX, Care R, Derrick JP. 2016. Dissection of the function of the RmpM periplasmic protein from Neisseria meningitidis. Microbiology 162:364–375. doi:10.1099/mic.0.000227

Maier B. 2021. How Physical Interactions Shape Bacterial Biofilms. Annu Rev Biophys 50:1–17. doi:10.1146/annurev-biophys-062920-063646

Maier B, Potter L, So M, Long CD, Seifert HS, Sheetz MP. 2002. Single pilus motor forces exceed 100 pN. Proc National Acad Sci 99:16012–16017. doi:10.1073/pnas.242523299

Mair DB, Williams MAC, Chen JF, Goldstein A, Wu A, Lee PHU, Sniadecki NJ, Kim D-H. 2022. PDMS–PEG Block Copolymer and Pretreatment for Arresting Drug Absorption in Microphysiological Devices. Acs Appl Mater Inter 14:38541–38549. doi:10.1021/acsami.2c10669

Mairey E, Genovesio A, Donnadieu E, Bernard C, Jaubert F, Pinard E, Seylaz J, Olivo-Marin J-C, Nassif X, Duménil G. 2006. Cerebral microcirculation shear stress levels determine Neisseria meningitidis attachment sites along the blood–brain barrier. J Exp Medicine 203:1939–1950. doi:10.1084/jem.20060482

Majdalani N, Gottesman S. 2005. THE RCS PHOSPHORELAY: A Complex Signal Transduction System. Annu Rev Microbiol 59:379–405. doi:10.1146/annurev.micro.59.050405.101230

Männik J, Driessen R, Galajda P, Keymer JE, Dekker C. 2009. Bacterial growth and motility in sub-micron constrictions. Proc National Acad Sci 106:14861–14866. doi:10.1073/pnas.0907542106

Männik J, Wu F, Hol FJH, Bisicchia P, Sherratt DJ, Keymer JE, Dekker C. 2012. Robustness and accuracy of cell division in Escherichia coli in diverse cell shapes. Proc National Acad Sci 109:6957–6962. doi:10.1073/pnas.1120854109

Manriquez V, Nivoit P, Urbina T, Echenique-Rivera H, Melican K, Fernandez-Gerlinger M-P, Flamant P, Schmitt T, Bruneval P, Obino D, Duménil G. 2021. Colonization of dermal arterioles by Neisseria meningitidis provides a safe haven from neutrophils. Nat Commun 12:4547. doi:10.1038/s41467-021-24797-z

Marceau AH, Bahng S, Massoni SC, George NP, Sandler SJ, Marians KJ, Keck JL. 2011. Structure of the SSB–DNA polymerase III interface and its role in DNA replication. Embo J 30:4236–4247. doi:10.1038/emboj.2011.305

Mark C, Grundy TJ, Strissel PL, Böhringer D, Grummel N, Gerum R, Steinwachs J, Hack CC, Beckmann MW, Eckstein M, Strick R, O'Neill GM, Fabry B. 2020. Collective forces of tumor spheroids in three-dimensional biopolymer networks. eLife 9:e51912. doi:10.7554/elife.51912

Mason G, Rojas ER. 2022. Mechanical compression induces persistent bacterial growth during bacteriophage predation. Biorxiv 2022.08.12.503793. doi:10.1101/2022.08.12.503793

Mathelié-Guinlet M, Asmar AT, Collet J-F, Dufrêne YF. 2020. Lipoprotein Lpp regulates the mechanical properties of the E. coli cell envelope. Nat Commun 11:1789. doi:10.1038/s41467-020-15489-1

Mathews CK. 1993. The cell-bag of enzymes or network of channels? J Bacteriol 175:6377–6381. doi:10.1128/jb.175.20.6377-6381.1993

Meer BJ van, Vries H de, Firth KSA, Weerd J van, Tertoolen LGJ, Karperien HBJ, Jonkheijm P, Denning C, IJzerman AP, Mummery CL. 2017. Small molecule absorption by PDMS in the context of drug response bioassays. Biochem Biophys Res Commun 482:323–328. doi:10.1016/j.bbrc.2016.11.062

Meglio ID, Trushko A, Guillamat P, Blanch-Mercader C, Abuhattum S, Roux A. 2022. Pressure and curvature control of the cell cycle in epithelia growing under spherical confinement. Cell Reports 40:111227. doi:10.1016/j.celrep.2022.111227

Melican K, Dumenil G. 2012. Vascular colonization by Neisseria meningitidis. Curr Opin Microbiol 15:50–56. doi:10.1016/j.mib.2011.10.008

Meng J, Young G, Chen J. 2021. The Rcs System in Enterobacteriaceae: Envelope Stress Responses and Virulence Regulation. Front Microbiol 12:627104. doi:10.3389/fmicb.2021.627104

Miguel A, Zietek M, Shi H, Sueki A, Maier L, Verheul J, Blaauwen T den, Valen DV, Typas A, Huang KC. 2022. Modulation of bacterial cell size and growth rate via activation of a cell envelope stress response. bioRxiv.

Mika JT, Poolman B. 2011. Macromolecule diffusion and confinement in prokaryotic cells. Curr Opin Biotech 22:117–126. doi:10.1016/j.copbio.2010.09.009

Milo R, Phillips R. 2015. Cell Biology By The Numbers.

Minton AP. 1983. The effect of volume occupancy upon the thermodynamic activity of proteins: some biochemical consequences. Mol Cell Biochem 55:119–140. doi:10.1007/bf00673707

Mishra R, Minc N, Peter M. 2022. Cells under pressure: how yeast cells respond to mechanical forces. Trends Microbiol 30:495–510. doi:10.1016/j.tim.2021.11.006

Mitchell AM, Silhavy TJ. 2019. Envelope stress responses: balancing damage repair and toxicity. Nat Rev Microbiol 17:417–428. doi:10.1038/s41579-019-0199-0

Mogk A, Huber D, Bukau B. 2011. Integrating protein homeostasis strategies in prokaryotes. Csh Perspect Biol 3:a004366–a004366. doi:10.1101/cshperspect.a004366

Mongera A, Pochitaloff M, Gustafson HJ, Stooke-Vaughan GA, Rowghanian P, Kim S, Campàs O. 2023. Mechanics of the cellular microenvironment as probed by cells in vivo during zebrafish presomitic mesoderm differentiation. Nat Mater 22:135–143. doi:10.1038/s41563-022-01433-9

Monteiro JM, Fernandes PB, Vaz F, Pereira AR, Tavares AC, Ferreira MT, Pereira PM, Veiga H, Kuru E, VanNieuwenhze MS, Brun YV, Filipe SR, Pinho MG. 2015. Cell shape dynamics during the staphylococcal cell cycle. Nat Commun 6:8055. doi:10.1038/ncomms9055

Moolman MC, Huang Z, Krishnan ST, Kerssemakers JW, Dekker NH. 2013. Electron beam fabrication of a microfluidic device for studying submicron-scale bacteria. J Nanobiotechnol 11:12–12. doi:10.1186/1477-3155-11-12

Moore SD. 2011. Strain Engineering, Methods and Protocols. Methods Mol Biol 765:155–169. doi:10.1007/978-1-61779-197-0_10

Mora-Bau G, Platt AM, Rooijen N van, Randolph GJ, Albert ML, Ingersoll MA. 2015. Macrophages Subvert Adaptive Immunity to Urinary Tract Infection. PLoS Pathog 11:e1005044. doi:10.1371/journal.ppat.1005044

Morrison JJ, Banas DA, Madden EK, DiBiasio EC, Rowley DC, Cohen PS, Camberg JL. 2023. Metabolic flux regulates growth transitions and antibiotic tolerance in uropathogenic Escherichia coli. bioRxiv 2023.05.09.540013. doi:10.1101/2023.05.09.540013

Morrison JJ, Conti J, Camberg JL. 2022. Assembly and architecture of Escherichia coli divisome proteins FtsA and FtsZ. J Biol Chem 298:101663. doi:10.1016/j.jbc.2022.101663

Mourão MA, Hakim JB, Schnell S. 2014. Connecting the Dots: The Effects of Macromolecular Crowding on Cell Physiology. Biophys J 107:2761–2766. doi:10.1016/j.bpj.2014.10.051

Mulvey MA, Schilling JD, Hultgren SJ. 2001. Establishment of a Persistent Escherichia coli Reservoir during the Acute Phase of a Bladder Infection. Infect Immun 69:4572–4579. doi:10.1128/iai.69.7.4572-4579.2001

Murray A, Hunt T. 1994. The cell cycle: An introduction. Mol Reprod Dev 39:247–247. doi:10.1002/mrd.1080390223

Nassif X, Lowy J, Stenberg P, O'Gaora P, Ganji A, So M. 1993. Antigenic variation of pilin regulates adhesion of Neisseria meningitidis to human epithelial cells. Mol Microbiol 8:719–725. doi:10.1111/j.1365-2958.1993.tb01615.x

Navarro PP, Vettiger A, Ananda VY, Llopis PM, Allolio C, Bernhardt TG, Chao LH. 2022. Cell wall synthesis and remodelling dynamics determine division site architecture and cell shape in Escherichia coli. Nat Microbiol 7:1621–1634. doi:10.1038/s41564-022-01210-z

Neurohr GE, Amon A. 2020. Relevance and Regulation of Cell Density. Trends Cell Biol 30:213–225. doi:10.1016/j.tcb.2019.12.006

Nijjer J, Li C, Zhang Q, Lu H, Zhang S, Yan J. 2021. Mechanical forces drive a reorientation cascade leading to biofilm self-patterning. Nat Commun 12:6632. doi:10.1038/s41467-021-26869-6

Nikaido H. 2003. Molecular Basis of Bacterial Outer Membrane Permeability Revisited. Microbiol Mol Biol R 67:593–656. doi:10.1128/mmbr.67.4.593-656.2003

Ojkic N, Serbanescu D, Banerjee S. 2022. Antibiotic Resistance via Bacterial Cell Shape-Shifting. mBio 13:e00659-22. doi:10.1128/mbio.00659-22

Oldewurtel ER, Kouzel N, Dewenter L, Henseler K, Maier B. 2015. Differential interaction forces govern bacterial sorting in early biofilms. Elife 4:e10811. doi:10.7554/elife.10811

Ollion J, Elez M, Robert L. 2019. High-throughput detection and tracking of cells and intracellular spots in mother machine experiments. Nat Protoc 14:3144–3161. doi:10.1038/s41596-019-0216-9

Otto K, Silhavy TJ. 2002. Surface sensing and adhesion of Escherichia coli controlled by the Cpx-signaling pathway. Proc National Acad Sci 99:2287–2292. doi:10.1073/pnas.042521699

Pachitariu M, Stringer C. 2022. Cellpose 2.0: how to train your own model. Nat Methods 19:1634–1641. doi:10.1038/s41592-022-01663-4

Paiva TO, Geoghegan JA, Dufrêne YF. 2023. High-force catch bonds between the Staphylococcus aureus surface protein SdrE and complement regulator factor H drive immune evasion. Commun Biology 6:302. doi:10.1038/s42003-023-04660-1

Park JT, Uehara T. 2008. How Bacteria Consume Their Own Exoskeletons (Turnover and Recycling of Cell Wall Peptidoglycan). Microbiol Mol Biol R 72:211–227. doi:10.1128/mmbr.00027-07

Parry BR, Surovtsev IV, Cabeen MT, O'Hern CS, Dufresne ER, Jacobs-Wagner C. 2014. The Bacterial Cytoplasm Has Glass-like Properties and Is Fluidized by Metabolic Activity. Cell 156:183–194. doi:10.1016/j.cell.2013.11.028

Patange O, Schwall C, Jones M, Villava C, Griffith DA, Phillips A, Locke JCW. 2018. Escherichia coli can survive stress by noisy growth modulation. Nat Commun 9:5333. doi:10.1038/s41467-018-07702-z

Pedrero JAF. 2013. The importance of diffusion. Rev Mex Ortodon 1:e6. doi:10.1016/s2395-9215(16)30114-3

Pelletier J, Halvorsen K, Ha B-Y, Paparcone R, Sandler SJ, Woldringh CL, Wong WP, Jun S. 2012. Physical manipulation of the Escherichia coli chromosome reveals its soft nature. Proc National Acad Sci 109:E2649–E2656. doi:10.1073/pnas.1208689109

Pérez-González C, Alert R, Blanch-Mercader C, Gómez-González M, Kolodziej T, Bazellieres E, Casademunt J, Trepat X. 2019. Active wetting of epithelial tissues. Nat Phys 15:79–88. doi:10.1038/s41567-018-0279-5

Persat A. 2017. Bacterial mechanotransduction. Curr Opin Microbiol 36:1–6. doi:10.1016/j.mib.2016.12.002

Persat A, Inclan YF, Engel JN, Stone HA, Gitai Z. 2015a. Type IV pili mechanochemically regulate virulence factors in Pseudomonas aeruginosa. Proc National Acad Sci 112:7563–7568. doi:10.1073/pnas.1502025112

Persat A, Nadell CD, Kim MK, Ingremeau F, Siryaporn A, Drescher K, Wingreen NS, Bassler BL, Gitai Z, Stone HA. 2015b. The Mechanical World of Bacteria. Cell 161:988–97. doi:10.1016/j.cell.2015.05.005

Persat A, Stone HA, Gitai Z. 2014. The curved shape of Caulobacter crescentus enhances surface colonization in flow. Nat Commun 5:3824. doi:10.1038/ncomms4824

Pinho MG, Kjos M, Veening J-W. 2013. How to get (a)round: mechanisms controlling growth and division of coccoid bacteria. Nat Rev Microbiol 11:601–614. doi:10.1038/nrmicro3088

Pittas T, Zuo W, Boersma AJ. 2023. Cell wall damage increases macromolecular crowding effects in the Escherichia coli cytoplasm. Iscience 26:106367. doi:10.1016/j.isci.2023.106367

Pönisch W, Eckenrode KB, Alzurqa K, Nasrollahi H, Weber C, Zaburdaev V, Biais N. 2018. Pili mediated intercellular forces shape heterogeneous bacterial microcolonies prior to multicellular differentiation. Sci Rep-uk 8:16567. doi:10.1038/s41598-018-34754-4

Popp PF, Mascher T. 2019. Coordinated Cell Death in Isogenic Bacterial Populations: Sacrificing some for the Benefit of Many? J Mol Biol 431:4656–4669. doi:10.1016/j.jmb.2019.04.024

Quellec LL, Aristov A, Ramos SG, Amselem G, Bos J, Baharoglu Z, Mazel D, Baroud CN. 2023. Measuring single-cell susceptibility to antibiotics within monoclonal bacterial populations. bioRxiv 2023.03.08.531654. doi:10.1101/2023.03.08.531654

Raaphorst R, Kjos M, Veening J. 2019. BactMAP: An R package for integrating, analyzing and visualizing bacterial microscopy data. Mol Microbiol 113:297–308. doi:10.1111/mmi.14417

Raghuraman S, Schubert A, Bröker S, Jurado A, Müller A, Brandt M, Vos BE, Hofemeier AD, Abbasi F, Stehling M, Wittkowski R, Ivaska J, Betz T. 2022. Pressure Drives Rapid Burst-Like Coordinated Cellular Motion from 3D Cancer Aggregates. Adv Sci 9:2104808. doi:10.1002/advs.202104808

Raivio TL. 2005. MicroReview: Envelope stress responses and Gram-negative bacterial pathogenesis: Envelope stress responses and virulence. Mol Microbiol 56:1119–1128. doi:10.1111/j.1365-2958.2005.04625.x

Ranft J, Basan M, Elgeti J, Joanny J-F, Prost J, Jülicher F. 2010. Fluidization of tissues by cell division and apoptosis. Proc National Acad Sci 107:20863–20868. doi:10.1073/pnas.1011086107

Rawicz W, Olbrich KC, McIntosh T, Needham D, Evans E. 2000. Effect of Chain Length and Unsaturation on Elasticity of Lipid Bilayers. Biophys J 79:328–339. doi:10.1016/s0006-3495(00)76295-3

Relman DA. 2012. Learning about who we are. Nature 486:194–195. doi:10.1038/486194a

Rivera-Yoshida N, Angel JAAD, Benítez M. 2018. Microbial multicellular development: mechanical forces in action. Curr Opin Genet Dev 51:37–45. doi:10.1016/j.gde.2018.05.006

Rizzuti IF, Mascheroni P, Arcucci S, Ben-Mériem Z, Prunet A, Barentin C, Rivière C, Delanoë-Ayari H, Hatzikirou H, Guillermet-Guibert J, Delarue M. 2020. Mechanical Control of Cell Proliferation Increases Resistance to Chemotherapeutic Agents. Phys Rev Lett 125:128103. doi:10.1103/physrevlett.125.128103

Robert L, Hoffmann M, Krell N, Aymerich S, Robert J, Doumic M. 2014. Division in Escherichia coli is triggered by a size-sensing rather than a timing mechanism. Bmc Biol 12:17–17. doi:10.1186/1741-7007-12-17

Rodesney CA, Roman B, Dhamani N, Cooley BJ, Katira P, Touhami A, Gordon VD. 2017. Mechanosensing of shear by Pseudomonas aeruginosa leads to increased levels of the cyclic-di-GMP signal initiating biofilm development. P Natl Acad Sci Usa 114:5906–5911. doi:10.1073/pnas.1703255114

Rojas ER. 2020. The Mechanical Properties of Bacteria and Why they Matter. Adv Exp Med Biol 1267:1–14. doi:10.1007/978-3-030-46886-6_1

Rojas ER, Billings G, Odermatt PD, Auer GK, Zhu L, Miguel A, Chang F, Weibel DB, Theriot JA, Huang KC. 2018. The outer membrane is an essential load-bearing element in Gram-negative bacteria. Nature 559:617–621. doi:10.1038/s41586-018-0344-3

Rojas ER, Huang KC. 2018. Regulation of microbial growth by turgor pressure. Curr Opin Microbiol 42:62–70. doi:10.1016/j.mib.2017.10.015

Rojas ER, Huang KC, Theriot JA. 2017. Homeostatic Cell Growth Is Accomplished Mechanically through Membrane Tension Inhibition of Cell-Wall Synthesis. Cell Syst 5:578-590.e6. doi:10.1016/j.cels.2017.11.005

Romberg L, Levin PA. 2003. ASSEMBLY DYNAMICS OF THE BACTERIAL CELL DIVISION PROTEIN FTSZ: Poised at the Edge of Stability. Annu Rev Microbiol 57:125–154. doi:10.1146/annurev.micro.57.012903.074300

Rosen DA, Hooton TM, Stamm WE, Humphrey PA, Hultgren SJ. 2007. Detection of Intracellular Bacterial Communities in Human Urinary Tract Infection. PLoS Med 4:e329. doi:10.1371/journal.pmed.0040329

Roth BL, Poot M, Yue ST, Millard PJ. 1997. Bacterial viability and antibiotic susceptibility testing with SYTOX green nucleic acid stain. Appl Environ Microbiol 63:2421–2431. doi:10.1128/aem.63.6.2421-2431.1997

Rothschild D, Weissbrod O, Barkan E, Kurilshikov A, Korem T, Zeevi D, Costea PI, Godneva A, Kalka IN, Bar N, Shilo S, Lador D, Vila AV, Zmora N, Pevsner-Fischer M, Israeli D, Kosower N, Malka G, Wolf BC, Avnit-Sagi T, Lotan-Pompan M, Weinberger A, Halpern Z, Carmi S, Fu J, Wijmenga C, Zhernakova A, Elinav E, Segal E. 2018. Environment dominates over host genetics in shaping human gut microbiota. Nature 555:210–215. doi:10.1038/nature25973

Rudner DZ, Losick R. 2010. Protein Subcellular Localization in Bacteria. Cold Spring Harb Perspect Biol 2:a000307. doi:10.1101/cshperspect.a000307

Rusconi R, Garren M, Stocker R. 2014. Microfluidics Expanding the Frontiers of Microbial Ecology. Biophysics 43:65–91. doi:10.1146/annurev-biophys-051013-022916

Saint-Ruf C, Garfa-Traoré M, Collin V, Cordier C, Franceschi C, Matic I. 2014. Massive Diversification in Aging Colonies of Escherichia coli. J Bacteriol 196:3059–3073. doi:10.1128/jb.01421-13

Saraiva BM, Krippahl L, Filipe SR, Henriques R, Pinho MG. 2021. eHooke: A tool for automated image analysis of spherical bacteria based on cell cycle progression. Biological Imaging 1:e3. doi:10.1017/s2633903x21000027

Sbalzarini IF, Koumoutsakos P. 2005. Feature point tracking and trajectory analysis for video imaging in cell biology. J Struct Biol 151:182–195. doi:10.1016/j.jsb.2005.06.002

Schmidt F, Zimmermann J, Tanna T, Farouni R, Conway T, Macpherson AJ, Platt RJ. 2022. Noninvasive assessment of gut function using transcriptional recording sentinel cells. Science 376:eabm6038. doi:10.1126/science.abm6038

Schmoller KM, Turner JJ, Kõivomägi M, Skotheim JM. 2015. Dilution of the cell cycle inhibitor Whi5 controls budding-yeast cell size. Nature 526:268–272. doi:10.1038/nature14908

Schneider JP, Basler M. 2016. Shedding light on biology of bacterial cells. Philosophical Transactions Royal Soc B Biological Sci 371:20150499. doi:10.1098/rstb.2015.0499

Schwechheimer C, Kuehn MJ. 2015. Outer-membrane vesicles from Gram-negative bacteria: biogenesis and functions. Nat Rev Microbiol 13:605–619. doi:10.1038/nrmicro3525

Shapiro L, McAdams HH, Losick R. 2009. Why and How Bacteria Localize Proteins. Science 326:1225–1228. doi:10.1126/science.1175685

Sharma K, Dhar N, Thacker VV, Simonet TM, Signorino-Gelo F, Knott GW, McKinney JD. 2021. Dynamic persistence of UPEC intracellular bacterial communities in a human bladder-chip model of urinary tract infection. Elife 10:e66481. doi:10.7554/elife.66481

Shimizu T, Ichimura K, Noda M. 2016. The Surface Sensor NlpE of Enterohemorrhagic Escherichia coli Contributes to Regulation of the Type III Secretion System and Flagella by the Cpx Response to Adhesion. Infect Immun 84:537–549. doi:10.1128/iai.00881-15

Si F, Busiek K, Margolin W, Sun SX. 2013. Organization of FtsZ Filaments in the Bacterial Division Ring Measured from Polarized Fluorescence Microscopy. Biophys J 105:1976–1986. doi:10.1016/j.bpj.2013.09.030

Si F, Li B, Margolin W, Sun SX. 2015. Bacterial growth and form under mechanical compression. Sci Rep-uk 5:11367. doi:10.1038/srep11367

Si F, Treut GL, Sauls JT, Vadia S, Levin PA, Jun S. 2019. Mechanistic Origin of Cell-Size Control and Homeostasis in Bacteria. Curr Biol 29:1760-1770.e7. doi:10.1016/j.cub.2019.04.062

Silhavy TJ, Kahne D, Walker S. 2010. The bacterial cell envelope. Csh Perspect Biol 2:a000414. doi:10.1101/cshperspect.a000414

Siryaporn A, Kuchma SL, O'Toole GA, Gitai Z. 2014. Surface attachment induces Pseudomonas aeruginosa virulence. P Natl Acad Sci Usa 111:16860–5. doi:10.1073/pnas.1415712111

Sledjeski DD, Gottesman S. 1996. Osmotic shock induction of capsule synthesis in Escherichia coli K-12. J Bacteriol 178:1204–1206. doi:10.1128/jb.178.4.1204-1206.1996

Souchaud A, Gallet F, Graner F. 2020. Cartographie des contraintes mécaniques in situ dans les tissus vivants. Thèse.

Spahn C, Gómez-de-Mariscal E, Laine RF, Pereira PM, Chamier L von, Conduit M, Pinho MG, Jacquemet G, Holden S, Heilemann M, Henriques R. 2022. DeepBacs for multi-task bacterial image analysis using open-source deep learning approaches. Commun Biol 5:688. doi:10.1038/s42003-022-03634-z

Spahn C, Grimm JB, Lavis LD, Lampe M, Heilemann M. 2018. Whole-Cell, 3D, and Multicolor STED Imaging with Exchangeable Fluorophores. Nano Lett 19:500–505. doi:10.1021/acs.nanolett.8b04385

Spence JM, Wright L, Clark VL. 2008. Laboratory Maintenance of Neisseria gonorrhoeae. Curr Protoc Microbiol 8:4A.1.1-4A.1.26. doi:10.1002/9780471729259.mc04a01s8

Spitzer J, Poolman B. 2013. How crowded is the prokaryotic cytoplasm? Febs Lett 587:2094–2098. doi:10.1016/j.febslet.2013.05.051

Stewart PS. 2014. Biophysics of biofilm infection. Pathog Dis 70:212–218. doi:10.1111/2049-632x.12118

Storz G, Hengge R. 2020. Bacterial Stress Responses. doi:10.1128/9781555816841

Stringer C, Wang T, Michaelos M, Pachitariu M. 2020. Cellpose: a generalist algorithm for cellular segmentation. Nat Methods 18:100–106. doi:10.1038/s41592-020-01018-x

Sun J, Rutherford ST, Silhavy TJ, Huang KC. 2021a. Physical properties of the bacterial outer membrane. Nat Rev Microbiol 1–13. doi:10.1038/s41579-021-00638-0

Sun J, Shi H, Huang KC. 2021b. Hyperosmotic Shock Transiently Accelerates Constriction Rate in Escherichia coli. Front Microbiol 12:718600. doi:10.3389/fmicb.2021.718600

Sun X, Weinlandt WD, Patel H, Wu M, Hernandez CJ. 2014. A microfluidic platform for profiling biomechanical properties of bacteria. Lab Chip 14:2491–2498. doi:10.1039/c3lc51428e

Swaminathan R, Hoang CP, Verkman AS. 1997. Photobleaching recovery and anisotropy decay of green fluorescent protein GFP-S65T in solution and cells: cytoplasmic viscosity probed by green fluorescent protein translational and rotational diffusion. Biophys J 72:1900–1907. doi:10.1016/s0006-3495(97)78835-0

Szczepaniak J, Holmes P, Rajasekar K, Kaminska R, Samsudin F, Inns PG, Rassam P, Khalid S, Murray SM, Redfield C, Kleanthous C. 2020. The lipoprotein Pal stabilises the bacterial outer membrane during constriction by a mobilisation-and-capture mechanism. Nat Commun 11:1305. doi:10.1038/s41467-020-15083-5

Taheri-Araghi S, Bradde S, Sauls JT, Hill NS, Levin PA, Paulsson J, Vergassola M, Jun S. 2014. Cell-size control and homeostasis in bacteria. Curr Biology Cb 25:385–91. doi:10.1016/j.cub.2014.12.009

Talà L, Fineberg A, Kukura P, Persat A. 2019. Pseudomonas aeruginosa orchestrates twitching motility by sequential control of type IV pili movements. Nat Microbiol 4:774–780. doi:10.1038/s41564-019-0378-9

Tanaka H, Yasuzawa K, Kohno K, Goshima N, Kano Y, Saiki T, Imamoto F. 1995. Role of HU proteins in forming and constraining supercoils of chromosomal DNA inEscherichia coli. Mol Gen Genet MGG 248:518–526. doi:10.1007/bf02423446

Thanbichler M, Shapiro L. 2008. Getting organized — how bacterial cells move proteins and DNA. Nat Rev Microbiol 6:28–40. doi:10.1038/nrmicro1795

Thomas WE, Trintchina E, Forero M, Vogel V, Sokurenko EV. 2002. Bacterial Adhesion to Target Cells Enhanced by Shear Force. Cell 109:913–923. doi:10.1016/s0092-8674(02)00796-1

Tiruvadi-Krishnan S, Männik Jaana, Kar P, Lin J, Amir A, Männik Jaan. 2022. Coupling between DNA replication, segregation, and the onset of constriction in Escherichia coli. Cell Reports 38:110539. doi:10.1016/j.celrep.2022.110539

Toepke MW, Beebe DJ. 2006. PDMS absorption of small molecules and consequences in microfluidic applications. Lab Chip 6:1484–1486. doi:10.1039/b612140c

Trejo M, Douarche C, Bailleux V, Poulard C, Mariot S, Regeard C, Raspaud E. 2013. Elasticity and wrinkled morphology of Bacillus subtilis pellicles. Proc National Acad Sci 110:2011–2016. doi:10.1073/pnas.1217178110

Treuner-Lange A, Søgaard-Andersen L. 2014. Regulation of cell polarity in bacteria. J Cell Biol 206:7–17. doi:10.1083/jcb.201403136

Trevors JT, Elsas JD van, Bej AK. 2012. The Molecularly Crowded Cytoplasm of Bacterial Cells: Dividing Cells Contrasted with Viable but Non-culturable (VBNC) Bacterial Cells. Curr issues Mol Biol 15:1–6.

Trivedi RR, Crooks JA, Auer GK, Pendry J, Foik IP, Siryaporn A, Abbott NL, Gitai Z, Weibel DB. 2018. Mechanical Genomic Studies Reveal the Role of D-Alanine Metabolism in Pseudomonas aeruginosa Cell Stiffness. Mbio 9:e01340-18. doi:10.1128/mbio.01340-18

Tyedmers J, Mogk A, Bukau B. 2010. Cellular strategies for controlling protein aggregation. Nat Rev Mol Cell Bio 11:777–788. doi:10.1038/nrm2993

Typas A, Banzhaf M, Gross CA, Vollmer W. 2012. From the regulation of peptidoglycan synthesis to bacterial growth and morphology. Nat Rev Microbiol 10:123–136. doi:10.1038/nrmicro2677

Ultee E, Ramijan K, Dame RT, Briegel A, Claessen D. 2019. Advances in Microbial Physiology. Adv Microb Physiol 74:97–141. doi:10.1016/bs.ampbs.2019.02.001

Unger MA, Chou H-P, Thorsen T, Scherer A, Quake SR. 2000. Monolithic Microfabricated Valves and Pumps by Multilayer Soft Lithography. Science 288:113–116. doi:10.1126/science.288.5463.113

Vandermeer J. 2010. How Populations Grow: The Exponential and Logistic Equations. Nature Education.

Velve-Casquillas G, Berre ML, Piel M, Tran PT. 2010. Microfluidic tools for cell biological research. Nano Today 5:28–47. doi:10.1016/j.nantod.2009.12.001

Veyrier FJ, Biais N, Morales P, Belkacem N, Guilhen C, Ranjeva S, Sismeiro O, Péhau-Arnaudet G, Rocha EP, Werts C, Taha M-K, Boneca IG. 2015. Common Cell Shape Evolution of Two Nasopharyngeal Pathogens. Plos Genet 11:e1005338. doi:10.1371/journal.pgen.1005338

Vollmer W, Blanot D, Pedro MAD. 2008a. Peptidoglycan structure and architecture. Fems Microbiol Rev 32:149–167. doi:10.1111/j.1574-6976.2007.00094.x

Vollmer W, Joris B, Charlier P, Foster S. 2008b. Bacterial peptidoglycan (murein) hydrolases. FEMS Microbiol Rev 32:259–286. doi:10.1111/j.1574-6976.2007.00099.x

Vorselen D, Wang Y, Jesus MM de, Shah PK, Footer MJ, Huse M, Cai W, Theriot JA. 2020. Microparticle traction force microscopy reveals subcellular force exertion patterns in immune cell–target interactions. Nat Commun 11:20. doi:10.1038/s41467-019-13804-z

Vulto P, Glade N, Altomare L, Bablet J, Tin LD, Medoro G, Chartier I, Manaresi N, Tartagni M, Guerrieri R. 2004. Microfluidic channel fabrication in dry film resist for production and prototyping of hybrid chips. Lab a Chip 5:158–162. doi:10.1039/b411885e

Wadhwa N, Phillips R, Berg HC. 2019. Torque-dependent remodeling of the bacterial flagellar motor. Proc National Acad Sci 116:11764–11769. doi:10.1073/pnas.1904577116

Waterbeemd B van de, Streefland M, Ley P van der, Zomer B, Dijken H van, Martens D, Wijffels R, Pol L van der. 2010. Improved OMV vaccine against Neisseria meningitidis using genetically engineered strains and a detergent-free purification process. Vaccine 28:4810–4816. doi:10.1016/j.vaccine.2010.04.082

Weart RB, Levin PA. 2003. Growth Rate-Dependent Regulation of Medial FtsZ Ring Formation. J Bacteriol 185:2826–2834. doi:10.1128/jb.185.9.2826-2834.2003

Weber H, Polen T, Heuveling J, Wendisch VF, Hengge R. 2005. Genome-Wide Analysis of the General Stress Response Network in Escherichia coli : **σ** S -Dependent Genes, Promoters, and Sigma Factor Selectivity. J Bacteriol 187:1591–1603. doi:10.1128/jb.187.5.1591-1603.2005

Wessel AK, Hmelo L, Parsek MR, Whiteley M. 2013. Going local: technologies for exploring bacterial microenvironments. Nat Rev Microbiol 11:337–348. doi:10.1038/nrmicro3010

Westling-Häggström B, Elmros T, Normark S, Winblad B. 1977. Growth pattern and cell division in Neisseria gonorrhoeae. J Bacteriol 129:333–342. doi:10.1128/jb.129.1.333-342.1977

Whitesides GM. 2006. The origins and the future of microfluidics. Nature 442:368–373. doi:10.1038/nature05058

Willis L, Huang KC. 2017. Sizing up the bacterial cell cycle. Nat Rev Microbiol 15:606–620. doi:10.1038/nrmicro.2017.79

Wolde PR ten, Mugler A. 2014. Chapter Twelve Importance of Crowding in Signaling, Genetic, and Metabolic Networks. Int Rev Cel Mol Bio 307:419–442. doi:10.1016/b978-0-12-800046-5.00012-6

Wright KJ, Seed PC, Hultgren SJ. 2007. Development of intracellular bacterial communities of uropathogenic Escherichia coli depends on type 1 pili. Cell Microbiol 9:2230–2241. doi:10.1111/j.1462-5822.2007.00952.x

Wu F, Swain P, Kuijpers L, Zheng X, Felter K, Guurink M, Solari J, Jun S, Shimizu TS, Chaudhuri D, Mulder B, Dekker C. 2019. Cell Boundary Confinement Sets the Size and Position of the E. coli Chromosome. Curr Biol 29:2131-2144.e4. doi:10.1016/j.cub.2019.05.015

Wu LJ, Errington J. 2012. Nucleoid occlusion and bacterial cell division. Nat Rev Microbiol 10:8–12. doi:10.1038/nrmicro2671

Xiang Y, Surovtsev IV, Chang Y, Govers SK, Parry BR, Liu J, Jacobs-Wagner C. 2021. Interconnecting solvent quality, transcription, and chromosome folding in Escherichia coli. Cell. doi:10.1016/j.cell.2021.05.037

Xu Y. 2018. Nanofluidics: A New Arena for Materials Science. Adv Mater 30:1702419. doi:10.1002/adma.201702419

Yakovenko O, Sharma S, Forero M, Tchesnokova V, Aprikian P, Kidd B, Mach A, Vogel V, Sokurenko E, Thomas WE. 2008. FimH Forms Catch Bonds That Are Enhanced by Mechanical Force Due to Allosteric Regulation*. J Biological Chem 283:11596–11605. doi:10.1074/jbc.m707815200

Yan J, Bassler BL. 2019. Surviving as a Community: Antibiotic Tolerance and Persistence in Bacterial Biofilms. Cell Host Microbe 26:15–21. doi:10.1016/j.chom.2019.06.002

Yan J, Fei C, Mao S, Moreau A, Wingreen NS, Košmrlj A, Stone HA, Bassler BL. 2018. Mechanical instability and interfacial energy drive biofilm morphogenesis. eLife 8:e43920. doi:10.7554/elife.43920

Yang D, Männik Jaana, Retterer ST, Männik Jaan. 2020. The effects of polydisperse crowders on the compaction of the Escherichia coli nucleoid. Mol Microbiol 113:1022–1037. doi:10.1111/mmi.14467

Yang DC, Blair KM, Salama NR. 2016. Staying in Shape: the Impact of Cell Shape on Bacterial Survival in Diverse Environments. Microbiol Mol Biol R 80:187–203. doi:10.1128/mmbr.00031-15

Yao X, Jericho M, Pink D, Beveridge T. 1999. Thickness and elasticity of gram-negative murein sacculi measured by atomic force microscopy. J Bacteriol 181:6865–75. doi:10.1128/jb.181.22.6865-6875.1999

Yao Z, Carballido-López R. 2014. Fluorescence Imaging for Bacterial Cell Biology: From Localization to Dynamics, From Ensembles to Single Molecules. Annu Rev Microbiol 68:1–18. doi:10.1146/annurev-micro-091213-113034

Yao Z, Kahne D, Kishony R. 2012. Distinct Single-Cell Morphological Dynamics under Beta-Lactam Antibiotics. Mol Cell 48:705–712. doi:10.1016/j.molcel.2012.09.016

Young KD. 2007. Bacterial morphology: why have different shapes? Curr Opin Microbiol 10:596–600. doi:10.1016/j.mib.2007.09.009

Young KD. 2006. The selective value of bacterial shape. Microbiol Mol Biology Rev Mmbr 70:660–703. doi:10.1128/mmbr.00001-06

Yu FB, Willis L, Chau RMW, Zambon A, Horowitz M, Bhaya D, Huang KC, Quake SR. 2017. Long-term microfluidic tracking of coccoid cyanobacterial cells reveals robust control of division timing. Bmc Biol 15:11. doi:10.1186/s12915-016-0344-4

Zaslaver A, Bren A, Ronen M, Itzkovitz S, Kikoin I, Shavit S, Liebermeister W, Surette MG, Alon U. 2006. A comprehensive library of fluorescent transcriptional reporters for Escherichia coli. Nat Methods 3:623–628. doi:10.1038/nmeth895

Zhang C, Shao PG, Kan JA van, Maarel JRC van der. 2009. Macromolecular crowding induced elongation and compaction of single DNA molecules confined in a nanochannel. Proc National Acad Sci 106:16651–16656. doi:10.1073/pnas.0904741106

Zhang M, Zhang J, Wang Y, Wang J, Achimovich AM, Acton ST, Gahlmann A. 2020. Non-invasive single-cell morphometry in living bacterial biofilms. Nat Commun 11:6151. doi:10.1038/s41467-020-19866-8

Zhang Q, Li J, Nijjer J, Lu H, Kothari M, Alert R, Cohen T, Yan J. 2021. Morphogenesis and cell ordering in confined bacterial biofilms. Proc National Acad Sci 118:e2107107118. doi:10.1073/pnas.2107107118

Zhang TY, Suen CY. 1984. A fast parallel algorithm for thinning digital patterns. Commun ACM 27:236–239. doi:10.1145/357994.358023

Zhou H-X, Rivas G, Minton AP. 2008. Macromolecular crowding and confinement: biochemical, biophysical, and potential physiological consequences. Annu Rev Biophys 37:375–97. doi:10.1146/annurev.biophys.37.032807.125817

Zhou X, Halladin DK, Rojas ER, Koslover EF, Lee TK, Huang KC, Theriot JA. 2015. Bacterial division. Mechanical crack propagation drives millisecond daughter cell separation in Staphylococcus aureus. Sci New York N Y 348:574–8. doi:10.1126/science.aaa1511

Zietek M, Miguel A, Khusainov I, Shi H, Asmar AT, Ram S, Wartel M, Sueki A, Schorb M, Goulian M, Collet J-F, Beck M, Huang KC, Typas A. 2022. Bacterial cell widening alters periplasmic size and activates envelope stress responses. bioRxiv. doi:10.1101/2022.07.26.501644

Zimmerman SB, Minton AP. 1993. Macromolecular Crowding: Biochemical, Biophysical, and Physiological Consequences. Annu Rev Bioph Biom 22:27–65. doi:10.1146/annurev.bb.22.060193.000331

Zimmerman SB, Murphy LD. 1996. Macromolecular crowding and the mandatory condensation of DNA in bacteria. Febs Lett 390:245–248. doi:10.1016/0014-5793(96)00725-9

Zou Y, Li Y, Dillon J-AR. 2017. The distinctive cell division interactome of Neisseria gonorrhoeae. BMC Microbiol 17:232. doi:10.1186/s12866-017-1140-1

Zuela-Sopilniak N, Lammerding J. 2022. Can't handle the stress? Mechanobiology and disease. Trends Mol Med 28:710–725. doi:10.1016/j.molmed.2022.05.010

# Credits

Figure 1 : Adapted from (Milo and Phillips, 2015), with permission from Springer
Figure 2 : Adapted from (Kysela et al., 2016), licensed under a Creative Common License
Figure 3 : Adapted from (Brown et al., 2015), with permission from Springer
Figure 4 : Adapted from (Sun et al., 2021a), with permission from Springer
Figure 5.A: Reproduced from (Egan et al., 2020), with permission from Springer
Figure 5.B: Adapted from (Typas et al., 2012) with permission from Springer
Figure 6: Adapted from (Goodsell, 2009), with permission from Springer
Figure 7.A-B: Reproduced from (Ellis, 2001), with permission from Elsevier
Figures 7.C-D, 8.C: Reproduced from (Xiang et al., 2021), with permission from Elsevier
Figure 7.E: Reproduced from (Parry et al., 2014), with permission from Elsevier
Figure 8.A-B: Reproduced from (Gray et al., 2019), with permission from Elsevier
Figure 9: Adapted from (Chien et al., 2012), with permission from Elsevier
Figure 10: Reproduced from (Wu and Errington, 2012), with permission from Springer
Figure 11.A: Reproduced from (Laub and Goulian, 2007), with permission from Annual Reviews
Figure11.B: Adapted from (Patange et al., 2018), licensed under a Creative Common License
Figure 12.A-B: Reproduced from (Mitchell and Silhavy, 2019), with permission from Springer
Figure 12.C: Adapted from (Hostetler, 2018), with permission from Zachary Hostetler
Figures 13, 15: Adapted from (Dufrêne and Persat, 2020), with permission from Springer
Figure 14.A: Adapted from (Iskratsch et al., 2014), with permission from Springer
Figure 14.B: Adapted from (Mishra et al., 2022), with permission from Elsevier
Figure 16.A: Reproduced from (Männik et al., 2012), with permission from PNAS
Figure 15.B-C: Reproduced from (Si et al., 2015), licensed under a Creative Common License
Figure 50: Adapted from (Alric, 2021), with permission from Baptiste Alric
Appendix: (Ershov et al., 2022), with permission from Springer

# Abstract

Microbes frequently proliferate within complex space-limited environments, where they experience and adapt to mechanical forces in order to survive and proliferate. However, the mechanisms involved in mechanical sensing and their physiological impact on bacterial communities remain poorly understood. To address this question, we designed microfluidic chambers connected to 400nm-wide channels to monitor bacterial growth upon confinement in a well-defined mechano-chemical environment, mimicking features of the complex environment encountered by bacteria during infection or biofilm formation. This device has been validated on various bacterial species with different shapes and envelopes, including pathogens. To decipher the impact of mechanical confinement on bacterial physiology, we use the biofilm-forming model organism Escherichia coli. We find that, as soon as bacteria become confluent in the chambers, their proliferation generates large mechanical forces on the surrounding microenvironment (~300kPa). Using high-resolution microscopy together with a machine-learning based image analysis pipeline, we show that mechanical stress induces a strong uncoupling between growth and division rates at the onset of confinement. This leads to a reversible morphological transition from rod-shaped to small quasi-isotropic bacteria, through multiple, fast divisions followed by division arrest. These non-dividing mini cells are characterized by a strong transcriptional reprogramming that favors bacterial survival, and an increase in cytoplasmic crowding, both being concomitant with mechanical stress build-up. In our current model, we propose that bacterial division is triggered early on upon confinement via a crowding-mediated fast increase in the concentration of a key component of the divisome machinery FtsZ, that bypasses the regulation of division by the envelope stress response. An additional increment in intracellular crowding up to a certain threshold finally inhibits bacterial division, potentially through nucleoid occlusion and the activity of the FtsZ polymerization antagonist SlmA. Altogether, we show that mechanical sensing via the bacterial envelope together with crowding sensing at the cytoplasmic level induce a unique physiological state in bacteria to adapt to large mechanical constraints, with important implications in bacterial survival and infection outcome.



# Résumé

Les microbes prolifèrent fréquemment dans des environnements restreints, où ils sont sujets à des contraintes mécaniques auxquelles ils s'adaptent pour survivre et proliférer. Cependant, les mécanismes impliqués dans la perception de ces contraintes et leur impact sur les communautés bactériennes restent méconnus. Afin d'explorer cette question, nous avons mis au point des chambres microfluidiques connectées à des canaux nanométriques, de largeur 400nm. Ces chambres nous ont permis d'étudier la prolifération des bactéries sous confinement dans un environnement mécano-chimique contrôlé, représentatif des environnements rencontrés par les bactéries au cours de l'infection, tel qu'au sein des biofilms. Ce système expérimental a été utilisé pour confiner plusieurs espèces bactériennes, y compris pathogènes, avec des formes et des enveloppes variées. Pour comprendre l'impact du confinement mécanique sur la physiologie bactérienne, nous avons utilisé la bactérie modèle *Escherichia coli*. Nous avons montré que la prolifération des bactéries, une fois à confluence, génère des contraintes mécaniques considérables sur le microenvironnement (~300kPa). Grâce à la microscopie de haute résolution combinée à une méthode d'analyse d'image basée sur le machine-learning, nous avons montré que ces contraintes mécaniques induisent un découplage immédiat de la croissance et de la division. Ce découplage conduit à l'émergence de changements morphologiques majeurs, au cours desquels les bactéries initialement en batônnets deviennent plus petites et adoptent une forme quasi isotropique. Cette transition morphologique est initiée par une série de divisions successives sans que les bactéries ne croissent, et conduit *in fine* a un arrêt de la division. Ces mini bactéries sont caractérisées par une reprogrammation transcriptionnelle, qui permet leur survie sous confinement, ainsi qu'une augmentation de l'encombrement cytoplasmique, tous deux induits par le confinement. Dans notre modèle actuel, nous proposons que la division bactérienne est rapidement déclenchée sous confinement, par l'augmentation de la concentration de FtsZ, un composant essentiel du complexe protéique responsable de la division, médiée par l'encombrement, contournant ainsi la régulation médiée par la voie de réponse au stress à l'enveloppe. Une augmentation supplémentaire de l'encombrement finit par inhiber la division, potentiellement via un mécanisme protecteur de l'ADN qui pourrait être régulé par la protéine SlmA, antagoniste de la polymérisation de FtsZ. Au cours de ce travail de thèse, nous avons donc montré que la perception des contraintes mécaniques à la fois au niveau de l'enveloppe et au niveau du cytoplasme induit un état physiologique unique chez les bactéries, qui leur permet de s'adapter aux contraintes mécaniques, avec des conséquences importantes dans la survie bactérienne et l'issue de l'infection.